

DOCTORAL THESIS

Machine Learning
Analysis of Baltic Sea
Surface Current Variability

Amirhossein Barzandeh

TALLINN UNIVERSITY OF TECHNOLOGY
DOCTORAL THESIS
42/2026

Machine Learning Analysis of Baltic Sea Surface Current Variability

AMIRHOSSEIN BARZANDEH



TALLINN UNIVERSITY OF TECHNOLOGY
School of Science
Department of Marine Systems

The dissertation was accepted for the defence of the degree of Doctor of Philosophy (in Physical Oceanography, Earth Sciences, LALD22 - Science) on 17 June 2026

Supervisor: Dr. Ilja Maljutenko,
Department of Marine Systems, Tallinn University of Technology,
Tallinn, Estonia

Co-supervisor: Dr. Sander Rikka,
Department of Marine Systems, Tallinn University of Technology,
Tallinn, Estonia

Advisor: Prof. Urmas Raudsepp,
Department of Marine Systems, Tallinn University of Technology,
Tallinn, Estonia

Opponents: Prof. Dr. Markus Meier,
Leibniz Institute for Baltic Sea Research Warnemünde (IOW),
Rostock, Germany

Opponents: Dr. Phys. Uldis Bethers,
Institute of Numerical Modelling, University of Latvia,
Riga, Latvia

Defence of the thesis: 16 July 2026, Tallinn

Declaration:

Hereby I declare that this doctoral thesis, my original investigation and achievement, submitted for the doctoral degree at Tallinn University of Technology, has not been submitted for any academic degree elsewhere.

Amirhossein Barzandeh

signature

Copyright: Amirhossein Barzandeh, 2026
ISSN 2585-6898 (paperback)
ISBN 978-9916-80-521-3 (paperback)
ISSN 2585-6901 (PDF)
ISBN 978-9916-80-522-0 (PDF)
<https://doi.org/10.23658/taltech.42/2026>

Barzandeh, A. (2026). *Machine Learning Analysis of Baltic Sea Surface Current Variability* [TalTech Press]. <https://doi.org/10.23658/taltech.42/2026>

TALLINN UNIVERSITY OF TECHNOLOGY
DOCTORAL THESIS
42/2026

Läänemere pinnahoovuste muutlikkuse analüüs masinõppe meetoditega

AMIRHOSSEIN BARZANDEH



Contents

List of Publications	7
Author's Contributions to the Publications	8
Abbreviations.....	10
1 Introduction	11
1.1 The Baltic Sea as the Study Region	11
1.1.1 Historical Development of Baltic Sea Circulation Studies	12
1.2 AI and Marine Data	14
1.3 Consolidation of the Research Justification and Goals	15
2 Materials and Methods.....	17
2.1 Main Data	17
2.1.1 Additional Data	17
2.2 Analysis of Baltic SSCs.....	17
2.2.1 SOM.....	17
2.2.2 Geostrophic and Ageostrophic Decomposition of Surface Currents .	19
2.3 Forecasting of Baltic SSCs	21
2.3.1 Data-driven model formulation and predictors	21
2.3.2 Convolutional U-shaped neural network architecture.....	22
2.3.3 Training strategy and one-step forecast evaluation.....	23
2.3.4 Recursive multi-day forecast experiment	25
2.3.5 XAI diagnostics	26
3 Results and Discussion	29
3.1 SSC variabilities.....	31
3.2 Decomposition of SSC into Geostrophic and Ageostrophic Components	36
3.3 Data-Driven Emulation of Daily SSC	38
3.3.1 Regional proof of concept: sciCUN in the Gulf of Riga.....	38
3.3.2 Basin-scale extension: DeepCUN over the Baltic Sea	39
3.3.3 Explainability of the learned SSC mapping	41
3.3.4 Potential multi-day forecast skill.....	42
3.4 From physical interpretation to efficient emulation	44
4 Conclusion.....	45
List of Figures	47
References.....	48
Acknowledgements	57
Abstract.....	58
Kokkuvõte	59
Appendix 1.....	61
Appendix 2	83

Appendix 3	99
Appendix 4	117
Curriculum Vitae	158
Elulookirjeldus.....	162

List of Publications

The present Ph.D. thesis is based on the following publications that are referred to in the text by Roman numbers.

- I J. Elken, A. Barzandeh, I. Maljutenko, and S. Rikka, “Reconstruction of baltic gridded sea levels from tide gauge and altimetry observations using spatiotemporal statistics from reanalysis,” *Remote Sensing*, vol. 16, no. 15, 2024
- II A. Barzandeh, I. Maljutenko, S. Rikka, P. Lagemaa, A. Männik, R. Uiboupin, and U. Raudsepp, “Sea surface circulation in the Baltic Sea: decomposed components and pattern recognition,” *Scientific Reports*, vol. 14, no. 1, p. 18649, 2024
- III A. Barzandeh, I. Maljutenko, S. Rikka, and U. Raudsepp, “sciCUN: A deep learning model for daily sea surface current fields inference—a case study of the Gulf of Riga,” *Ocean Modelling*, vol. 201, p. 102693, 2026
- IV A. Barzandeh, C. Manss, F. Stahl, I. Maljutenko, S. Rikka, and U. Raudsepp, “Data-driven emulation of numerically simulated Baltic Sea surface currents with a deep convolutional U-Net: Explainability and potential forecast skill,” *JGR: Machine Learning and Computation*, 2026. Accepted for publication / In press

Author's Contributions to the Publications

I I was responsible for data curation and validation.

II I was the primary author, responsible for all technical and editorial aspects.

III I was the primary author, responsible for all technical and editorial aspects.

IV I was the primary author, responsible for all technical and editorial aspects.

Approbation

I presented the results of the thesis at the following conferences:

1. **A. Barzandeh**, C. Manß, F. Stahl, I. Maljutenko, S. Rikka, and U. Raudsepp. 'Partial Emulation of Simulated Sea-Surface Currents in the Baltic Sea: An Assessment of Explainability and Potential Forecast Skill', European Geosciences Union (EGU) General Assembly 2026 3-8 May, Vienna, Austria
2. **A. Barzandeh**, I. Maljutenko, S. Rikka, and U. Raudsepp. 'Data-Driven Retrieval of Ageostrophic Surface Currents from Satellite Geostrophy and Reanalysis Winds in a Marginal Sea', 5th ECMWF-ESA Machine Learning Workshop 2026 13-17 April, Bologna, Italy
3. **A. Barzandeh**, I. Maljutenko, S. Rikka, and U. Raudsepp. 'A Surrogate Model for Daily Sea Surface Current Fields Prediction Using CNN-UNET', European Geosciences Union (EGU) General Assembly 2025 27 April–2 May, Vienna, Austria
4. **A. Barzandeh**, I. Maljutenko, S. Rikka, and U. Raudsepp. 'Sea Surface Current Fields Prediction with a Surrogate Deep Learning Model Using CNN-UNET: A Case Study of the Gulf of Riga', Baltic Sea Science Congress 2025 26-30 May, Sopot, Poland
5. **A. Barzandeh**. 'Sea surface current components in the Baltic Sea'. The School of Science XV Conference 2023, 29 November 2023, Tallinn, Estonia.
6. **A. Barzandeh**, I. Maljutenko, S. Rikka, and U. Raudsepp. 'Geostrophic and Ageostrophic Components of Sea Surface Currents in the Baltic Sea', Baltic Sea Science Congress 2023 21-25 May, Helsinki, Finland.
7. **A. Barzandeh**, I. Maljutenko, S. Rikka, and U. Raudsepp. 'Geostrophic component of sea surface current in the Baltic Sea', International Baltic Earth Winter School for Young Scientists on "Earth System Science for the Baltic Sea Region" 2023, 17–21 March 2023, Warnemünde, Germany.

Abbreviations

AI	Artificial Intelligence
BMU	Best-Matching Unit
CMEMS	Copernicus Marine Environment Monitoring Service
CNN	Convolutional Neural Network
DeepCUN	Deep convolutional U-Net
DJE	Diagonal Jacobian Elasticity
ECMWF	European Centre for Medium-Range Weather Forecasts
EOF	Empirical Orthogonal Function
ERA5	Fifth-generation ECMWF atmospheric reanalysis
LRP	Layer-wise Relevance Propagation
MAE	Mean Absolute Error
NEMO	Nucleus for European modeling of the Ocean
PCA	Principal Component Analysis
SLA	Sea-level Anomaly
SOM	Self-Organizing Map
SSC	Sea Surface Current
sciCUN	surface current inference using CNN-U-Net
U-Net	U-shaped neural network architecture
XAI	Explainable Artificial Intelligence

1 Introduction

1.1 The Baltic Sea as the Study Region

The Baltic Sea is a semi-enclosed brackish marginal sea in northeastern Europe, connected to the North Sea through the Danish Straits. It is bordered by nine countries and is one of the world's largest brackish-water bodies [5, 6, 7, 8]. Geographically, the Baltic Sea, including the Danish Straits, extends from about 54.0° N to 66.0° N and from 9.0° E to 30.0° E. It covers roughly 4.1×10^5 km² and is shallow, with a mean depth of about 54 m [9, 10]. Its internal structure is organized into several sub-basins separated by sills, channels, and shallow regions. For clarity and consistency in the following sections, the main sub-basins are referred to in generalized form as the Baltic Proper, the Bothnian Sea, the Bothnian Bay, the Gulf of Finland, and the Gulf of Riga [11]. Figure 1 shows the bathymetry of the Baltic Sea and these main sub-basin divisions.

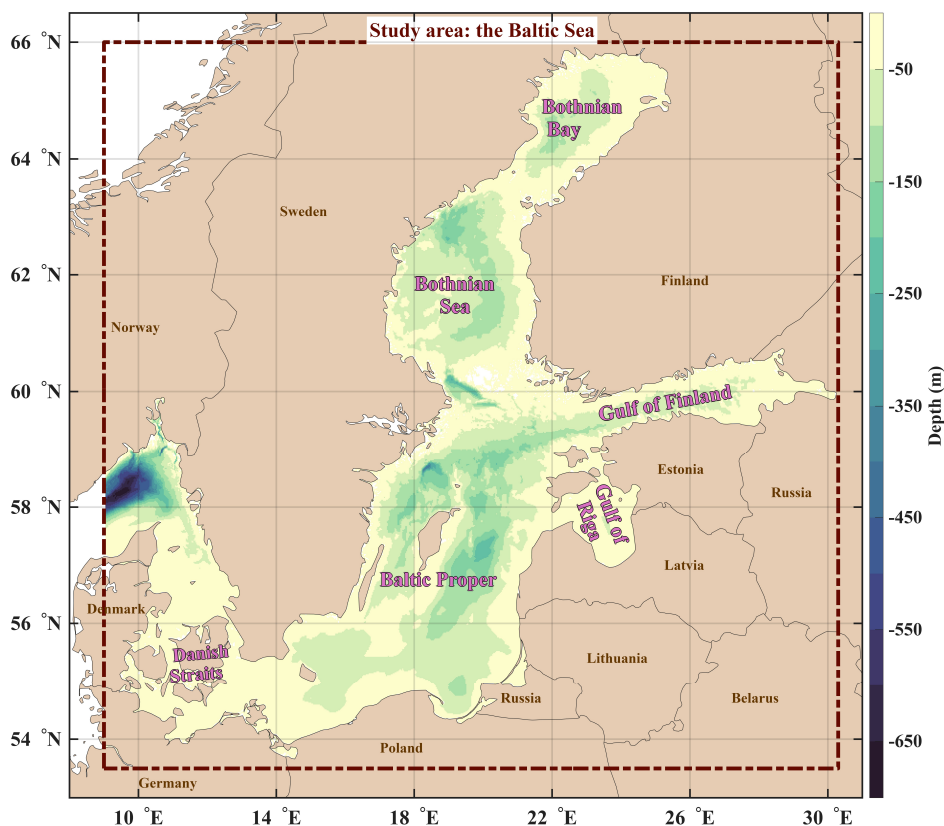


Figure 1: Bathymetry and main sub-basin divisions of the Baltic Sea.

The Baltic Proper forms the central and deepest part of the system and contains the main deep basins, where persistent haline stratification separates brackish surface water from more saline deep water and restricts vertical exchange [12, 13]. The Bothnian Sea is less saline than the Baltic Proper and has weaker stratification and more effective deep-water ventilation [14, 15]. The Bothnian Bay is the northernmost and freshest major sub-basin, with hydrography strongly shaped by river runoff, low salinity, and seasonal sea-ice cover [16, 17, 18]. The Gulf of Finland is an elongated estuarine sub-basin where the longi-

tudinal salinity gradient, variable stratification, and wind forcing support frequent circulation reversals [19, 20, 21]. The Gulf of Riga is a shallow semi-enclosed sub-basin in which riverine freshwater input, seasonal stratification, wind forcing, and exchange through the Irbe Strait jointly shape basin-scale gyres, mean currents, and freshwater transport pathways [22, 23, 24].

The sub-basin differences described above are superimposed on external controls acting at the open boundary and the sea surface. At the western boundary, exchange through the narrow and shallow Danish Straits regulates inflows and outflows between the Baltic Sea and the North Sea, while weak tidal forcing means that circulation is not primarily organized by a regular tidal cycle [25, 26, 27]. At the sea surface, wind stress, air-sea heat exchange, and freshwater input act directly on the upper ocean, but their effects are redistributed locally by bathymetry, coastline orientation, sill geometry, river plumes, ice cover, and the interaction between upper-layer vertical mixing and stratification [28, 29, 30]. Consequently, comparable atmospheric forcing can produce different near-surface circulation responses among sub-basins, and the high-latitude seasonal cycle further modulates these responses through changes in wind conditions, surface buoyancy fluxes, river runoff, and ice cover [31, 32, 33].

In this shallow, heterogeneous, and atmospherically responsive setting, sea surface currents (SSCs) are a central dynamical variable rather than a secondary descriptor of the marine environment. In the upper ocean, they integrate momentum input, pressure-gradient adjustment, density structure, boundary exchange, and local topographic control, providing a diagnostic role for the ocean surface comparable to that of near-surface winds in atmospheric dynamics [34, 35, 36]. In the Baltic Sea, this role is particularly important because surface currents connect basin-scale circulation with local transport pathways, coastal exposure, wave-current interaction, and the redistribution of freshwater, heat, particles, and biological material [37, 38, 39]. Their variability therefore cannot be reduced to a single mean circulation pattern; generalized circulation descriptions must be resolved further in space and time to capture the locally forced and transient dynamics of Baltic surface flow [40, 41].

1.1.1 Historical Development of Baltic Sea Circulation Studies

Investigation of Baltic Sea circulation began in the nineteenth century, when Struve (1864) argued that the general currents are driven by salinity differences arising from the interaction between freshwater supplied by runoff and more saline oceanic water entering through the Danish Straits [42]. These early ideas established the estuarine framework that still underpins further interpretations of Baltic circulation. Soon after, Knudsen (1900) placed this framework on a quantitative basis by formulating a hydrographic theorem for exchange through the Baltic outflow system from conservation of water and salt, thereby linking inflow, outflow, and freshwater supply to the salinity structure of the straits [43, 44]. Classical twentieth-century studies then identified cyclonic circulation as a persistent first-order feature of the basin, particularly in the synthesis of Palmén (1930) [45]. This view was later supported numerically. For example, Sarkisjan (1975) reproduced large cyclonic surface gyres in model calculations [46], Lehmann and Hinrichsen (2000) showed that the annual mean circulation remains predominantly cyclonic despite strong atmospheric variability [47], Omstedt and Axell (2003) emphasized the combined roles of baroclinic exchange, strait inflow, and runoff [16], and Jędrasik et al. (2008) demonstrated strong modulation of surface currents by large-scale wind forcing [48].

A major advance came when basin-wide modeling moved beyond the simple picture of surface gyres and resolved the Baltic as a vertically differentiated and topographically

steered circulation system. Meier (2007) showed that strong cyclonic gyres dominate above and below the halocline in the Baltic Proper and the Bothnian Sea, whereas circulation in the Gulf of Riga, Gulf of Finland, and Bothnian Bay is weaker and less persistent [49]. Hagen and Feistel (2007) further showed that deep circulation follows sills, channels, and basin slopes, including a pronounced rim current around the Gotland Deep, highlighting the importance of halocline-separated exchange and bathymetric control in the Baltic mean state [50].

Subregional studies then demonstrated that local circulation can differ substantially from the basin-scale mean. In the Gulf of Finland, Andrejev et al. (2004a) showed that even the mean circulation contains multiple loops and vertical complexity [51], Elken et al. (2011) distinguished a more channel-like western regime from a dynamically richer eastern regime [52], and Lilover et al. (2011) confirmed the roles of wind, seiches, and topographic steering [53]. In the Bothnian Sea and Bothnian Bay, Myrberg and Andrejev (2006) confirmed the traditional view of mean cyclonic circulation, but also showed that this broad gyre-like pattern is modified by mesoscale features and coastal jets [14]. At the same time, transport studies made clear that realistic pathways depend strongly on model resolution. For example, Soomere et al. (2011) identified direction-dependent transport pathways, semi-persistent routes, and closed-circulation areas in the Gulf of Finland [54], while Andrejev et al. (2011) showed that these transport characteristics change markedly with grid size, implying that mesoscale eddies and narrow currents are dynamically essential rather than secondary details [55].

Using multi-sensor satellite imagery, Gade et al. (2012) derived mesoscale surface currents in the Baltic Proper [56]. In the Gulf of Riga, Soosaar et al. (2014) showed that river-induced buoyancy forcing can reverse the expected cyclonic pattern and generate a double-gyre structure [23], while Lips et al. (2016a, 2016b) demonstrated that circulation there is strongly seasonal, mesoscale-rich, and sensitive to plume dynamics, stratification, and Irbe Strait inflow [24, 57]. Viitak et al. (2016) further showed during the St. Jude storm that spatially variable surface currents and sea-level can modify significant wave height by up to about 20%, highlighting the practical relevance of circulation variability for coastal hazards [38].

As modeling matured, the literature increasingly distinguished between robustness of the broad circulation picture and uncertainty in its quantitative expression. Placke et al. (2018) found that Baltic models consistently reproduce the large-scale cyclonic circulation, but differ substantially in current strength and transports [30]. Jędrasik and Kowalewski (2019) confirmed the mean cyclonic circulation of the Baltic Proper, identified marked seasonal differences, and linked current variability to large-scale atmospheric indices [58]. In the Gulf of Finland, Maljutenko and Raudsepp (2019) revealed a westward coastal current and two large summer anticyclonic gyres whose intensity varies strongly between years and depends on zonal wind forcing [59, 60]. Bednorz et al. (2021) further showed that regional atmospheric circulation patterns induce coastal upwelling in different parts of the Baltic Sea, with the response depending strongly on coastline orientation and predominantly associated with alongshore winds [61]. Furthermore, Kanarik et al. (2021) then showed that surface-current variability has its strongest coupled-wave effects in dynamically active regions such as the Gulf of Finland, the Western Gotland Basin, and the Åland Sea [39]. Additionally, Liblik et al. (2022) documented quasi-steady mesoscale circulation regimes in the central Baltic Proper lasting for weeks under sustained atmospheric forcing [33]. This multiscale view was pushed further by Väli et al. (2024), who showed with 250 m resolution modeling that the Baltic surface eddy field is highly inhomogeneous in space and season, with especially active submesoscale regions in the Gulf of Finland, the

Gdańsk Basin, and the western northern Baltic Proper [62].

1.2 AI and Marine Data

Modern marine science increasingly relies on high-dimensional, gridded, and time-evolving datasets produced by numerical models, satellite observations, in situ measurements, and reanalysis products. In this context, the main challenge is not only data availability, but the extraction of dynamically meaningful information from large spatiotemporal fields while preserving their spatial organization, temporal evolution, and scale interactions. This is particularly relevant for marine surface variables, including SSCs, whose structure is often heterogeneous, nonlinear, and only partly represented by mean states or low-order statistical summaries [63, 64].

Conventional statistical methods remain essential for description, interpretation, and the identification of dominant modes of variability [65]. However, their limitations become more apparent when the target process includes nonlinear relationships, regime dependence, evolving covariance structures, and localized spatial features. Under these conditions, data-driven methods provide a complementary framework by learning structure directly from the data rather than prescribing it through fixed parametric assumptions or predefined diagnostics [66, 67]. Machine learning is therefore useful not only for prediction, but also for identifying latent organization, dominant states, regime transitions, and structured departures from the mean in complex marine datasets [68, 69, 70].

For gridded ocean-current fields, physically relevant information is often contained in the organization of the full vector field rather than in scalar diagnostics alone. A pattern-based perspective is therefore more appropriate than approaches that focus only on domain averages, seasonal means, pointwise statistics, or individual features such as eddies. Eddy tracking is useful when coherent vortices are the explicit target, but it provides a restricted representation of circulation. In marginal and semi-enclosed seas, important circulation states may also involve estuarine reversals, broad cyclonic or anticyclonic regimes, coastal jets, channelized flows, and transitional configurations. Pattern-based methods retain the spatial structure of the complete current field and can therefore represent both eddy-like and non-eddy circulation regimes within the same analysis.

This methodological need is supported by previous applications to ocean-current fields. In the Gulf of Finland, Westerlund et al. (2019) showed that seasonal averaging can obscure circulation features that change position or direction, while self-organizing maps (SOMs) resolved dominant states associated with normal estuarine circulation, reverse estuarine circulation, and transitional flow configurations [21]. Similarly, Dey et al. (2023) used SOMs with 23 years of daily satellite-derived surface-current maps in the Bay of Bengal to identify dominant large-scale circulation patterns and their temporal transitions [71]. These studies show that mean circulation fields may arise from the interaction of multiple recurrent patterns rather than representing a single persistent state.

Compared with purely linear or partition-based approaches, SOMs are particularly suitable for this type of analysis. EOF-based methods and clustering can support circulation classification, but prior linear projection may restrict the representation of states that differ by geometry, asymmetry, or localized flow reorganization [72]. Hisaki (2013) compared SOM, hierarchical clustering, K-means clustering, and EOF-based dimensional reduction for surface-current classification and showed that SOM provided physically meaningful classifications while being less sensitive to dimensionality-reduction choices than some partitioning methods [73]. More broadly, SOMs have been shown to extract characteristic circulation patterns from oceanographic fields, preserve neighbourhood relationships among patterns, and perform favourably relative to linear methods in feature

extraction [74, 75, 76, 77, 78]. For these reasons, SOM provides an appropriate framework for identifying dominant SSC patterns from large gridded archives before moving to forecasting or emulation tasks.

For prediction and emulation, deep learning extends this pattern-based logic by learning spatial mappings directly from gridded fields. Convolutional neural networks (CNNs) are especially relevant because they preserve local spatial structure and exploit neighbourhood relationships in discretized geophysical data [79]. Recent ocean applications show that convolutional models can estimate surface currents from gridded predictors, downscale sea surface height and current fields, and recover higher-resolution ocean states from coarser inputs [80, 81, 82]. At the same time, reliable treatment of coastlines and land boundaries remains an important challenge for nearshore prediction [83].

Encoder–decoder architectures such as U-Net are well suited to geophysical field prediction because they combine large-scale contextual learning with the recovery of fine-scale spatial detail. Their skip connections retain both coarse and localized information, which is important when the target field contains basin-scale circulation patterns together with coastal jets, narrow straits, and boundary-influenced structures [79]. This makes U-Net-type architectures suitable for field-to-field mappings in which one gridded ocean state, or a sequence of states and forcings, is transformed into a predicted current field on the same grid.

This also motivates the use of deep-learning emulators. Numerical ocean models remain the physically grounded basis for generating dynamically consistent ocean states, whereas emulators learn efficient surrogate mappings from model-generated data to reproduce selected outputs or state evolution at substantially lower computational cost [84, 85, 86]. In this thesis context, unsupervised pattern recognition and convolutional deep learning therefore serve complementary roles: SOM is used to identify and interpret dominant SSC patterns, while CNN/U-Net-based models provide a framework for efficient gridded field prediction and emulation.

1.3 Consolidation of the Research Justification and Goals

SSCs are among the most informative and practically important expressions of upper-ocean dynamics. Operationally, they are directly relevant to search and rescue, drift prediction, pollutant transport, and coastal hazard response [36]. Their importance is especially pronounced over shorter timescales, such as from one day to the next, when the evolving surface flow itself matters more than seasonal means or long-term climatology. This relevance is particularly strong in the Baltic Sea, which is not only a climatically sensitive high-latitude basin [87, 88] but also a heavily used maritime region [89], so that improved understanding of SSCs is important both for advancing regional ocean and climate science and for supporting operational applications.

At the same time, Baltic SSCs remain less comprehensively characterized than variables such as sea level, temperature, and salinity, partly because basin-wide direct current observations are sparse and because surface currents require high spatial and temporal resolution to resolve wind-driven, coastal, and mesoscale responses. Although the existence of basin-scale cyclonic circulation is well established, from the literature review (Section 1.1.1) can be interpreted that a consistent basin-scale characterization of dominant circulation regimes at daily resolution remains limited. This creates a specific scientific challenge: Baltic SSCs are both physically important and methodologically difficult to describe because of the basin's large spatial extent, the complex interplay among multiple sub-basins, and the broad range of processes that influence surface flow [90, 91].

Recent advances in artificial intelligence (AI) provide a practical way to approach this

problem [92, 93]. When supported by temporally extensive and spatially resolved data, such methods make it possible to analyse Baltic SSC variability beyond conventional mean-state descriptions, to identify dominant structures more systematically, and to examine whether part of this structured variability can be learned for efficient prediction. This also places strong emphasis on data selection and consolidation, because data-driven methods depend on the quality, continuity, spatial coverage, and dynamical consistency of the fields used for analysis and learning. Article I provides an additional methodological contribution to the data-selection framework of the present thesis, rather than constituting a separate scientific objective on SSC variability. Against this background, the thesis has two main goals. The first is to clarify how Baltic SSC variability is organized in space and time through basin-scale analysis, pattern-based classification, and dynamical decomposition. The second is to examine whether this variability can be represented efficiently within a data-driven forecasting framework. More specific sub-goals, connected to the individual publications, can be formulated as follows:

- To quantify the relative contributions of geostrophic and ageostrophic components to Baltic SSCs and analyse their spatial and temporal variability. This objective is related to Article II and is extended in the present thesis through a more comprehensive basin-scale analysis.
- To identify dominant circulation regimes through pattern recognition. This objective is pursued through SOM analysis. In methodological terms, Article III provides the main basis for this part by demonstrating how SSC variability can be organized into dominant circulation states suitable for further interpretation and comparison.
- To assess whether daily SSC evolution can be represented efficiently through data-driven surrogate forecasting. This objective is addressed first in Article III through the regional sciCUN design for the Gulf of Riga and then in Article IV through the basin-scale DeepCUN design for the full Baltic Sea. In both cases, the aim is to test whether daily evolution of the surface-current field can be learned from a restricted set of physically meaningful inputs.
- To examine whether such forecasting designs can be interpreted in physically meaningful terms. This objective is associated with the design framework developed initially in Article II and, in a more mature form, in Article IV, where predictor sensitivity and explainable artificial intelligence (XAI) diagnostics are incorporated to relate the learned forecasting operator to the structure of the input information.

Accordingly, the results will be presented in a progression from reference-data justification, to quantification of the geostrophic–ageostrophic balance in Baltic SSC variability, to pattern recognition, and finally to data-driven forecasting design and its physical interpretation. In this way, the thesis is intended to contribute both to the physical study of Baltic Sea surface circulation and to the methodological development of regional oceanography under limited direct observational constraints.

2 Materials and Methods

2.1 Main Data

To analyse Baltic SSCs, this study used the Copernicus Marine Baltic Sea Physics Reanalysis (product ID: `BALTICSEA_MULTIIYEAR_PHY_003_011`), a multi-year physical reanalysis covering the Baltic Sea and the transition area to the North Sea over the period 1993–2024, at an approximate horizontal resolution of 1 nautical mile and with 56 vertical levels. The product provides daily, monthly, and annual mean fields of sea level, temperature, salinity, mixed-layer depth, sea ice variables, and horizontal currents [94, 95]. Although direct validation of Baltic SSCs remains limited by the scarcity of suitable publicly available current observations, this limitation is a known operational and scientific constraint. Nevertheless, the reanalysis is accompanied by quality information documents and validation results showing generally acceptable performance for the main physical state variables, including temperature, salinity, mixed-layer depth, and sea surface height [96]. This provides indirect support for using the product as a physically consistent reference for near-surface circulation, even if the current field itself cannot be validated as comprehensively as temperature, salinity, or sea level. Accordingly, in the absence of sufficiently extensive public current observations, the reanalysis is treated here as the best available basin-scale reference dataset for Baltic SSC analysis. For this reanalysis product, the underlying ocean model is the Baltic Monitoring and Forecasting Centre (BAL MFC) implementation of NEMO version 4.0 coupled with the SI3 sea ice model and adapted for Baltic Sea conditions [95, 97, 98, 99]. SSC were represented by the uppermost model level, centered at 0.50 m depth, and both zonal and meridional velocity components.

2.1.1 Additional Data

Additional datasets were used for specific purposes throughout the study. Sea-level anomaly (SLA) from the same Baltic Sea physics reanalysis was used in the dynamical decomposition of surface currents. Atmospheric forcing fields were taken from ERA5 reanalysis and were used mainly in the forecasting framework [100]. Satellite-derived SLA was taken from the Copernicus Marine European Seas Level-4 sea surface height product [101], while satellite-based total surface-current fields were taken from the Copernicus Marine GlobCurrent product for comparative and diagnostic analyses [102]. These datasets are introduced in more detail in the relevant methodological sections.

2.2 Analysis of Baltic SSCs

2.2.1 SOM

Following the methodological justification given in Section 1.2, Baltic SSC variability was analysed with the SOM method [103]. In the present study, each sample corresponds to one complete daily Baltic SSC field. The SOM was therefore used to classify basin-scale circulation states rather than individual grid points.

Let

$$\mathbf{x} \in \mathbb{R}^D \quad (1)$$

denote one input vector, where D is the number of scalar elements describing one SSC field. A SOM with lattice size $n \times m$ contains

$$K = nm \quad (2)$$

neurons, each associated with a prototype vector

$$\mathbf{w}_j \in \mathbb{R}^D, \quad j = 1, \dots, K. \quad (3)$$

For a given input vector, the best-matching unit (BMU) is defined as the neuron whose prototype is closest to the input in Euclidean distance (ED):

$$c = \arg \min_j \|\mathbf{x} - \mathbf{w}_j\|. \quad (4)$$

Here, $\arg \min$ means “the value of j that gives the smallest distance”, so c is the index of the prototype vector most similar to the input vector \mathbf{x} .

After the BMU is identified, both the BMU and its neighbouring neurons on the SOM lattice are updated toward the input vector:

$$\mathbf{w}_j^{\text{new}} = \mathbf{w}_j^{\text{old}} + \alpha(\tau) h_{cj}(\tau) (\mathbf{x} - \mathbf{w}_j^{\text{old}}), \quad (5)$$

where $\alpha(\tau)$ is the learning rate, $h_{cj}(\tau)$ is the neighbourhood function centred on the BMU, and τ denotes the training step. In this way, the SOM performs both vector quantization and topological ordering: similar SSC fields are mapped to the same or neighbouring neurons.

After training, each neuron represents one prototype circulation state, and each sample is assigned to its BMU. The SOM thus provides a discrete classification of Baltic SSC fields together with an ordered relation among the resulting classes. For each prescribed lattice size, the network was initialized and trained for 200 epochs. The trained network yields two outputs: a codebook matrix containing the prototype circulation states and a label series assigning each sample to its BMU.

No additional normalization was applied to the current-field vectors before SOM training. The classification therefore operates on the original velocity magnitudes of the re-analysis fields. This preserves physically meaningful differences in circulation strength, but it also means that locations with larger temporal variability contribute more strongly to the Euclidean-distance metric. The resulting classes should therefore be interpreted as circulation states defined by the full SSC field in its original physical scale.

The choice of lattice size controls the level of detail in the classification. Small SOMs represent broad large-scale states, whereas larger SOMs resolve finer distinctions within the dataset. Increasing the number of neurons does not change the dimensionality of the input data; it only increases the number of prototype states used to represent Baltic SSC variability [21, 73].

For each analyzed field, both components (the eastward component u_{SSC} and the northward component v_{SSC}) were extracted on the native horizontal grid and transformed into a one-dimensional representation suitable for SOM training. The data were land-masked before vectorization.

Let the retained sea points be denoted by

$$\Omega = \{\mathbf{r}_1, \mathbf{r}_2, \dots, \mathbf{r}_N\}, \quad (6)$$

where N is the number of valid grid points after masking. For each sample, the input vector was then formed by pairing the two horizontal velocity components at each retained location and arranging them in interleaved form:

$$\mathbf{x} = \begin{bmatrix} u_{\text{SSC}}(\mathbf{r}_1) \\ v_{\text{SSC}}(\mathbf{r}_1) \\ u_{\text{SSC}}(\mathbf{r}_2) \\ v_{\text{SSC}}(\mathbf{r}_2) \\ \vdots \\ u_{\text{SSC}}(\mathbf{r}_N) \\ v_{\text{SSC}}(\mathbf{r}_N) \end{bmatrix} \in \mathbb{R}^{2N}. \quad (7)$$

Thus, each retained sea point contributes one local velocity pair (u_{SSC}, v_{SSC}) to the input vector, and the same ordering is preserved for all samples.

After vectorization, all sample vectors were assembled columnwise into the input matrix

$$\mathbf{X} = \begin{bmatrix} | & | & \cdots & | \\ \mathbf{x}_1 & \mathbf{x}_2 & \cdots & \mathbf{x}_S \\ | & | & \cdots & | \end{bmatrix} \in \mathbb{R}^{2N \times S}, \quad (8)$$

where S is the total number of analysed SSC fields. In this arrangement, each column represents one complete Baltic SSC state, and each row corresponds to one scalar element of the interleaved velocity vector. This general framework is consistent with Article III, where SOM was used for daily SSC classification in the Gulf of Riga, but is applied here to the full Baltic Sea domain [3].

2.2.2 Geostrophic and Ageostrophic Decomposition of Surface Currents

To assess the relative roles of pressure-gradient-driven and residual non-geostrophic processes, the near-surface SSC field was decomposed into geostrophic and ageostrophic components.

For each analyzed field, the total SSC velocity was written as

$$\mathbf{u}_{SSC} = (u_{SSC}, v_{SSC}), \quad (9)$$

where u_{SSC} and v_{SSC} denote the eastward and northward components of the total near-surface current obtained from the reanalysis. As mentioned in Section 2.1.1, the SLA field η from the same reanalysis product was used to estimate the geostrophic contribution at each grid point. Under the geostrophic approximation, the surface geostrophic velocity is given by

$$u_{SSC,geo} = -\frac{g}{f} \frac{\partial \eta}{\partial y}, \quad v_{SSC,geo} = \frac{g}{f} \frac{\partial \eta}{\partial x}, \quad (10)$$

where g is the gravitational acceleration and

$$f = 2\Omega \sin \phi \quad (11)$$

is the Coriolis parameter, with Ω the Earth's angular velocity and ϕ latitude.

Because the SLA field is provided on a regular longitude–latitude grid, the horizontal derivatives were evaluated numerically after conversion of grid spacing from angular coordinates to metric distance. Let $\Delta\lambda$ and $\Delta\phi$ denote the longitudinal and latitudinal grid increments in degrees. Then the corresponding zonal and meridional distances at latitude ϕ are

$$\Delta x = R \cos \phi \left(\Delta\lambda \frac{\pi}{180} \right), \quad \Delta y = R \Delta\phi \left(\frac{\pi}{180} \right), \quad (12)$$

where R is the Earth's radius. The sea-level gradients were approximated using a 7-point stencil recommended by Arbic et al. (2012) [104]. Thus, for an interior grid point (i, j) ,

$$\left. \frac{\partial \eta}{\partial x} \right|_{i,j} \approx \frac{\eta_{i+3,j} - 9\eta_{i+2,j} + 45\eta_{i+1,j} - 45\eta_{i-1,j} + 9\eta_{i-2,j} - \eta_{i-3,j}}{60\Delta x_{i,j}}, \quad (13)$$

and

$$\left. \frac{\partial \eta}{\partial y} \right|_{i,j} \approx \frac{\eta_{i,j+3} - 9\eta_{i,j+2} + 45\eta_{i,j+1} - 45\eta_{i,j-1} + 9\eta_{i,j-2} - \eta_{i,j-3}}{60\Delta y_{i,j}}. \quad (14)$$

Before differentiation, missing values in the SLA field were locally filled only for numerical stability of the derivative stencil near irregular coastlines. The final geostrophic velocities were evaluated only at valid sea points of the analysis domain.

Once the geostrophic component had been estimated, the residual ageostrophic component was defined by subtraction from the total SSC:

$$u_{SSC,ageo} = u_{SSC} - u_{SSC,geo}, \quad v_{SSC,ageo} = v_{SSC} - v_{SSC,geo}. \quad (15)$$

Hence, the total near-surface SSC was partitioned as

$$\mathbf{u}_{SSC} = \mathbf{u}_{SSC,geo} + \mathbf{u}_{SSC,ageo}, \quad (16)$$

where

$$\mathbf{u}_{SSC,geo} = (u_{SSC,geo}, v_{SSC,geo})$$

is the geostrophic component and

$$\mathbf{u}_{SSC,ageo} = (u_{SSC,ageo}, v_{SSC,ageo})$$

is the residual ageostrophic component.

To assess how strongly each component contributed to the direction of the total current, projected percentage contributions were defined from the scalar projection of each component onto the total SSC vector. The ageostrophic contribution was written as

$$P_{ageo} = 100 \frac{u_{SSC,ageo} u_{SSC} + v_{SSC,ageo} v_{SSC}}{u_{SSC}^2 + v_{SSC}^2}, \quad (17)$$

and the geostrophic contribution as

$$P_{geo} = 100 \frac{u_{SSC,geo} u_{SSC} + v_{SSC,geo} v_{SSC}}{u_{SSC}^2 + v_{SSC}^2}. \quad (18)$$

These quantities measure the percentage contribution of each component in the direction of the total SSC vector. Positive values indicate that the component supports the total flow direction, whereas negative values indicate an opposing contribution. Owing to the decomposition in Eq. (15), the two projected contributions satisfy

$$P_{geo} + P_{ageo} = 100 \quad (19)$$

where the total current magnitude is non-zero.

To summarize the local balance between the two contributions, a normalized dominance index was further defined as

$$D = 100 \frac{P_{geo} - P_{ageo}}{|P_{geo}| + |P_{ageo}|}. \quad (20)$$

With this definition, $D > 0$ indicates geostrophic dominance, $D < 0$ indicates ageostrophic dominance, and $D = 0$ indicates equal projected influence of the two components. The index is bounded between -100 and 100 , which facilitates comparison among regions and circulation states.

This decomposition provides a dynamical complement to the SOM classification. Whereas the SOM groups surface-current fields according to their full spatial similarity, the geostrophic-ageostrophic partition helps interpret the physical nature of those patterns by indicating whether a given circulation state is more strongly associated with sea-level-gradient-driven flow or with residual processes not captured by the geostrophic approximation. In this way, the classification of dominant circulation regimes can be linked to a physically interpretable balance between dynamically distinct components of the near-surface current field.

2.3 Forecasting of Baltic SSCs

The preceding subsections addressed the extraction and interpretation of dominant circulation patterns from historical surface-current fields. The next step of the study was to investigate whether Baltic Sea near-surface SSCs can also be predicted efficiently in a data-driven framework. The purpose of this forecasting stage was not to replace dynamical ocean modeling in a general sense, but to construct a computationally inexpensive surrogate for the evolution of the sea-surface current field itself. In this setting, the target quantity is restricted to the horizontal near-surface current, whereas the three-dimensional hydrodynamic model remains the reference source of dynamically consistent training data, since a full three-dimensional numerical ocean simulation remains computationally expensive when the practical target is only the surface-current field [105, 106, 107, 108, 109].

Within the thesis, this forecasting framework was developed in two connected stages. First, Article III introduced a regional proof-of-concept design, denoted *sciCUN*, for daily SSC emulation in the Gulf of Riga. Second, Article IV extended the same general design logic to the full Baltic Sea by introducing a deeper and more expressive basin-scale architecture, denoted *DeepCUN*. The methodological basis is therefore common to both articles: in each case, a convolutional encoder–decoder network is trained to emulate the one-day evolution of the SSC field from the antecedent SSC state and atmospheric forcing. The present Methods section summarizes this common forecasting formulation and then describes the final basin-scale design used in Article IV, while the regional *sciCUN* configuration from Article III is treated as its methodological precursor.

The forecasting problem was formulated as a one-step update of the daily surface-current field. Rather than integrating the full three-dimensional momentum, thermodynamic, and free-surface equations forward in time, the deep-learning model was trained to map the known SSC state at day t , together with atmospheric forcing aligned to day $t + 1$, to the predicted SSC state at day $t + 1$. In this sense, the method constitutes a partial emulation of the regional ocean simulation, designed specifically for SSC forecasting.

2.3.1 Data-driven model formulation and predictors

The forecast target was the daily mean Baltic Sea near-surface current field derived from the same Copernicus Marine Baltic Sea reanalysis introduced above. Let

$$\mathbf{U}_{\text{SSC}}(i, j, t) = \begin{bmatrix} u_{\text{SSC}}(i, j, t) \\ v_{\text{SSC}}(i, j, t) \end{bmatrix} \quad (21)$$

denote the zonal and meridional SSC components at horizontal grid point (i, j) and day t . These reanalysis fields were treated as the reference target fields for the forecasting framework.

Atmospheric forcing was taken from ERA5 reanalysis. Initially, a broader candidate predictor set was considered, including 10 m zonal and meridional wind components, mean sea-level pressure, 2 m air temperature, and 2 m dew-point temperature. However, a subsequent predictor-sensitivity analysis showed that, once the antecedent SSC field and wind forcing were included, the additional thermodynamic and pressure variables contributed only marginally to forecast skill. The final forecasting models considered in the thesis therefore retained only the previous-day SSC field and the next-day wind components as predictors. This reduced predictor design was first explored in the regional *sciCUN* framework of Article III and was then formalized and tested more systematically for the basin-scale *DeepCUN* framework in Article IV.

All predictor and target fields were placed on a common regular analysis grid. For numerical compatibility with the encoder–decoder architecture, the original domain was

slightly cropped at the land-dominated outer margins, yielding a grid of dimensions

$$S_1 = 736, \quad S_2 = 768. \quad (22)$$

This ensured that the spatial dimensions were divisible by 2^5 , consistent with five successive downsampling operations in the basin-scale DeepCUN network. Let \mathcal{D}_o denote the ocean part of this grid, defined by the sea mask. All fields were retained on the full rectangular grid, while land points were masked and set to zero during training and evaluation.

To preserve the physical magnitude of the target field, the two SSC components were kept in their original units. The atmospheric predictor fields were first restricted to ocean points and then linearly rescaled using training-period extrema so that their numerical range was comparable to that of the SSC components. For a generic atmospheric predictor A_c , the normalized field was written as

$$A_c^{\text{norm}}(i, j, t) = \left(\frac{A_c(i, j, t) - \min_{\mathcal{D}_o}(A_c)}{\max_{\mathcal{D}_o}(A_c) - \min_{\mathcal{D}_o}(A_c)} \right) \left(\max_{\mathcal{D}_o}(\text{SSC}) - \min_{\mathcal{D}_o}(\text{SSC}) \right) + \min_{\mathcal{D}_o}(\text{SSC}), \quad (23)$$

where the extrema were computed over all ocean points in the training period, and the pooled SSC range was obtained from both zonal and meridional components together.

With this preprocessing, the forecasting problem was formulated as a mapping from a four-channel input tensor to a two-component predicted SSC field. The finalized input tensor was

$$\mathbf{X}(i, j, :, t) = \begin{bmatrix} u_{\text{SSC}}(i, j, t) \\ v_{\text{SSC}}(i, j, t) \\ u_{\text{wind}}^{\text{norm}}(i, j, t+1) \\ v_{\text{wind}}^{\text{norm}}(i, j, t+1) \end{bmatrix}, \quad (24)$$

and the corresponding predicted output field was

$$\hat{\mathbf{U}}_{\text{SSC}}(i, j, t+1) = \begin{bmatrix} \hat{u}_{\text{SSC}}(i, j, t+1) \\ \hat{v}_{\text{SSC}}(i, j, t+1) \end{bmatrix}. \quad (25)$$

The forecasting model therefore approximated the mapping

$$\hat{\mathbf{U}}_{\text{SSC}}(i, j, t+1) = \mathcal{F}_{\theta}(\mathbf{X}(i, j, :, t)), \quad (26)$$

where \mathcal{F}_{θ} denotes the neural-network predictor with trainable parameters θ .

This formulation is physically interpretable. The SSC field at day t provides the antecedent dynamical state, while the wind at day $t+1$ represents the primary external forcing acting over the predicted day. The resulting network therefore learns a conditional one-day update of the surface-circulation field rather than an unconstrained statistical interpolation.

2.3.2 Convolutional U-shaped neural network architecture

The forecasting architectures used in Articles III and IV share the same basic design principle: both are convolutional encoder-decoder networks that learn image-to-image mappings from gridded predictors to the next-day SSC field. Article III used this design in the regional *sciCUN* configuration for the Gulf of Riga, where the aim was to demonstrate the feasibility of daily SSC emulation in a restricted but dynamically complex domain. Article IV then extended the same general framework to the scale of the full Baltic Sea by introducing a deeper and more expressive architecture, hereafter referred to as *DeepCUN*. The transition from *sciCUN* to *DeepCUN* was motivated by the greater spatial extent, stronger

heterogeneity, and broader range of circulation structures present in the full Baltic Sea, which required higher representational capacity than the regional proof-of-concept design.

To approximate the mapping in Eq. (26), the final basin-scale forecasting framework adopted in this thesis used DeepCUN. The choice of a convolutional U-Net structure was motivated by the fact that SSCs are gridded vector fields with strong spatial organization across multiple scales. In the Baltic Sea, relevant structures range from basin-scale gyres and broad exchange flows to coastal jets, narrow straits, and localized eddy-like features. A forecasting model must therefore capture both large-scale contextual information and fine-scale spatial detail.

DeepCUN consists of five encoder levels, a bottleneck layer, and five decoder levels connected by skip connections. In the encoder, each level applies a 3×3 convolution followed by group normalization and a rectified linear unit. A 2×2 max-pooling operation then reduces the spatial resolution by a factor of two. The number of feature channels increases with depth according to

$$(32, 64, 128, 256, 512), \quad (27)$$

followed by a bottleneck layer with 1024 channels. This progressive reduction in spatial resolution allows the network to aggregate increasingly large-scale spatial context.

The decoder mirrors the encoder. At each level, transposed convolution is used to up-sample the feature maps, which are then concatenated with the corresponding encoder activations through skip connections. A further convolution-normalization-activation block refines the reconstructed features. The final layer is a 1×1 convolution that maps the decoder output to the two predicted SSC components, \hat{u}_{SSC} and \hat{v}_{SSC} . In practical terms, the encoder extracts progressively more abstract multi-scale features from the antecedent SSC and wind fields, while the decoder reconstructs a full-resolution next-day SSC map that preserves both basin-scale structure and localized coastal detail.

Thus, the relationship between the two article-specific designs is as follows. Article III introduced sciCUN as the regional proof-of-concept architecture and established the practical feasibility of daily SSC emulation. Article IV retained the same basic encoder-decoder forecasting concept but implemented it in the deeper basin-scale DeepCUN architecture, which is the final forecasting design adopted in this thesis for the whole Baltic Sea. Figure 2 shows the schematic framework used for the final basin-scale forecasting setup. Detailed operator-level descriptions of the individual building blocks, including convolution, normalization, rectified linear unit (ReLU), and upsampling, are given in Articles III and IV.

2.3.3 Training strategy and one-step forecast evaluation

The forecasting model was trained using the Baltic Sea reanalysis period 2015–2023, while the full year 2024 was reserved as an independent test period. Each sample consisted of one day-pair $(t, t + 1)$, such that the input tensor $\mathbf{X}(i, j, :, t)$ was paired with the reference SSC field $\mathbf{U}_{\text{SSC}}(i, j, t + 1)$.

The trainable parameters were optimized by minimizing a penalized squared-error loss,

$$\mathcal{L}_{\text{tot}} = \mathcal{L}_{\text{data}} + \lambda \|\mathbf{W}\|_2^2, \quad (28)$$

with

$$\mathcal{L}_{\text{data}} = (\hat{u}_{\text{SSC}} - u_{\text{SSC}})^2 + (\hat{v}_{\text{SSC}} - v_{\text{SSC}})^2, \quad (29)$$

where \mathbf{W} denotes the set of learnable network weights and λ is an L_2 regularization coefficient. The loss therefore penalizes discrepancies in both SSC components while limiting excessive weight growth.

Because the full multi-year, high-resolution dataset is memory-intensive, training was carried out in a sequential annual streaming procedure. The model was first initialized on the earliest training year and then updated iteratively through subsequent years while retaining the learned weights. In this way, the network was exposed to the full multi-year variability of the Baltic Sea without requiring all samples to reside simultaneously in memory. Optimization was performed with the Adam algorithm.

Forecast skill for the one-step problem was assessed using three complementary metrics. First, the vector error at each grid point was quantified by the ED

$$\text{ED}(i, j, t) = \sqrt{(\hat{u}_{\text{SSC}}(i, j, t) - u_{\text{SSC}}(i, j, t))^2 + (\hat{v}_{\text{SSC}}(i, j, t) - v_{\text{SSC}}(i, j, t))^2}. \quad (30)$$

Second, component-wise mean absolute error (MAE) was used to summarize amplitude mismatch in the zonal and meridional SSC components. Third, the Pearson correlation coefficient (CC) was calculated at each grid point over the test period to quantify the temporal agreement between predicted and reference currents.

In addition to these pointwise skill measures, the preservation of rotational structure was evaluated using the relative vorticity

$$\zeta = \frac{\partial v_{\text{SSC}}}{\partial x} - \frac{\partial u_{\text{SSC}}}{\partial y}, \quad (31)$$

with the same operator applied to both reference and predicted SSC fields. This diagnostic was used to assess whether the forecast model preserved the sign and organization of rotational features such as eddy-like structures, meanders, and sharp coastal flow curvature.

2.3.4 Recursive multi-day forecast experiment

Although DeepCUN was trained only for one-day prediction, it was also deployed recursively to assess its potential multi-day forecast behavior. In this experiment, the predicted SSC field from one lead time was fed back as the antecedent state for the next lead time, while the atmospheric forcing was prescribed for the corresponding future day.

Let the forecast be initialized from the known reference SSC field at day t ,

$$\hat{\mathbf{U}}_{\text{SSC}}(i, j, t) = \mathbf{U}_{\text{SSC}}(i, j, t) = \begin{bmatrix} u_{\text{SSC}}(i, j, t) \\ v_{\text{SSC}}(i, j, t) \end{bmatrix}. \quad (32)$$

Then, for lead time $n \geq 0$, the recursive input was formed as

$$\hat{\mathbf{X}}(i, j, :, t+n) = \begin{bmatrix} \hat{u}_{\text{SSC}}(i, j, t+n) \\ \hat{v}_{\text{SSC}}(i, j, t+n) \\ u_{\text{wind}}^{\text{norm}}(i, j, t+n+1) \\ v_{\text{wind}}^{\text{norm}}(i, j, t+n+1) \end{bmatrix}, \quad (33)$$

and the recursion became

$$\hat{\mathbf{U}}_{\text{SSC}}(i, j, t+n+1) = \mathcal{F}_{\theta}(\hat{\mathbf{X}}(i, j, :, t+n)). \quad (34)$$

Repeated application of this one-step mapping yielded multi-day forecasts up to the chosen lead horizon.

This recursive experiment was designed as a controlled assessment of forecast stability and potential predictability, rather than as a fully operational forecast system. In particular, the atmospheric forcing used in the recursive rollout was taken from reanalysis rather than from independent numerical weather prediction forecasts, and the initial condition was likewise taken from the reanalysis. The resulting experiment therefore represents an idealized upper-bound test of how forecast errors accumulate when the one-step learned operator is applied repeatedly under effectively perfect forcing. It should not be interpreted as a direct operational forecast benchmark, but rather as an assessment of the internal stability and medium-range potential of the learned SSC mapping.

2.3.5 XAI diagnostics

Because the forecasting model is a deep nonlinear mapping from gridded predictors to gridded SSC fields, additional diagnostics were required to examine how the trained network uses the available input information. In this study, XAI was introduced in two sequential stages. First, it was used during model configuration to test which predictors contributed independent forecast information. Second, after the final model had been trained, it was used to interpret how the retained predictors entered the learned one-step forecast operator. The detailed implementation is given in Article IV [4]; here the main methodological construction is summarized.

The first stage was based on occlusion sensitivity. Let the unperturbed input tensor for one sample be denoted by

$$\mathbf{X}(i, j, :, t) = \begin{bmatrix} u_{\text{SSC}}(i, j, t) \\ v_{\text{SSC}}(i, j, t) \\ u_{\text{wind}}^{\text{norm}}(i, j, t + 1) \\ v_{\text{wind}}^{\text{norm}}(i, j, t + 1) \\ \dots \end{bmatrix}, \quad (35)$$

where the ellipsis denotes the additional candidate predictors considered before channel reduction. Let $X_c(i, j, t)$ denote channel c of the input tensor. To occlude channel c , that channel was replaced by a temporally averaged background field,

$$\bar{X}_c(i, j) = \frac{1}{T} \sum_{\tau=1}^T X_c(i, j, \tau), \quad (36)$$

so that the perturbed input became

$$X_{c'}^{(\text{occ}, c)}(i, j, t) = \begin{cases} \bar{X}_c(i, j), & c' = c, \\ X_{c'}(i, j, t), & c' \neq c. \end{cases} \quad (37)$$

The trained network was then evaluated with both the original and occluded inputs, and the resulting degradation in out-of-sample forecast skill was measured. In this way, occlusion provides an intervention-based estimate of predictor importance: a large loss of skill indicates that the masked channel contains information that is not recoverable from the remaining inputs. Applied to the candidate predictor set, this analysis showed that previous-day SSC components and next-day wind components carried the dominant predictive signal, whereas mean sea-level pressure and near-surface thermodynamic variables added only marginal skill once persistence and wind forcing were already included. The final forecasting model was therefore restricted to the reduced four-channel input defined in Eq. (24).

After predictor selection, post hoc XAI was applied to the finalized network. Two complementary aspects of the learned mapping were then examined: *existence* and *elasticity*. Existence refers here to the spatial distribution of attributed support in the input, that is, where the network finds the information it uses to construct the forecast. Elasticity refers to local responsiveness, that is, how strongly the forecast changes under a small perturbation of the input. These two aspects are intentionally separated, because the predictor that provides structural support for the forecast is not necessarily the same predictor to which the forecast is most locally sensitive.

Existence was examined with Layer-wise Relevance Propagation (LRP) [110]. Let the trained forecasting network be denoted by

$$\widehat{\mathbf{U}}_{\text{SSC}}(t+1) = \mathcal{F}_{\theta}(\mathbf{X}(t)), \quad (38)$$

where \mathbf{X} is the multi-channel input tensor and $\widehat{\mathbf{U}}_{\text{SSC}}$ is the two-component predicted SSC field. LRP starts from one predicted output component and redistributes that prediction backward through the trained network toward the input layer. Denoting by $R^{(\ell)}$ the relevance at layer ℓ , the redistribution is written schematically as

$$R^{(\ell-1)} = \Phi_{\text{LRP}}^{(\ell)}(R^{(\ell)}), \quad (39)$$

where $\Phi_{\text{LRP}}^{(\ell)}$ denotes the relevance-propagation rule for layer ℓ . Repeated application of this backward redistribution from the output layer to the input layer yields an input-side relevance field

$$R_{c,k}(i, j, t), \quad (40)$$

where c indexes the input channel, k the predicted SSC component, and (i, j) the grid location. Thus, $R_{c,k}(i, j, t)$ measures how strongly input channel c at location (i, j) contributes to the prediction of SSC component k for sample t . Averaging these fields over many samples yields spatial maps of persistent attributed support. In physical terms, these maps indicate where the emulator organizes its forecast mainly around antecedent-state memory and where it organizes it more strongly around wind forcing.

Elasticity was examined with a gradient-based diagnostic termed diagonal Jacobian elasticity (DJE) [111, 112]. Whereas LRP asks where the forecast finds support, DJE asks where the forecast is locally responsive to perturbations in the input. For input channel c and predicted SSC component k , the local elasticity target was defined as

$$D_{c,k}(i, j, t) = \frac{\partial \widetilde{U}_{\text{SSC},k}(i, j, t+1)}{\partial X_c(i, j, t)}, \quad (41)$$

where $\widetilde{U}_{\text{SSC},k}$ denotes a differentiable magnitude representation of the predicted SSC component k . Thus, $D_{c,k}(i, j, t)$ measures how strongly the magnitude of predicted component k at grid point (i, j) changes in response to an infinitesimal perturbation of input channel c at the same location. In this way, the diagnostic quantifies local input-output sensitivity in a strictly co-located sense.

Because the complete Jacobian of the Baltic-wide input-output mapping is too large to construct explicitly, only its spatially diagonal part was estimated numerically, following the randomized probing strategy described in Article IV [4]. High values of $D_{c,k}(i, j, t)$ therefore indicate regions where the prediction of SSC component k is especially sensitive to local perturbations in predictor channel c , and where local forecast quality may consequently depend more strongly on local predictor accuracy.

Taken together, these diagnostics address three complementary methodological questions. Occlusion identifies which predictors contain independent forecast information. LRP identifies where the trained network repeatedly finds the attributed support used to construct the forecast. DJE identifies where the forecast is most locally sensitive to perturbations in those predictors. Their combined use was intended to move the analysis beyond black-box predictive skill alone and toward a more physically interpretable account of the balance among antecedent-state memory, wind-driven adjustment, and geographically structured sensitivity in Baltic Sea SSC forecasting.

It should be noted that, the quantitative evaluation measures used in this thesis, including ED, MAE, and related diagnostics, follow the conventional formulations adopted in the associated publications [1, 2, 3, 4] and are therefore not repeated here in full detail.

3 Results and Discussion

A data-driven analysis and prediction framework for SSCs requires a reference dataset that is physically meaningful, spatially continuous, temporally extensive, and suitable for basin-scale application. Direct observations are essential for validation, but they are not sufficient as the primary reference field in the Baltic Sea because openly available observing systems do not provide spatially continuous SSC coverage. Drifters provide Lagrangian trajectories rather than fixed-location current fields, acoustic Doppler current profilers (ADCPs) are sparse and usually sample below the immediate surface layer, and high-frequency (HF) radar products are geographically restricted and mainly coastal. Ship-of-opportunity systems such as FerryBox are also not well suited to this role, because they primarily provide underway hydrographic observations rather than spatially consistent SSC fields, and any route-based current information remains strongly limited in coverage. Mooring-based current meters are likewise very limited in the openly accessible Baltic Sea archive [113].

Satellite observations provide an important alternative, but they also do not directly resolve total SSC. Altimetry measures sea-level gradients and therefore supports estimation of the geostrophic component of surface circulation when combined with mean dynamic topography [114, 115]. However, the total surface current also includes ageostrophic contributions associated with wind-driven Ekman transport, frictional and turbulent processes, inertial motions, wave-related effects, and coastal or topographic adjustments [116, 117, 118, 119]. Although some satellite-based products approximate total currents by combining geostrophic currents with simplified wind-driven corrections [120, 121], this approach is limited in the Baltic Sea because the basin is shallow, strongly stratified, topographically complex, and characterized by narrow gulfs, sills, coastal jets, fronts, and rapidly varying winds. Such products are therefore useful for comparison and diagnostic interpretation, but they are not sufficient as the main reference for total SSC.

This data-selection argument is supported by Article I. Although Article I focused on Baltic sea level rather than SSC, it demonstrated a key methodological point relevant to the present thesis: basin-scale reconstruction in the Baltic Sea benefits from combining observational constraints with model-derived spatiotemporal structure. In that study, the best gridded sea-level reconstruction was obtained when tide-gauge and altimetry observations were used together, while reconstructions based on only one observational source were weaker relative to the other. Model reanalysis was required to provide the dynamically balanced, spatially complete background statistics needed for basin-wide reconstruction [1]. This supports the use of reanalysis here as the most suitable reference field for SSC analysis, because it provides physically consistent, spatially continuous, and temporally extensive total surface-current fields.

The comparison in Figure 3 further illustrates the resolution and structural differences between products. The CMEMS Baltic reanalysis and the CMEMS GlobCurrent product show broadly similar large-scale flow orientation, but the reanalysis resolves substantially richer spatial structure, including narrow coastal jets, intensified currents in the Danish Straits and transition zone, and sub-basin-scale recirculations [102]. The satellite-based Level-4 product, provided on a coarser 0.25° grid, is smoother and does not resolve many mesoscale and coastal features that previous Baltic studies identify as dynamically important, as reviewed in Section 1.1.1.

These considerations led to the final data selection adopted in this thesis. Among the current datasets that were openly accessible and available to this study, the CMEMS Baltic Sea physical reanalysis was selected as the principal reference dataset for total SSC, because it provides spatially continuous, dynamically consistent, long-term near-surface

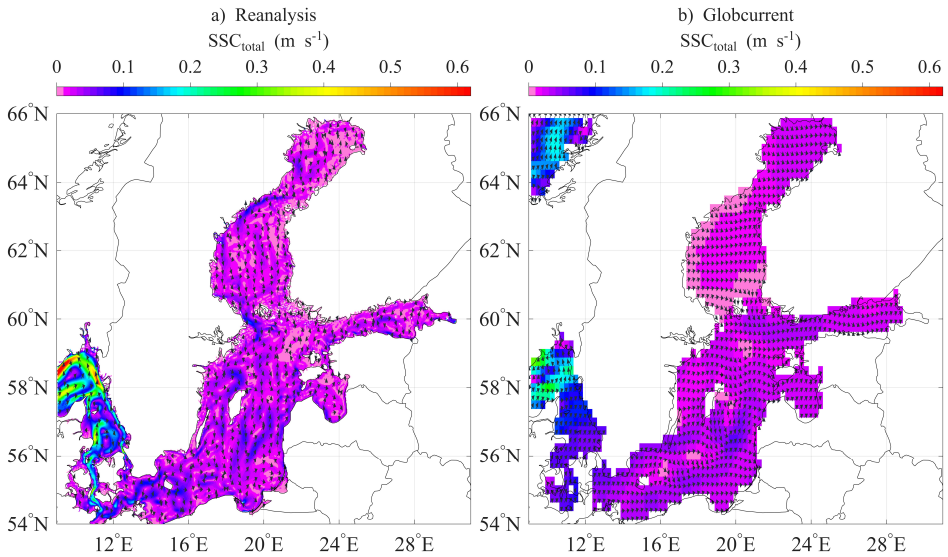


Figure 3: Comparison of long-term mean total surface current speed and vectors from (a) the CMEMS Baltic Sea physical reanalysis and (b) the CMEMS GlobCurrent multi-platform product. For improved viewing in digital mode, a high-resolution version of this figure is available in the supplementary figure repository at <https://doi.org/10.48726/3ryhg-bbt08> [122].

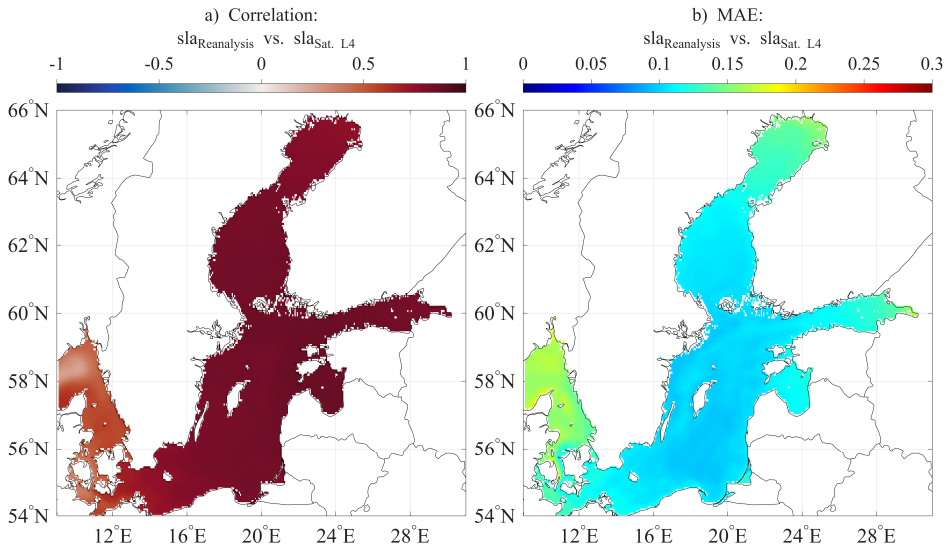


Figure 4: Agreement between SLA data from CMEMS European Seas Level-4 satellite and Baltic reanalysis (interpolated to the satellite data grid) over 2014–2023. (a) Grid-point correlation between daily SLA time series. (b) Mean absolute error (MAE, m).

current fields over the whole Baltic Sea and resolves both coastal and basin-scale structures required for the subsequent analyses.

For further insight, however, SLA remains a useful observational constraint. Figure 4 compares Baltic reanalysis SLA with the Copernicus Marine European Seas Level-4 satellite product over 2014–2023 [101]. The generally high spatial correlation and relatively low mean absolute error indicate that satellite sea-level captures much of the basin-scale variability relevant to the geostrophic structure. At the same time, this shows that geostrophy alone is not sufficient to represent total SSC variability in the Baltic Sea, where ageostrophic contributions remain important, thereby providing further support for the geostrophic-ageostrophic decomposition.

3.1 SSC variabilities

For the purpose of an initial assessment of the suitability of the data used in the present study, the climatological cycles during 1993–2024 are plotted in Figure 5. In most months, the interior basins of the Baltic Sea are characterized by relatively weak mean SSCs, generally remaining below about 0.2 m s^{-1} . By contrast, the highest climatological current speeds are consistently found in the western part of the domain, especially around the Danish Straits transition zone, where monthly mean values frequently exceed 0.2 m s^{-1} and locally approach 0.4 m s^{-1} .

This spatial contrast persists throughout the annual cycle, indicating that it is a robust feature of the long-term mean circulation. The monthly climatology also shows a general increase in current intensity during autumn, while the overall spatial organization of the flow remains broadly similar from month to month. Inspection of the monthly mean vector fields suggests that the annual cycle is mainly expressed as changes in current strength within a predominantly cyclonic circulation pattern, rather than as a seasonal alternation between cyclonic and anticyclonic basin-scale regimes. These results are further presented by identifying the months with the strongest departures from the climatological mean, among which May and December can be considered the most representative states, and are discussed in greater detail in Article II.

To evaluate the variability of SSC further, SOM analysis was applied using several grid dimensions. Figure 6 shows the mean ED between each daily SSC field from the original reanalysis and the SOM prototype to which that field was assigned. In total, 17 SOM configurations were tested in order to assess whether the daily SSC variability is more complex than what can be inferred from the monthly climatological cycle alone (Fig. 6: X-axis). For comparison, the corresponding ED obtained when each daily field is represented by the long-term monthly climatology of its respective month, as well as by the overall mean field for 1993–2024, is also shown.

At the same time, Figure 6 shows that increasing the SOM size leads to a gradual reduction in ED, implying a more accurate prototype assignment. The decrease is clear from the smallest tested configuration toward the larger grids, although the improvement becomes progressively smaller with increasing map size. This behaviour suggests that the main dominant SSC patterns are captured already with relatively few nodes, while additional nodes mainly refine the representation of secondary variations around those dominant states. Therefore, a larger SOM provides higher accuracy, but with diminishing returns at the upper end of the tested dimensions.

An important feature of the results is that the topology of the SOM itself appears to have only a limited effect on the representation error. For example, configurations such as 3×2 and 6×1 , or 4×3 and 12×1 , produce nearly the same ED despite their different two-dimensional and one-dimensional layouts. This indicates that, for the Baltic SSC data

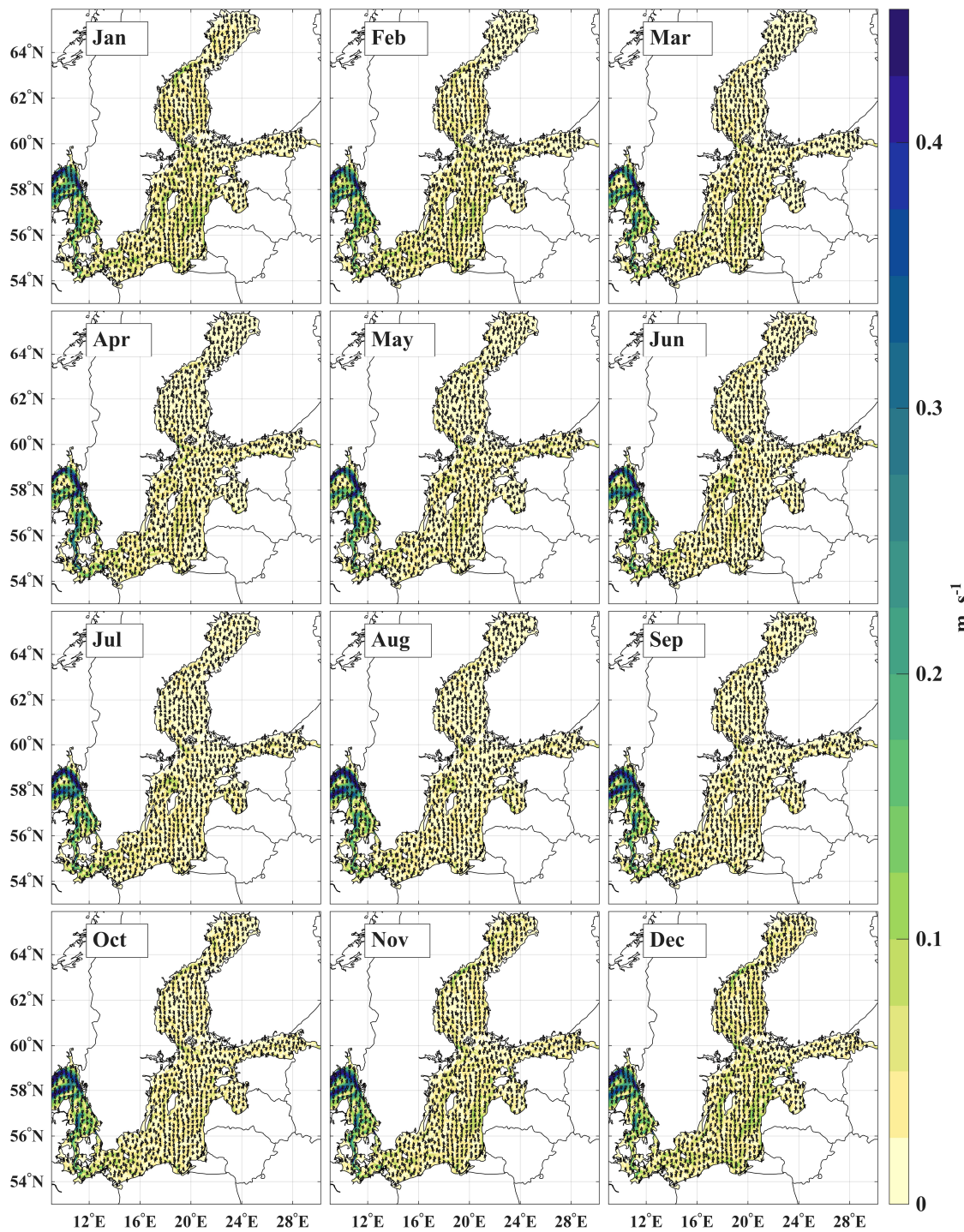


Figure 5: Baltic SSC monthly mean climatology (1993-2024). For improved viewing in digital mode, a high-resolution version of this figure is available in the supplementary figure repository at <https://doi.org/10.48726/3ryhg-bbt08> [122].

considered here, the representation error depends more strongly on the number of prototypes than on whether they are arranged in one or two dimensions. Under the present ED-based evaluation, the benefit of a two-dimensional SOM topology therefore appears limited. In other words, the dominant variability of SSC seems to be organized along a relatively low-dimensional continuum of dominant circulation states, so that introducing a two-dimensional SOM topology does not lead to a clearly different partitioning of the data space.

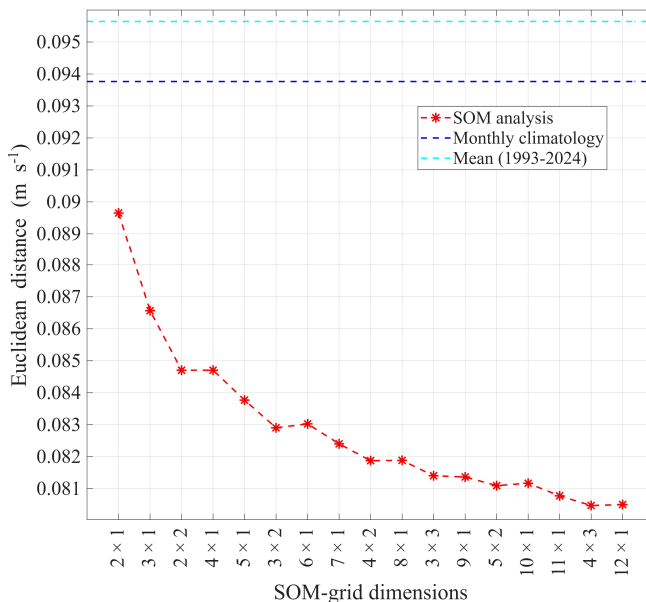


Figure 6: Mean ED between daily SSC fields from the reanalysis and their assigned SOM prototypes for different SOM-grid dimensions. The dashed blue and cyan lines indicate the corresponding reference distances obtained when the daily fields are represented by the monthly climatology and the overall mean field for 1993–2024, respectively.

Overall, the SOM-based representation provides a more realistic description of Baltic Sea daily SSC variability than either the long-term mean field or the monthly climatological cycle. Following the same procedure, the SOM analysis presented in Article III was restricted to the Gulf of Riga, whereas in the present thesis, the same framework is extended to the entire Baltic Sea.

As an example, Figure 7 shows the temporal distribution of the daily assignments to the 12×1 SOM over the full 1993–2024 reanalysis period. The SOM classes from 1 to 12 are ranked according to the spatially averaged SSC kinetic energy of their representative prototypes; accordingly, the color progression from blue to red broadly reflects a transition from less energetic to more energetic SSC states at the scale of the whole Baltic Sea. The assignments are highly heterogeneous in time: all 12 prototypes recur throughout the record, and in most calendar months several prototypes occur within the same month and year. At the same time, the temporal sequences are typically organized into relatively short-lived episodes, often lasting only a few days and commonly not persisting beyond about one week, which indicates that the SOM classes represent dominant circulation states rather than isolated outliers. However, the overlap between months remains substantial, and only limited evidence is found for a clear and comprehensive

seasonal cycle in prototype occurrence. Therefore, the daily SSC is more variable than can be satisfactorily represented by a single characteristic state for each calendar month. Instead, the temporal assignment pattern suggests that similar months in the climatological sense may still be composed of markedly different daily circulation realizations, whose occurrence is intermittent, uneven in time, and only partly seasonally organized.

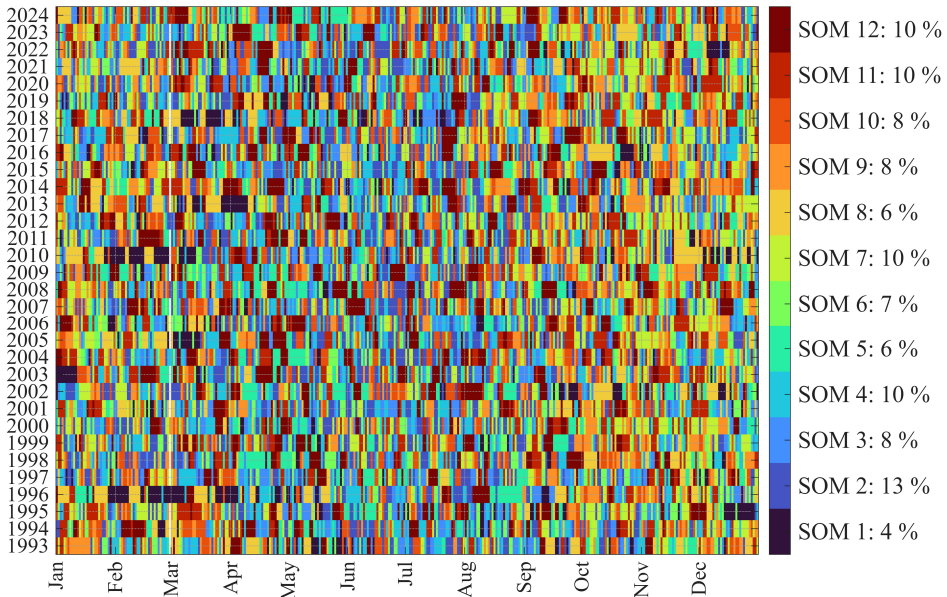


Figure 7: Temporal distribution of daily assignments to the 12×1 SOM for Baltic Sea SSC during 1993–2024. Percentages indicate the relative occurrence of each SOM prototype in the full reanalysis record.

Accordingly, Figure 8 presents the corresponding prototype fields. A common feature of all prototypes is the persistently energetic exchange region around the Danish Straits, which remains the dynamically most active part of the domain in every class. By contrast, the main differences between prototypes emerge over the interior Baltic Sea, especially in the Baltic Proper, the Gulf of Finland, the Gulf of Riga, the Bothnian Sea, and the Bothnian Bay. Some prototypes are characterized by weak interior currents, with the strongest SSC largely confined to the western entrance region, whereas others show a much broader intensification along the southern Baltic rim, the eastern side of the Gulf of Bothnia, and the Gulf of Finland. In this sense, the SOM patterns qualify the interpretation based on monthly climatology: the monthly mean fields remain useful as a first-order seasonal description, but they do not correspond to unique daily circulation states. Rather, they are composite fields produced by averaging several dynamically distinct realizations that can occur within the same calendar month.

This point becomes clearer when the SOM occupancies are compared with calendar-month averaging. The 12 SOM classes are not equally populated, with frequencies ranging from 4% for SOM 1 to 13% for SOM 2, while calendar-month binning imposes nearly uniform sample sizes by construction, approximately 7.7–8.5% (from 28/365 to 31/365) of the total number of days depending on month length. Hence monthly climatology partitions the record into fixed temporal bins that are not aligned with the actual recurrence of the SSC states. By contrast, the SOM clustering adapts the partitioning to the structure of

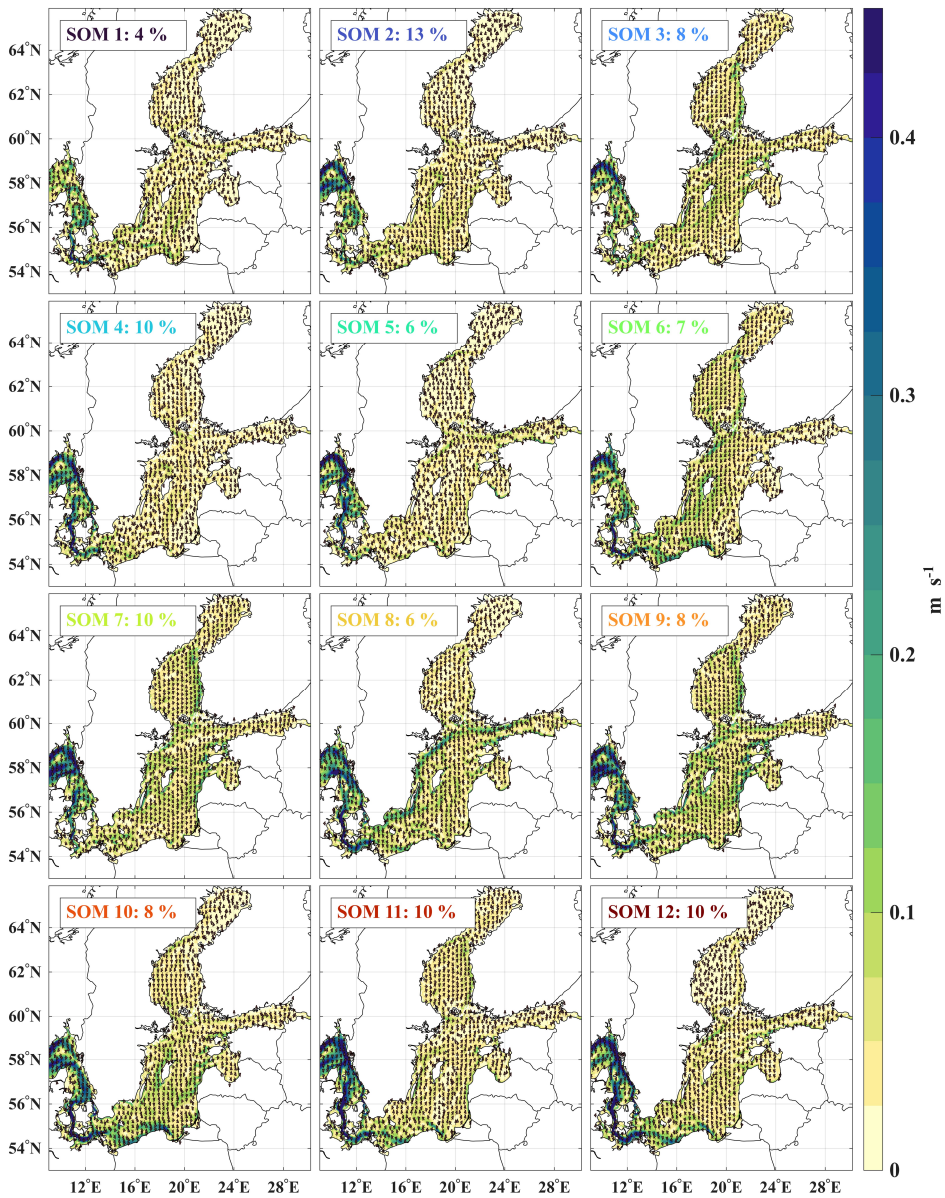


Figure 8: Prototype SSC fields obtained from the 12×1 SOM classification. Percentages indicate the relative occurrence of each prototype in the full 1993–2024 record. For improved viewing in digital mode, a high-resolution version of this figure is available in the supplementary figure repository at <https://doi.org/10.48726/3ryhg-bbt08> [122].

the data itself, allowing common states to occupy a larger fraction of the record and rarer states a smaller one. This provides a more realistic representation of the underlying SSC variability than equal calendar-based averaging.

3.2 Decomposition of SSC into Geostrophic and Ageostrophic Components

The geostrophic–ageostrophic decomposition was used to separate the part of the surface-current field associated with sea-level-gradient-driven flow from the residual component. In this section, the three diagnostics are presented in sequence: the time-mean fields describe the spatial structure of the decomposition, the alignment contrast examines scale dependence between daily and monthly variability, and the trend fields evaluate which component is most closely associated with long-term change.

The time-mean fields show the spatial partitioning of the total SSC into geostrophic and residual ageostrophic components (Fig. 9). The total and geostrophic mean fields have similar large-scale organization, with the strongest mean currents in the western Baltic, the Danish Straits, and adjacent transition regions. Weaker mean speeds occur over large parts of the central and northern basin interiors. The ageostrophic mean field has smaller magnitudes over most of the domain, but remains more visible in coastal zones, narrow passages, semi-enclosed gulfs, and other regions where frictional effects, bathymetric steering, and local wind response can modify the balanced flow.

Thus, Fig. 9 establishes the mean spatial structure of the decomposition. It does not by itself address how the relative contributions vary with averaging period or how they enter the long-term trend; these questions are treated separately in the following diagnostics. This mean-state partition is consistent with Article II, where the geostrophic component was shown to reproduce the main basin-scale gyre organization of Baltic SSC [2].

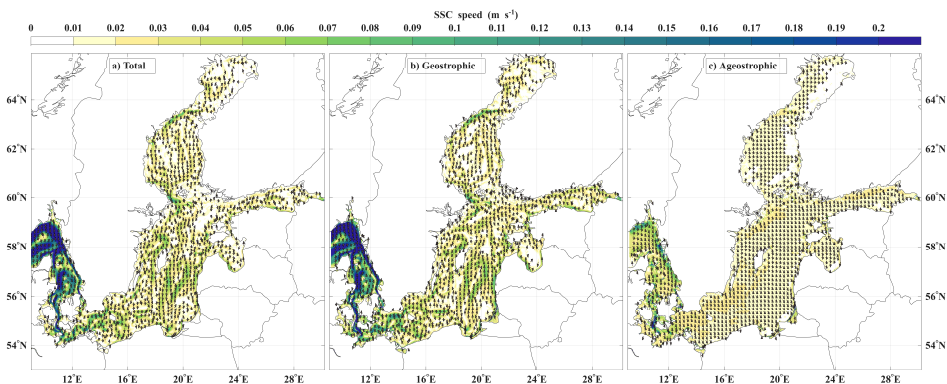


Figure 9: Time-mean sea surface current (SSC) speed and vectors for the (a) total, (b) geostrophic, and (c) ageostrophic components. The colour shading shows SSC magnitude ($m s^{-1}$), and arrows indicate the mean flow direction. For improved viewing in digital mode, a high-resolution version of this figure is available in the supplementary figure repository at <https://doi.org/10.48726/3ryhg-bbt08> [122].

The alignment contrast examines the decomposition from a different perspective by asking which component is more closely oriented with the total flow at different averaging scales (Fig. 10). At the daily scale, the alignment field is spatially heterogeneous, with alternating positive and negative regions. This indicates that the instantaneous direction

of the total SSC is not controlled uniformly by one component across the basin. Positive values occur mainly in energetic boundary regions and narrow straits, whereas negative values are more frequent in parts of the basin interiors, including central and northern areas. After monthly averaging, the field becomes more coherent and positive values cover a larger fraction of the domain. The daily-monthly contrast therefore shows that short-timescale departures are more spatially variable, while temporal averaging emphasizes the more coherent low-frequency component of the flow.

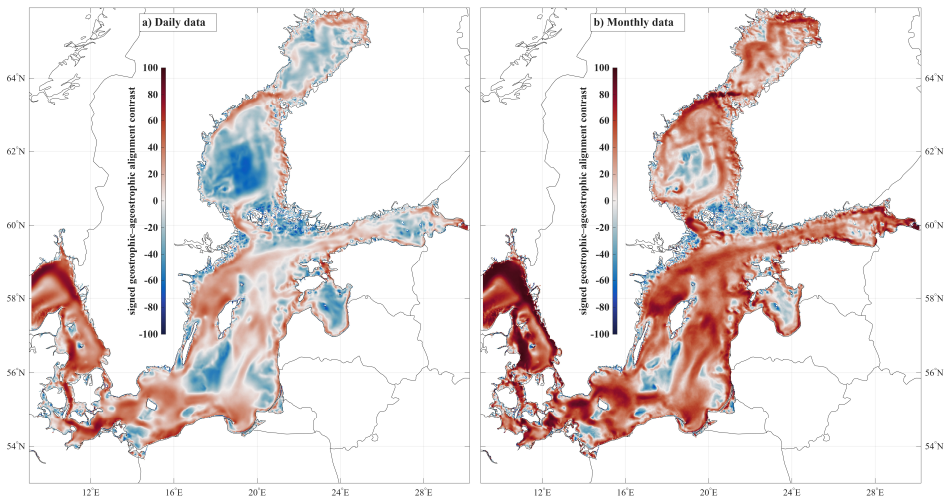


Figure 10: Signed geostrophic–ageostrophic alignment contrast relative to the total surface current for (a) daily and (b) monthly data. Positive values indicate stronger geostrophic alignment with the total flow, whereas negative values indicate relatively stronger ageostrophic alignment.

The alignment result also clarifies the seasonal interpretation reported in Article II. There, May and December were identified as dominant seasonal states, while March and September acted as transition months [2]. In the present synthesis, Fig. 10 adds that the transition from daily to monthly averaging changes the apparent dynamical balance: short-term fields retain stronger regional ageostrophic departures, whereas monthly fields emphasize the more coherent component of the circulation.

The trend fields address the long-term component of the decomposition rather than the mean state or the daily-monthly alignment contrast (Fig. 11). During 1993–2024, the spatial pattern of the total SSC speed trend is more similar to the geostrophic trend than to the ageostrophic trend. Positive tendencies are widespread in the total and geostrophic fields, especially in energetic corridors and coastal-transition regions, whereas negative tendencies are more localized. The ageostrophic trend field is weaker and less spatially organized, with significant changes confined mainly to selected coastal, northern, and eastern areas. The trend analysis therefore indicates that the multi-decadal change in SSC speed is expressed primarily through the geostrophic component, while the ageostrophic component contributes more locally.

Taken together, the three diagnostics provide a logical progression. The mean fields show the spatial partition between total, geostrophic, and residual ageostrophic SSC; the alignment contrast shows that this partition depends on averaging scale; and the trend fields show which component is most closely associated with multi-decadal change. The combined result is that the basin-scale and low-frequency organization of Baltic SSC is

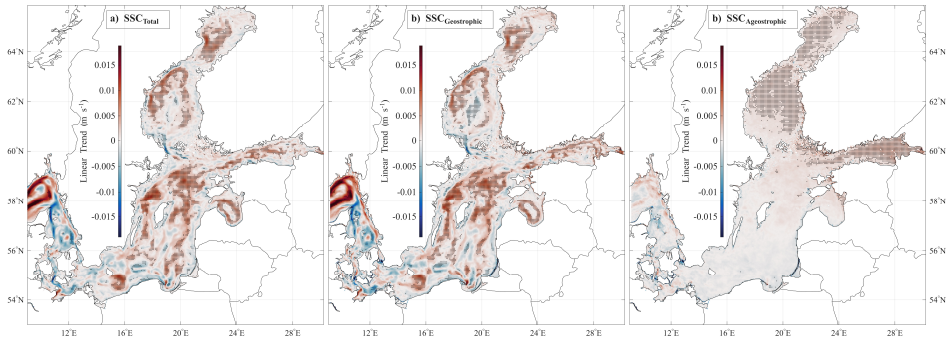


Figure 11: Linear trends in SSC speed in 1993-2024 for the (a) total, (b) geostrophic, and (c) ageostrophic components. The color shading denotes the trend magnitude ($m s^{-1} decade^{-1}$). Areas showing a significant trend (i.e., p -value < 0.05) are stippled on the maps.

mainly geostrophic, while the residual ageostrophic component is most important for daily variability, coastal and strait-scale departures, and localized trend features.

3.3 Data-Driven Emulation of Daily SSC

The thesis proceeds from physical decomposition to data-driven emulation in two steps. First, Article III develops a regional proof of concept for daily SSC emulation in the Gulf of Riga, a shallow and dynamically variable semi-enclosed basin where forecasting is particularly challenging [3]. Second, Article IV generalizes this approach to the full Baltic Sea by introducing a deeper convolutional U-Net architecture, refining the input set through occlusion sensitivity, and extending the analysis to post hoc explainability and recursive forecast-skill assessment [4]. In this way, the forecasting part of the thesis is a direct continuation of the decomposition analysis: the analytical results identify why SSC is difficult to predict, and the emulation results assess how much of that complexity can be captured from reduced-input data-driven mappings.

3.3.1 Regional proof of concept: sciCUN in the Gulf of Riga

Article III examined the feasibility of daily SSC emulation in the Gulf of Riga using the sciCUN architecture, a CNN-U-Net surrogate trained on hydrodynamic reanalysis outputs [3]. The Gulf of Riga provides a demanding test environment because its circulation is influenced by restricted exchange with adjacent basins, atmospheric forcing, freshwater inflows, shallow bathymetry, and mesoscale variability. In this setting, daily SSC forecasting requires more than reproducing a climatological or slowly varying background state.

The central idea of sciCUN was to emulate only the target surface-current field rather than the full ocean state. The previous-day SSC field was combined with atmospheric forcing aligned to the forecast day, allowing the network to learn a one-step surface-current update in which the antecedent circulation provides the inherited state and the atmospheric forcing modifies this state into the next-day current field [3]. Thus, sciCUN should not be interpreted as a simple image-to-image smoother or as a shifted copy of the previous-day circulation. The consecutive-day examples presented in Article III show that the model can reproduce substantial reorganization of the surface-current field, indicating that it learns how atmospheric forcing acts on the existing circulation to modify current direction and intensity (Fig. 11 in [3]).

The results of Article III demonstrated that this regional surrogate approach is viable.

Over the 2020–2023 testing period, sciCUN achieved an average ED of 2.30 cm s^{-1} between predicted and reference SSC vectors, an average component-wise MAE of 1.45 cm s^{-1} , and an average correlation coefficient of 0.92 [3]. The spatial structure of the errors is also informative. The largest deviations were concentrated near coastal regions close to river mouths and along the Irbe Strait, where boundary exchange and localized freshwater effects are especially strong [3]. This indicates both the strength and limitation of the regional emulator: the dominant daily circulation response can be captured efficiently from antecedent SSC and atmospheric forcing, but errors increase in dynamically constrained boundary zones where additional unresolved processes influence the surface flow.

A further result of Article III is that predictive success should be assessed not only pointwise but also in terms of circulation-pattern fidelity. Using SOM-based post-processing, sciCUN predictions reproduced the dominant daily current-pattern classes with 97% accuracy when the circulation was grouped into two prototypes and 87% accuracy when the grouping was refined to 12 prototypes [3]. This is important for the thesis because it shows that the emulator preserved not only component-wise magnitudes but also much of the dynamically meaningful spatial organization of the full vector field.

Taken together, these findings position Article III as the regional proof of concept of the thesis. It demonstrates that daily SSC forecasting by partial emulation is feasible in a coastal marginal-sea setting, but also reveals that forecast difficulty increases precisely where the circulation is most strongly affected by unresolved boundary-related and small-scale processes [3]. That result provides the immediate motivation for the more general basin-scale framework developed in Article IV.

3.3.2 Basin-scale extension: DeepCUN over the Baltic Sea

Article IV extends the forecasting framework from the Gulf of Riga to the full Baltic Sea by introducing DeepCUN, a deeper and more expressive convolutional U-Net architecture for basin-scale SSC emulation [4]. This extension is not a simple enlargement of the regional problem. Compared with the Gulf of Riga, the full Baltic Sea contains much stronger spatial heterogeneity, multiple loosely connected sub-basins, narrow straits, strong boundary-influenced corridors, and a wider range of circulation regimes. Accordingly, the basin-scale problem requires greater representational capacity and a more systematic treatment of input selection and interpretability [4].

DeepCUN uses a five-level encoder–decoder structure with skip connections and GN. This design was selected to increase the representational capacity of the network for the larger and more heterogeneous full Baltic Sea domain. To support this finalized design choice, we performed an architecture ablation and baseline comparison using the independent 2024 test period.

Figure 12 compares the finalized DeepCUN model design with two trainable variants, a DeepCUN variant in which GN is replaced by BN and a sciCUN-style three-level architecture, as well as two naive baselines, one-day persistence and daily climatology from 2015–2023. The finalized DeepCUN configuration generally maintains the lowest ED throughout the independent 2024 test period. Using BN instead of GN slightly but consistently increases the error, supporting the use of GN under the adopted training setup. The larger errors of the sciCUN-style model indicate that the additional depth in DeepCUN improves representation of the full Baltic Sea’s spatial heterogeneity. The persistence and daily climatology baselines produce substantially larger errors than the trainable neural-network configurations, showing that the trained models learn a nontrivial one-day mapping beyond simple persistence and stable climatological assumptions.

The one-step emulation results show that DeepCUN captures the dominant spatial

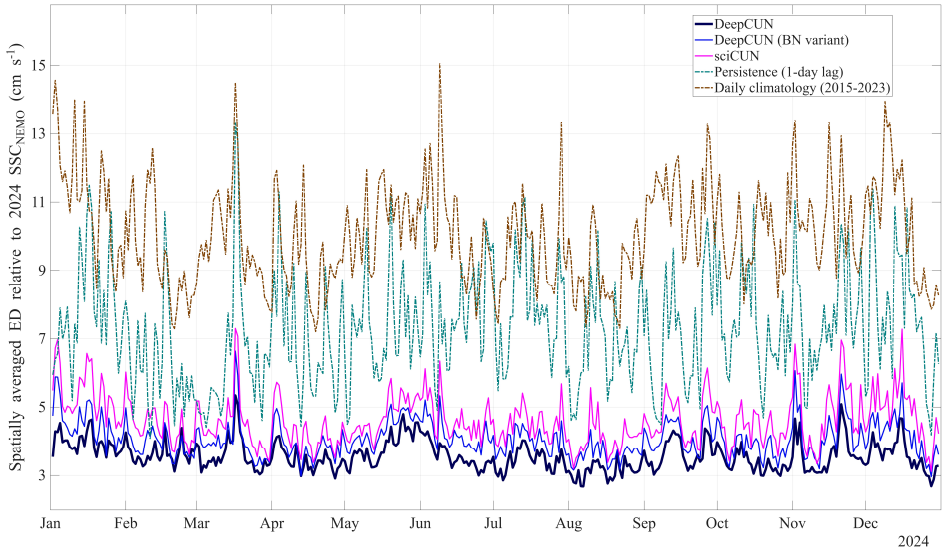


Figure 12: Architecture ablation and baseline comparison during the independent 2024 test period. Curves show the daily spatially averaged ED relative to SSC_{NEMO} for three trainable neural-network configurations and two naive reference baselines. The trainable configurations are the finalized DeepCUN model, the DeepCUN variant with batch normalization (BN), and the previous sciCUN-style three-level architecture trained for the whole Baltic Sea. The naive baselines are one-day persistence and daily climatology computed from 2015–2023. Lower ED indicates better agreement with SSC_{NEMO} [4].

patterns and temporal variability of Baltic SSC with high skill [4]. The highest errors were concentrated in the southwestern boundary exchange corridor and in narrow straits, whereas the basin interior showed substantially lower error levels and correlations exceeding 0.9 in most locations [4]. This result is physically consistent with the decomposition analysis presented earlier in the chapter: the largest forecast difficulties arise in dynamically active exchange regions, while much of the basin interior is governed by more coherent large-scale structure that is easier to emulate from antecedent state and wind forcing.

Article IV also evaluated whether the model preserved not only SSC amplitude but also dynamically relevant rotational structure. The comparison of predicted and reference vorticity fields showed strong sign agreement, including approximately 88% agreement in an easier representative case and still more than 80% agreement in the most difficult example dominated by strong western-boundary jets [4]. This indicates that DeepCUN reproduces the sign and organization of cyclonic and anticyclonic structures even when local velocity magnitudes are imperfectly estimated. In the context of Baltic Sea circulation, this is a substantial result because it suggests that the emulator retains the main structure of rotational flow features rather than merely minimizing pointwise component errors.

The Baltic-wide results also sharpen the interpretation of the regional findings from Article III. The Gulf of Riga study showed that partial emulation is feasible in a relatively compact but dynamically complex basin. Article IV demonstrates that this principle remains valid at the scale of the entire Baltic Sea, provided that the network capacity is increased and the input configuration is carefully pruned [4]. At the same time, both studies identify a common limitation: forecast errors remain largest in boundary-influenced,

geometrically constrained, and exchange-dominated regions. This consistency across the regional and basin scales strengthens the thesis argument that the most difficult part of SSC emulation is not the broad interior circulation, but the combination of sharp gradients, narrow passages, and boundary-conditioned dynamics.

3.3.3 Explainability of the learned SSC mapping

A major addition of Article IV is that it does not treat the emulator as a purely black-box predictor. Instead, explainable-AI analyses were introduced to characterize how the trained DeepCUN mapping distributes its reliance across the retained inputs [4]. This is particularly important in the thesis framework because the forecasting problem follows directly from the earlier physical decomposition. If the model skill depends primarily on the antecedent SSC field, the learned mapping would mainly reflect persistence. If it depends primarily on wind, the mapping would be more directly aligned with ageostrophic forcing. The XAI analyses were designed to examine this balance more explicitly.

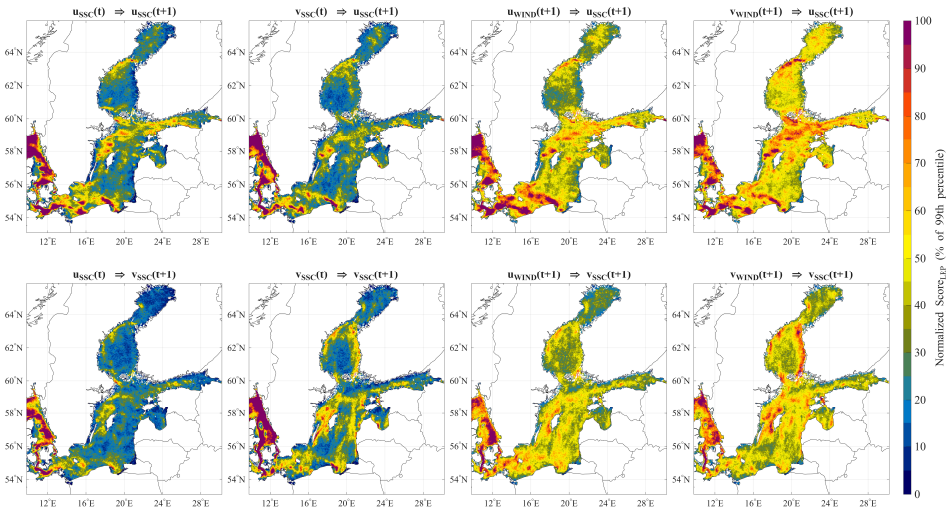


Figure 13: LRP results for DeepCUN averaged over all 2023 samples. Panels show spatial relevance maps for each input channel contributing to the prediction of $u_{SSC}(t+1)$ and $v_{SSC}(t+1)$. Relevance is normalized per sample by an ocean-only P_{99} factor pooled across all 4×2 input-output maps and clipped to $[0, 100]$ before averaging [4].

Article IV separated interpretability into two complementary notions: *attributed support* and *elasticity* [4]. Attributed support was assessed with Layer-wise Relevance Propagation (LRP), which identifies where the network repeatedly recruits information from the inputs when constructing the next-day SSC prediction. Elasticity was assessed with DJE, which quantifies how strongly the predicted SSC magnitude at a grid point responds to small co-located perturbations in an input channel [4]. These diagnostics do not answer the same question. LRP indicates where useful predictive information is drawn from, whereas DJE indicates where the local forecast is most sensitive to local input accuracy.

The LRP results reveal a physically coherent spatial division of roles (Fig. 13). Wind inputs show broadly elevated relevance across the Baltic interior and along coherent coastal bands, indicating that wind provides basin-scale predictive support for the next-day SSC field. By contrast, antecedent SSC inputs are more spatially localized, with hotspots concentrated near coasts, narrow straits, and boundary-influenced regions [4]. This means

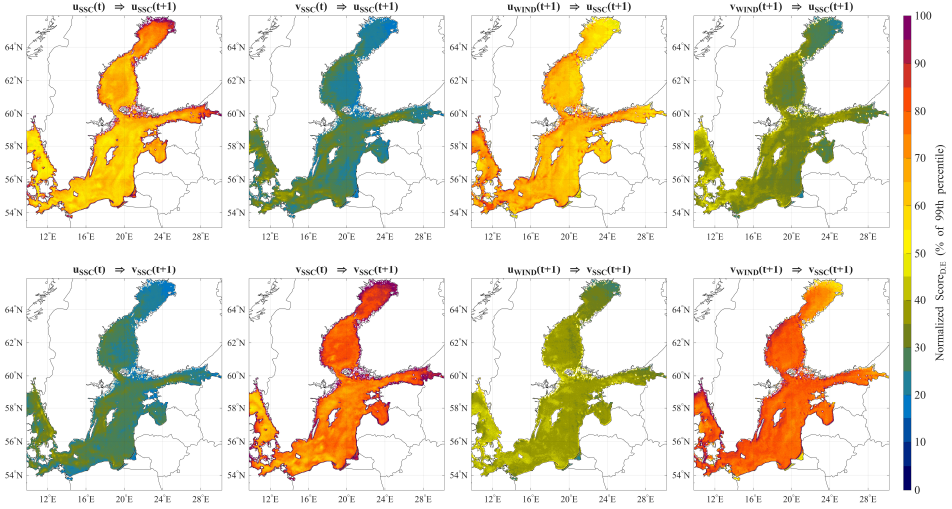


Figure 14: DJE results for DeepCUN averaged over all 2023 samples. Panels show spatial-diagonal elasticity maps (0–100%) quantifying the local sensitivity of the predicted SSC component magnitude to infinitesimal perturbations in each input channel at the same grid point. Elasticity is standardized by the ocean-domain variability of each input channel and normalized per sample by an ocean-only P_{99} factor pooled across all 4×2 input–output maps before averaging [4].

that DeepCUN does not use persistence uniformly across the basin. Rather, the previous-day SSC field acts as a stronger source of state memory where circulation is geometrically constrained, while wind provides a broader basin-scale forcing signal.

The DJE results complement this interpretation (Fig. 14). Local responsiveness is strongest along shorelines, narrow gulfs, and geometrically constrained coastal regions, while much of the open basin interior exhibits lower and more spatially uniform sensitivity. Channel-wise, DJE is dominated by same-component pathways: for $u_{SSC}(t+1)$, the strongest local sensitivity is associated with $u_{SSC}(t)$ and $u_{wind}(t+1)$, and for $v_{SSC}(t+1)$, the dominant pathways are $v_{SSC}(t)$ and $v_{wind}(t+1)$ [4]. Cross-component effects are much weaker in the strictly local DJE sense, suggesting that much of the inter-component coupling occurs through nonlocal spatial pathways rather than pointwise co-located dependence.

These explainability results are valuable because they link the emulator back to the physical interpretation established earlier in the thesis. The decomposition analysis showed that Baltic SSC combines a persistent large-scale structure with more transient wind-related departures. The XAI analysis shows that the trained network internalizes a corresponding division of predictive roles: wind contributes broad basin-scale support, while state memory is more localized and particularly important in coasts, straits, and boundary-influenced regions [4]. In this sense, the explainability results do not merely decorate the machine-learning model; they help demonstrate that the learned mapping is dynamically plausible in light of the physical circulation structure discussed in Article II.

3.3.4 Potential multi-day forecast skill

Article IV further extended the one-step emulation framework by assessing its recursive deployment over multiple days (Fig. 15). This experiment was deliberately framed as a *potential forecast-skill* assessment rather than as an operational forecast benchmark,

because the recursive runs used reanalysis winds and reanalysis initialization rather than independent atmospheric forecasts and operational initial conditions [4]. The purpose was therefore to test the internal stability of the learned one-step operator under the most effective forcing rather than to claim a fully realized operational forecast system.

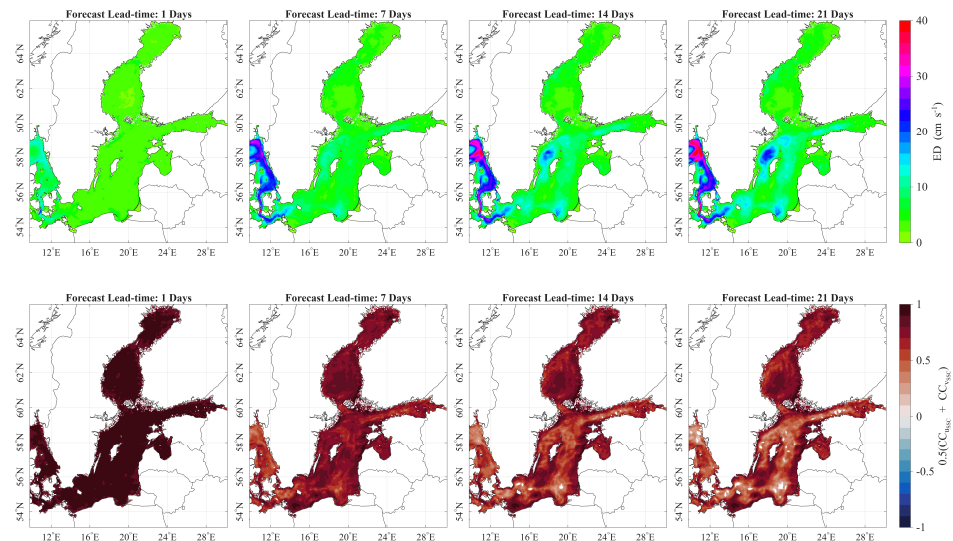


Figure 15: Spatial distribution of DeepCUN forecasting skill at selected lead times. Top row: ED between predicted and reference SSC. Bottom row: spatially averaged CC for u and v component of SSC $\overline{CC} = \frac{1}{2}(CC_{u_{SSC}} + CC_{v_{SSC}})$. Shown are averages for lead times of 1, 7, 14, and 21 days over the 2024 testing period [4].

The recursive results show a smooth and physically plausible degradation of skill with increasing lead time [4]. Domain-mean MAE grows from approximately 2.5 cm s^{-1} at day 1 to about 6.0 cm s^{-1} at day 21, while correlation decreases from values above 0.9 at short lead times to approximately 0.65 by day 21 [4]. This behavior indicates monotonic but not catastrophic error growth. In other words, the recursive forecasts do not collapse rapidly into unrealistic states; instead, they retain meaningful structure over multi-week horizons under the most effective forcing conditions.

The spatial pattern of recursive degradation is also informative. As in the one-step evaluation, the highest errors remain concentrated in the southwestern exchange corridor and in other dynamically active regions, while large parts of the basin interior degrade more gradually [4]. This result is consistent with the one-step performance maps, the XAI analysis, and the earlier decomposition results. The same regions that are dynamically most constrained and most difficult to emulate over one day remain the dominant sources of error growth over longer lead times.

Within the thesis narrative, these recursive results should be interpreted carefully. They do not demonstrate that DeepCUN is already a stand-alone 21-day operational forecast model. Rather, they show that the learned one-step SSC mapping remains sufficiently stable under autoregressive application to preserve nontrivial forecast skill over multi-day to multi-week horizons when the forcing is prescribed ideally [4]. This is an important distinction. The experiment establishes a meaningful upper-bound estimate of forecast potential, while also showing where practical deployment will remain limited by wind-forecast uncertainty, initialization, and unresolved boundary influences.

3.4 From physical interpretation to efficient emulation

Articles II–IV define a progression from physical decomposition to data-driven prediction. Article II established the dynamical basis for separating Baltic SSC into geostrophic and residual ageostrophic components [2]. Articles III and IV then used this physical framing to motivate data-driven emulation, where the forecasting problem is not treated as an unconstrained image-prediction task but as a reduced representation of the evolving surface-current field under antecedent ocean-state information and atmospheric forcing [3, 4].

Article III then demonstrated that daily SSC fields can be emulated efficiently in a shallow, highly variable sub-basin using a reduced-input CNN-U-Net surrogate [3]. The main lesson of that work is that the forecasting challenge is strongest where the circulation is most strongly constrained by river discharge, coastal geometry, and exchange with adjacent basins. Article IV generalizes this logic to the full Baltic Sea, showing that a deeper and more expressive emulator can retain high one-step skill at basin scale, while also revealing through XAI that the learned mapping combines basin-scale wind support with localized state memory [4].

A key outcome of this progression is conceptual rather than only technical. The thesis does not argue that deep learning replaces hydrodynamic modeling. On the contrary, both Article III and Article IV emphasize that the emulator is trained on physically consistent hydrodynamic reanalysis data and should be understood as a *partial emulator* of the target surface-current product rather than as a substitute for full ocean simulation [3, 4]. This distinction is essential, because the computational advantage of emulation arises precisely from restricting the task to a selected variable—SSC—rather than solving the full three-dimensional ocean state.

At the same time, the thesis shows that this restriction can still produce scientifically useful and dynamically interpretable results. The forecasting models preserve dominant current patterns, reproduce much of the observed temporal variability, and retain substantial information about rotational structure and spatial organization [3, 4]. Their limitations are also physically meaningful: the largest errors remain concentrated in boundary-influenced regions, narrow straits, river-affected coastal zones, and energetic exchange corridors, i.e. in the same parts of the Baltic system where unresolved forcing, sharp gradients, and nonlocal influences are strongest [3, 4]. This consistency suggests that the emulators are not failing arbitrarily, but rather at the same locations where the underlying circulation itself is most difficult.

Accordingly, the forecasting part of the thesis should be viewed as a continuation of the physical analysis rather than as a separate machine-learning exercise. The decomposition of SSC clarified the balance between dynamically distinct current components. The emulation studies then asked whether a reduced-input neural surrogate can learn enough of that balance to reproduce daily SSC fields efficiently. The answer, based on Articles III and IV, is affirmative but qualified: much of the daily SSC variability can be emulated with useful skill from antecedent state and wind forcing, yet boundary-conditioned processes, unresolved exchange influences, and local geometric complexity remain the principal sources of forecast difficulty [3, 4]. In this sense, the combined contribution of the thesis is twofold: it advances the physical interpretation of Baltic surface circulation and shows how that interpretation can be used to design efficient, explainable, and computationally tractable emulators for daily SSC analysis and forecasting.

4 Conclusion

This thesis investigated Baltic SSCs through a combined framework of data assessment, dynamical decomposition, pattern recognition, surrogate forecasting, and XAI.

The first main finding is that Baltic SSCs have a dynamically composite structure. The geostrophic component explains much of the large-scale and low-frequency organization of the surface circulation, whereas the ageostrophic component becomes more important in coastal zones, narrow passages, and locally forced regions.

The second main finding is that SOM analysis can organize daily SSC fields into dominant circulation states with unequal temporal occurrence. This pattern-based perspective retains spatial structures that are partly smoothed out in monthly or seasonal means.

The third main finding is that daily SSC evolution can be emulated efficiently with data-driven surrogate models. The regional sciCUN experiment in the Gulf of Riga showed that one-day SSC updates can be learned from antecedent SSC and atmospheric forcing. The basin-scale DeepCUN model then demonstrated that this approach can be extended to the full Baltic Sea with high one-step forecast skill and meaningful skill retained in recursive multi-day forecasts under prescribed forcing. These results show that surrogate modeling is useful when it is designed to emulate the target surface-current field directly, rather than to replace full ocean modeling in general. The fourth main finding is that the forecasting framework can be interpreted in physically meaningful terms. Predictor-sensitivity analysis showed that antecedent SSC and wind forcing contain most of the useful forecast information, while additional atmospheric predictors add only limited skill. XAI diagnostics further indicated that wind provides broad basin-scale predictive support, whereas state memory is especially important in coastal, geometrically constrained, and boundary-influenced regions.

Overall, the thesis shows that Baltic SSCs are best understood as a multiscale surface field with both robust large-scale organization and important regional structure. Their variability is partly controlled by geostrophic adjustment, but their daily evolution also depends on wind forcing, coastline and bathymetric constraints, exchange through the Danish Straits and between sub-basins, and ageostrophic processes. The principal contribution of the thesis is therefore twofold: it advances the physical interpretation of Baltic Sea surface circulation, and it demonstrates that this structure can be used to develop efficient and explainable surrogate forecasts of daily SSCs.

The main limitation of the study is the limited availability of independent direct current observations for basin-wide validation. Future work should therefore focus on testing the forecasting framework with operational atmospheric forcing, validating SSC estimates against independent current measurements where available, and developing retrieval or forecasting methods that target the ageostrophic component more directly. The broader conclusion is that machine learning is most useful in regional oceanography when it is built around physical structure rather than applied as a purely statistical substitute for ocean dynamics.

List of Figures

1	Bathymetry and main sub-basin divisions of the Baltic Sea	11
2	DeepCUN architecture and multi-day forecasting framework. Encoder (E1–E5, pink), bottleneck (B, orange), decoder (D5–D1, yellow), and output head (O, green; 1×1 Conv \rightarrow regression loss) [4].	24
3	Comparison of long-term mean total surface current speed and vectors from (a) the CMEMS Baltic Sea physical reanalysis and (b) the CMEMS GlobCurrent multi-platform product. For improved viewing in digital mode, a high-resolution version of this figure is available in the supplementary figure repository at https://doi.org/10.48726/3ryhg-bbt08 [122]. ..	30
4	Agreement between SLA data from CMEMS European Seas Level-4 satellite and Baltic reanalysis (interpolated to the satellite data grid) over 2014–2023. (a) Grid-point correlation between daily SLA time series. (b) Mean absolute error (MAE, m).	30
5	Baltic SSC monthly mean climatology (1993–2024). For improved viewing in digital mode, a high-resolution version of this figure is available in the supplementary figure repository at https://doi.org/10.48726/3ryhg-bbt08 [122].	32
6	Mean ED between daily SSC fields from the reanalysis and their assigned SOM prototypes for different SOM-grid dimensions. The dashed blue and cyan lines indicate the corresponding reference distances obtained when the daily fields are represented by the monthly climatology and the overall mean field for 1993–2024, respectively.	33
7	Temporal distribution of daily assignments to the 12×1 SOM for Baltic Sea SSC during 1993–2024. Percentages indicate the relative occurrence of each SOM prototype in the full reanalysis record.....	34
8	Prototype SSC fields obtained from the 12×1 SOM classification. Percentages indicate the relative occurrence of each prototype in the full 1993–2024 record. For improved viewing in digital mode, a high-resolution version of this figure is available in the supplementary figure repository at https://doi.org/10.48726/3ryhg-bbt08 [122].	35
9	Time-mean sea surface current (SSC) speed and vectors for the (a) total, (b) geostrophic, and (c) ageostrophic components. The colour shading shows SSC magnitude (m s^{-1}), and arrows indicate the mean flow direction. For improved viewing in digital mode, a high-resolution version of this figure is available in the supplementary figure repository at https://doi.org/10.48726/3ryhg-bbt08 [122].	36
10	Signed geostrophic–ageostrophic alignment contrast relative to the total surface current for (a) daily and (b) monthly data. Positive values indicate stronger geostrophic alignment with the total flow, whereas negative values indicate relatively stronger ageostrophic alignment.	37
11	Linear trends in SSC speed in 1993–2024 for the (a) total, (b) geostrophic, and (c) ageostrophic components. The color shading denotes the trend magnitude ($\text{m s}^{-1} \text{ decade}^{-1}$). Areas showing a significant trend (i.e., p -value < 0.05) are stippled on the maps.....	38

12	Architecture ablation and baseline comparison during the independent 2024 test period. Curves show the daily spatially averaged ED relative to SSC_{NEMO} for three trainable neural-network configurations and two naive reference baselines. The trainable configurations are the finalized DeepCUN model, the DeepCUN variant with batch normalization (BN), and the previous sciCUN-style three-level architecture trained for the whole Baltic Sea. The naive baselines are one-day persistence and daily climatology computed from 2015–2023. Lower ED indicates better agreement with SSC_{NEMO} [4].	40
13	LRP results for DeepCUN averaged over all 2023 samples. Panels show spatial relevance maps for each input channel contributing to the prediction of $u_{SSC}(t+1)$ and $v_{SSC}(t+1)$. Relevance is normalized per sample by an ocean-only P_{99} factor pooled across all 4×2 input-output maps and clipped to $[0, 100]$ before averaging [4].	41
14	DJE results for DeepCUN averaged over all 2023 samples. Panels show spatial-diagonal elasticity maps (0–100%) quantifying the local sensitivity of the predicted SSC component magnitude to infinitesimal perturbations in each input channel at the same grid point. Elasticity is standardized by the ocean-domain variability of each input channel and normalized per sample by an ocean-only P_{99} factor pooled across all 4×2 input-output maps before averaging [4].	42
15	Spatial distribution of DeepCUN forecasting skill at selected lead times. Top row: ED between predicted and reference SSC. Bottom row: spatially averaged CC for u and v component of SSC $\overline{CC} = \frac{1}{2}(CC_{u_{SSC}} + CC_{v_{SSC}})$. Shown are averages for lead times of 1, 7, 14, and 21 days over the 2024 testing period [4].	43

References

- [1] J. Elken, A. Barzandeh, I. Maljutenko, and S. Rikka, "Reconstruction of baltic gridded sea levels from tide gauge and altimetry observations using spatiotemporal statistics from reanalysis," *Remote Sensing*, vol. 16, no. 15, 2024.
- [2] A. Barzandeh, I. Maljutenko, S. Rikka, P. Lagema, A. Männik, R. Uiboupin, and U. Raudsepp, "Sea surface circulation in the Baltic Sea: decomposed components and pattern recognition," *Scientific Reports*, vol. 14, no. 1, p. 18649, 2024.
- [3] A. Barzandeh, I. Maljutenko, S. Rikka, and U. Raudsepp, "sciCUN: A deep learning model for daily sea surface current fields inference—a case study of the Gulf of Riga," *Ocean Modelling*, vol. 201, p. 102693, 2026.
- [4] A. Barzandeh, C. Manss, F. Stahl, I. Maljutenko, S. Rikka, and U. Raudsepp, "Data-driven emulation of numerically simulated Baltic Sea surface currents with a deep convolutional U-Net: Explainability and potential forecast skill," *JGR: Machine Learning and Computation*, 2026. Accepted for publication / In press.
- [5] F. V. Wulff, L. Rahm, and P. Larsson, *A systems analysis of the Baltic Sea*, vol. 148. Springer Science & Business Media, 2001.
- [6] M. Leppäranta and K. Myrberg, *Physical oceanography of the Baltic Sea*. Springer Science & Business Media, 2009.
- [7] H. Schubert, D. Schories, B. Schneider, and U. Selig, "Brackish water as an environment," *Biological Oceanography of the Baltic Sea*, pp. 3–21, 2017.
- [8] K. Myrberg, S. Korpinen, and L. Uusitalo, "Physical oceanography sets the scene for the marine strategy framework directive implementation in the Baltic Sea," *Marine Policy*, vol. 107, p. 103591, 2019.
- [9] B. Szymczycha, A. Zaborska, J. Bełdowski, K. Kuliński, A. Beszczyńska-Möller, M. Kędra, and J. Pempkowiak, "Chapter 4 - the baltic sea," in *World Seas: an Environmental Evaluation (Second Edition)* (C. Sheppard, ed.), pp. 85–111, Academic Press, second edition ed., 2019.
- [10] Finnish Meteorological Institute, "Seas," 2023. Accessed: 2026-05-18.
- [11] HELCOM, "Subbasins division level 2, helcom map and data service." <https://maps.helcom.fi>, 2022. The Baltic Marine Environment Protection Commission (HELCOM), Helsinki, Finland.
- [12] J. H. Reissmann, H. Burchard, R. Feistel, E. Hagen, H. U. Lass, V. Mohrholz, G. Nausch, L. Umlauf, and G. Wieczorek, "Vertical mixing in the Baltic Sea and consequences for eutrophication – a review," *Progress in Oceanography*, vol. 82, no. 1, pp. 47–80, 2009.
- [13] V. Stockmayer and A. Lehmann, "Variations of temperature, salinity and oxygen of the Baltic Sea for the period 1950 to 2020," *Oceanologia*, vol. 65, no. 3, pp. 466–483, 2023.
- [14] K. Myrberg and O. Andrejev, "Modelling of the circulation, water exchange and water age properties of the Gulf of Bothnia," *Oceanologia*, vol. 48, no. S, 2006.

- [15] M. Raateoja, "Deep-water oxygen conditions in the Bothnian Sea," *Boreal environment research*, vol. 18, no. 3-4, p. 235, 2013.
- [16] A. Omstedt and L. Axell, "Modeling the variations of salinity and temperature in the large gulfs of the Baltic Sea," *Continental Shelf Research*, vol. 23, no. 3, pp. 265–294, 2003.
- [17] M. Granskog, H. Kaartokallio, H. Kuosa, D. N. Thomas, and J. Vainio, "Sea ice in the Baltic Sea – a review," *Estuarine, Coastal and Shelf Science*, vol. 70, no. 1, pp. 145–160, 2006. Applying the Ecohydrology approach to the Guadiana estuary and coastal areas: lessons learned from dam impacted ecosystems.
- [18] T. Vihma and J. Haapala, "Geophysics of sea ice in the Baltic Sea: A review," *Progress in Oceanography*, vol. 80, no. 3, pp. 129–148, 2009.
- [19] T. Liblik, J. Laanemets, U. Raudsepp, J. Elken, and I. Suhhova, "Estuarine circulation reversals and related rapid changes in winter near-bottom oxygen conditions in the Gulf of Finland, Baltic Sea," *Ocean Science*, vol. 9, no. 5, pp. 917–930, 2013.
- [20] T. Liblik and U. Lips, "Variability of pycnoclines in a three-layer, large estuary: the Gulf of Finland," *Boreal Environment Research*, vol. 22, pp. 27–47, 2017.
- [21] A. Westerlund, L. Tuomi, P. Alenius, K. Myrberg, E. Miettunen, R. E. Vankevich, and R. Hordoir, "Circulation patterns in the Gulf of Finland from daily to seasonal timescales," *Tellus A: Dynamic Meteorology and Oceanography*, vol. 71, no. 1, p. 1627149, 2019.
- [22] U. Raudsepp, "Interannual and seasonal temperature and salinity variations in the Gulf of Riga and corresponding saline water inflow from the baltic proper," *Hydrology Research*, vol. 32, pp. 135–160, 04 2001.
- [23] E. Soosaar, I. Maljutenko, and U. Raudsepp, "Modeling surface currents in the Gulf of Riga: Seasonal and wind-forcing influences," *Oceanologia*, vol. 56, no. 2, pp. 327–343, 2014.
- [24] U. Lips, V. Zhurbas, M. Skudra, and G. Väli, "A numerical study of circulation in the Gulf of Riga, Baltic Sea. part i: Whole-basin gyres and mean currents," *Continental Shelf Research*, vol. 112, pp. 1–13, 2016.
- [25] A. Omstedt, J. Elken, A. Lehmann, and J. Piechura, "Knowledge of the Baltic Sea physics gained during the baltex and related programmes," *Progress in Oceanography*, vol. 63, no. 1, pp. 1–28, 2004.
- [26] V. Mohrholz, "Major baltic inflow statistics – revised," *Frontiers in Marine Science*, vol. 5, p. 384, 2018.
- [27] A. Lehmann, K. Myrberg, P. Post, I. Chubarenko, I. Dailidienė, H.-H. Hinrichsen, K. Hüseyin, T. Liblik, H. E. M. Meier, U. Lips, and T. Bukanova, "Salinity dynamics of the Baltic Sea," *Earth System Dynamics*, vol. 13, no. 1, pp. 373–392, 2022.
- [28] A. Lehmann, W. Krauss, and H.-H. Hinrichsen, "Effects of remote and local atmospheric forcing on circulation and upwelling in the Baltic Sea," *Tellus A: Dynamic Meteorology and Oceanography*, vol. 54, no. 3, pp. 299–316, 2002.

- [29] H. M. Meier, "Modeling the pathways and ages of inflowing salt-and freshwater in the Baltic Sea," *Estuarine, Coastal and Shelf Science*, vol. 74, no. 4, pp. 610–627, 2007.
- [30] M. Placke, H. E. M. Meier, U. Gräwe, T. Neumann, C. Frauen, and Y. Liu, "Long-term mean circulation of the Baltic Sea as represented by various ocean circulation models," *Frontiers in Marine Science*, vol. 5, p. 287, 2018.
- [31] H. E. M. Meier, M. Kniebusch, C. Dieterich, M. Gröger, E. Zorita, R. Elmgren, K. Myrberg, M. P. Ahola, A. Bartosova, E. Bonsdorff, F. Börgel, R. Capell, I. Carlén, T. Carlund, J. Carstensen, O. B. Christensen, V. Dierschke, C. Frauen, M. Frederiksen, E. Gaget, A. Galatius, J. J. Haapala, A. Halkka, G. Hugelius, B. Hünicke, J. Jaagus, M. Jüssi, J. Käyhkö, N. Kirchner, E. Kjellström, K. Kulinski, A. Lehmann, G. Lindström, W. May, P. A. Miller, V. Mohrholz, B. Müller-Karulis, D. Pavón-Jordán, M. Quante, M. Reckermann, A. Rutgersson, O. P. Savchuk, M. Stendel, L. Tuomi, M. Viitasalo, R. Weisse, and W. Zhang, "Climate change in the Baltic Sea region: a summary," *Earth System Dynamics*, vol. 13, no. 1, pp. 457–593, 2022.
- [32] A. Rutgersson, E. Kjellström, J. Haapala, M. Stendel, I. Danilovich, M. Drews, K. Jylhä, P. Kujala, X. G. Larsén, K. Halsnæs, I. Lehtonen, A. Luomaranta, E. Nilsson, T. Olsson, J. Särkkä, L. Tuomi, and N. Wasmund, "Natural hazards and extreme events in the Baltic Sea region," *Earth System Dynamics*, vol. 13, no. 1, pp. 251–301, 2022.
- [33] T. Liblik, G. Väli, K. Salm, J. Laanemets, M.-J. Lilover, and U. Lips, "Quasi-steady circulation regimes in the Baltic Sea," *Ocean Science*, vol. 18, no. 3, pp. 857–879, 2022.
- [34] N. Maximenko, R. Lumpkin, and L. Centurioni, "Chapter 12 - ocean surface circulation," in *Ocean Circulation and Climate* (G. Siedler, S. M. Griffies, J. Gould, and J. A. Church, eds.), vol. 103 of *International Geophysics*, pp. 283–304, Academic Press, 2013.
- [35] J. Isern-Fontanet, J. Ballabrera-Poy, A. Turiel, and E. García-Ladona, "Remote sensing of ocean surface currents: a review of what is being observed and what is being assimilated," *Nonlinear Processes in Geophysics*, vol. 24, no. 4, pp. 613–643, 2017.
- [36] J. Röhrs, G. Sutherland, G. Jeans, M. Bedington, A. K. Sperrevik, K.-F. Dagestad, Y. Gusdal, C. Mauritzen, A. Dale, and J. H. LaCasce, "Surface currents in operational oceanography: Key applications, mechanisms, and methods," *Journal of Operational Oceanography*, vol. 16, no. 1, pp. 60–88, 2023.
- [37] A. Griffa, A. Haza, T. M. Özgökmen, A. Molcard, V. Taillandier, K. Schroeder, Y. Chang, and P.-M. Poulain, "Investigating transport pathways in the ocean," *Deep Sea Research Part II: Topical Studies in Oceanography*, vol. 85, pp. 81–95, 2013. Modern Physical Oceanography and Professor H.T. Rossby.
- [38] M. Viitak, I. Maljutenko, V. Alari, Ü. Suursaar, S. Rikka, and P. Lagemaä, "The impact of surface currents and sea level on the wave field evolution during st. jude storm in the eastern Baltic Sea," *Oceanologia*, vol. 58, pp. 176–186, 2016.
- [39] H. Kanarik, L. Tuomi, J.-V. Björkqvist, and T. Kärnä, "Improving Baltic Sea wave forecasts using modelled surface currents," *Ocean Dynamics*, vol. 71, no. 6, pp. 635–653, 2021.

- [40] J. Elken, W. Matthäus, *et al.*, “Physical system description,” *Assmesment of Climate Change for the Baltic Sea Basin*, edited by: BACC Author Team, chap. Annex A, vol. 1, pp. 379–386, 2008.
- [41] J. Elken and A. Omstedt, “Water exchange in the Baltic Sea: a historical view of research approaches from basin scales to submesoscale,” *Frontiers in Earth Science*, vol. 13, p. 1598983, 2025.
- [42] F. G. W. Struve, “Ueber die strömungen der ostsee,” *Memoires de l’Academie Imperiale des Sciences de St. Petersbourg*, vol. 7, pp. 1–39, 1864. In German.
- [43] M. Knudsen, “Ein hydrographischer lehrsatz,” *Annalen der Hydrographie und Maritimen Meteorologie*, vol. 28, no. 7, pp. 316–320, 1900.
- [44] H. Burchard, K. Bolding, R. Feistel, U. Gräwe, K. Klingbeil, P. MacCready, V. Mohrholz, L. Umlauf, and E. M. van der Lee, “The knudsen theorem and the total exchange flow analysis framework applied to the Baltic Sea,” *Progress in Oceanography*, vol. 165, pp. 268–286, 2018.
- [45] E. Palmén, “Untersuchungen über die strömungen in den finnland umgebenden meeren,” *Commentationes Physico-Mathematicae / Societas Scientiarum Fennica*, vol. 12, pp. 1–94, 1930.
- [46] A. Sarkisyan, A. Staškiewicz, and Z. Kowalik, “Diagnostic calculations of summer circulation in the Baltic Sea,” *Okeanologiya*, vol. 15, no. 6, pp. 1002–1009, 1975.
- [47] A. Lehmann and H.-H. Hinrichsen, “On the wind driven and thermohaline circulation of the Baltic Sea,” *Physics and Chemistry of the Earth, Part B: Hydrology, Oceans and Atmosphere*, vol. 25, no. 2, pp. 183–189, 2000.
- [48] J. Jędrasik, M. Kowalewski, J. Nowak, and T. Wolski, “Influence of wind variability on the hydrodynamic conditions in the Baltic Sea: A case study using the m3d model,” *Oceanologia*, vol. 50, no. 3, pp. 345–365, 2008.
- [49] H. E. M. Meier, “Modeling the pathways and ages of inflowing salt- and freshwater in the Baltic Sea,” *Estuarine, Coastal and Shelf Science*, vol. 74, no. 4, pp. 610–627, 2007.
- [50] E. Hagen and R. Feistel, “Synoptic changes in the deep rim current during stagnant hydrographic conditions in the eastern gotland basin, Baltic Sea,” *Oceanologia*, vol. 49, no. 2, 2007.
- [51] O. Andrejev, K. Myrberg, P. Alenius, and P. A. Lundberg, “Mean circulation and water exchange in the Gulf of Finland—a study based on three-dimensional modelling,” *Boreal Environment Research*, vol. 9, no. 1, p. 1, 2004.
- [52] J. Elken, M. Nömm, and P. Lagemaa, “Circulation patterns in the Gulf of Finland derived from the eof analysis of model results,” *Boreal environment research*, vol. 16, p. 84, 2011.
- [53] M.-J. Lilover, J. Pavelson, and T. Kouts, “Wind forced currents over the shallow naisaar bank in the Gulf of Finland,” *Boreal environment research*, vol. 16, p. 164, 2011.

- [54] T. Soomere, N. Delpeche, B. Viikmae, E. Quak, H. M. Meier, and K. Doeoes, "Patterns of current-induced transport in the surface layer of the Gulf of Finland," *Boreal environment research*, vol. 16, p. 49, 2011.
- [55] O. Andrejev, T. Soomere, A. Sokolov, and K. Myrberg, "The role of the spatial resolution of a three-dimensional hydrodynamic model for marine transport risk assessment," *Oceanologia*, vol. 53, pp. 309–334, 2011. Changing water, energy and biogeochemical cycles in the Baltic Sea basin. The 6th Study Conference on BALTEX, Międzyzdroje, 14-18 June 2010.
- [56] M. Gade, B. Seppke, and L. Dreschler-Fischer, "Mesoscale surface current fields in the Baltic Sea derived from multi-sensor satellite data," *International Journal of Remote Sensing*, vol. 33, no. 10, pp. 3122–3146, 2012.
- [57] U. Lips, V. Zhurbas, M. Skudra, and G. Väli, "A numerical study of circulation in the Gulf of Riga, Baltic Sea. part ii: Mesoscale features and freshwater transport pathways," *Continental Shelf Research*, vol. 115, pp. 44–52, 2016.
- [58] J. Jędrasik, M. Kowalewski, and J. Nowak, "Analysis of long-term variability of the Baltic Sea surface currents using a 44-year model hindcast," *Oceanologia*, vol. 61, no. 4, pp. 428–440, 2019.
- [59] I. Maljutenko and U. Raudsepp, "Long-term mean, interannual and seasonal circulation in the Gulf of Finland—the wide salt wedge estuary or gulf type rofi," *Journal of Marine Systems*, vol. 195, pp. 1–19, 2019.
- [60] I. Maljutenko and U. Raudsepp, "Modeling surface currents in the Gulf of Finland: The effect of wind forcing resolution," *Oceanologia*, vol. 61, no. 1, pp. 44–54, 2019.
- [61] E. Bednorz, M. Pórolniczak, and A. M. Tomczyk, "Regional circulation patterns inducing coastal upwelling in the Baltic Sea," *Theoretical and Applied Climatology*, vol. 144, pp. 905–916, 2021.
- [62] G. Väli, H. M. Meier, T. Liblik, H. Radtke, K. Klingbeil, U. Gräwe, and U. Lips, "Sub-mesoscale processes in the surface layer of the central Baltic Sea: A high-resolution modelling study," *Oceanologia*, vol. 66, no. 1, pp. 78–90, 2024.
- [63] Y. Liu, M. Qiu, C. Liu, and Z. Guo, "Big data challenges in ocean observation: a survey," *Personal and Ubiquitous Computing*, vol. 21, no. 1, pp. 55–65, 2017.
- [64] P. De Mey-Frémaux, N. Ayoub, A. Barth, R. Brewin, G. Charria, F. Campuzano, S. Ciavatta, M. Cirano, C. A. Edwards, I. Federico, *et al.*, "Model-observations synergy in the coastal ocean," *Frontiers in Marine Science*, vol. 6, p. 436, 2019.
- [65] R. E. Thomson and W. J. Emery, *Data analysis methods in physical oceanography*. Elsevier, 2024.
- [66] C. Qian, B. Huang, X. Yang, and G. Chen, "Data science for oceanography: from small data to big data," *Big Earth Data*, vol. 6, no. 2, pp. 236–250, 2022.
- [67] C. Dong, G. Xu, G. Han, B. J. Bethel, W. Xie, and S. Zhou, "Recent developments in artificial intelligence in oceanography," *Ocean-Land-Atmosphere Research*, vol. 2022, p. 9870950, 2022.

- [68] H. Ahmad, "Machine learning applications in oceanography," *Aquatic Research*, vol. 2, no. 3, pp. 161-169, 2019.
- [69] K. Malde, N. O. Handegard, L. Eikvil, and A.-B. Salberg, "Machine intelligence and the data-driven future of marine science," *ICES Journal of Marine Science*, vol. 77, no. 4, pp. 1274-1285, 2020.
- [70] R. Hao, Y. Zhao, S. Zhang, and X. Deng, "Deep learning for ocean forecasting: A comprehensive review of methods, applications, and datasets," *IEEE Transactions on Cybernetics*, vol. 55, no. 6, pp. 2879-2898, 2025.
- [71] S. Dey, R. Sikhakolli, D. P. Dogra, and S. Sil, "On the variability of ocean surface current in the bay of bengal using self-organizing map (som)," *Deep-Sea Research Part I*, vol. 199, p. 104103, 2023.
- [72] K. T. Hjelmervik and K. Hjelmervik, "Improved estimation of oceanographic climatology using empirical orthogonal functions and clustering," in *OCEANS - Bergen, MTS/IEEE*, 2013.
- [73] Y. Hisaki, "Classification of surface current maps," *Deep-Sea Research Part I*, vol. 73, pp. 117-126, 2013.
- [74] Y. Liu and R. H. Weisberg, "Patterns of ocean current variability on the west florida shelf using the self-organizing map," *Journal of Geophysical Research: Oceans*, vol. 110, p. C06003, 2005.
- [75] Y. Liu, R. H. Weisberg, and C. N. K. Mooers, "Performance evaluation of the self-organizing map for feature extraction," *Journal of Geophysical Research: Oceans*, vol. 111, p. C05018, 2006.
- [76] Y. Liu, R. H. Weisberg, and R. He, "Sea surface temperature patterns on the west florida shelf using growing hierarchical self-organizing maps," *Journal of Atmospheric and Oceanic Technology*, vol. 23, no. 2, pp. 325-338, 2006.
- [77] Y. Liu, R. H. Weisberg, and L. K. Shay, "Current patterns on the west florida shelf from joint self-organizing map analyses of hf radar and adcp data," *Journal of Atmospheric and Oceanic Technology*, vol. 24, no. 4, pp. 702-712, 2007.
- [78] Y. Liu and R. H. Weisberg, "A review of self-organizing map applications in meteorology and oceanography," in *Self Organizing Maps—Applications and Novel Algorithm Design*, (ed Dr. Josphat Igadwa Mwasiagi, J. I.), 2011.
- [79] O. Ronneberger, P. Fischer, and T. Brox, "U-net: Convolutional networks for biomedical image segmentation," in *Medical Image Computing and Computer-Assisted Intervention - MICCAI 2015* (N. Navab, J. Hornegger, W. M. Wells, and A. F. Frangi, eds.), pp. 234-241, Cham: Springer, 2015.
- [80] A. Sinha and R. Abernathey, "Estimating ocean surface currents with machine learning," *Frontiers in Marine Science*, vol. 8, p. 672477, 2021.
- [81] T. Archambault, A. Chédin, L. Bertino, and S. Thiria, "Sea surface height super-resolution using high-resolution sea surface temperature with a subpixel convolutional residual network," *Environmental Data Science*, vol. 1, p. e26, 2022.

- [82] B. Yuan, B. Jacob, W. Chen, and J. Staneva, "Downscaling sea surface height and currents in coastal regions using convolutional neural network," *Applied Ocean Research*, vol. 151, p. 104153, 2024.
- [83] R. Furner *et al.*, "The challenge of land in a neural network ocean model," *Environmental Data Science*, vol. 3, p. e13, 2024.
- [84] M. Nonnenmacher and D. S. Greenberg, "Deep emulators for differentiation, forecasting, and parametrization in earth system simulators," *Journal of Advances in Modeling Earth Systems*, vol. 13, no. 7, p. e2021MS002554, 2021.
- [85] P. B. Gibson and *et al.*, "Training machine learning models on climate model output yields skillful interpretable seasonal precipitation forecasts," *Communications Earth & Environment*, vol. 2, p. 159, 2021.
- [86] Y. Cui *et al.*, "Forecasting the eddying ocean with a deep neural network," *Nature Communications*, vol. 16, p. 2268, 2025.
- [87] A. Stigebrandt and B. G. Gustafsson, "Response of the Baltic Sea to climate change—theory and observations," *Journal of Sea Research*, vol. 49, no. 4, pp. 243–256, 2003.
- [88] H. Markus Meier, L. Barghorn, F. Börgel, M. Gröger, L. Naumov, and H. Radtke, "Multidecadal climate variability dominated past trends in the water balance of the Baltic Sea watershed," *npj Climate and Atmospheric Science*, vol. 6, no. 1, p. 58, 2023.
- [89] J.-P. Jalkanen, L. Johansson, and J. Kukkonen, "A comprehensive inventory of the ship traffic exhaust emissions in the Baltic Sea from 2006 to 2009," *Ambio*, vol. 43, no. 3, pp. 311–324, 2014.
- [90] J. Elken, A. Lehmann, and K. Myrberg, *Second Assessment of Climate Change for the Baltic Sea Basin*, ch. Recent Change—Marine Circulation and Stratification, pp. 131–144. Springer International Publishing, 2015.
- [91] M. Placke, H. E. M. Meier, and T. Neumann, "Sensitivity of the Baltic Sea overturning circulation to long-term atmospheric and hydrological changes," *Journal of Geophysical Research: Oceans*, vol. 126, no. 3, p. e2020JC016079, 2021.
- [92] Q. Zhao *et al.*, "Applications of deep learning in physical oceanography: a comprehensive review," *Frontiers in Marine Science*, vol. 11, p. 1396322, 2024.
- [93] M. Muppala, *Digital Oceans: Artificial Intelligence, IoT, and Sensor Technologies for Marine Monitoring and Climate Resilience*. Deep Science Publishing, July 2025.
- [94] Copernicus Marine Service, "Baltic Sea physics reanalysis," 2026. Product ID: BALTICSEA_MULTIYEAR_PHY_003_011, accessed 2026-04-03.
- [95] I. Ringgaard, V. Korabel, L. Spruch, A. Lindenthal, and V. Huess, *Copernicus Marine Product User Manual for BALTICSEA_MULTIYEAR_PHY_003_011 and BALTICSEA_MULTIYEAR_BGC_003_012*. Mercator Ocean International, June 2024. Issue 1.0, Ref. CMEMS-BAL-PUM-003-006-007.

- [96] T. Panteleit, S. Verjovkina, S. Jandt-Scheelke, L. Spruch, and V. Huess, "Quality information document: Baltic Sea physics reanalysis product (baltic-sea_multiyear_phy_003_011)," 2025. Baltic Sea Production Centre.
- [97] G. Madec and the NEMO System Team, *NEMO Ocean Engine Reference Manual*, 2023.
- [98] R. Hordoir, L. Axell, A. Höglund, C. Dieterich, F. Fransner, M. Gröger, Y. Liu, P. Pemberton, S. Schimanke, H. Andersson, P. Ljungemyr, P. Nygren, S. Falahat, A. Nord, A. Jönsson, I. Lake, K. Döös, M. Hieronymus, H. Dietze, U. Löptien, I. Kuznetsov, A. Westerlund, L. Tuomi, and J. Haapala, "Nemo-nordic 1.0: a nemo-based ocean model for the baltic and north seas – research and operational applications," *Geoscientific Model Development*, vol. 12, no. 1, pp. 363–386, 2019.
- [99] T. Kärnä, P. Ljungemyr, S. Falahat, I. Ringgaard, L. Axell, V. Korabel, J. Murawski, I. Maljutenko, A. Lindenthal, S. Jandt-Scheelke, S. Verjovkina, I. Lorkowski, P. Lagema, J. She, L. Tuomi, A. Nord, and V. Huess, "Nemo-nordic 2.0: operational marine forecast model for the Baltic Sea," *Geoscientific Model Development*, vol. 14, no. 9, pp. 5731–5749, 2021.
- [100] Copernicus Climate Change Service (C3S), "Era5 hourly data on single levels from 1940 to present," 2018. Climate Data Store dataset.
- [101] EU Copernicus Marine Service Information, "European seas gridded l4 sea surface heights and derived variables reprocessed 1993 ongoing," 2025. Copernicus Marine Service dataset, product ID: SEALEVEL_EUR_PHY_L4_MY_008_068.
- [102] EU Copernicus Marine Service Information, "Global total (copernicus-globcurrent), ekman and geostrophic currents at the surface and 15m," 2025. Copernicus Marine Service dataset, product ID: MULTIOBS_GLO_PHY_MYNRT_015_003.
- [103] T. Kohonen, *Self-Organizing Maps*, vol. 30 of *Springer Series in Information Sciences*. Berlin, Heidelberg: Springer, 3 ed., 2001.
- [104] B. K. Arbic, R. B. Scott, D. B. Chelton, J. G. Richman, and J. F. Shriver, "Effects of stencil width on surface ocean geostrophic velocity and vorticity estimation from gridded satellite altimeter data," *Journal of Geophysical Research: Oceans*, vol. 117, p. C03029, 2012.
- [105] D. Haidvogel, A. Robinson, and E. Schulman, "The accuracy, efficiency, and stability of three numerical models with application to open ocean problems," *Journal of Computational Physics*, vol. 34, no. 1, pp. 1–53, 1980.
- [106] J. C. McWilliams, "Modeling the oceanic general circulation," *Annual Review of Fluid Mechanics*, vol. 28, no. 1, pp. 215–248, 1996.
- [107] E. Allen, C. Kruger, F.-Y. Leung, and J. C. Stephens, "Diverse perceptions of stakeholder engagement within an environmental modeling research team," *Journal of Environmental Studies and Sciences*, vol. 3, pp. 343–356, 2013.
- [108] C. A. Eschenbach, "Bridging the gap between observational oceanography and users," *Ocean Science*, vol. 13, no. 1, pp. 161–173, 2017.
- [109] E. P. Chassignet and X. Xu, "On the importance of high-resolution in large-scale ocean models," *Advances in Atmospheric Sciences*, vol. 38, pp. 1621–1634, 2021.

- [110] G. Montavon, A. Binder, S. Lapuschkin, W. Samek, and K.-R. Müller, *Layer-Wise Relevance Propagation: An Overview*, pp. 193–209. Cham: Springer International Publishing, 2019.
- [111] Y. A. LeCun, L. Bottou, G. B. Orr, and K.-R. Müller, *Efficient BackProp*, pp. 9–48. Berlin, Heidelberg: Springer Berlin Heidelberg, 2012.
- [112] K. Simonyan, A. Vedaldi, and A. Zisserman, “Deep inside convolutional networks: Visualising image classification models and saliency maps,” 2014.
- [113] EU Copernicus Marine Service Information, “Baltic Sea - in situ near real time observations,” 2024. Copernicus Marine Service dataset, product ID: IN-SITU_BAL_PHYBGCWAV_DISCRETE_MYNRT_013_032.
- [114] G. Jin-Yun, C. Xiao-Tao, H. Cheinway, S. Jia-Long, and H. Yan-Ben, “Oceanic surface geostrophic velocities determined with satellite altimetric crossover method,” *Chinese Journal of Geophysics*, vol. 53, no. 6, pp. 926–934, 2010.
- [115] J. M. Sánchez-Reales, M. I. Vigo, S. Jin, and B. F. Chao, “Global surface geostrophic ocean currents derived from satellite altimetry and goce geoid,” *Marine Geodesy*, vol. 35, no. sup1, pp. 175–189, 2012.
- [116] S. T. Gille, F. Ardhuin, and A. V. Bôas, “Wind, waves, and surface currents: Interactions at mesoscales and submesoscales,” *Annual Review of Marine Science*, vol. 18, no. 17, pp. 1–24, 2026.
- [117] M.-H. Rio and F. Hernandez, “High-frequency response of wind-driven currents measured by drifting buoys and altimetry over the world ocean,” *Journal of Geophysical Research: Oceans*, vol. 108, no. C8, p. 3283, 2003.
- [118] M.-H. Rio, S. Mulet, and N. Picot, “Beyond goce for the ocean circulation estimate: Synergetic use of altimetry, gravimetry, and in situ data provides new insight into geostrophic and ekman currents,” *Geophysical Research Letters*, vol. 41, no. 24, pp. 8918–8925, 2014.
- [119] H. Chen, S. Li, J. Song, and H. He, “Wave-modified ekman current solutions for the time-dependent vertical eddy viscosity,” *Journal of Marine Science and Engineering*, vol. 9, no. 6, 2021.
- [120] J. Sudre, C. Maes, and V. Garçon, “On the global estimates of geostrophic and ekman surface currents,” *Limnology and Oceanography: Fluids and Environments*, vol. 3, no. 1, pp. 1–20, 2013.
- [121] K. Dohan, “Ocean surface currents from satellite data,” *Journal of Geophysical Research: Oceans*, vol. 122, no. 4, pp. 2647–2651, 2017.
- [122] A. Barzandeh, “Supplementary high-resolution figures for phd thesis - machine learning analysis of Baltic Sea surface current variability,” May 2026.

Acknowledgements

I would like to acknowledge all my colleagues in the Department of Marine Systems at TalTech. Being among them over the past almost five years has been a genuine pleasure, and I remain grateful for having shared this period of my life with them. Their daily presence, together with their kind and positive attitudes, has been a constant encouragement throughout my work and activities.

I would also like to acknowledge my supervisory team — Dr. Maljutenko, Dr. Rikka, and my advisor Prof. Raudsepp — for the role they played in a process that not only moved my studies forward, but also shaped me into a more independent, more self-confident, and braver researcher than I was five years ago.

I would like to thank Prof. Elken for his trust during our joint work on the paper. I am also grateful to the German Research Center for Artificial Intelligence (DFKI) in Oldenburg, Germany, especially Dr. Manß and Dr. Stahl, for their valuable insight during my short research visit in May 2025.

Even so, the significant and valuable parts of this work were brought to their present form, piece by piece, through perseverance, discipline, personal determination, and resilience in overcoming obstacles. In that spirit, I include here a poetic reflection that expresses several important themes of my journey:

Disorder should not be mistaken for insignificance; what appears chaotic may hold deeper order.

(Perception)

In such a world, it is often the oppressor who ultimately envies the oppressed; for those who endure with quiet strength carry the weight of hope, patience, and faith.

(Aspiration)

But ultimately, if you seek glory, stay away from unworthy people; history shows that solitude is often more fruitful than begging for false companionship.

(Dignity)

Meanwhile, never forget: arrogance is a clear sign of ignorance!

(Modesty)

— Hafez of Shiraz, 14th century. *Diivān of Hafez, Ghazal No. 218, Verses 6–7.*

Abstract

Machine Learning Analysis of Baltic Sea Surface Current Variability

This doctoral thesis investigates the variability of Baltic Sea surface currents by combining pattern recognition and data-driven emulation approaches with the results of physical ocean models. The work is motivated by the fact that Baltic Sea surface circulation is shaped by strongly variable factors in space and time, such as wind, stratification, coastal geometry, and exchange between sub-basins. The combined influence of these processes makes surface-current dynamics physically complex and imposes high computational demands on both the analysis and forecasting of current fields.

The study uses a physical reanalysis produced with a numerical ocean model as the principal dataset for Baltic Sea surface currents. The first main part of the thesis focuses on the analysis of Baltic Sea surface-current variability and its physical interpretation. Long time series of surface-current fields are used to identify dominant circulation states through a self-organizing-map clustering method. To interpret the characteristic current-field types dynamically, the total current is decomposed into geostrophic and ageostrophic components. The thesis shows that, particularly in offshore and open-basin areas, the dominant large-scale and low-frequency variability of Baltic Sea surface currents is mainly associated with geostrophic circulation. In contrast, ageostrophic currents play a more important role in coastal areas, narrow straits, and short-term variability of the current field.

The second part of the thesis addresses the forecasting of Baltic Sea surface currents using deep-learning-based emulators. The main objective is to replace the current-field forecast steps of a three-dimensional hydrodynamic model with a convolutional neural-network emulator trained on the same dataset and using an optimized set of input variables for prediction. A regional proof of concept for the Gulf of Riga shows that one-day surface-current forecasts can be emulated with high accuracy while preserving all dominant circulation patterns in the daily mean current fields. The results of the DeepCUN emulator, extended to the full Baltic Sea, show that the dominant spatial patterns and temporal variability of surface currents can be predicted at basin scale with high one-step skill and retained meaningful skill in recursive multi-day forecasts.

In addition to data-driven forecasting, the thesis examines the application of explainable artificial intelligence to interpret emulator results. Predictor-sensitivity analysis shows that antecedent surface currents and variables describing wind influence are the main predictive inputs, while adding further atmospheric variables improves the results only slightly. The explainability diagnostics indicate that wind mainly controls basin-scale current patterns, whereas current-field memory plays a more important role in narrow straits and coastal regions. The thesis also demonstrates the recursive application of the current-field emulator, which enables stable prediction of current fields over periods of up to several weeks when optimized input data are used. Such predictions should not, however, be interpreted as operational forecasts, but rather as long-term dynamic reconstructions of current fields. The main result of the doctoral thesis is to show that the complex variability of Baltic Sea surface currents can be described and predicted by combining the outputs of physical process-based models with data-driven machine-learning methods. This novel artificial-intelligence-based approach provides not only computational efficiency, but also new opportunities for analysing and interpreting surface-current variability and the processes that shape it.

Kokkuvõte

Läänemere pinnahoovuste muutlikkuse analüüs masinõppe meetoditega

Käesolev doktoritöö uurib Läänemere pinnahoovuste muutlikkust, ühendades muustritu-vastuse ja andmepõhise emulatsiooni lähenemisviisid füüsikaliste meremudelite tulemus-tega. Töö lähtub asjaolust, et Läänemere pinnatsirkulatsiooni kujundavad ruumis ja ajas tugevalt muutlikud tegurid, nagu tuul, stratifikatsioon, rannikugeomeetria ning basseini-devaheline veevahetus. Nende protsesside koosmõju muudab pinnahoovuste dünaamika füüsikaliselt keerukaks ning seab suuri arvutuslikke nõudeid nii hoovusväljade analüüsi-misele kui ka prognoosimisele.

Uuringus kasutatakse Läänemere pinnahoovuste peamise andmestikuna numbrilise meremudeli abil koostatud füüsikalist reanalüüsi. Töö esimene põhiosa keskendub Läänemere pinnahoovuste muutlikkuse analüüsile ja selle füüsikalisele tõlgendamisele. Pinnahoovusväljade pikkade aegridade põhjal tuvastatakse domineerivad tsirkulatsiooniseisundid iseorganiseeruvate kaartide klasterdamismeetodi abil. Iseloomulike hoovusväljatüüpide dünaamiliseks tõlgendamiseks jaotatakse koguhoovus geostroofiliseks ja ageostroofiliseks komponendiks. Töös näidatakse, et eelkõige avamere- ja avabasseinialadel on Läänemere pinnahoovuste domineeriv suuremõõtmeline ja madalsageduslik muutlikkus peamiselt seotud geostroofilise tsirkulatsiooniga. Seevastu ageostroofilised hoovused mängivad olulisemat rolli rannikualadel, kitsastes väinades ning hoovusvälja lühiajalises muutlikkuses.

Töö teine osa käsitleb Läänemere pinnahoovuste prognoosimist süvaõppel põhinevate emulaatorite abil. Põhieesmärk on asendada kolmemõõtmelise hüdrodünaamilise mudeli hoovusvälja prognoosisammud samal andmestikul treenitud konvolutsioonilise tehisnärvivõrgu emulaatoriga, mis kasutab prognoosimiseks optimeeritud sisendmuutujate hulka. Regionaalne kontseptsiooni tõestus Liivi lahe näitel näitab, et ühepäevaseid pinnahoovuste prognoose on võimalik suure täpsusega emuleerida, säilitades päeva keskmistes hoovusväljades kõik domineerivad tsirkulatsioonimustrid. Kogu Läänemerele laiendatud DeepCUN-emulaatori tulemused näitavad, et domineerivaid pinnahoovuste ruumilisi mustreid ja ajalist muutlikkust saab basseini-mastaabis ennustada suure täpsusega ühe sammu prognoosis ning tähendusliku oskuse säilimisega rekursiivsetes mitmepäevastes prognoosides.

Lisaks andmepõhisele prognoosimisele käsitleb töö selgitava tehisintellekti rakendamist emulaatorite tulemuste tõlgendamisel. Sisendtundlikkuse analüüs näitab, et peamised prognoosivad sisendid on eelmise ajahetke pinnahoovused ja tuule mõju kirjeldavad muutujad, samas kui täiendavate atmosfäärimuutujate lisamine parandab tulemusi vaid vähesel määral. Selgitava tehisintellekti diagnostika näitab, et tuul kontrollib peamiselt basseini-mastaapseid hoovusmustreid, samas kui hoovusvälja mälu mängib olulisemat rolli kitsastes väinades ja rannikualadel. Töös demonstreeritakse ka hoovusvälja emulaatori rekursiivset rakendamist, mis võimaldab optimeeritud sisendandmete abil stabiilselt ennustada hoovusvälju kuni mitme nädala ulatuses. Selliseid ennustusi ei tule siiski tõlgendada operatiivsete prognoosidena, vaid pigem hoovusväljade pikaajaliste dünaamiliste rekonstruktsioonidena. Doktoritöö peamine tulemus on näidata, et Läänemere pinnahoovuste keerukat muutlikkust on võimalik kirjeldada ja prognoosida, ühendades füüsikalistel protsessidel põhinevate mudelite väljundid andmepõhiste masinõppemeetoditega. Selline uudne tehisintellektil põhinev lähenemine pakub lisaks arvutuslikule tõhususele ka uusi võimalusi pinnahoovuste muutlikkuse ning seda kujundavate protsesside analüüsimiseks ja tõlgendamiseks.

Appendix 1

I

J. Elken, A. Barzandeh, I. Maljutenko, and S. Rikka, "Reconstruction of baltic gridded sea levels from tide gauge and altimetry observations using spatiotemporal statistics from reanalysis," *Remote Sensing*, vol. 16, no. 15, 2024

Article

Reconstruction of Baltic Gridded Sea Levels from Tide Gauge and Altimetry Observations Using Spatiotemporal Statistics from Reanalysis

Jüri Elken , Amirhossein Barzandeh , Ilja Maljutenko and Sander Rikka

Department of Marine Systems, Tallinn University of Technology, Akadeemia 15A, EE12618 Tallinn, Estonia; amirhossein.barzandeh@taltech.ee (A.B.); ilja.maljutenko@taltech.ee (I.M.); sander.rikka@taltech.ee (S.R.)

* Correspondence: juri.elken@taltech.ee

Abstract: A method for reconstructing weekly Baltic gridded sea levels was developed and tested. This method uses input data from tide gauge and altimetry observations. The reconstruction is based on sea level empirical orthogonal function (EOF) modes, calculated as spatiotemporal statistics from daily model reanalysis results available from the Copernicus Marine Service for the 1993–2021 period. In the semi-enclosed, tideless Baltic Sea, the four leading EOF modes cover 99% of the sea level variance. Several experiments with different combinations of input data were carried out. This method was validated against coastal tide gauges and altimetry data. The best reconstruction was obtained when both the tide gauges and altimetry data were used as inputs. An assessment of the centered root-mean-square difference (cRMSD) of the reconstruction versus the tide gauges revealed a value of 0.05 m, and a result of 0.10 m was revealed versus altimetry. The average coefficient of determination (R^2) was determined to be 0.93 for the tide gauges and 0.82 for the altimetry data. In the cases where only one type of input data was used, the reconstruction worsened with respect to other data sources. The reconstruction method demonstrated its usefulness for the reconstruction of coastal sea levels in unsampled locations and the calculation of changes in sea volume.



Citation: Elken, J.; Barzandeh, A.; Maljutenko, I.; Rikka, S. Reconstruction of Baltic Gridded Sea Levels from Tide Gauge and Altimetry Observations Using Spatiotemporal Statistics from Reanalysis. *Remote Sens.* **2024**, *16*, 2702. <https://doi.org/10.3390/rs16152702>

Academic Editors: Sergei Badulin, Antonio Sánchez-Román, Juan M. Sayol and Bàrbara Barceló-Llull

Received: 3 June 2024
Revised: 5 July 2024
Accepted: 15 July 2024
Published: 24 July 2024



Copyright: © 2024 by the authors. Licensee MDPI, Basel, Switzerland. This article is an open access article distributed under the terms and conditions of the Creative Commons Attribution (CC BY) license (<https://creativecommons.org/licenses/by/4.0/>).

Keywords: sea level; reconstruction; tide gauges; altimetry

1. Introduction

The spatiotemporal features of sea level variability in the semi-enclosed Baltic Sea are rather different from those in the ocean and tidally dominated seas. Enhanced observation-based knowledge of sea levels, including gridded data, is essential both for addressing practical issues related to sea levels and for understanding the dynamics of the sea.

1.1. Sea Level Variability in the Baltic Sea

Sea level variations are one of the main concerns of ongoing climate change, pointing to the adverse effects of global sea levels rising, including the increase in floods and other extreme events [1]. In the semi-enclosed, tideless Baltic Sea, sea level dynamics are governed by a multitude of oceanographic, atmospheric, hydrological, and geological processes, which have temporal scales ranging from minutes to millennia and geological time scales [2,3]. In the northern regions, water is seemingly retreating from the coasts, the reason for which is land uplift after the Ice Age. From the hydrodynamic point of view, sea level variations with a time scale from a few days to several years can be divided by their forcing mechanisms into external (50–80% of the total variance) and internal variability [4]. The highest pulse-like sea level elevations—floods due to storm surges—have been observed in the southwestern, eastern, and northern ends of the sea (3.4 m in Kiel (1872), 4.2 m in St. Petersburg (1824), and 2.1 m in Kemi (1984), respectively).

The longest instrumental sea level data series in the Baltic Sea originates from coastal tide gauges. In Stockholm, observations started in 1774 [5]. Tide gauges register the

relative sea level with respect to the local geodetic height system. A second data source—altimetry—has provided offshore absolute sea levels along satellite tracks since the early 1990s [6]. A third data source—numerical modeling—has been used for short-term storm surge predictions since the 1950s [7], but this method only became mature enough for comprehensive sea level variability analysis in the 2000s [8,9].

On the longest secular time scales, the dominant sea level signal in the Baltic Sea is glacial isostatic adjustment (GIA), for which the direction and magnitude depend on the sub-region [10]. In the northern Fennoscandia region, the recent global mean sea level rise [11,12] has been superseded by land uplift, resulting in a relative lowering in sea level of a few millimeters per year, and the associated coastal land gain [13–15].

On weekly-to-multidecadal scales, the mean sea level is controlled by the changes in sea volume (i.e., filling and emptying of the sea) caused by climate forcing in terms of the mean wind and temperature, river discharge, and precipitation/evaporation. Multiyear sea level changes are connected to variations in climate indices such as the North Atlantic Oscillation (NAO) [16] and other atmospheric circulation descriptors [17]. The annual sea level cycle is well distinguished because of cyclic atmospheric forcing and river runoff [18]. For weekly scales, Svansson [19] applied a Helmholtz resonator model on a basin representing simplified geometry of the Baltic Sea. A resonant period of ~10 days was found for filling and emptying the sea basin, resulting from variable forcing from the open ocean side.

Storm surges [20] and other weather-forced sea level oscillations [21], including basin eigenoscillations (seiches), have time scales ranging from hours to several days; they redistribute the water within the sea, on top of the mean sea level in the forcing period. Extreme storm surges occur with specific preconditioning [22], such as high filling of the sea and the occurrence of selected weather patterns and storm tracks, generating high surges [23,24]. On top of the storm surge sea level elevation, the local wave setup can further elevate the water line on sloping coasts [3,25].

1.2. Overview of Sea Level Reconstruction

Extending beyond time series analysis from Baltic Sea tide gauges [5,14], spatiotemporal analysis requires gridded sea level data. Simple coast-to-coast interpolation techniques are not considered to be appropriate in the Baltic Sea, and recent studies have proposed methods that statistically combine the three abovementioned data sources. These studies differ in terms of their statistical methods, selected spectral windows of reconstruction, and preprocessing of geodetic and altimetry data.

Estimates of global sea surface variability have used gridded data since the 1990s [26], when empirical orthogonal function (EOF) reconstruction was introduced based on remote sensing data for sea surface temperature. For sea level variability, in the earliest studies, the statistical covariance patterns were calculated using early altimetry data [27,28]. For the pre-altimetry era (i.e., before 1985), only sparse tide gauge records were used as input data for reconstruction on a $1^\circ \times 1^\circ$ grid with a monthly resolution. Another option is to calculate the covariance patterns from the model's reanalysis results [29–32]. With improved model results (longer calculation period and better resolution and accuracy) becoming available, this approach has the benefit of providing more detailed and robust covariance estimates than observations. In the case of a few tide gauge observations being available, the cyclostationary empirical orthogonal function (CEOF) method has better performance than standard EOF reconstruction techniques [33].

In the global ocean, the main interest is to detect and quantify the global sea level rise. Therefore, preprocessing of tide gauge data includes sophisticated correction of generally unknown datum shifts between the locations, as shown by Church et al. [28]. Short-term variations in winds and air pressure, as well as tides, cause unwanted noise for sea level trend estimations; their impact is corrected or suppressed.

One important field of sea level reconstruction is the study of ocean dynamics [34].

In the Baltic Sea, the comparison of observations and model results [9] revealed that in the 2000s, the model results matched observations better on shorter time scales (i.e., characteristic time of less than 2 months) than on longer scales. However, during extreme storm surges, the model errors were up to 25 cm, a few times higher than the background centered root-mean-square difference (cRMSD) of 8 cm. For the period 1993–2011, the comparison of the monthly mean tide gauge and altimetry data revealed a cRMSD of 3.4 cm, while the standard deviation (STD) was ~15 cm [35]. In this analysis, the original L3 altimetry data along the tracks were averaged during a month over $0.25^\circ \times 0.25^\circ$ grid boxes. Model reanalysis showed similar performance results to the two reconstructed data sets.

Recently, the reconstruction of gridded monthly sea level data was performed for the period 1900–2014. The method used tide gauges and altimetry as input data, whereas model reanalysis was used for estimation of covariance matrices for each reconstruction grid point [36]. Over the longer period, the cRMSD at coastal tide gauges was estimated to be 3.8 cm, as in the variability study [35] for the shorter period. Another study focused on the annual sea level cycle [37]. The CEOF method was applied for the estimation of sea level background statistics, using the model reanalysis data. In this study, monthly sea levels reconstructed from either tide gauges or altimetry data demonstrated similar variability on the annual and longer time scales.

In the present study, observation-based sea level reconstruction methods were validated in the Baltic Sea for the monthly time scale as the shortest period, whereas hourly-to-weekly time scales remained unresolved.

1.3. Aims and Study Design

The present study aimed to develop and test a computationally efficient method for the reconstruction of Baltic gridded sea levels from tide gauge and altimetry observations. The method should be applicable on shorter-than-monthly time scales. Spatiotemporal sea level variability statistics, needed for the optimized reconstruction, are estimated from the model reanalysis data that cover the study domain with high resolution over a long period without gaps.

Sea level dynamics have well-defined basin-scale variation patterns, as described in Section 1.1. To suppress shorter period variability that has more complex covariance patterns, we used weekly average sea level data. By “computationally efficient”, we mean that new weekly sea level maps, necessary for the bias correction of operational numerical forecasts, could be reconstructed nearly immediately when new observations become available, without the need to conduct new, computationally demanding numerical model runs. This study was made possible by the newly available altimetry and model data sets from the Copernicus Marine Service [38], along with the continued delivery of tide gauge data.

Covariance estimates reveal that high covariance values occur over considerable distances. These basin-guided covariance patterns can be mathematically represented by EOF modes [39], and their physical interpretation is the response of the basin to the forcing fields (e.g., atmosphere, rivers, adjacent sea area) at scales comparable to or larger than the basin dimensions. The reconstruction of the large-scale gridded sea surface temperature and salinity data from sparse observations (e.g., monitoring data, FerryBox, buoy stations) proved useful [39]. The method is based on finding the values of principal components (PCs, also called EOF amplitudes) that satisfy the least-squares minimization of differences between observed values and superpositions of leading EOF modes. This method has been successfully applied in operational forecasts for the data assimilation of sea surface temperature and salinity [40].

This manuscript starts with the Introduction (Section 1), followed by the description of data and methods in Section 2. After introducing the used source data, the steps of data preparation are outlined. Section 2 also presents the EOF reconstruction framework and specifies the conducted reconstruction experiments. The results are presented in Section 3, which contains the calculated EOF modes, comparisons of reconstructed and observed sea

levels, reconstruction of coastal sea levels in unsampled locations, and sample estimation of changes in sea volume. The paper ends with the Discussion (Section 4) and Conclusions (Section 5).

2. Data and Methods

2.1. Source Data from the Copernicus Marine Service

2.1.1. Reanalysis 1993–2021

Gridded data from the recent Copernicus Baltic Sea reanalysis were used for the evaluation of spatiotemporal statistics of sea level variability [38]. NEMO 4.0 was used for this reanalysis in combination with the sea ice and thermodynamic model SI3. This has a horizontal resolution of ~1 nautical mile (1'40"E by longitude and 1'N by latitude), and it has up to 56 levels along the vertical direction, with a grid step of ~1 m at the surface, but with depth, the grid step increases up to 25 m, whereas the maximum depth is 712 m. The model domain covers the Baltic Sea and North Sea; data are extracted from 9° to 30.2°E and 53° to 65.9°N on a grid of 763 by 774 points along longitude and latitude, respectively. The model was forced by atmospheric data from the ERA5 reanalysis data set available from the Copernicus Climate Service, river discharge data from the Ehype model, and open boundary conditions from the North West Shelf model. Reanalysis involved the assimilation of temperature and salinity, but not for the sea level. Data assimilation was carried out using the LESTKF filter within the PDAF (Parallel Data Assimilation Framework, [41]). All of the physical variables are presented on the Copernicus data portal for the period 1993–2021 as daily mean gridded values. In the delivered NetCDF files, the sea level variable is *sla* (sea level anomaly), calculated with the boundary conditions from the CMEMS North West Shelf multiyear product.

2.1.2. Tide Gauges

The Copernicus Marine Service provides hourly sea level data from 105 coastal stations during 1993–2021 (Figure 1), as presented in the technical report of in situ TAC [42]. The data contain the variable *slev* (water surface height above a specific datum) in reference to BSCD2000. The data have undergone quality check, and each data record has a quality flag. Basic statistical (e.g., mean, trends, variability) and geodetic (e.g., coordinates, leveling) details of tide gauge observations have been presented in several research papers, with variable numbers of involved stations [2–4,13,15,18,21,35–37]. Because of the low tidal activity [21], the sea level instruments in the Baltic are often named also called “mareographs”. Data coverage over time is variable in the Copernicus Service [15,42]; however, for technical reasons, we decided not to search for other sources of data, such as the Permanent Service for Mean Sea Level, referenced by Kapsi et al. [15]. There is nearly gap-free data coverage during the study period from Gedser to Hamina (counting the stations clockwise), but only ~50% from Kronstadt to Kolka (the data records in the Copernicus service start mainly from 2005 onwards) and 30% from Gdansk to Rostock. For a basin-wide overview along the coast, we selected 21 stations from different coastal sections for detailed analysis, as shown in Figure 1 by the station names.

2.1.3. L3 Altimetry

Altimetry data, observed along the satellite tracks, were acquired from the Copernicus Marine Service multiyear observations “European Seas Along Track L3 Sea Surface Heights Reprocessed” [43,44], tailored for data assimilation into the models. The data originate from altimeter Copernicus missions (Sentinel-6A, Sentinel-3A/B) and other collaborative or opportunity missions (e.g., Jason-3, Saral[-DP]/AltiKa, Cryosat-2, OSTM/Jason2, Jason-1, Topex/Poseidon, Envisat, GFO, ERS-1/2, Haiyang-2A/B). The data from these >20 satellites are presented at various times on the initial grid, with a step of 7 km.

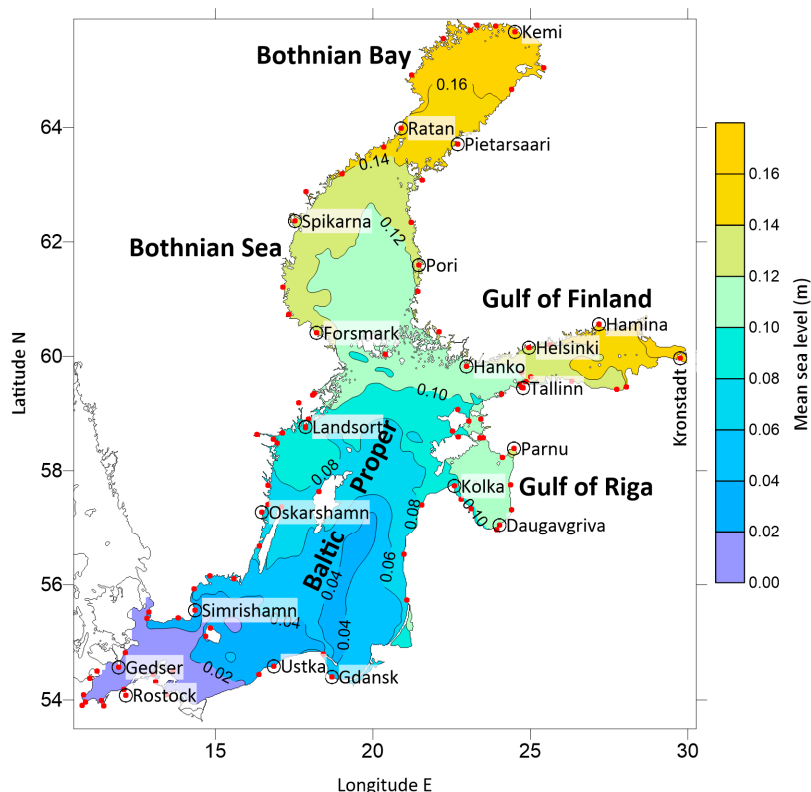


Figure 1. Map of Baltic mean sea level, 1993–2021, with locations of coastal tide gauge stations (red dots). Coastal stations selected for analysis are indicated by black circles and station names. The regions Baltic Proper, Bothnian Sea, Bothnian Bay, Gulf of Finland, and Gulf of Riga are shown.

The data records of the altimetry product [43] contain sea level variables given in Table 1.

Table 1. Sea level variables in the L3 altimetry product.

Variable Name	Explanation
<i>sla_unfiltered</i>	raw sea level anomaly measurement including noises; corrected for the <i>dac</i> , <i>lwe</i> , <i>ocean_tide</i> and <i>internal_tide</i>
<i>sla_filtered</i>	sea level anomaly low pass filtered for noise reduction; corrected for the <i>dac</i> , <i>lwe</i> , <i>ocean_tide</i> and <i>internal_tide</i>
<i>mdt</i>	mean dynamic topography (long-term mean of sea surface height 1993–2012 above geoid) that is constant for grid point during time; it is used to compute the absolute dynamic topography $adt = sla + mdt$
<i>dac</i>	dynamic atmospheric correction for the removal of high frequency variability induced by the atmospheric forcing and aliased by the altimetric measurements; the <i>sla</i> is already corrected for the <i>dac</i>
<i>lwe</i>	long wavelength error due to changes in satellite orbits; the <i>sla</i> is already corrected for the <i>lwe</i> ; it is stored with opposite sign compared to the other corrections so if the user wants to uncorrect it or to use another correction instead, he must subtract it from the <i>sla</i> in the product
<i>ocean_tide</i>	ocean barotropic tide correction (including S1S2 signal) based on tidal model; the <i>sla</i> is already corrected for the <i>ocean_tide</i>
<i>internal_tide</i>	internal tide correction: coherent part of the baroclinic tide (phase-locked with barotropic tide frequency); the <i>sla</i> is already corrected for the <i>internal_tide</i>

2.2. Preparation of the Data

2.2.1. Selecting the Reference Levels

Although the different data sets—model reanalysis η_M , tide gauges η_T , and altimetry η_A —should ideally have the same mean reference field $\bar{\eta} = \bar{\eta}(x, y)$, the actual references for $\bar{\eta}_M$, $\bar{\eta}_T$, and $\bar{\eta}_A$ are somewhat different [45,46]. From the oceanographic viewpoint, the adopted common reference should provide realistic gradients of $\bar{\eta}$ that are consistent with known circulation. Among the three data sources, model reanalysis is the only one that produces dynamically balanced sea levels. Sea level gradients cause pressure gradients and therefore, induce water motions. On the other hand, horizontal divergence or convergence of vertically integrated water motions causes lowering or rising of the sea level due to the continuity equation. With the aim of following these dynamical balances, the model-based reference $\bar{\eta}_M$ (also named as mean dynamic topography, MDT_m) was adopted as the baseline reference (Figure 1). Model-based leveling was also proposed for the European Vertical Reference System [47]. Note that, in other studies, geodetically refined MDT_g has also been adopted [48].

Model reanalysis and tide gauge stations have different mean sea level values at coastal stations; therefore, this pointwise determined bias was subtracted prior to the sea level reconstruction. While comparing the reconstruction with TG observations, pointwise corrections were added again, to follow the mean local coastal reference.

Regarding altimetry data, mean dynamic topography ($mdt = MDT_a$) in the Copernicus product has been defined independent of the model results. The dynamic topography is variable over time due to the changes in forcing and internal circulation. The averaging periods are also different: 1993–2012 for altimetry and 1993–2021 for reanalysis. According to the rough analysis, the mean dynamic topography determined from the altimetry is ~0.20 m higher than that determined from the model reanalysis (mean sea level in Figure 1). The difference in dynamic topographies is slightly space-dependent, from 0.19 m in the Western Baltic and the northern part of the Bay of Bothnia, to 0.26 m in the southern part of the Baltic Proper. During the sea level reconstruction, the altimetry values were brought to the model reanalysis background using the space-dependent bias between the two topographies.

2.2.2. Selecting the Weekly Interval

While operational modeling provides sea level forecasts with hourly intervals, altimetry data have been used mainly for the monthly scale [35–37]. From a physical point of view, the weekly average sea level allows for the suppression of short-period oscillations due to local wind tilt, storm surges, Kelvin waves, and seiches that are presently not resolved by the altimetry data, but allows for keeping sea level changes related to circulation and water exchange between the sea's sub-basins, along with the external forcing from the North Sea. For the sake of reasoning, Samuelsson and Stigebrandt [4] divided the sea level variability into short-term internal variability with a time scale of up to a few days, and longer-term variability that is forced by water exchange in the sea. Raudsepp et al. [49] estimated the temporal correlation radius of sea level oscillations in the Estonian coastal area for 10 days.

Temporal autocorrelation and spectral analysis studies over extended regions have revealed that weekly and longer period sea level changes can be effectively separated from shorter period oscillations just by taking the weekly average and residual values [50]. In this context, Lagemaas et al. [51] found that a weekly average filter length is optimal for correcting the bias of short-term sea level forecasts, using recent observations. Soomere and Pindsoo [52] have shown the importance of weekly-scale high water levels within the sea basins in forming superimposed extreme storm surges.

2.2.3. Averaging and Filtering of the Data

The sea level reanalysis data were used in the following aggregations:

1. Weekly mean data on the basic grid, with the tide-dominated Kattegat and Danish Straits excluded, as shown in Figure 1. The excluded areas have higher sea level variability [36] and are not of interest for the present study.
2. Weekly mean time series at model grid points corresponding to coastal tide gauge stations (Figure 1).
3. Extracts of weekly mean sea levels at L3 altimetry grid points.

When calculating weekly average tide gauge observations as input and validation data for reconstruction, the weeks with more than 25% missing observations were blanked out. All of the available tide gauge data were used in the sea level reconstruction procedure. Detailed results for the 21 selected stations will be presented in Section 3.2.

Along-track altimetry data need to be converted to their weekly averaged form while also maintaining reasonable spatial averaging. With the example from an earlier study [35], where typical satellite tracks are shown, a coarse “altimetry grid” was introduced with steps of 0.25°E (~ 14 km) and 0.25°N (~ 27 km). This adopted grid for the altimetry data consisted of 89 points by longitude and 53 points by latitude. Grid cells with missing or low numbers of altimetry data were blanked. For the inclusion of weekly altimetry data, the reasonable criterion was set that non-averaged altimetry data are found at least in 25 grid cells of the fine reconstruction grid, within a 0.25°E by 0.25°N box, during the week. On average, 36 altimetry grid cells were used for reconstruction.

2.3. EOF Reconstruction Framework

As described in [39,40], we used the $M \times N$ space-time data matrix \mathbf{X} , which contains time slices \mathbf{x}_i as spatial state vectors of length M at time i , where $i = 1 \dots N$. The spatial vectors, containing deviations from the space-dependent temporal mean vector $\bar{\mathbf{x}}_m$, are mapped from one-, two-, or three-dimensional physical coordinates into the one-dimensional vector. The covariance matrix $\mathbf{B} = \mathbf{X}^T \mathbf{X} / N$ (averaging over time) is used to calculate the eigenvector matrix \mathbf{E} containing spatial empirical orthogonal function (EOF) vectors \mathbf{e}_k . Principal components (PCs), or “amplitudes”, are found for each time i from $\mathbf{a}_i = \mathbf{E}^T \mathbf{x}_i$ when \mathbf{x}_i is known. Then, \mathbf{x}_i is decomposed as $\mathbf{x}_i = \mathbf{E} \mathbf{\Lambda} \mathbf{a}_i$, where $\mathbf{\Lambda}$ is the diagonal matrix of eigenvalues.

When reconstructing the field of interest at time i from observations \mathbf{y}_i of length L_i , they are then taken from different locations (usually $L < M$) from the model grid points. For the comparison of observations with the model, gridded data are transformed to the observation points by the observation operator \mathbf{H}_i , using the formula $\mathbf{H}_i \tilde{\mathbf{x}}_i = \mathbf{H}_i \mathbf{E} \tilde{\mathbf{a}}_i$, where $\tilde{\mathbf{a}}_i$ is the “observational” PC to be found. The values $\tilde{\mathbf{a}}_i$ should follow least-squares minimization of reconstruction error in relation to observations $\|\mathbf{y}_i - \mathbf{H}_i \mathbf{E} \tilde{\mathbf{a}}_i\|^2 \Rightarrow \min$. The expressions to find observational PCs and reconstructed fields are found using matrix-vector formulation of least-squares estimators [53] in the following form:

$$\tilde{\mathbf{a}}_i = \left(\mathbf{E}^T \mathbf{H}_i^T \mathbf{H}_i \mathbf{E} \right)^{-1} \mathbf{E}^T \mathbf{H}_i^T \mathbf{y}_i \quad (1)$$

$$\tilde{\mathbf{x}}_i = \mathbf{E} \tilde{\mathbf{a}}_i \quad (2)$$

There is also a possibility of using the time-dependence of observation data for each reconstruction time step, assuming linear time-dependence of EOF amplitudes within the calculation interval. In the present study, the dependence option was not used.

The field of interest is reconstructed by superposition of continuous model-based mode patterns multiplied by observational amplitudes that meet adopted statistical limits based on the eigenvalues of the specific mode [39].

2.4. Performed Sea Level Reconstruction Experiments

One sea level reconstruction experiment followed the flowchart presented in Figure 2. Calculation of gridded EOF modes (Section 2.3) was performed once from the reanalysis data (Section 2.1.1). For each timestep during the study period, the initial data consisted of tide gauge data (Section 2.1.2) and altimetry data (Section 2.1.3), which were brought to the selected reference (Section 2.2.1) and later filtered to the weekly values (Section 2.2.3). The observational data were merged, and in case of enough data, EOF reconstruction was performed using Formulae (1) and (2) (Section 2.3). If the calculated PC of the EOF was within acceptable limits up to the selected highest mode, the final 2D sea level grid was saved.

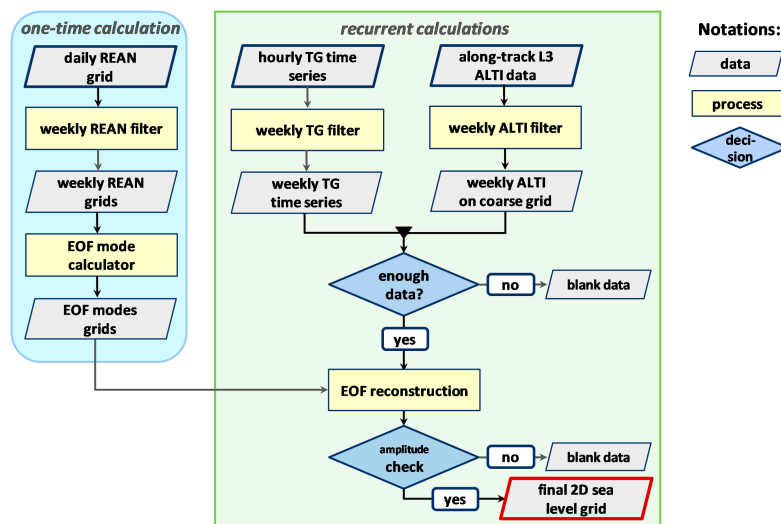


Figure 2. Flowchart of EOF reconstruction of weekly sea level: one-time calculation of EOF modes from reanalysis (REAN), which are used for recurrent calculations of gridded sea level, using tide gauge (TG) and altimetry (ALTI) data at each time step.

While performing the experiments, unified data and mode selection procedures were introduced to handle cases with few or spatially unfavorably distributed data. In case of too few observations being available—i.e., fewer than 25—reconstruction was not performed for this time step.

The number of EOF modes included in the reconstruction was determined for each time interval. For this, amplitude limits were set for the reconstructed fields, based on the EOF statistics from the model reanalysis. Based on [39], a reasonable limit is double the standard deviation of the PC time series of reanalysis. When the amplitude of a particular mode exceeded its limit, then this mode and higher modes were considered to be too noisy, and they were trimmed from the reconstruction. The success of reconstruction depends on the number and spatial configuration of observations [39]. This is usually considered undesirable since variable number of included EOF modes creates changes in feature resolution; however, by our experience in this study, it has less effect on the accuracy than inclusion of modes with outlier amplitudes, which may create completely distorted patterns. In most cases, 6 to 10 leading modes was found to be acceptable; the mean number of modes was 7.

The skill of sea level reconstruction was evaluated with five experiments using different combinations of tide gauge and altimetry data (Table 2). Regarding altimetry, it is not yet clear which of the several data options would be best for the semi-enclosed non-tidal Baltic Sea, where weather forcing and seiches play important roles. Therefore, we selected three options, from rec2 to rec4, with different altimetry data.

Table 2. Main features of the performed sea level reconstruction experiments. Altimetry sea level data were taken according to Table 1.

Name	Tide Gauges	Altimetry	Description
rec1	Y	N	Input from tide gauge data only; altimetry comparison with rec4.
rec2	Y	Y	Input from tide gauge and altimetry $sla_filtered$; sea level anomalies accounted for on top of model-based dynamic topography.
rec3	Y	Y	Input from tide gauge and altimetry $ADT = sla_filtered + mdt$; sea level anomalies accounted for on top of altimetry-based dynamic topography.
rec4	Y	Y	Input from tide gauge and altimetry $ADT_c0 = sla_filtered + dac + ocean_tide + iw - lwe + mdt$; same as rec3, but corrections to $sla_filtered$ removed.
rec5	N	Y	Same as rec3, but tide gauge data not included.

3. Results

3.1. Calculated EOF Modes of Sea Level

The full covariance matrix $\mathbf{B} = \mathbf{X}^T \mathbf{X} / N$ contains M^2 pairs of second-order statistical moments, whereas spatial lag between the correlated points amounts from the model grid step ~ 2 km to the basin scale ~ 1500 km. When conducting widespread optimal interpolation [54], it is assumed that the spatial correlation function (derived from covariance) follows a spatial decay that depends on the distance between the correlated points that can be fitted by an exponential, Gaussian “bell curve”, or some other function. It is also often assumed that statistical properties such as variance are not changing between the spatial locations (i.e., homogeneity assumption). In our case, sea level covariance calculated from the model reanalysis has a complex two-dimensional histogram that is dependent on the spatial lag between the points over the whole sea domain (Figure 3). Covariance estimates cover the pairs of points within and between different basins of the sea (Figure 1); multiple maxima occur in covariance histogram extracts at fixed lags. Therefore, it is justified to use the empirical orthogonal function (EOF) framework, which considers the full covariance matrix but allows it to be reduced to a few of the most energetic EOF modes.

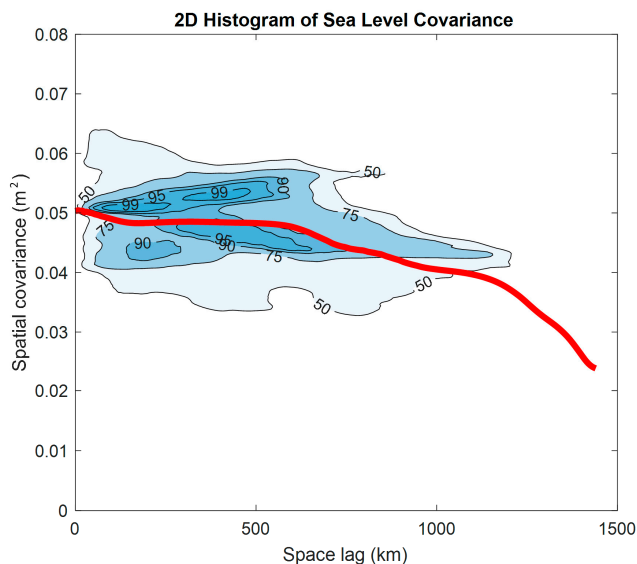


Figure 3. Mean covariance (red line) and two-dimensional (2D) histogram of sea level covariance (contours) as a function of spatial lag between the analyzed model grid points. Shown are the 50th, 75th, 90th, 95th, and 99th percentiles, the numerical values of which were calculated from the whole set of covariance data.

The EOF modes represent the perturbations to the mean sea level shown in Figure 1. The first mode, which contains 94.6% of the overall variance, is nearly flat, meaning that it represents filling and emptying (predominantly through the Danish Straits) of the whole sea basin. The modes from two to four represent tilting of the sea level in different directions, forced mainly by variable weather patterns. In the PC time series (Figure 4c), the dominant first mode is rather variable. Although in the seasonal average there are high PC values (and mean sea level) in winter and low PC values in summer, this is not evident from the data of individual years. Exceptionally high winter PC values were noted for the years 1996, 2003, 2010, 2013, and 2018.

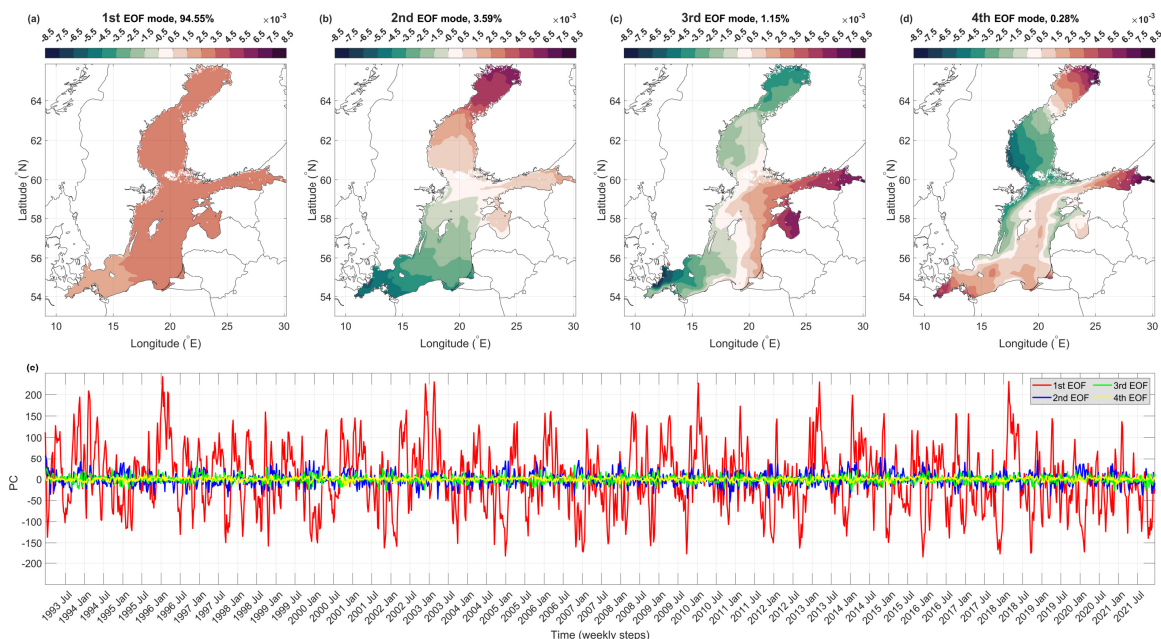


Figure 4. Maps of leading EOF modes (a–d) and their PC time series (e). Partition of variance: (a) 1st mode—94.6%; (b) 2nd mode—3.6%; (c) 3rd mode—1.2%; (d) 4th mode—0.3%.

The reconstruction sums the mean sea level and contributions of different modes, whose superposition weights are calculated by the reconstruction procedure based on the location of observations and observed values. The first 10 modes were calculated; however, the first four modes, presented in Figure 4, already cover 99% of the total sea level variance during 1993–2021 over the entire sea.

3.2. Comparison of Reconstructed and Observed Sea Levels

Weekly mean sea levels vary in a range of more than a meter. Examples of the sea level time series, extracted for 2007, are given for Helsinki coastal station (Figure 5). Data from experiments rec1 to rec4, which used tide gauge data for sea level reconstruction, show similar results, close to the observed values. Data from rec5, which used only altimetry data and did not use tide gauge data for reconstruction, are also close to the tide gauge observations, although some deviations are visible.

Model data were used to set up the long-term (1993–2021) datum (mean reference level) for observations; however, the variability in modeled sea levels at coastal points (an example is shown in Figure 5) shows greater differences from the observed values than the reconstructions. Specifically, the centered root-mean-square difference (cRMSD) of the model results from the tide gauge observations is 0.085 m, while experiments from rec1 rec4 show cRMSD ranging from 0.034 to 0.046 m, and rec5 has the highest value of 0.106 m.

Pearson's coefficient of determination (R^2) is higher than 0.90 for rec1 to rec4, but only 0.66 for rec5. The standard deviation (STD) of the model results at coastal points is 0.222 m, 22% higher than the STD of the observations (0.182 m). Reconstruction experiments rec1 to rec4 reveal STD from 0.176 to 0.198 m, while rec5 provides a smaller STD of 0.163 m.

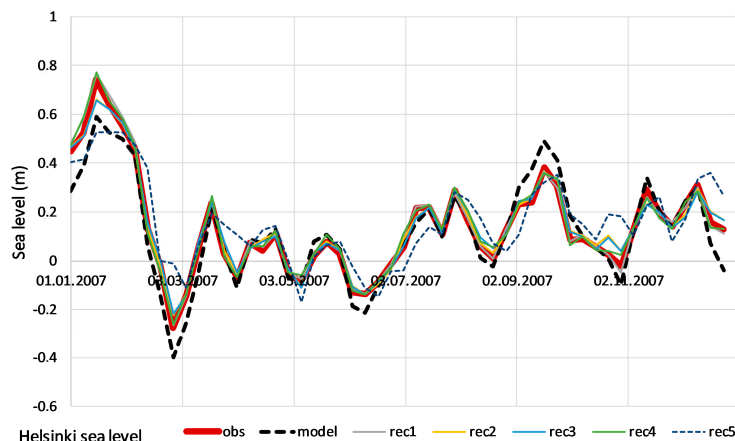


Figure 5. Example of observed (obs), modeled (mod), and reconstructed (rec1 to rec5) weekly sea level in Helsinki during 2007. Model and reconstruction data were shifted to the mean level of the observations by adding the estimated datum 0.118 m.

As one option for the comparison of reconstructed and observed sea levels, along-coast changes in the statistical characteristics of the reconstruction experiments versus selected coastal tide gauge observations (locations in Figure 1) are presented in Figure 6. In the Bothnian Sea and Bothnian Bay, the mean observed sea levels (Figure 6a) on the Swedish coastal section from Forsmark to Ratan are ~0.1 m higher than on the opposite Finnish coastal section from Kemi to Hanko. This coast-to-coast difference is considered further in the Discussion. On the Swedish coastal section in the Baltic Proper, from Simrishamn to Landsort, the mean observed sea levels are higher as well. The reconstruction experiments give similar mean sea levels to the model results, except for rec5, which produces higher mean sea levels in the eastern part of the sea, from Hamina to Kolka.

Regarding the standard deviation over the study period (Figure 6b), the inclusion of altimetry data reduces the STD from rec1 (closest results to the observations; altimetry data not included in the reconstruction) to rec5. Comparison of rec1 to rec5 with tide gauge observations, using cRMSD and R^2 , reveals the closest match (i.e., smallest cRMSD and highest R^2) for rec1 and the worst reproduction for rec5. Along the coast, larger reconstruction uncertainties are found in the Swedish section of the Bothnian Sea and Bothnian Bay (Forsmark to Ratan), as well as on the Polish and German sections of the western Baltic (Gdansk to Rostock).

The numerical results of the statistical comparison of the reconstructed data with the tide gauge and altimetry data are presented in Table 3. It can be concluded that combination of data from coastal tide gauges and altimetry (rec2 to rec4) give the best results in terms of the minimum cRMSD and maximum R^2 in both the coastal (i.e., tide gauges) and offshore (i.e., altimetry) observation domains. Omitting the altimetry input data (rec1) improves the accuracy at the coastal stations insignificantly (the cRMSD of 0.034 m in rec1 is slightly smaller than the 0.046 m in rec2 and rec3, and 0.040 m in rec4) but reduces the offshore accuracy (the cRMSD of 0.112 m in rec1 is larger than the 0.060 m and 0.066 m in rec2 and rec3, and 0.086 m in rec4). The other specific case—input from altimetry data only (rec5)—provides roughly the same offshore accuracy as other altimetry-based reconstruction experiments, but the coastal accuracy is reduced (the cRMSD of 0.106 in rec5 is higher than the 0.046 in rec2 and rec3). The experiment rec4, with input from tide gauge

and altimetry ADT_c0 (Table 2), yields higher accuracy in relation to tide gauges compared to rec2 and rec3, but it provides slightly worse offshore accuracy.

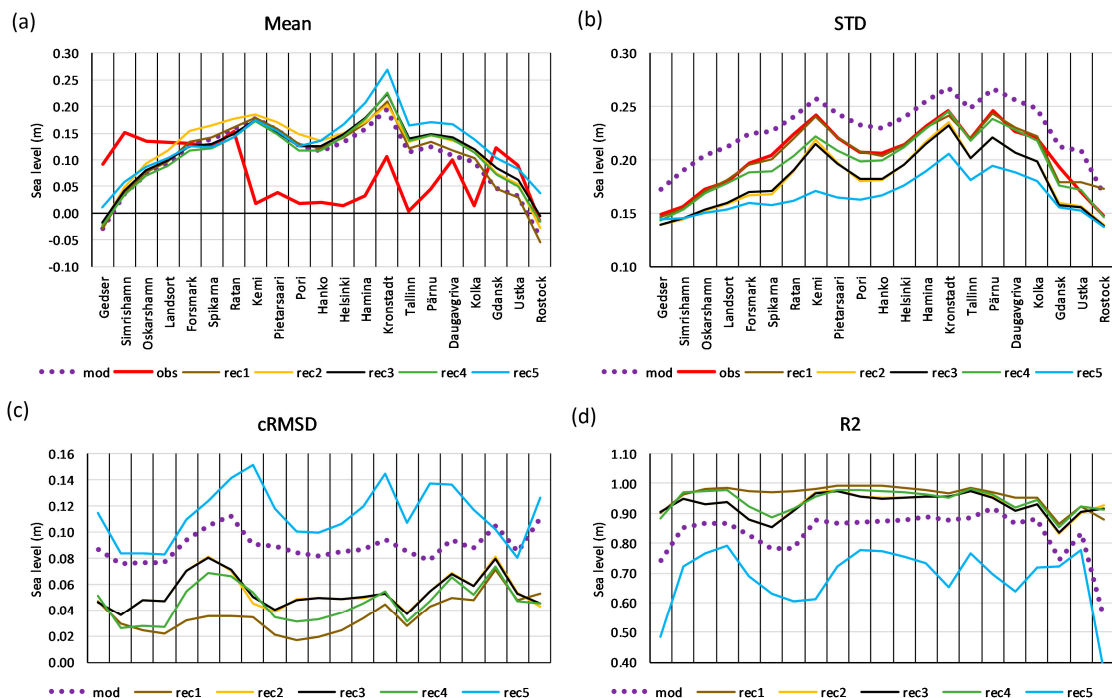


Figure 6. Evaluation of the results of reconstruction experiments rec1 to rec5 at 21 selected coastal tide gauge stations; also shown are the reanalysis model results (mod) and tide gauge observations (obs). Station names are given in (a,b), and their locations are given in Figure 1. The mean (a) and standard deviation (b) of sea levels (m) at different points over the period, along with the centered root-mean-square difference (c) and coefficient of determination (d) relative to the tide gauge observations.

Table 3. Statistical sea level characteristics of reconstruction experiments rec1 to rec5 compared to the observations at tide gauges and altimetry observations. Tide gauge and altimetry data were shifted to the model reanalysis reference during the reconstruction.

	rec1	rec2	rec3	rec4	rec5
Tide gauges at coastal stations					
Mean, tide gauges (m)			0.085		
Mean, reconstruction (m)	0.089	0.106	0.101	0.095	0.117
STD, tide gauges (m)			0.182		
STD, reconstruction (m)	0.198	0.176	0.176	0.190	0.163
cRMSD, reconstruction to tide gauges (m)	0.034	0.046	0.046	0.040	0.106
R ² coefficient of determination, reconstruction to tide gauges	0.952	0.935	0.935	0.948	0.659
Altimetry points					
Mean, altimetry (m)	0.101	0.143	0.117	0.101	0.117
Mean, reconstruction (m)	0.103	0.126	0.112	0.103	0.117
STD, altimetry (m)	0.206	0.168	0.167	0.206	0.167
STD, reconstruction (m)	0.201	0.175	0.174	0.193	0.162
cRMSD, reconstruction to altimetry (m)	0.112	0.060	0.066	0.086	0.094
R ² coefficient of determination, reconstruction to altimetry	0.723	0.881	0.855	0.827	0.930

Regarding the altimetry options from rec2 to rec4, the cRMSD and R^2 values are rather similar, and within this study, it was not possible to determine which of the altimetry options is better suited for the Baltic Sea's conditions.

The two-dimensional histograms of the observed versus reconstructed sea levels, presented in Figure 7 for rec1, rec3, and rec5, illustrate that although the reconstruction procedure is of good quality, the most accurate reconstruction in both the coastal stations and offshore regions was obtained for rec3 when both the tide gauge and altimetry data were involved.

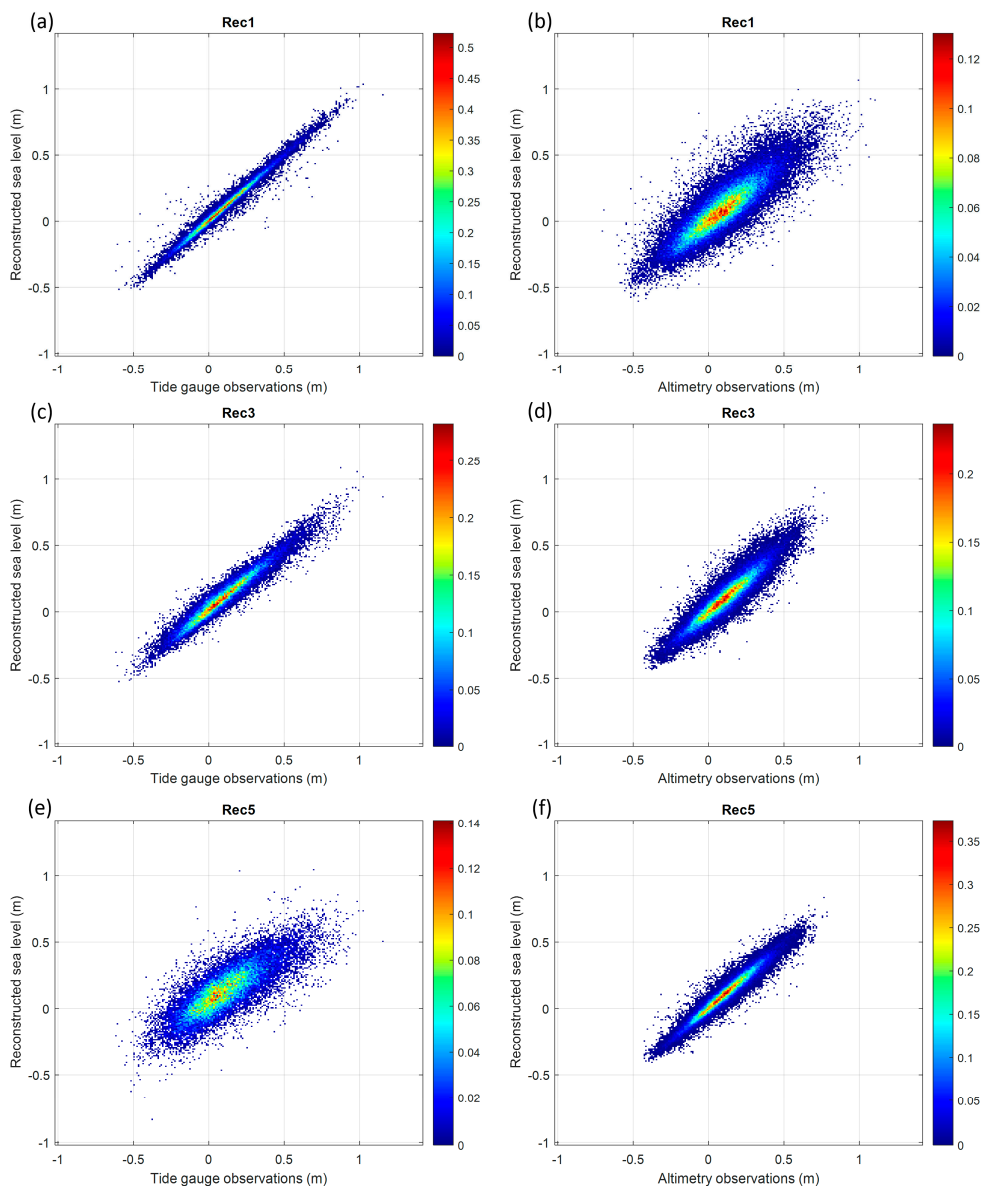


Figure 7. Two-dimensional histograms of observed (tide gauges (a,c,e) and altimetry (b,d,f)) versus reconstructed sea levels within the experiments rec1 (a,b), rec3 (c,d), and rec 5 (e,f, Table 2). The color scale shows the percentage of observations in 0.01×0.01 m bins.

3.3. Reconstruction of Coastal Sea Levels in Unsamplred Locations

Spatial coverage of coastal tide gauges has increased over time. Still, it remains a challenging task to obtain reliable sea level characteristics for the coastal locations where observations are missing. Therefore, an experiment rec1b, modified from rec1 (Table 2), was conducted with a reduced number of input tide gauge locations. The calculations were made using input data from 21 “named” coastal tide gauges, as shown by the station names in Figure 1. The evaluation was carried out over all 105 stations. Some of the data were considered to be missing and were not used in the reconstruction, but after the reconstruction the full data set was used for skill estimates. It should be noted that the statistical characteristics of reconstruction at these stations, based on full input data, are given in Figure 6.

The modified experiment rec1b revealed very similar statistical characteristics to those presented in Table 3 and Figure 6. Specifically, the mean sea level calculated over all of the stations during 1993–2021 differed by less than 0.001 m, where the mean level was 0.089 m. The overall STD of all weekly sea levels was 0.198 m for rec1 and 0.196 m for the modified rec1b (a STD map is presented in Figure 8a). It should be noted that sea level variability is higher in the northern and eastern regions (i.e., Bothnian Sea, Gulf of Finland, Gulf of Riga) than in the central Baltic Proper. The change in the reconstructed sea level patterns from rec1 to rec1b is visualized by their cRMSD map shown in Figure 8b. The main differences between the experiments became evident in the southwestern region of the sea, close to the Danish Straits, with the tidal influence from the North Sea. In the coastal areas, the highest weekly sea level cRMSD was 0.03 m, or 15% of the standard deviation. Greater differences, up to 0.07 m, were found in the deep basins of the Baltic Proper, which can be interpreted as a loss of reconstruction quality due to the reduction in the input data. It should be noted that, in both the rec1 and rec1b experiments, altimetry input data were not used for reconstruction, in order to imitate earlier time periods when only limited tide gauge data were available. Pearson’s coefficient of determination (R^2) revealed a close match with the reconstructed sea levels; the R^2 of reconstruction with observations was higher than 0.95 for both the main and the modified experiments.

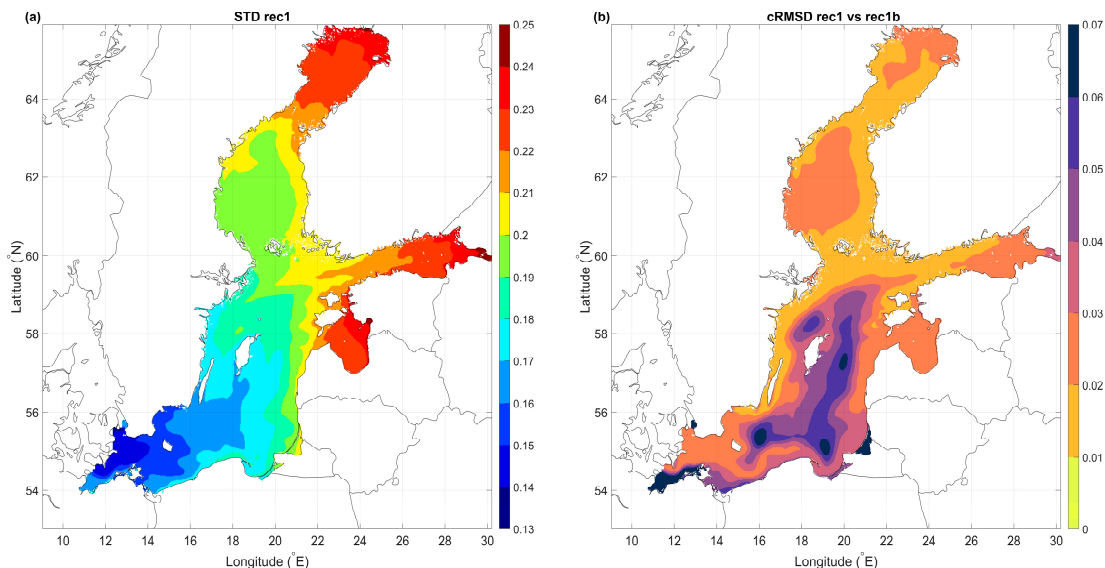


Figure 8. Maps of the standard deviation of weekly sea level in experiment rec1 (a) and centered root-mean-square difference (b) of rec1 and the modified experiment rec1b with fewer input data from tide gauges (only the 21 stations shown in Figure 1 with station names were kept for the input). The unit of the color scales is m.

The results show that weekly sea levels can be reliably estimated in unsampled locations.

3.4. Changes in Sea Volume

One of the indicators of sea level variability is sea volume, which is of primary interest for water budget calculations [55]. When calculating the changes in sea volume from gridded data, it is convenient to convert the results to the mean sea level. Since the western sea area was excluded from the reconstruction domain (Figure 1), we calculated the domain area of 379,100 km² from the gridded data. From the weekly reconstructed time series, annual and seasonal courses (Figure 9) were calculated. The reconstruction results of experiments rec1 to rec4 revealed a close match. Experiment rec5, which had only altimetry data as inputs, gave higher mean sea levels than the other experiments, especially starting from 2011, when the surplus amounted to between 0.04 and 0.08 m. The annual mean sea levels shown in Figure 9a correlate well ($R^2 = 0.93$) with the earlier results reported by Madsen et al. [36].

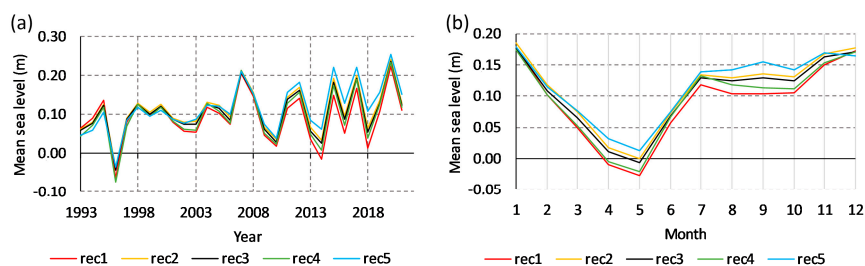


Figure 9. Annual (a) and monthly (b) mean sea levels in the Baltic Sea (over the whole basin) for the reconstruction experiments rec1 to rec5.

On the seasonal scale (Figure 9b), the known maximum sea volume in winter and minimum sea volume in spring [56] were well reproduced. The annual spatial mean sea level amplitude is ~ 0.18 m, as reported by previous altimetry data.

4. Discussion

4.1. Reconstruction Skill

The sea level height variation is practically the most important on the coastline, where the location of the moving waterline affects many aspects of human life; it is also important for navigation in harbors and shallow ship passages.

The reconstruction skill is estimated by differences between two data sets (estimated/modeled and observed), calculating the cRMSD and Pearson's coefficient of determination (R^2) using standard formulae [36,57]. Bias, when presented, is only considered indicative, due to the uncertainty of the sea level reference. As benchmarks for the present study, previous skill assessments of gridded sea level data are presented in Table 4, together with the results from the present study. For comparison, gridded data were extracted at the times and locations of the observations. The same approach was followed in the present study.

Copernicus reanalysis data (fifth line in the table) were used in the present study for spatial covariance estimates. Since the reanalysis has already been evaluated versus tide gauge data [38], comparison of the reanalysis results with sea level reconstruction was performed only in certain cases. Lower R^2 values with tide gauges for reanalysis [38] than for the operational model [57] might be related to the specifics of atmospheric forcing; the reanalysis was forced by the ERA5 atmospheric reanalysis with a resolution of 0.25°E by 0.25°N, while the operational forecast used the 2.5 km MetCoOP HARMONIE model [57].

Table 4. Skill estimates for the gridded sea level data sets.

Source	Compared Variables	Period	Time Interval	cRMSD (m)	R ²
Madsen et al., 2019 [36]	Reconstruction—tide gauges	1900–2014	Month	0.04	0.92
Madsen et al., 2019 [36]	Reconstruction—altimetry in Baltic Proper	1900–2014	Month	0.06	0.81
Present study	Reconstruction—tide gauges	1993–2021	Week	0.05	0.93
Present study	Reconstruction—altimetry	1993–2021	Week	0.10	0.82
Copernicus Reanalysis, 2023 [38]	Reanalysis—tide gauges	1993–2018	Day	0.10	0.77
Kärna et al., 2021 [57]	Operational forecast—tide gauges	2014–2016	Hour	0.10	0.90
Hordoir et al., 2019 [58]	Research model—tide gauges	2011–2012	Hour	0.06	0.90
Jahanmard et al., 2022 [50]	Bias-corrected research model—tide gauges	2017–2020	Hour	0.03	0.90
Mostafavi et al., 2023 [52]	Bias-corrected research model—altimetry	2017–2019	Hour	0.09	na

The reconstructed weekly sea level products in our study were compared with coastal tide gauge data, with cRMSD less than 0.05 m, and altimetry data, with cRMSD less than 0.1 m, when both of the data sources were included as input data. The average coefficient of determination was 0.93 when comparing the sea level reconstruction with coastal tide gauges and 0.82 in comparison with altimetry. The reconstructed sea levels at the coastal stations were closer to the observations than the reanalysis data set, as also indicated by Madsen et al. [36]. Reconstruction on shorter time scales—hours or days—was not performed in our initial study since the spatiotemporal coverage of altimetry data becomes more irregular for shorter time intervals. Operational forecasting [57] and bias-corrected research modeling [50,52,57] have revealed an hourly cRMSD of less than 0.1 m at most of the coastal stations.

The sea level trends have not been considered in our 29-year study, although they may also have some effect in such an interval. Tide gauge data were adopted from the Copernicus Marine Service without modification. In further implementations of the EOF reconstruction, the trend and reference level corrections can be easily introduced, following the example from oceanic [28] and Baltic Sea [36] applications.

Mostafavi et al. [52] have shown along-track altimetry sea level variations of up to 0.2 m that can be dynamically attributed to meandering unsteady frontal systems and mesoscale eddies. The appropriate resolution, reconstruction, and/or assimilation of such features would be a challenge for the significant improvement of physical circulation models.

4.2. Reference Level Problem for Flow Calculation

Geodetic height systems around the Baltic Sea have recently been updated [51]. The reported tide gauge observations reveal that the mean sea levels in the Gulf of Bothnia (including the Bothnian Sea and Bothnian Bay) drop from 0.10 to 0.15 m from the Swedish to the Finnish coast (Figure 6a). This drop is insignificant for coastal engineering and management, but it creates problems in the water budget calculations. The mean sea level drop between Ratan and Pietarsaari, on the opposite coasts of the Bothnian Sea, is 0.003 m (from 0.158 m in Ratan to 0.155 m in Pietarsaari) in the model reanalysis, but the observations with local datums give a difference of 0.114 m (from 0.154 m in Ratan to 0.040 m in Pietarsaari). Regarding the circulation and water budget, where sea level slope is an important driver of water motions, this difference between the modeled and observed sea level drops is an item of concern.

Let us consider simplified flow calculations. Over a long period, the stationary river discharge to the Gulf of Bothnia is $Q = 193 \text{ km}^3 \text{ year}^{-1}$ [59], which equals to $6100 \text{ m}^3 \text{ s}^{-1}$. Geostrophic transport due to the sea level slope can be estimated in the first approach as $Q_\eta = gH\Delta\eta/f$ [60], where $g = 9.81 \text{ m s}^{-2}$ is the gravity acceleration, $H = 80 \text{ m}$ is the approximate depth of the Bothnian Bay, $\Delta\eta$ is the sea level drop across the Bothnian Bay, and $f = 0.00013 \text{ s}^{-1}$ is the Coriolis parameter at a latitude of 65°N . For the modeled

$\Delta\eta = 0.003$ m, the estimated $Q_\eta = 17,800 \text{ m}^3 \text{ s}^{-1}$, while for $\Delta\eta = 0.114$ m, the estimated $Q_\eta = 678,700 \text{ m}^3 \text{ s}^{-1}$. The volume transport estimated by the modeled sea level drop can be considered realistic, since in addition to the river discharge, there is also the inflow of water from the adjacent sea area, which is usually a few times greater than the river discharge [61].

It is anticipated that assimilating the geodetic sea level differences in the order $\Delta\eta = 0.12$ m into the circulation model may distort the water exchange between the basins of the Baltic Sea. In addition to the freshwater budget, in estuarine systems such as the Baltic Sea, the circulation calculated by the models should follow the salinity budget [61].

4.3. Applicability of EOF Reconstruction

Reconstruction is a computationally fast procedure, since the only operations it contains are Equations (1) and (2), with matrices whose maximum size is the number of grid points. Therefore, the sea level maps can be updated nearly immediately when new observations become available. This feature can be used for bias correction in various applications. For example, Lagemaa et al. [47] introduced interval pointwise bias correction at each forecast step based on a backward weekly average model to observe differences using recent observations. Spatial reconstruction allows the bias to be corrected over the whole forecast domain. It has been shown that when bias correction has been applied to the sea level operational model forecast, the cRMSD in the Gulf of Finland has been reduced [50].

Reliable sea level estimates all over the coastline can be obtained using the presented reconstruction method from only a limited number of observations. This means that, based on tide gauge observations, available from the 19th century, it is possible to reconstruct historical weekly sea levels to estimate changes in sea volume and water budget variations for specific Baltic sub-regions, such as larger gulfs and smaller bays. It is also possible to evaluate high and low sea level cases and associated events (storm surges, coastal erosion events, etc.) in the areas of missing tide gauge observations. This is particularly important for navigation in harbors and shallow ship passages.

Estimates of sea level trends, including vertical land motions, can be refined from the present point-wise estimates, but this requires more harmonization of the reference levels from different data sets. The reconstructed gridded sea levels can be used for the quantification of changes in sea volume. It is also interesting to consider variations in the Baltic Sea's circulation that affect the ecosystem state. However, it is still a challenge to obtain reliable circulation indices.

5. Conclusions

A new method for the reconstruction of Baltic gridded sea levels from tide gauge and altimetry observations was developed and tested. The method is based on sea level EOF modes, calculated as spatiotemporal statistics from weekly model reanalysis results. The leading EOF modes converge well, and the first four modes already cover 99% of sea level variance. The reconstruction uses observations at coastal tide gauges and altimetry as input data. Because of the limitations of data coverage, weekly averages were considered as the shortest time interval to be resolved.

Several experiments were carried out with different combinations of input data. The method was validated against coastal tide gauges and altimetry data. The best reconstruction skill was obtained when both the tide gauges and altimetry data were taken into account. The cRMSD of the reconstruction was determined to be 0.05 m versus tide gauges and 0.10 m versus altimetry. The coefficient of determination R^2 averaged 0.93 for the tide gauges and 0.82 for the altimetry data. In the cases where only one type of input data was used, the reconstruction became worse with respect to other data sources. For example, using only altimetry data for the input improved the R^2 for altimetry data to 0.93, but it worsened the R^2 for tide gauge data to 0.66.

The reconstruction method proved useful for the reconstruction of coastal sea levels in unsampled locations and for the calculation of changes in sea volume.

Author Contributions: J.E. developed the method and performed the reconstruction experiments. A.B. carried out basic work with the altimetry data, from preparing the intermediate data sets to the validation. I.M. was responsible for the proper handling of the reanalysis model data, and S.R. was responsible for the altimetry and tide gauge data. All authors participated in the conceptualization and planning of the study. While J.E. wrote the first draft of the manuscript, all authors participated in complementary writing, review, and editing. All authors have read and agreed to the published version of the manuscript.

Funding: This study was co-funded by the European Union and the Estonian Research Council via project TEM-TA38 (Digital Twin of Marine Renewable Energy).

Data Availability Statement: All of the data were taken and downloaded from the Copernicus Marine Service <https://marine.copernicus.eu/> accessed on 16 November 2023 [38,42,43].

Acknowledgments: Discussions with our colleagues Urmas Raudsepp, Priidik Lagemaa, and Rivo Uiboupin are highly appreciated.

Conflicts of Interest: The authors declare no conflicts of interest.

References

- Meier, H.M.; Dieterich, C.; Gröger, M.; Dutheil, C.; Börgel, F.; Safonova, K.; Christensen, O.B.; Kjellström, E. Oceanographic regional climate projections for the Baltic Sea until 2100. *Earth Syst. Dyn.* **2022**, *13*, 159–199. [CrossRef]
- Hünicke, B.; Zorita, E.; Soomere, T.; Madsen, K.S.; Johansson, M.; Suursaar, Ü. Recent change—Sea level and wind waves. In *Second Assessment of Climate Change for the Baltic Sea Basin*; Springer: Cham, Switzerland; Heidelberg, Germany; New York, NY, USA; Dordrecht, The Netherlands; London, UK, 2015; pp. 155–185.
- Weisse, R.; Dailidienė, I.; Hünicke, B.; Kahma, K.; Madsen, K.; Omstedt, A.; Parnell, K.; Schöne, T.; Soomere, T.; Zhang, W.; et al. Sea level dynamics and coastal erosion in the Baltic Sea region. *Earth Syst. Dyn.* **2021**, *12*, 871–898. [CrossRef]
- Samuelsson, M.; Stigebrandt, A. Main characteristics of the long-term sea level variability in the Baltic Sea. *Tellus A* **1996**, *48*, 672–683. [CrossRef]
- Ekman, M. Climate changes detected through the world’s longest sea level series. *Glob. Planet. Chang.* **1999**, *21*, 215–224. [CrossRef]
- Cazenave, A.; Palanisamy, H.; Ablain, M. Contemporary sea level changes from satellite altimetry: What have we learned? What are the new challenges? *Adv. Space Res.* **2018**, *62*, 1639–1653. [CrossRef]
- Hansen, W. Theorie zur Errechnung des Wasserstandes und der Strömungen in Randmeeren nebst Anwendungen 1. *Tellus* **1956**, *8*, 287–300. [CrossRef]
- Meier, H.M.; Broman, B.; Kjellström, E. Simulated sea level in past and future climates of the Baltic Sea. *Clim. Res.* **2004**, *27*, 59–75. [CrossRef]
- Novotny, K.; Liesch, G.; Lehmann, A.; Dietrich, R. Variability of sea surface heights in the Baltic Sea: An intercomparison of observations and model simulations. *Mar. Geod.* **2006**, *29*, 113–134. [CrossRef]
- Steffen, H.; Wu, P. Glacial isostatic adjustment in Fennoscandia—A review of data and modeling. *J. Geodyn.* **2011**, *52*, 169–204. [CrossRef]
- Jevrejeva, S.; Moore, J.C.; Grinsted, A.; Matthews, A.P.; Spada, G. Trends and acceleration in global and regional sea levels since 1807. *Glob. Planet. Chang.* **2014**, *113*, 11–22. [CrossRef]
- Passaro, M.; Müller, F.L.; Oelsmann, J.; Rautiainen, L.; Dettmering, D.; Hart-Davis, M.G.; Abulaitijiang, A.; Andersen, O.B.; Hoyer, J.L.; Madsen, K.S.; et al. Absolute Baltic Sea level trends in the satellite altimetry era: A revisit. *Front. Mar. Sci.* **2021**, *8*, 647607. [CrossRef]
- Johansson, M.; Boman, H.; Kahma, K.K.; Launiainen, J. Trends in sea level variability in the Baltic Sea. *Boreal Environ. Res.* **2001**, *6*, 159–180.
- Suursaar, Ü.; Sooäär, J. Decadal variations in mean and extreme sea level values along the Estonian coast of the Baltic Sea. *Tellus A Dyn. Meteorol. Oceanogr.* **2007**, *59*, 249–260. [CrossRef]
- Kapsi, I.; Kall, T.; Liibus, A. Sea Level Rise and Future Projections in the Baltic Sea. *J. Mar. Sci. Eng.* **2023**, *11*, 1514. [CrossRef]
- Dailidienė, I.; Davulienė, L.; Tilickis, B.; Stankevičius, A.; Myrberg, K. Sea level variability at the Lithuanian coast of the Baltic Sea. *Boreal Environ. Res.* **2006**, *11*, 109–121.
- Karabil, S.; Zorita, E.; Hünicke, B. Contribution of atmospheric circulation to recent off-shore sea-level variations in the Baltic Sea and the North Sea. *Earth Syst. Dyn.* **2018**, *9*, 69–90. [CrossRef]
- Hünicke, B.; Zorita, E. Trends in the amplitude of Baltic Sea level annual cycle. *Tellus A Dyn. Meteorol. Oceanogr.* **2008**, *60*, 154–164. [CrossRef]
- Svansson, A. Exchange of water and salt in the Baltic and adjacent seas. *Oceanol. Acta* **1980**, *3*, 431–440.

20. Rutgeresson, A.; Kjellström, E.; Haapala, J.; Stendel, M.; Danilovich, I.; Drews, M.; Jylhä, K.; Kujala, P.; Larsén, X.G.; Halsnæs, K.; et al. Natural hazards and extreme events in the Baltic Sea region. *Earth Syst. Dyn.* **2022**, *13*, 251–301. [CrossRef]
21. Metzner, M.; Gade, M.; Hennings, I.; Rabinovich, A.B. The observation of seiches in the Baltic Sea using a multi data set of water levels. *J. Mar. Syst.* **2000**, *24*, 67–84. [CrossRef]
22. André, E.; Su, J.; Dahl Larsen, M.A.; Drews, M.; Stendel, M.; and Skovgaard Madsen, K. The role of preconditioning for extreme storm surges in the western Baltic Sea. *Nat. Hazards Earth Syst. Sci.* **2023**, *23*, 1817–1834. [CrossRef]
23. Post, P.; Kouts, T. Characteristics of cyclones causing extreme sea levels in the northern Baltic Sea. *Oceanologia* **2014**, *56*, 241–258. [CrossRef]
24. Suursaar, Ü.; Sepp, M.; Post, P.; Mäll, M. An inventory of historic storms and cyclone tracks that have caused met-ocean and coastal risks in the eastern Baltic Sea. *J. Coast. Res.* **2018**, *85*, 531–535. [CrossRef]
25. Soomere, T.; Pindsoo, K.; Kudryavtseva, N.; Eelsalu, M. Variability of distributions of wave set-up heights along a shoreline with complicated geometry. *Ocean Sci.* **2020**, *16*, 1047–1065. [CrossRef]
26. Smith, T.M.; Reynolds, R.W.; Livezey, R.E.; Stokes, D.C. Reconstruction of historical sea surface temperatures using empirical orthogonal functions. *J. Clim.* **1996**, *9*, 1403–1420. [CrossRef]
27. Chambers, D.P.; Mehlhaff, C.A.; Urban, T.J.; Fujii, D.; Nerem, R.S. Low-frequency variations in global mean sea level: 1950–2000. *J. Geophys. Res. Ocean.* **2002**, *107*, 1–10. [CrossRef]
28. Church, J.A.; White, N.J.; Coleman, R.; Lambeck, K.; Mitrovica, J.X. Estimates of the regional distribution of sea level rise over the 1950–2000 period. *J. Clim.* **2004**, *17*, 2609–2625. [CrossRef]
29. Bergé-Nguyen, M.; Cazenave, A.; Lombard, A.; Llovel, W.; Viarre, J.; Cretaux, J.F. Reconstruction of past decades sea level using thermosteric sea level, tide gauge, satellite altimetry and ocean reanalysis data. *Glob. Planet. Chang.* **2008**, *62*, 1–13. [CrossRef]
30. Ray, R.D.; Douglas, B.C. Experiments in reconstructing twentieth-century sea levels. *Prog. Oceanogr.* **2011**, *91*, 496–515. [CrossRef]
31. Meyssignac, B.; Becker, M.; Llovel, W.; Cazenave, A. An assessment of two-dimensional past sea level reconstructions over 1950–2009 based on tide-gauge data and different input sea level grids. *Surv. Geophys.* **2012**, *33*, 945–972. [CrossRef]
32. Mu, D.; Yan, H.; Feng, W. Assessment of sea level variability derived by EOF reconstruction. *Geophys. J. Int.* **2018**, *214*, 79–87. [CrossRef]
33. Strassburg, M.W.; Hamlington, B.D.; Leben, R.R.; Kim, K.Y. A comparative study of sea level reconstruction techniques using 20 years of satellite altimetry data. *J. Geophys. Res. Ocean.* **2014**, *119*, 4068–4082. [CrossRef]
34. Sanchez-Franks, A.; Frajka-Williams, E.; Moat, B.I.; Smeed, D.A. A dynamically based method for estimating the Atlantic meridional overturning circulation at 26° N from satellite altimetry. *Ocean Sci.* **2021**, *17*, 1321–1340. [CrossRef]
35. Xu, Q.; Cheng, Y.; Plag, H.P.; Zhang, B. Investigation of sea level variability in the Baltic Sea from tide gauge, satellite altimeter data, and model reanalysis. *Int. J. Remote Sens.* **2015**, *36*, 2548–2568. [CrossRef]
36. Madsen, K.S.; Hoyer, J.L.; Suursaar, Ü.; She, J.; Knudsen, P. Sea level trends and variability of the Baltic Sea from 2D statistical reconstruction and altimetry. *Front. Earth Sci.* **2019**, *7*, 243. [CrossRef]
37. Cheng, Y.; Xu, Q.; Li, X. Spatio-temporal variability of annual sea level cycle in the Baltic Sea. *Remote Sens.* **2018**, *10*, 528. [CrossRef]
38. Ringgaard, I.; Korabel, V.; Spruch, L.; Lindenthal, A.; Huess, V. Baltic Sea Physics Reanalysis. BALTICSEA_MULTITYEAR_PHY_003_011. Available online: https://data.marine.copernicus.eu/product/BALTICSEA_MULTITYEAR_PHY_003_011/description (accessed on 13 October 2023).
39. Elken, J.; Zujev, M.; She, J.; Lagema, P. Reconstruction of large-scale sea surface temperature and salinity fields using sub-regional EOF patterns from models. *Front. Earth Sci.* **2019**, *7*, 232. [CrossRef]
40. Zujev, M.; Elken, J.; Lagema, P. Data assimilation of sea surface temperature and salinity using basin-scale reconstruction from empirical orthogonal functions: A feasibility study in the northeastern Baltic Sea. *Ocean Sci.* **2021**, *17*, 91–109. [CrossRef]
41. Nerger, L.; Tang, Q.; Mu, L. Efficient ensemble data assimilation for coupled models with the Parallel Data Assimilation Framework: Example of AWI-CM (AWI-CM-PDAF 1.0). *Geosci. Model Dev.* **2020**, *13*, 4305–4321. [CrossRef]
42. In Situ TAC Partners. Baltic Sea- In Situ Near Real Time Observations. INSITU_BAL_PHYBGCWAV_DISCRETE_MYNRT_013_032. Available online: https://data.marine.copernicus.eu/product/INSITU_BAL_PHYBGCWAV_DISCRETE_MYNRT_013_032/description (accessed on 9 October 2023).
43. Pujol, M.I. European Seas Along Track L3 Sea Surface Heights Reprocessed 1993 Ongoing Tailored For Data Assimilation. SEALEVEL_EUR_PHY_L3_MY_008_061. Available online: https://data.marine.copernicus.eu/product/SEALEVEL_EUR_PHY_L3_MY_008_061/description (accessed on 16 November 2023).
44. Pujol, M.I.; Dupuy, S.; Vergara, O.; Sánchez Román, A.; Faugère, Y.; Prandi, P.; Dabat, M.L.; Dagneaux, Q.; Lievin, M.; Cadier, E.; et al. Refining the Resolution of DUACS Along-Track Level-3 Sea Level Altimetry Products. *Remote Sens.* **2023**, *15*, 793. [CrossRef]
45. Liibus, A.; Kall, T.; Rikka, S.; Uiboupin, R.; Suursaar, Ü.; Tseng, K.H. Validation of Copernicus Sea Level Altimetry Products in the Baltic Sea and Estonian Lakes. *Remote Sens.* **2020**, *12*, 4062. [CrossRef]
46. Jahanmard, V.; Hordoir, R.; Delpeche-Ellmann, N.; Ellmann, A. Quantification of hydrodynamic model sea level bias utilizing deep learning and synergistic integration of data sources. *Ocean Model.* **2023**, *186*, 102286. [CrossRef]
47. Afrasteh, Y.; Slobbe, D.C.; Sacher, M.; Verlaan, M.; Jahanmard, V.; Klees, R.; Guarneri, H.; Keyzer, L.; Pietrzak, J.; Snellen, M.; et al. Realizing the European Vertical Reference System using model-based hydrodynamic leveling data. *J. Geod.* **2023**, *97*, 86. [CrossRef]

48. Mostafavi, M.; Delpeche-Ellmann, N.; Ellmann, A.; Jahanmard, V. Determination of accurate dynamic topography for the Baltic Sea using satellite altimetry and a marine geoid model. *Remote Sens.* **2023**, *15*, 2189. [[CrossRef](#)]
49. Raudsepp, U.; Toompuu, A.; Kõuts, T. A stochastic model for the sea level in the Estonian coastal area. *J. Mar. Syst.* **1999**, *22*, 69–87. [[CrossRef](#)]
50. Soomere, T.; Eelsalu, M.; Kurkin, A.; Rybin, A. Separation of the Baltic Sea water level into daily and multi-weekly components. *Cont. Shelf Res.* **2015**, *103*, 23–32. [[CrossRef](#)]
51. Lagemaa, P.; Elken, J.; Kõuts, T. Operational sea level forecasting in Estonia. *Est. J. Eng.* **2011**, *17*, 301–331. [[CrossRef](#)]
52. Soomere, T.; Pindsoo, K. Spatial variability in the trends in extreme storm surges and weekly-scale high water levels in the eastern Baltic Sea. *Cont. Shelf Res.* **2016**, *115*, 53–64. [[CrossRef](#)]
53. Von Storch, H.; Zwiers, F.W. *Statistical Analysis in Climate Research*; Cambridge University Press: Cambridge, UK, 1999. [[CrossRef](#)]
54. Reynolds, R.W.; Smith, T.M. Improved global sea surface temperature analyses using optimum interpolation. *J. Clim.* **1994**, *7*, 929–948. [[CrossRef](#)]
55. Omstedt, A.; Elken, J.; Lehmann, A.; Piechura, J. Knowledge of the Baltic Sea physics gained during the BALTEX and related programmes. *Prog. Oceanogr.* **2004**, *63*, 1–28. [[CrossRef](#)]
56. Stramska, M.; Kowalewska-Kalkowska, H.; Świrgoń, M. Seasonal variability in the Baltic Sea level. *Oceanologia* **2013**, *55*, 787–807. [[CrossRef](#)]
57. Kärnä, T.; Ljungemyr, P.; Falahat, S.; Ringgaard, I.; Axell, L.; Korabel, V.; Murawski, J.; Maljutenko, I.; Lindenthal, A.; Jandt-Scheelke, S.; et al. Nemo-Nordic 2.0: Operational marine forecast model for the Baltic Sea. *Geosci. Model Dev.* **2021**, *14*, 5731–5749. [[CrossRef](#)]
58. Hordoir, R.; Axell, L.; Höglund, A.; Dieterich, C.; Fransner, F.; Gröger, M.; Liu, Y.; Pemberton, P.; Schimanke, S.; Andersson, H.; et al. Nemo-Nordic 1.0: A NEMO-based ocean model for the Baltic and North seas—Research and operational applications. *Geosci. Model Dev.* **2019**, *12*, 363–386. [[CrossRef](#)]
59. Bergström, S.; Carlsson, B. River runoff to the Baltic Sea 1950–1990. *Ambio* **1994**, *23*, 280–287.
60. Toulany, B.; Garrett, C. Geostrophic control of fluctuating barotropic flow through straits. *J. Phys. Oceanogr.* **1984**, *14*, 649–655. [[CrossRef](#)]
61. Burchard, H.; Bolding, K.; Feistel, R.; Gräwe, U.; Klingbeil, K.; MacCready, P.; Mohrholz, V.; Umlauf, L.; van der Lee, E.M. The Knudsen theorem and the Total Exchange Flow analysis framework applied to the Baltic Sea. *Prog. Oceanogr.* **2018**, *165*, 268–286. [[CrossRef](#)]

Disclaimer/Publisher's Note: The statements, opinions and data contained in all publications are solely those of the individual author(s) and contributor(s) and not of MDPI and/or the editor(s). MDPI and/or the editor(s) disclaim responsibility for any injury to people or property resulting from any ideas, methods, instructions or products referred to in the content.

Appendix 2


II

A. Barzandeh, I. Maljutenko, S. Rikka, P. Lagemaa, A. Männik, R. Uiboupin, and U. Raudsepp, "Sea surface circulation in the Baltic Sea: decomposed components and pattern recognition," *Scientific Reports*, vol. 14, no. 1, p. 18649, 2024



OPEN

Sea surface circulation in the Baltic Sea: decomposed components and pattern recognition

Amirhossein Barzandeh , Ilja Maljutenko, Sander Rikka, Priidik Lagemaa, Aarne Männik, Rivo Uiboupin & Urmas Raudsepp


By decomposing the total sea surface current into its geostrophic and ageostrophic components, we examined the contribution of each to the long-term variability of the total sea surface current. Our findings demonstrate the importance of geostrophic currents in Baltic Sea gyre formations. Additionally, ageostrophic currents contribute significantly to the flow across the region. Quantifying the difference between total sea surface current fields has revealed two dominant general sea surface circulation patterns in the Baltic Sea, whose characteristics correspond to the monthly mean climatology of sea surface current fields in May and December. Subsequently, a machine learning technique was employed to effectively detect the types of sea surface circulation patterns using wind vectors and sea level anomaly fields. This underscored the combined influence of sea level anomaly-driven and wind-driven components in shaping surface current vectors in the Baltic Sea, consistent with geostrophic and ageostrophic decompositions.

Keywords Geostrophic current, Ageostrophic current, Baltic Sea, Circulation pattern, Machine learning

The surface circulation in the ocean and marginal seas has become an increasing research focus in recent years, driven mainly by the success of satellite remote sensing. Among the dominant components of ocean surface dynamics, the geostrophic and Ekman currents stand out^{1–3}. Various datasets, such as Ocean Surface Current Analyses Real-time (OSCAR) and Geostrophic and Ekman Current Observatory (GECKO) products, offer daily maps illustrating these primary currents. Each dataset provides global surface current information derived directly from satellite altimetry and ocean vector winds^{4,5}. Their methodologies differ primarily in their handling of geostrophic currents at the equator, addressing wind-driven turbulence, and incorporating adjustments based on sea surface temperature gradients. Despite not encompassing more complex physics such as nonlinearities, these methods stand out due to their minimal assumptions, striving to produce surface current measurements on a consistent global grid at regular intervals that closely resemble direct satellite observations^{6–8}. Nonetheless, while these products offer valuable insights into open oceans and some major upwelling zones by emphasizing the role of the wind-driven component in total sea surface current, their estimations may not provide precise details about coastal and marginal seas.

However, validating satellite-based surface currents remains a challenging task due to the scarcity of surface measurements unaffected by surface wind drag on floats^{9–11}. Hence, numerical circulation models with acceptable accuracy serve as references for circulation patterns. Additionally, existing knowledge about surface water circulation is invaluable. Understanding the intricate patterns of surface circulation is crucial as a benchmark for remotely sensed circulation data. In our study, we concentrate on a comprehensive analysis of the surface circulation in the Baltic Sea, leveraging its well-studied nature and the reasonably accurate circulation models we rely upon. The central focus of our study is understanding the appearances of geostrophic and ageostrophic circulation. It is essential to note that our analysis of circulation in this study does not involve a comparison or analysis of the circulation derived from satellite remote sensing products.

The Baltic Sea (Fig. 1) has been extensively studied over the last centuries, leading to the development of relatively accurate circulation models despite its complex arrangement of loosely connected sub-basins. Investigation into the circulation patterns of the Baltic Sea began in the nineteenth century, when Struve (1864) first noted that general currents are caused by a difference in salinity due to the interaction of two distinct water masses within the Baltic basin: the freshwater from extensive runoff and the saline ocean water originating from the North Atlantic Ocean and entering via the Danish Strait¹². Subsequent studies further substantiated and elaborated

Department of Marine Systems, Tallinn University of Technology, 12618 Tallinn, Estonia.  email: amirhossein.barzandeh@taltech.ee

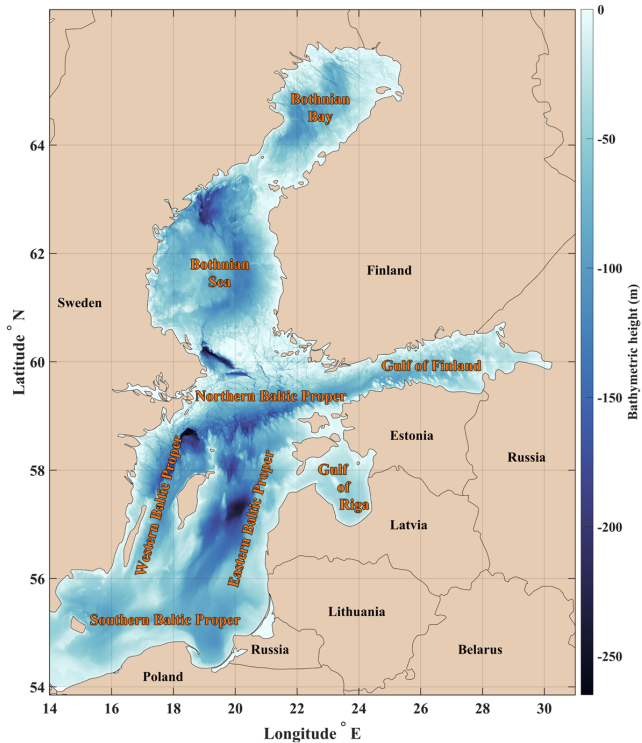


Figure 1. Map of the study area, the Baltic Sea, includes subbasin and country names. The colour scale shows the depth according to the General Bathymetric Chart of the Oceans (GEBCO)²⁶ and the final map were generated using MATLAB r2022b programming platform²⁷.

upon these initial observations. Sarkisjan et al. were the first to conduct a model-based study that confirmed the presence and significance of cyclonic gyres within the Baltic Sea¹³. Lehmann and Hinrichsen demonstrated that despite significant variability in atmospheric forcing factors, such as wind and sea level pressure, relatively stable annual mean circulation patterns exist in the Baltic Sea, with only occasional inter-annual variations observed in the magnitude of basin-wide cyclonic gyre transports¹⁴. Omstedt and Axell showed the significant impact of baroclinic flows between the Baltic Sea sub-basins and the Baltic proper while emphasizing the importance of barotropic flow through the Danish Straits and the influence of river runoff¹⁵. According to Jędrasik et al., surface currents within the Baltic Sea are predominantly influenced by wind dynamics, leading to substantial variability, notably driven by prevailing western winds that produce stronger eastern currents, with an increasing long-term trend in sea surface current intensity¹⁶. In general, numerous studies employing ocean models have highlighted the prevalence of cyclonic gyres in the overall circulation patterns of both the Baltic Sea as well as its sub-basins^{17–23}. In addition, Maljutenko and Raudsepp, and Soosaar et al. illustrated that the general circulation in the Gulf of Finland and the Gulf of Riga can be anticyclonic during spring and summer due to seasonal shifts in the forces driving the sea surface currents^{24,25}. Understanding these variations necessitates an assessment of both barotropic and baroclinic perspectives, given their reliance on distinct atmospheric conditions.

Our objective is to analyze the monthly climatology of surface circulation in the Baltic Sea, identifying the dominant spatial patterns of sea surface geostrophic and ageostrophic current components over an annual cycle. Therefore, we aim to decompose the total sea surface current into geostrophic and ageostrophic components. Geostrophic currents are derived from gridded sea surface height anomaly data by calculating the sea level slope. Ageostrophic currents, which can be amplified by various factors, are primarily driven by wind or other non-linear interactions^{28,29}. While ageostrophic currents globally may include inertial currents, tidal currents, and Stokes drift, in the Baltic Sea, they are predominantly influenced by Coriolis forces, sea surface topography, and friction, with other factors being negligible³⁰. This suggests that geostrophic and wind-driven currents are more significant in this region. However, the combined impact of geostrophic and ageostrophic components on the overall sea surface circulation in the Baltic Sea is still unclear.

The influence of geostrophic and ageostrophic currents on total circulation can change over time due to various forcing factors. This study will also explore the origins of ageostrophic components in the Baltic Sea and their comparison with the geostrophic component caused by sea level anomalies. Our ultimate goal is to categorize each monthly mean circulation pattern into clusters representing dominant circulation patterns. We

plan to employ machine learning to determine the dominant type of monthly circulation based on sea surface anomalies and wind fields. Additional spatial and temporal analyses will offer further interpretive insights into the dynamics of sea surface circulation in the Baltic Sea.

Data and methods

Data product description and geostrophic/ageostrophic decomposition

The sea level height (h) and total sea surface current data (u_{tot}, v_{tot}) for the Baltic Sea (lon: 14 °E to ~31 °E and lat: 54 °N to ~66 °N) were extracted from the Copernicus Marine Service (CMS) Baltic Sea Physics Reanalysis from January 1993 to December 2021 with a spatial resolution of 1 nautical mile. This data has been produced by the NEMO ocean model of a North Sea and Baltic Sea regional configuration Nemo-Nordic 2.0^{31,32} and it is accompanied by a Quality Information Document (QUID), where it has been reported that the mean correlation between the available tide gauges and CMS Baltic Sea Physical Reanalysis Sea level outputs for the entire Baltic Sea is 0.88 with a root mean square deviation (RMSD) of 0.136 m³³. The geostrophic velocity components (u_{geo}, v_{geo}) of sea surface current have been calculated from the sea level data as follows³⁴:

$$u_{geo} = \frac{-g}{f} \frac{\partial h}{\partial y}, \quad (1a)$$

$$v_{geo} = \frac{+g}{f} \frac{\partial h}{\partial x}, \quad (1b)$$

The Eqs. (1a, 1b) are estimated using the 9-point stencil width classic centred difference method³⁵. Then, the ageostrophic components (u_{ageo}, v_{ageo}) of sea surface current were calculated by subtracting the geostrophic components from the total current components:

$$u_{ageo} = u_{tot} - u_{geo}, \quad (2a)$$

$$v_{ageo} = v_{tot} - v_{geo}, \quad (2b)$$

The long-term mean and monthly means of total, geostrophic and ageostrophic currents over the study period were calculated. The monthly means of the current anomaly were calculated by subtracting the respective monthly mean from the long-term mean calculated over the period of 1993–2021.

Euclidean distance

The Euclidean distance (ED) was implemented as a useful criterion for determining a single index for assessing the difference between two gridded sea surface current vector fields as below:

$$ED = \frac{1}{n \times m} \left(\sum_{i=1}^n \sum_{j=1}^m \sqrt{(u_{ij}^A - u_{ij}^B)^2 + (v_{ij}^A - v_{ij}^B)^2} \right), \quad (3)$$

where the superscripts *A* and *B* denote two different sea surface current fields, each two-dimensionally gridded along the *x*-axis accounted by subscript *i* with a total number of points *n*, and along the *y*-axis by subscript *j* with a total number of points *m*.

Convolutional neural network

A 2-dimensional convolutional neural network (CNN2D) model was trained with monthly mean sea level and wind vector fields to detect the monthly sea surface circulation types (SSCT). The SSCT is defined as a single categorical number representing a specific SSCT. At the preprocessing stage, the wind data from the global atmosphere reanalysis dataset of ERA5³⁶ for the period 1993–2021 was extracted over the Baltic Sea area and resampled into the same grids as the CMS data. To feed into CNN2D, each input batch consists of 3 matrices sized 584 × 709, representing monthly mean fields of sea level anomaly (sla), along with zonal (u-wind) and meridional (v-wind) components of 10 m wind speed. The dataset was split into training, validation, and testing sets based on time-based segmentation. The CNN2D was trained on 228 (~66%) time-instances of monthly mean fields from 1993 to 2011, validated on 60 (~17%) instances from 2012 to 2016, and then tested on the last 60 (~17%) instances from 2017 to 2021.

The architecture of the CNN2D model used for SSCT recognition is presented in Fig. 2. The network starts with an input layer tailored to the size of the training data, followed by convolutional layers designed with filter sizes of 8 × 8 and 16 filters, initially enhancing feature extraction. Rectified Linear Unit (ReLU) activation functions are utilized to introduce non-linearity, followed by average pooling layers of 4 × 4 size to downsample the data³⁷. The network further consists of additional convolutional layers with 32 filters with sizes of 4 × 4, followed by similar ReLU activation and average pooling layers of 2 × 2 size. This two-step convolutional approach addresses the large spatial dimensions of the input layers, leading to categorical outputs. A fully connected layer with the number of outputs corresponding to the number of recognized dominant SSCTs precedes the softmax classification layer, facilitating the classification of SSCTs. The network was trained using the 'adam' optimizer with a maximum of 12 epochs, a mini-batch size of 4, an initial learning rate of 0.001, and employed validation data for model evaluation every two epochs³⁸.

Furthermore, to gain deeper insights into the contribution of each input feature map—sla, u-wind, and v-wind—in our CNN2D model, we used occlusion sensitivity mapping to analyze the contribution of each input

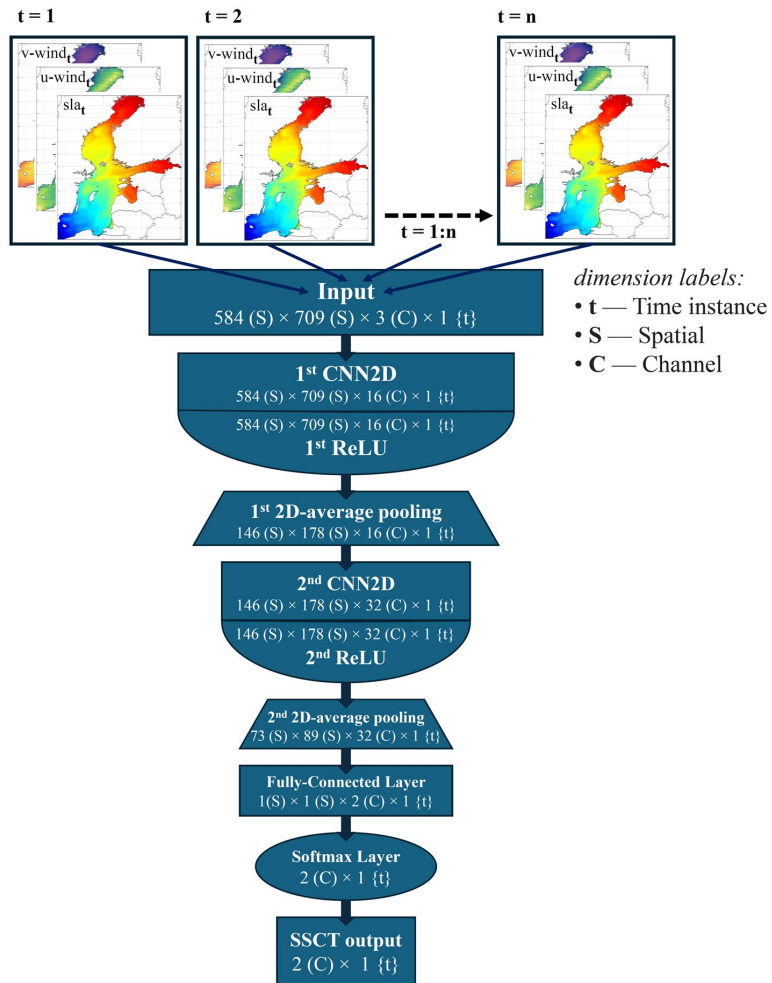


Figure 2. Diagram of the CNN2D model architecture for SSCT recognition from sea level and wind input data.

feature in detection of the SSCTs. This involved excluding each feature map from input batches during the testing phase of the trained CNN2D model. Subsequently, we compared the SSCT recognition results with those obtained from the original CNN2D model.

Through these tests, conducted three times with each test excluding one of the maps from the input batches, we evaluated the importance of each component in the CNN2D’s decision-making process. Higher error rates observed in these occlusion experiments compared to the original CNN2D results indicate greater dependency of the model on the excluded input component. During the exclusion process, each map—sla, u-wind, and v-wind—was neutralized by filling it with zeros, simulating the absence of data similar to land areas in the data preparation phase. The cumulative number of incorrect SSCT detections, compared to the original labels, was then divided by the total number of time instances to provide the error percentage for the absence of each feature map in the input batches.

Results

Mean sea surface current

Long-term mean sea surface current fields of the Baltic Sea and its decomposition into geostrophic and ageostrophic components are presented in Fig. 3. Geostrophic currents (Fig. 3b) show strong similarity with total currents (Fig. 3a), both in terms of current speeds and patterns. The mean ageostrophic component (Fig. 3c) mainly comprises southeastward currents. Spatial averages are 0.022 m/s for the total currents, 0.025 m/s for the geostrophic currents, and 0.016 m/s for the ageostrophic currents. The geostrophic current primarily represents

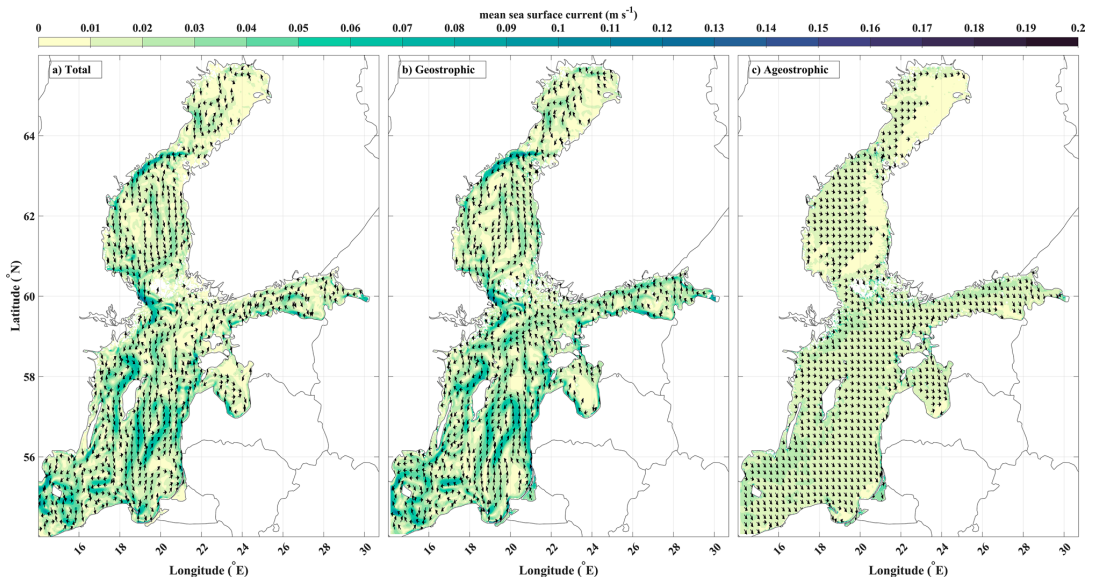


Figure 3. The mean values of (a) total, (b) geostrophic, and (c) ageostrophic surface currents throughout the entire 29-year period (vectors with magnitudes > 0.01 m/s are shown).

cyclonic water movement and shapes the dominant gyres (Fig. 3). These gyres exhibit high intensity, particularly around their edges. The weaker ageostrophic currents serve as a uniform background flow almost everywhere.

Ageostrophic currents have a tendency to weaken from the northwestern coast towards the southeastern coasts at the sub-basin scale. Total circulations show prominently cyclonic gyres in the Bothnian Bay, the Bothnian Sea, and the eastern Baltic Proper. Anticyclonic gyres dominate in the Gulf of Riga, the western Baltic Proper, and the eastern part of the Gulf of Finland (Fig. 3a,b). All these patterns are attributed to the geostrophic surface currents, and their magnitude reaches up to ~ 0.15 m/s at the rim of the gyres. The similarity in pattern and strength between total and geostrophic currents indicates that the geostrophic component primarily explains total currents. The ageostrophic component, characterized by a relatively uniform spatial flow direction and lesser speed, contributes secondarily to the total currents.

Monthly climatology

We present climatological monthly mean circulations for geostrophic, ageostrophic, and total sea surface current. Monthly climatology of geostrophic currents retains its basic spatial structure throughout the year (Supplement, Fig. 2), which is similar to the long-term mean of geostrophic current distribution (Fig. 3b). The ageostrophic component is more variable (Supplement, Fig. 3) in terms of current directions, but the currents still remain directed to the eastward semi-circle in all months (Fig. 3c). The geostrophic currents provide a major contribution to the total currents, which results in the total currents keeping their basic mean structure as well (Supplement, Fig. 1).

In order to quantify the disparity between the monthly climatology (Supplement, Figs. 1–3) and the mean maps (Fig. 3), we used ED (Fig. 4a). In this context, the ED reflects the monthly deviation of a particular type of current (total, geostrophic, or ageostrophic) from its long-term mean. The higher the ED value, the greater the difference in the circulation pattern from its reference (Fig. 4).

Figure 4a shows that the SSCTs differ the most from the respective climatological mean in May and December and are most similar in March and September for geostrophic, ageostrophic, and total currents. This means that either the SSCTs in May and December (March and September) are similar to each other or pairwise different. To find out, we conducted an analysis by calculating the ED between each monthly climatological mean circulation and the other 11 monthly means. Our pairwise comparison of monthly climatological circulations revealed that the monthly mean circulations are most closely related to the circulations of the previous and following months (Fig. 4b–d). Notably, there are two significant peaks for each component in May and December, marking the most distinct variation within the year. Furthermore, the SSCTs in April and from June to August exhibit a resemblance to the May SSCT. On the other hand, the SSCTs in October, November, January, and February align closely with the December SSCT. The SSCTs in March and September can be considered as transitional phases, as they separate two distinctive classes (May and December) while being similar to each other.

To understand differences between characteristic circulations in May and December, we look at the respective anomalies. Geostrophic circulation in May represents the situation when prevailing cyclonic circulation in the eastern Baltic proper, the Bothnian Sea, and the Bothnian Bay is most distorted (Fig. 5a). Although climatological mean May circulation is still evident, the circulation anomaly shows a dominantly anticyclonic flow scheme

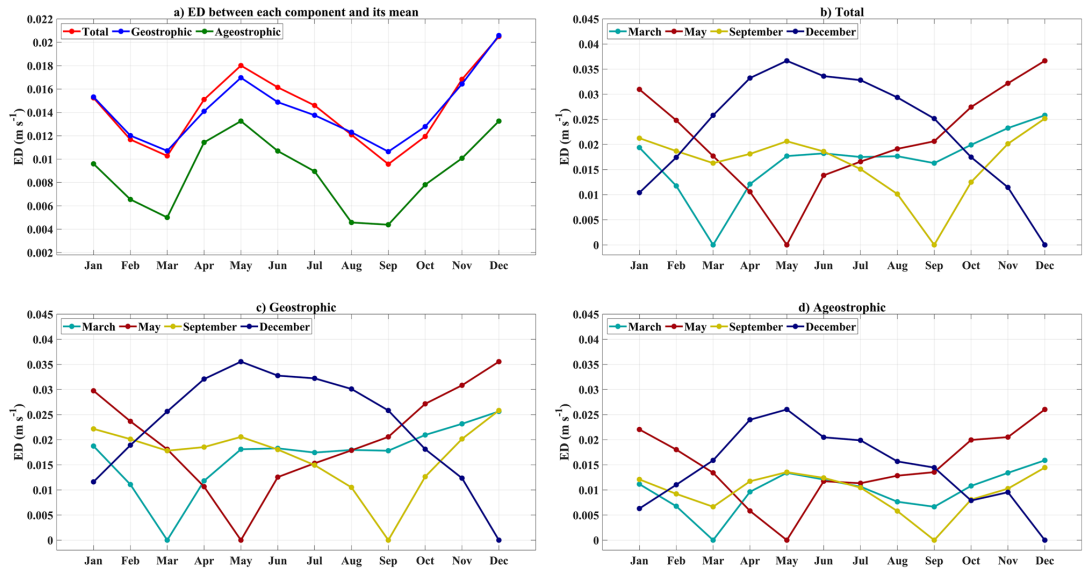


Figure 4. Euclidean distances: (a) Euclidean distance between each monthly climatology map and the long-term mean fields. (b) Euclidean distance between each monthly climatology map of “total” sea surface current and the mean total current fields in March, May, September, and December. (c) Euclidean distance between each monthly climatology map of “geostrophic” current and the mean geostrophic current fields of March, May, September, and December. (d) Euclidean distance between each monthly climatology map of “ageostrophic” correct and the mean ageostrophic current fields of March, May, September, and December. A zero value indicates identical circulation patterns. As the ED increases, the disparity between the two circulation patterns also grows.

(Fig. 5b). The currents in the Gulf of Riga, the Gulf of Finland, and the western Baltic proper are different from the overall anticyclonic tendency. Instead, cyclonic circulation is evident there. The same is true for the circulation in the western Baltic Proper. Predominantly anticyclonic circulation patterns are also present in the anomaly fields of April, June, July, and August (Supplement, Figs. 5 & 6).

Geostrophic circulation in December repeats mean geostrophic circulation in the main circulation directions, but the magnitude of the currents has increased (Fig. 5c). This is well emphasized in the anomaly of the currents in December (Fig. 5d). In most sub-basins of the Baltic Sea, cyclonic gyres dominate. Anticyclonic circulation cells in the western Baltic Proper do not exist in the anomaly field. The separate circulation patterns in the eastern and western Baltic Proper have merged into a single dominant cyclonic gyre that covers the entire Baltic proper. In addition, the anticyclonic circulation in the Gulf of Riga and anticyclonic eddies in the southern Gulf of Finland have disappeared. Predominantly cyclonic circulation patterns are also present in the anomaly fields of October, November, January, and February (Supplement).

Monthly climatological ageostrophic circulation follows qualitatively the same seasonal tendency as geostrophic currents. In May, mean ageostrophic currents exhibit anticyclonic circulation, primarily confined to the coastal areas. The offshore ageostrophic currents are minimal, with speeds less than 0.01 m/s (Fig. 6a). The anomalies of ageostrophic current in May also exhibit anticyclonic shear over the Baltic Sea (Fig. 6b). A similar pattern of ageostrophic currents in the subregions is present in April, June, July, and August (Supplement). Cyclonic shear is dominant from October to February (Supplement), with December being the month most characteristic of cyclonic shear (Fig. 6c,d). The circulation in March and September represents a transition from one SST to the other. The currents at that time match the long-term mean patterns the most (Fig. 3c).

Monthly realizations of SSTs

We have identified two primary SSTs: the strong cyclonically dominated circulation in December represented by climatological December circulation and the weaker one in May represented by climatological May circulation. To measure the monthly prevalence of a dominant SST, EDs are calculated pairwise between these SSTs and all monthly circulations. The smaller of the two EDs each month indicates the presence of the corresponding SST for that month. The monthly pattern of this SST’s dominance supports the seasonality of the characteristic sea surface circulation patterns (Fig. 7). A strong or weak cyclonic circulation is predominant in autumn and winter, or spring and summer, respectively. In transitional months, such as February, March, and September, the similarity to the May or December SSTs is not clearly defined. During the 29-year study period, there was at least one instance in May or December when the circulation resembled the typical December or May SST more closely.

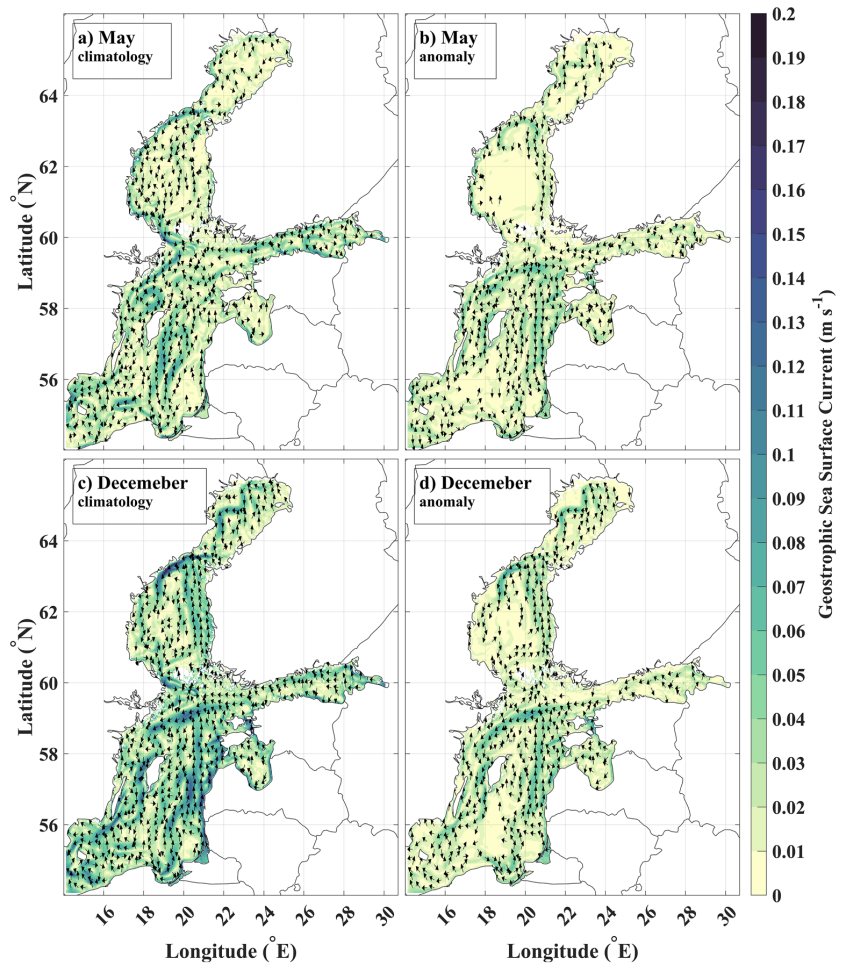


Figure 5. Dominant geostrophic circulation patterns in May and December (vectors with magnitude >0.01 m/s are shown): (a) May climatology. (b) May anomaly. (c) December climatology (d) December anomaly.

CNN2D pattern detection

A CNN2D model was utilized to categorize monthly circulation patterns into two distinct SSCTs that represent the climatological circulations of May and December. The inputs for the model included the monthly mean wind vectors and sea level anomaly fields. The classification results were verified by comparing the SSCTs from the model with the corresponding SSCTs defined by the ED. The smaller ED between the monthly circulation and the climatological circulations of May and December determines the dominant SSCT for each month. Figure 8 depicts the comparison of the model and ED results in identifying SSCTs in the Baltic Sea. The CNN2D model achieved an accuracy of 58 out of 60 in correctly identifying the inherent SSCTs.

Due to the sensitivity of CNN2D, we conducted 12 trials to assess the variability in errors across different training instances. Each trial of CNN2D was conducted with the same configuration and input yet yielded slightly varying outcomes. The most robust trained CNN2D trial resulted in $\sim 97\%$ accuracy or 2 errors over 60 testing time instances (Fig. 8a). The range of errors has been changed between different trials from $\sim 92\%$ to $\sim 97\%$ (from 2 to 5 errors over 60 testing time instances). In addition, the cumulative error temporal variability distribution has been checked for the 12 trials (Fig. 8b). In general, results show that the not-accurate CNN2D detection is at the months where the sea surface current ED from May is close to the sea surface current ED from December. Specifically, errors are most prevalent in March 2021, January 2021, October 2019, August 2019, and November 2018.

Our analysis proceeded with an examination of how *sla*, *u*-wind, and *v*-wind contribute to the decision-making process of our CNN2D model, focusing on the occlusion sensitivity of each map within the input batches. Utilizing our pre-trained CNN2D model, which incorporates all three input fields, we discovered that

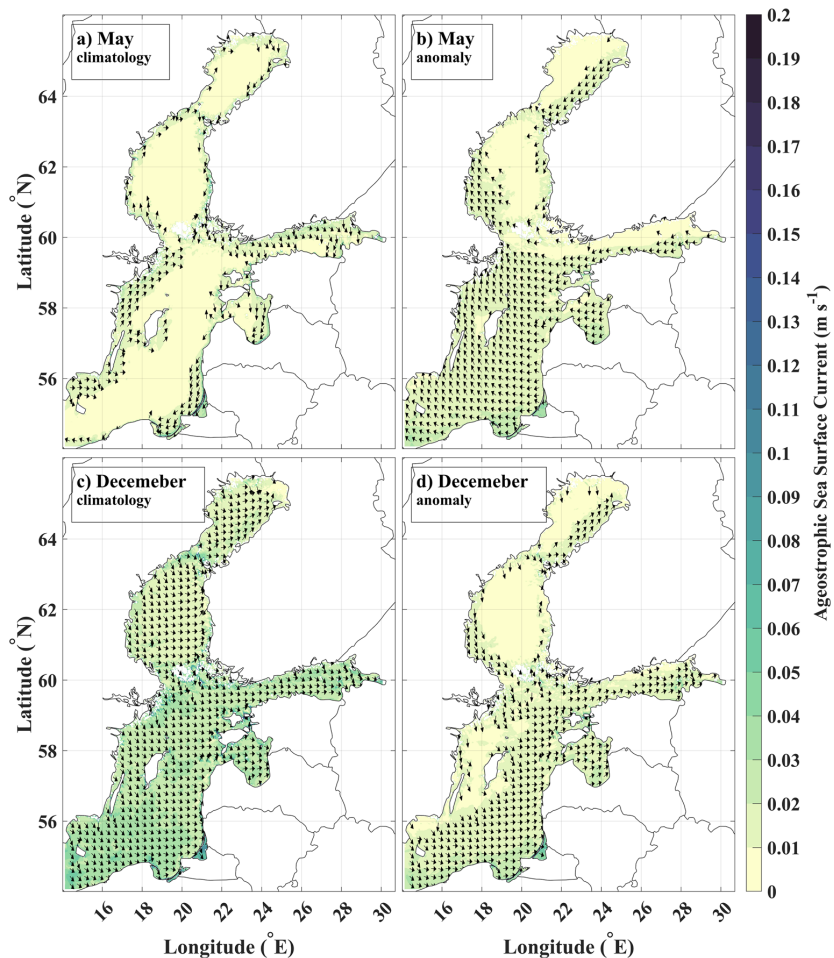


Figure 6. Dominant ageostrophic circulation patterns in May and December (vectors with magnitude > 0.01 m/s are shown): (a) May climatology. (b) May anomaly. (c) December climatology (d) December anomaly.

the omission of *sla*, while maintaining *u*-wind and *v*-wind, led to a 12% error rise in the precise identification of the SSCT. We performed a comparable occlusion sensitivity analysis for both *u*-wind and *v*-wind. The results indicate an 8% error increase in identifying the correct SSCT when *u*-wind data is absent. Conversely, the error rises to 33% when *v*-wind data is missing.

Discussion

By decomposing the total sea surface currents into their geostrophic and ageostrophic components, alongside their long-term mean and monthly climatology, our findings underscore the pivotal role of geostrophic currents in forming prevailing gyre structures throughout the Baltic Sea. Accompanying these, the weaker ageostrophic currents provide a consistent background flow across the region. These results strongly imply that the main circulation dynamics in the Baltic Sea are primarily steered by the geostrophic component that is intricately linked to the spatial distribution of static *sla*. Previous studies have emphasized the significant influence of large-scale wind and air pressure fields on Baltic Sea level variability, with observed correlations with indices such as the North Atlantic Oscillation^{39–43}. Indeed, long-term sea surface currents in the Baltic Sea exhibit a direct association with sea level anomalies, which are influenced by wind dynamics, too. Previous studies have considered wind as the primary driver of sea surface currents^{23,44}. Our study demonstrates that in the surface layer of the Baltic Sea, geostrophic currents resulting from sea level anomalies can reliably explain the main orientation of sea surface circulations in the Baltic Sea.

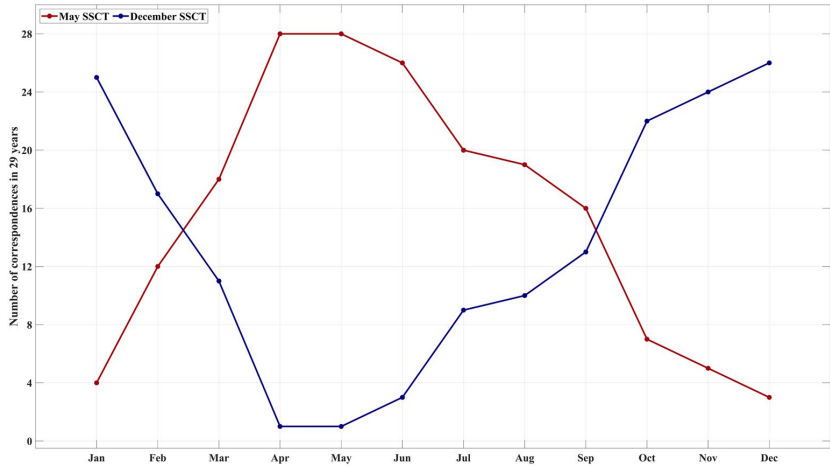


Figure 7. Frequency of SSCT correspondence in each month.

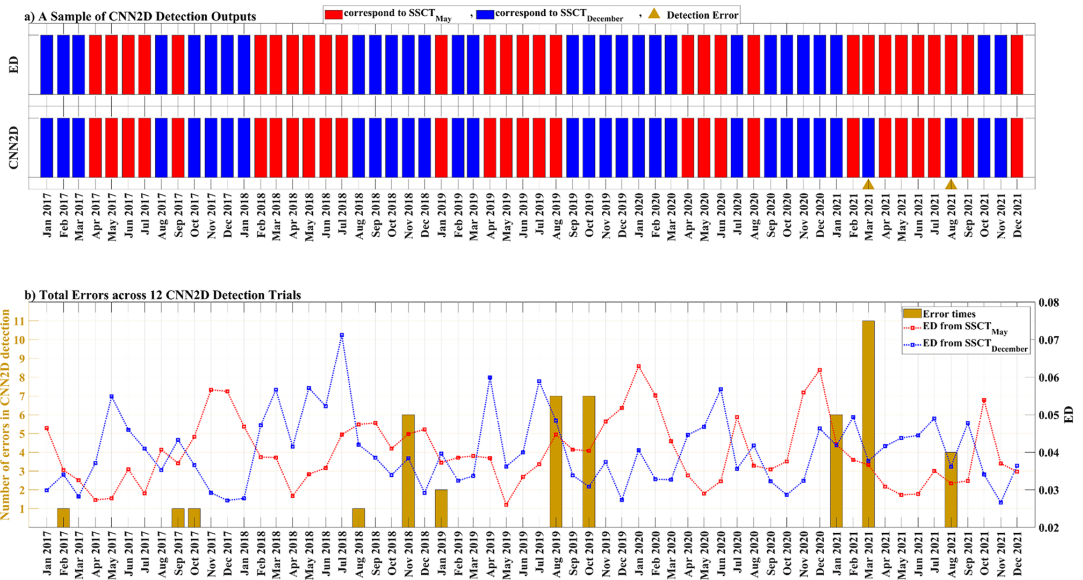


Figure 8. CNN2D results: (a) Comparison of the best trial's predicted results with the original SSCT. (b) Summary of CNN2D performance across all trials, indicating the number of errors per time instance and the corresponding EDs for each original SSCT.

Our analysis indicates that ageostrophic currents within the Baltic Sea can be directly driven by wind, as evidenced by their uniform direction with a ~90-degree deviation from the prevailing wind direction^{45,46}, contributing to an increased anticyclonic tendency in surface circulation patterns. Notably, the intensity of ageostrophic currents decreases from west to east, indicative of the varying influence of wind patterns across the Baltic Sea basin¹⁷. Our interpretation of the origins of ageostrophic currents in the Baltic Sea is further reinforced by observing their maximum intensity along the Swedish east coast and the Finnish coast⁴⁸. This pattern aligns with the expected dynamics of coastal upwelling events^{49,50}, where upwelled waters are horizontally driven towards offshore areas. Furthermore, similar to some previous studies, our analysis has revealed a consistent impact of these ageostrophic components as a share of total sea surface current^{51,52}.

Our investigation into the spatio-temporal variability of sea surface currents in the Baltic Sea reveals a predominant categorization into two distinct SSCTs, aligning closely with the mean SSCTs observed in May and December. Moreover, pairwise comparisons between monthly circulation patterns highlight the transitional role of March and September, serving as intermediary phases between the discernible SSCTs identified in May and December. Specifically, the May SSCT is mainly characterized by anticyclonic anomalies, with pronounced differences in circulation patterns across various Baltic Sea subregions. In contrast, December features heightened cyclonic anomalies in the direction of the prevailing circulations of the Baltic Sea. Similar seasonal tendencies are observed in both monthly geostrophic and ageostrophic current distributions and their anomalies, reinforcing the seasonal dominance of SSCT in the Baltic Sea. The frequency distribution of dominant SSCTs underscores the prevalence of strong circulations around autumn and weak circulations around spring, with transitional months exhibiting variability in SSCT dominance.

Despite variations in the intensity of the currents between May and December SSCTs, their directional patterns remain consistent, aligning with the semi-persistence of sea surface currents in the Baltic Sea⁵³. Cyclonic circulation predominates in the Bothnian Bay and Bothnian Sea, while anticyclonic circulation characterizes the Gulf of Finland and the Gulf of Riga. However, notable differences in gyre formations persist within the Baltic Proper. In the December SSCT, intensified currents extend from the southern Baltic Proper to the northern Baltic Proper through the eastern Baltic Proper. These currents merge with the outflow from the Gulf of Finland and Bothnian Sea before sharply turning southward in the western Baltic Proper (west of Gotland Island), forming a larger cyclonic gyre that covers the whole Baltic Proper. Conversely, in the May SSCT, where currents are weaker, the northward flow from the southern Baltic Proper turns southward along the eastern coast of Gotland Island, forming a cyclonic gyre in the eastern Baltic Proper. Simultaneously, dynamic interactions from the northern Baltic Proper induce an anticyclonic gyre in the western Baltic Proper. This results in the dominance of the May SSCT being characterized by a sea surface gyre dipole in the eastern and western Baltic Proper, a feature absent in the December SSCT. This finding aligns with previous studies that have examined the seasonal variability of the Baltic Sea inflow and outflow^{23,24}. Generally, the Baltic Sea inflows/outflows cause high/low sea level anomalies and large-scale meridional gradients in the warm/cold months^{55–57} that support weak and strong geostrophic currents. Also, high/low intensity of wind in the cold/warm months^{58,59} aligns with the strong/weak ageostrophic currents. In fact, the effect of inflow and outflow on sea level and wind distribution refers to how their intensifying and weakening can form different SSCTs in different seasons. While earlier research typically concentrated on water transport across various layers^{60,61}, our study has uncovered evidence suggesting that the integration of stronger inflows during colder months into surface layers consolidates into the eastern Baltic currents, reinforcing the December SSCT. By contrast, in the May SSCT, the strengthening of outflows weakens general cyclonic circulation of the Baltic Sea and lays a groundwork for the formation of anticyclonic circulation structures. This nuanced understanding underscores the dynamic interplay between seasonal inflows, outflows, and surface currents, enriching our comprehension of the complex hydrodynamics within the Baltic Sea.

The dominant SSCTs in the Baltic Sea exhibit a sophisticated nature for categorizing the sea surface circulation, especially during the transition months. This implies that being close to May or December in temporal terms does not guarantee an accurate prediction of the sea surface circulation pattern in the Baltic Sea. The results of the present study have shown that the ED can be an efficient and robust metric for SSCT classification in the Baltic Sea. Furthermore, the 2D convolutional neural network model is used for the feasibility study to detect the SSCT with only the potential drivers of wind and sla fields. However, due to the insights gained from the decomposition of total sea surface currents and the uncertainty regarding the origin of the ageostrophic component, the decision was made to exclude other oceanographic quantities or parameters, such as temperature and salinity⁶². This exclusion was deliberate, aimed at preventing any potential bias or artificial improvement in the network's predictive accuracy. Therefore, the constructed CNN2D architecture consists of several layers aimed at processing the spatio-temporal data of wind vectors and sla matrices in the Baltic Sea, accompanied by the fact that both geostrophic and ageostrophic components have important roles in the formation of total sea surface currents in the Baltic Sea.

The CNN2D outcomes demonstrate promising results for SSCT recognition, achieving high accuracy. However, it remains sensitive across different training trials for the network. This sensitivity arises from the complex interactions within the neural network during the training process, leading to different weight adjustments and, consequently, divergent classification results⁶³. Notably, the accuracy across the twelve CNN2D trials fluctuates between 2 and 5 errors each time among the 60 time-instances tested. The summation of errors across our twelve trials highlights that the discrepancies correspond to the time-instances when the ED of the sea surface current vector fields for both May and December SSCTs are close to each other. So, it can be concluded that if the wind and sea level distributions in the Baltic Sea are significantly different from the monthly mean climatology distributions, they can cause unusual patterns in the SSCT, which cannot be well categorized into the dominant SSCTs.

Our occlusion experiments revealed that neutralizing sla values while retaining u-wind and v-wind in our pre-trained CNN2D model resulted in a notable 12% increase in error for SSCT detection. Conversely, when either u-wind or v-wind was individually neutralized from the input batches, we observed significant variations in error rates, particularly concerning the meridional component of wind speed. Neutralizing u-wind led to an 8% increase in errors, whereas neutralizing v-wind resulted in a substantial 33% increase in errors. These findings underscore the critical role of wind-driven currents in shaping the different SSCTs.

It's important to note that our pre-trained model, utilizing all three inputs, aims to capture the spatial variability essential for SSCT recognition. However, it is well known that the spatial variability of these quantities, including sla and wind speed, in the Baltic Sea also exhibits a strong seasonal pattern^{64–66}. Therefore, these occlusion experiments results are not in conflict with our previous statements regarding the predominant impact of geostrophic currents over ageostrophic currents in the Baltic Sea. This could be the result of seasonal variations in the values of these three inputs, which correspond in such a way that they can partially compensate for

the absence of each other. However, they clearly underscore the significance of wind-driven currents in SSCT recognition.

Furthermore, we showed that the higher importance was assigned to the meridional component of winds compared to the zonal component. Previously, it has also been reported that changes in meridional winds were consistent with changes in upwelling frequency, further highlighting the importance of this wind component^{46,67}, emphasizing the significant influence of the north–south directionality of wind on Baltic Sea surface dynamics. This also corresponds with the ageostrophic current directional tendencies resulting in the present study. Given the dominance of southeasterly wind in the Baltic Sea, as well as the Ekman theory for deviation of potential wind-driven currents from wind direction, when zonal wind components dominate in the Baltic Sea, then wind-driven currents tend to be more south-ward than east-ward. However, our results for the monthly climatology of ageostrophic currents, as well as the long-term mean of them, showed an eastward tendency of ageostrophic currents in comparison to southward tendencies. This tendency is more observable in the northern sections of the Baltic Sea. This supports the conclusion that wind-driven currents play an important role in SSCTs within the Baltic Sea, with the north–south directionality of wind exerting more influence on circulation patterns.

Eventually, the high accuracy of our main trained model with the full set of inputs, along with the results from our occlusion experiments, supports the hypothesis that, particularly over long-term timescales like monthly averages and beyond, the sea surface ageostrophic component is primarily influenced by wind, with other expected factors being negligible in the ageostrophic stability of the Baltic Sea. In fact, these results suggest that the sea surface circulation fields in the Baltic Sea are predictable well with an AI model which is trained solely on wind and sea level data. Here, the gridded reanalysis database is given an initial insight in this regard. However, remote sensing datasets for both wind and sea level anomaly with reasonable accuracy and spatial resolution may have wonderful potential for the estimation of the sea surface currents in the ocean as well as in coastal and marginal seas⁶⁸. This insight can be useful for conducting future research into the importance of the application of AI in the Baltic Sea surface current and sea level dynamics.

Data availability

The initial datasets utilized in this study are publicly available and can be accessed from the following sources: 1—The sea level anomaly and total surface current from Baltic Sea Physics Reanalysis data are available at Copernicus Marine Service (<http://marine.copernicus.eu/>). 2—ERA5 wind data are available at Climate Data Store, Copernicus Climate Change Service (<https://cds.climate.copernicus.eu/>). All other datasets presented in this study are outcomes derived from the procedures outlined in the [Data and methods](#) section, and they can be replicated using the aforementioned data and the described methods in the manuscript. Additionally, all datasets generated in this study are available from the corresponding author upon request.

Received: 18 March 2024; Accepted: 5 August 2024

Published online: 12 August 2024

References

- Lagerloef, G. S. E., Mitchum, G. T., Lukas, R. B. & Niiler, P. P. Tropical Pacific near-surface currents estimated from altimeter, wind, and drifter data. *J. Geophys. Res. Ocean.* **104**, 23313–23326 (1999).
- Rio, M., Mulet, S. & Picot, N. Beyond GOCE for the ocean circulation estimate: Synergetic use of altimetry, gravimetry, and in situ data provides new insight into geostrophic and Ekman currents. *Geophys. Res. Lett.* **41**, 8918–8925 (2014).
- Hauser, D. *et al.* Satellite remote sensing of surface winds, waves, and currents: Where are we now? *Surv. Geophys.* **44**, 1357–1446. <https://doi.org/10.1007/s10712-023-09771-2> (2023).
- Dohan, K. Ocean surface currents from satellite data. *J. Geophys. Res. Ocean.* **122**, 2647–2651 (2017).
- Sudre, J., Maes, C. & Garçon, V. On the global estimates of geostrophic and Ekman surface currents. *Limnol. Oceanogr. Fluids Environ.* **3**, 1–20 (2013).
- Bonjean, F. & Lagerloef, G. S. E. Diagnostic model and analysis of the surface currents in the tropical Pacific Ocean. *J. Phys. Oceanogr.* **32**, 2938–2954 (2002).
- Dohan, K. & Maximenko, N. Monitoring ocean currents with satellite sensors. *Oceanography* **23**, 94–103 (2010).
- Sánchez-Realles, J. M., Vigo, M. I., Jin, S. & Chao, B. F. Global surface geostrophic ocean currents derived from satellite altimetry and GOCE geoid. *Mar. Geod.* **35**, 175–189 (2012).
- Sikhakolli, R. *et al.* Improved determination of Indian Ocean surface currents using satellite data. *Remote Sens. Lett.* **4**, 335–343 (2013).
- Wagner, T. J. W., Eisenman, I., Ceroli, A. M. & Constantinou, N. C. How winds and ocean currents influence the drift of floating objects. *J. Phys. Oceanogr.* **52**, 907–916 (2022).
- Röhrs, J. *et al.* Surface currents in operational oceanography: Key applications, mechanisms, and methods. *J. Oper. Oceanogr.* **16**, 60–88 (2023).
- Struve, H. *Über den Salzgehalt der Ostsee*. vol. 6 (Eggers, 1864).
- Sarkisyan, A. S., Staškiewicz, A. & Kowalik, Z. Diagnostic calculations of summer circulation in the Baltic Sea. *Okeanologiya* **15**, 1002–1009 (1975).
- Lehmann, A. & Hinrichsen, H.-H. On the wind driven and thermohaline circulation of the Baltic Sea. *Phys. Chem. Earth Part B Hydrol. Ocean. Atmos.* **25**, 183–189 (2000).
- Omstedt, A. & Axell, L. B. Modeling the variations of salinity and temperature in the large Gulfs of the Baltic Sea. *Cont. Shelf Res.* **23**, 265–294 (2003).
- Jędrasik, J., Cieślakiewicz, W., Kowalewski, M., Bradtke, K. & Jankowski, A. 44 Years Hindcast of the sea level and circulation in the Baltic Sea. *Coast. Eng.* **55**, 849–860 (2008).
- Lehmann, A. A three-dimensional baroclinic eddy-resolving model of the Baltic Sea. *Tellus A* **47**, 1013–1031 (1995).
- Meier, M. *First results of multi-year simulations using a 3D Baltic Sea model*. (SMHI, 1999).
- Meier, H. E. M. & Kauker, F. Modeling decadal variability of the Baltic Sea: 2. Role of freshwater inflow and large-scale atmospheric circulation for salinity. *J. Geophys. Res. Ocean.* **108**(C11), 3368. <https://doi.org/10.1029/2003JC001799> (2003).
- Elken, J. & Matthäus, W. Baltic Sea oceanography. *Assess. Clim. Chang. Balt. Sea Basin*, Ed. by BACC Author Team, Springer-Verlag, Berlin 379–386 (2008).

21. Meier, H. E. M. Modeling the pathways and ages of inflowing salt-and freshwater in the Baltic Sea. *Estuar. Coast. Shelf Sci.* **74**, 610–627 (2007).
22. Placke, M. et al. Long-term mean circulation of the Baltic Sea as represented by various ocean circulation models. *Front. Mar. Sci.* **5**, 287 (2018).
23. Jędrasik, J. & Kowalewski, M. Mean annual and seasonal circulation patterns and long-term variability of currents in the Baltic Sea. *J. Mar. Syst.* **193**, 1–26 (2019).
24. Maljutenko, I. & Raudsepp, U. Long-term mean, interannual and seasonal circulation in the Gulf of Finland—The wide salt wedge estuary or gulf type ROFI. *J. Mar. Syst.* **195**, 1–19 (2019).
25. Soosaar, E., Maljutenko, I., Raudsepp, U. & Elken, J. An investigation of anticyclonic circulation in the southern Gulf of Riga during the spring period. *Cont. Shelf Res.* **78**, 75–84 (2014).
26. Book, I.-I. G. C. & Contributors, O. D. GEBCO_2019 Grid.
27. Inc., T. M. MATLAB version: 9.13.0 (R2022b). <https://www.mathworks.com> (2022).
28. Rossby, C.-G. On the mutual adjustment of pressure and velocity distributions in certain simple current systems, II. *J. Mar. Res.* **1**, 239–263 (1938).
29. Veronis, G. Partition of energy between geostrophic and non-geostrophic oceanic motions. *Deep Sea Res.* **3**, 157–177 (1956).
30. Leppäranta, M. & Myrberg, K. *Physical Oceanography of the Baltic Sea* (Springer Science & Business Media, 2009).
31. Madec, G. et al. NEMO ocean engine. (2017).
32. Kärnä, T. et al. Nemo-Nordic 2.0: Operational marine forecast model for the Baltic Sea. *Geosci. Model Dev.* **14**, 5731–5749 (2021).
33. Panteleit, T., Verjovkina, S., Jandt-Scheelke, S., Spruch, L. & Huess, V. Baltic Sea production centre BALTICSEA_MULTITYEAR_PHY_003_011. *Innovation* **2**, 22–28 (2019).
34. Gill, A. E. *Atmosphere–Ocean Dynamics* Vol. 30 (Academic Press, 1982).
35. Arbic, B. K., Scott, R. B., Chelton, D. B., Richman, J. G. & Shriver, J. F. Effects of stencil width on surface ocean geostrophic velocity and vorticity estimation from gridded satellite altimeter data. *J. Geophys. Res. Ocean.* **117**, C03029. <https://doi.org/10.1029/2011JC007367> (2012).
36. Hersbach, H. et al. The ERA5 global reanalysis. *Q. J. R. Meteorol. Soc.* **146**, 1999–2049 (2020).
37. Agarap, A. F. Deep learning using rectified linear units (relu). *arXiv Prepr. arXiv1803.08375* (2018).
38. Jahanmard, V., Hordoïr, R., Delpeche-Ellmann, N. & Ellmann, A. Quantification of hydrodynamic model sea level bias utilizing deep learning and synergistic integration of data sources. *Ocean Model.* **186**, 102286 (2023).
39. Andersson, H. C. Influence of long-term regional and large-scale atmospheric circulation on the Baltic sea level. *Tellus A Dyn. Meteorol. Oceanogr.* **54**, 76–88 (2002).
40. Jevrejeva, S., Moore, J. C., Woodworth, P. L. & Grinsted, A. Influence of large-scale atmospheric circulation on European sea level: results based on the wavelet transform method. *Tellus A Dyn. Meteorol. Oceanogr.* **57**, 183–193 (2005).
41. Ekman, M. The changing level of the Baltic Sea during 300 years: A clue to understanding the Earth, Summer Inst. *Hist. Geophys. Al. Islands* (2009).
42. Lehmann, A., Höfllich, K., Post, P. & Myrberg, K. Pathways of deep cyclones associated with large volume changes (LVCs) and major Baltic inflows (MBIs). *J. Mar. Syst.* **167**, 11–18 (2017).
43. Omstedt, A. et al. Progress in physical oceanography of the Baltic Sea during the 2003–2014 period. *Prog. Oceanogr.* **128**, 139–171 (2014).
44. Lass, H. U. & Matthäus, W. On temporal wind variations forcing salt water inflows into the Baltic Sea. *Tellus A* **48**, 663–671 (1996).
45. Price, J. F., Weller, R. A. & Schudlich, R. R. Wind-driven ocean currents and Ekman transport. *Science (80-)*. **238**, 1534–1538 (1987).
46. Bierstedt, S. E., Hünicke, B. & Zorita, E. Variability of wind direction statistics of mean and extreme wind events over the Baltic Sea region. *Tellus A Dyn. Meteorol. Oceanogr.* **67**, 29073 (2015).
47. Liblik, T. et al. Quasi-steady circulation regimes in the Baltic Sea. *Ocean Sci. Discuss.* **2022**, 1–37 (2022).
48. Lehmann, A., Myrberg, K. & Höfllich, K. A statistical approach to coastal upwelling in the Baltic Sea based on the analysis of satellite data for 1990–2009. *Oceanologia* **54**, 369–393 (2012).
49. Haapala, J. Upwelling and its influence on nutrient concentration in the coastal area of the Hanko Peninsula, entrance of the Gulf of Finland. *Estuar. Coast. Shelf Sci.* **38**, 507–521 (1994).
50. Bednorz, E., Pórolniczak, M. & Tomczyk, A. M. Regional circulation patterns inducing coastal upwelling in the Baltic Sea. *Theor. Appl. Climatol.* **144**, 905–916 (2021).
51. Ubelmann, C. et al. Reconstructing ocean surface current combining altimetry and future spaceborne Doppler data. *J. Geophys. Res. Ocean.* **126**, e2020JC016560 (2021).
52. Lee, E. A. & Kim, S. Y. A diagnosis of surface currents and sea surface heights in a coastal region. *Cont. Shelf Res.* **226**, 104486 (2021).
53. Dietze, H. & Löptien, U. Effects of surface current–wind interaction in an eddy-rich general ocean circulation simulation of the Baltic Sea. *Ocean Sci.* **12**, 977–986 (2016).
54. Boulahia, A. K., García-García, D., Vigo, M. I., Trottni, M. & Sayol, J.-M. The water cycle of the Baltic Sea Region from GRACE/GRACE-FO missions and ERA5 data. *Front. Earth Sci.* **10**, 879148 (2022).
55. Hünicke, B. & Zorita, E. Influence of temperature and precipitation on decadal Baltic Sea level variations in the 20th century. *Tellus A Dyn. Meteorol. Oceanogr.* **58**, 141–153 (2006).
56. Lehmann, A. & Post, P. Variability of atmospheric circulation patterns associated with large volume changes of the Baltic Sea. *Adv. Sci. Res.* **12**, 219–225 (2015).
57. Lehmann, A. et al. Salinity dynamics of the Baltic Sea. *Earth Syst. Dyn.* **13**, 373–392 (2022).
58. Ruosteenoja, K., Vihma, T. & Venäläinen, A. Projected changes in European and North Atlantic seasonal wind climate derived from CMIP5 simulations. *J. Clim.* **32**, 6467–6490 (2019).
59. Najafzadeh, F., Kudryavtseva, N. & Soomere, T. Effects of large-scale atmospheric circulation on the Baltic Sea wave climate: application of the EOF method on multi-mission satellite altimetry data. *Clim. Dyn.* **57**, 3465–3478 (2021).
60. Dargahi, B., Kolluru, V. & Cvetkovic, V. Multi-layered stratification in the Baltic Sea: Insight from a modeling study with reference to environmental conditions. *J. Mar. Sci. Eng.* **5**, 2 (2017).
61. Raudsepp, U., Maljutenko, I., Barzandeh, A., Uiboupin, R. & Lagemaa, P. Baltic Sea freshwater content. *State Planet* **1**, 1–14 (2023).
62. Sinha, A. & Abernathy, R. Estimating ocean surface currents with machine learning. *Front. Mar. Sci.* **8**, 672477 (2021).
63. Maxwell, R. M., Condon, L. E. & Melchior, P. A physics-informed, machine learning emulator of a 2D surface water model: What temporal networks and simulation-based inference can help us learn about hydrologic processes. *Water* **13**, 3633 (2021).
64. Plag, H.-P. & Tsimplis, M. N. Temporal variability of the seasonal sea-level cycle in the North Sea and Baltic Sea in relation to climate variability. *Glob. Planet. Change* **20**, 173–203 (1999).
65. Medvedev, I. P. Seasonal fluctuations of the Baltic Sea level. *Russ. Meteorol. Hydrol.* **39**, 814–822 (2014).
66. Kahru, M., Elmgren, R. & Savchuk, O. P. Changing seasonality of the Baltic Sea. *Biogeosciences* **13**, 1009–1018 (2016).
67. Duthheil, C., Meier, H. E. M., Gröger, M. & Börgel, F. Understanding past and future sea surface temperature trends in the Baltic Sea. *Clim. Dyn.* **58**, 3021–3039 (2022).
68. Taburet, G. et al. DUACS DT2018: 25 years of reprocessed sea level altimetry products. *Ocean Sci.* **15**, 1207–1224 (2019).

Author contributions

A.B: Conducted calculations and analyses, visualized results, conceptualized the study, and drafted the original manuscript. Contributed to reviewing and editing the manuscript. I.M: Designed the study, provided advisory input on methodology, and contributed to reviewing and editing the manuscript. S.R: Designed the study, provided advisory input on methodology, and contributed to reviewing and editing the manuscript. P.L: Contributed to conceptualization and participated in reviewing and editing the manuscript. A.M: Contributed to conceptualization and participated in reviewing and editing the manuscript. R.U: Contributed to conceptualization and participated in reviewing and editing the manuscript. U.R: Designed the study, provided advisory input on methodology, visualized results, drafted the original manuscript, and contributed to reviewing and editing it.

Competing interests

The authors declare no competing interests.

Additional information

Supplementary Information The online version contains supplementary material available at <https://doi.org/10.1038/s41598-024-69463-8>.

Correspondence and requests for materials should be addressed to A.B.

Reprints and permissions information is available at www.nature.com/reprints.

Publisher's note Springer Nature remains neutral with regard to jurisdictional claims in published maps and institutional affiliations.

Open Access This article is licensed under a Creative Commons Attribution 4.0 International License, which permits use, sharing, adaptation, distribution and reproduction in any medium or format, as long as you give appropriate credit to the original author(s) and the source, provide a link to the Creative Commons licence, and indicate if changes were made. The images or other third party material in this article are included in the article's Creative Commons licence, unless indicated otherwise in a credit line to the material. If material is not included in the article's Creative Commons licence and your intended use is not permitted by statutory regulation or exceeds the permitted use, you will need to obtain permission directly from the copyright holder. To view a copy of this licence, visit <http://creativecommons.org/licenses/by/4.0/>.

© The Author(s) 2024

Appendix 3

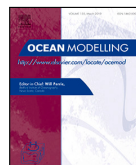
III

A. Barzandeh, I. Maljutenko, S. Rikka, and U. Raudsepp, “sciCUN: A deep learning model for daily sea surface current fields inference—a case study of the Gulf of Riga,” *Ocean Modelling*, vol. 201, p. 102693, 2026



Contents lists available at ScienceDirect

Ocean Modelling

journal homepage: www.elsevier.com/locate/ocemod

sciCUN: A deep learning model for daily sea surface current fields inference—A case study of the Gulf of Riga

Amirhossein Barzandeh ¹*, Ilja Maljutenko, Sander Rikka, Urmas Raudsepp

Department of Marine Systems, Tallinn University of Technology, Akadeemia tee 15a, Tallinn, 12618, Estonia

ARTICLE INFO

Keywords:

Sea surface current
CNN
U-net
Gulf of Riga

ABSTRACT

The precise forecasting of sea surface currents is essential for applications including navigation, pollution management, and ecosystem monitoring. Conventional high-resolution hydrodynamic models, such as NEMO, provide detailed short-term forecasts; however, they are computationally intensive and resource-demanding. To address these challenges, we introduce sciCUN: a deep-learning model for surface current inference using CNN-U-Net. As a case study, we used sciCUN to forecast daily current fields in the Gulf of Riga. During the training process, the model learns how the atmospheric forcing of the next day affects the fields of previous sea surface currents. sciCUN was trained from 1993 to 2019 and evaluated over a 4-year (2020–2023) prediction performance test. The results of the performance evaluations showed that somewhat less accurate predictions were mostly found in coastal regions close to river mouths and along the Baltic Sea border in the Irbe Strait, where, in contrast to hydrodynamic models, the data-driven modeling process did not apply boundary conditions. Nevertheless, sciCUN showed good predictive performance throughout its four-year testing period, achieving an average Euclidean distance of 2.30 cm/s between its prediction outputs and the original data. Furthermore, sciCUN obtained an average component-wise MAE of 1.45 cm/s and an average correlation coefficient of 0.92. sciCUN further demonstrated its ability to predict dominant daily surface current patterns through additional SOM analyses, using various clustering grid sizes to classify daily surface current maps into groups ranging from two to twelve prototypes. When the cluster size was reduced to two, focusing on the most dominant and distinctive patterns, sciCUN-predicted outputs achieved 97% accuracy in matching the correct cluster. By increasing the clustering grid size to categorize daily sea surface current maps into 12 prototypes, sciCUN still achieved 87% accuracy. Notably, most mismatches occurred between clusters whose prototypes exhibited closely resembling internal patterns. These results show that sciCUN is a computationally efficient and reliable way to emulate daily sea surface current forecasts.

1. Introduction

In general, surface ocean current data across broad spatial and temporal fields are derived primarily from satellite remote sensing and numerical modeling, supplementing limited direct measurements. Geostrophic currents are estimated from satellite altimetry using sea surface height gradients; the residual currents, defined as ageostrophic, are assumed to be dominated by wind-driven (Ekman) flow, which can be approximated from satellite-derived surface wind data (Dohan and Maximenko, 2010; J. M. Sánchez-Reales and Chao, 2012; Sudre et al., 2013). However, their precision decreases in coastal and semi-enclosed areas, where factors such as freshwater input, complex topography, and shallow subbasins significantly affect currents (Klemas, 2012; Laignel et al., 2023). In addition, sea surface current estimation, based on geostrophic and Ekman components, is more accurate

on longer timescales, such as weekly or monthly averages, where geostrophic components predominate. In contrast, shorter timescales, such as daily averages, display greater variability due to dynamic influences, including ageostrophic factors. These short-term fluctuations introduce significant instability, complicating precise current estimation (Griffiths et al., 1982; McWilliams, 2016; Lee and Kim, 2021; Ubelmann et al., 2021; Morales-Márquez et al., 2021). For short-term risk assessment (e.g., flood impacts), shorter-term averaged predictions provide actionable insights and avoid the oversimplification inherent in longer time frames. In this regard, the advantage of hydrodynamic ocean models lies in their ability to calculate the total sea surface current for extended spatial and temporal fields by incorporating all possible forcing mechanisms based on the solution of primitive equations. These models take into account complex interactions between

* Corresponding author.

E-mail address: amirhossein.barzandeh@taltech.ee (A. Barzandeh).

<https://doi.org/10.1016/j.ocemod.2026.102693>

Received 28 December 2024; Received in revised form 29 January 2026; Accepted 30 January 2026

Available online 30 January 2026

1463-5003/© 2026 Elsevier Ltd. All rights are reserved, including those for text and data mining, AI training, and similar technologies.

wind stress, Coriolis effects, pressure gradients, thermohaline processes, river discharge, etc., offering a more comprehensive representation of ocean dynamics. However, running fully resolved hydrodynamic simulations for high-resolution fields is computationally expensive and time-consuming, often necessitating the use of high-performance computing resources, and requires numerous inputs, such as more than ten atmospheric variables and complete initial and boundary conditions.

In recent years, deep learning techniques have emerged as a promising alternative to improve the accuracy and efficiency of predictive models for complex environmental phenomena (Zhao et al., 2024). Unlike hydrodynamic models, deep learning surrogate systems offer a more cost-effective approach to emulating specific ocean parameters and variables, as demonstrated by recent studies such as Minuzzi and Farina (2023), Liu et al. (2024), Durand et al. (2024). This is particularly advantageous in operational oceanography, where the focus is often on predicting a limited set of variables rather than generating the full suite of outputs required in traditional hydrodynamic models (Sonnewald et al., 2021; Dong et al., 2022). Once a deep learning model is trained, it can produce predictions of oceanic variable fields at an incomparable fraction of the computational cost associated with numerical simulations. These models bypass direct solving of physical equations by learning complex relationships between inputs, such as atmospheric variables, and outputs, such as sea surface currents (Grossi et al., 2020; Ouala et al., 2023; Xu et al., 2024a). This capability enables deep learning models to deliver rapid and targeted forecasts, making them highly effective for real-time operational applications. In addition, their adaptability makes them particularly valuable in regional oceanography, where they can efficiently update temporally limited datasets generated from previous research project outcomes, enhancing their utility for localized forecasting applications.

The Gulf of Riga (Fig. 1), a semi-enclosed sub-basin of the Baltic Sea, spans an area of 16,330 km², with average and maximum depths of approximately 26 and 60 m, respectively (Szaniawska, 2018). Situated between Latvia and Estonia (approximately 57.0° –58.5°N, 22.0° –24.5°E), its shallower nature compared to the Baltic Sea significantly influences its hydrodynamic behavior, making it highly susceptible to external environmental factors (Astok et al., 1999; Savchuk, 2002; Skudra and Lips, 2017). The Gulf's semi-enclosed structure, limited water exchange with the Baltic Proper and the Gulf of Finland, freshwater inflows from multiple rivers, and pronounced atmospheric impacts further contribute to the complexity of its upper-layer dynamics (Raudsepp, 2001; Najafzadeh et al., 2024). These dynamics are characterized by anisotropic wind conditions and highly variable sea surface currents (Astok et al., 1999; Lips et al., 2016a). Observational evidence further suggests that, in some nearshore settings, current variability may be dominated by wave-driven motions, with weak residual flow and highly intermittent velocity fluctuations (Eelsalu et al., 2025). Among the Baltic Sea sub-basins, the Gulf of Riga exhibits heightened sensitivity of surface-driven water redistribution to atmospheric forcing, accompanied by pronounced variability in sea level and frequent extremes (Pindsoo and Soomere, 2020; Weisse et al., 2021; Elken et al., 2024; Jahanmard et al., 2025). Within this variable setting, upper-layer circulation does not follow a single regime but instead reflects the superposition of multiple forcing mechanisms acting across scales. Spatially, a density-driven estuarine circulation pattern has been described, characterized by northward transport of buoyant freshwater along the eastern coast and a compensating southward subsurface flow of saltier water along the western slope (Yurkovskis et al., 1993). Superimposed on this background, spatially uniform wind forcing can induce depth-averaged topographic gyres with downwind coastal currents and return flow in the deeper central basin, while basin-scale topographic waves introduce cyclonic rotation of current vectors on synoptic timescales (Raudsepp et al., 2003). In addition, vertical structure modulates circulation in the Gulf of Riga during stratified periods and in localized features; however, basin-scale circulation is predominantly controlled by depth-averaged processes, making surface currents

an integrated response to multiple forcing mechanisms rather than an expression of strongly decoupled vertical dynamics. Seasonal stratification in the Gulf of Riga is primarily controlled by freshwater input and net air–sea heat fluxes, leading to the formation of a shallow halocline and thermocline during spring and summer (Stipa et al., 1999; Liblik et al., 2017). In contrast, autumn and winter are characterized by weak or absent stratification due to enhanced wind-driven mixing and surface buoyancy loss associated with cooling and increased vertical convection. The relatively shallow bathymetry promotes frequent vertical mixing events, limiting persistent vertical isolation between surface and bottom layers and enabling rapid adjustment of the water column to changing air–sea buoyancy forcing and momentum fluxes. Consequently, buoyancy-driven processes modulate circulation mainly on seasonal and regional scales, whereas short-term variability is strongly governed by atmospherically forced mixing and basin-scale adjustment (Köuts and Håkansson, 1995; Myrberg and Lehmann, 2013; Omstedt et al., 2014; Lehmann et al., 2022). Accordingly, sea surface circulation variability in the Gulf of Riga is expected to be associated with both atmospheric momentum forcing and thermodynamic air–sea exchanges, acting through their modulation of stratification and vertical mixing.

Temporal variations in the Gulf's sea surface currents, including seasonal shifts, are defined not only by fluctuations in intensity – alternating between periods of weakening and intensification – but also by transitions between mesoscale anticyclonic and cyclonic circulation modes (Soosaar et al., 2014; Lips et al., 2016b). At climatological scales, the upper-layer circulation in the Gulf of Riga is most often organized into basin-wide anticyclonic gyre structures, with relatively intensified currents along the southwestern rim, indicating a higher prevalence of anticyclonic conditions compared to cyclonic ones. On longer timescales, while geostrophic balance governs the dominant circulation patterns, the ageostrophic component contributes appreciably through seasonal modulation, influencing both coastal boundary regions and the central basin (Barzandeh et al., 2024). Superimposed on this mean state, the Gulf represents an eddy-active environment in which mesoscale eddies, typically 5–10 km in radius and persisting for a few days, generate recirculating pathways and enhance synoptic-to-daily variability. As a result, day-to-day sea surface currents can depart substantially from climatological patterns, reflecting the combined effects of transient atmospheric forcing, evolving sea-level gradients, and mesoscale eddy dynamics (Travkin et al., 2024). Additionally, freshwater inflows from multiple rivers, mainly along its eastern and southern boundaries, are critical in shaping the Gulf's surface currents and augmenting its distinctive physical characteristics. Notably, inflows from the Daugava River play a particularly significant role (Soosaar et al., 2016). These freshwater contributions, combined with spatial variations in sea surface circulation, produce diverse patterns across the Gulf, with distinct differences observed between the northern and southern areas as well as between the eastern and western regions (Suursaar et al., 2012; Maljutenko, 2019). The Gulf also features small inner islands that further complicate its hydrodynamics. These dynamic and variable behaviors collectively pose challenges for understanding and accurately predicting the Gulf's sea surface current patterns, necessitating advanced methodologies and comprehensive data integration. In addition, given the heavy vessel traffic between its shores and islands, a thorough understanding of the dynamics of the Gulf sea surface is crucial for operational purposes.

Building on the aforementioned concepts, this study aims to develop a surrogate model for predicting daily sea surface current fields in the Gulf of Riga, thereby reducing reliance on resource-intensive hydrodynamic model simulations. This surrogate model is intended to be designed within a deep learning framework, based on existing knowledge of the processes influencing surface circulation variability in the region, and mainly aims to showcase how efficient, variable-specific daily surface-current fields can be obtained by emulating only the target output (sea-surface current vectors, in our case) from a

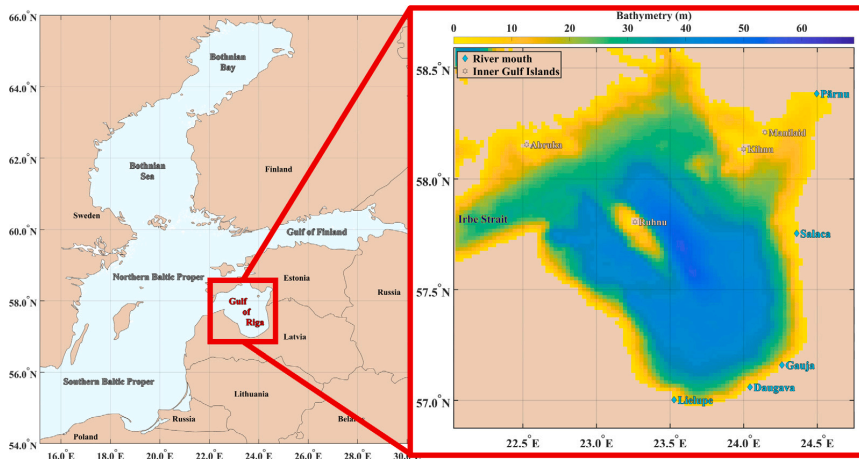


Fig. 1. Study area: The Gulf of Riga, including the inner islands and the locations of river mouths with high discharge, is illustrated.

limited set of relevant inputs, rather than running a full hydrodynamic model to resolve the complete ocean state. We hypothesize that atmospheric variables – momentum forcing (e.g., wind and mean sea level pressure) and thermodynamic forcing (e.g., air temperature and humidity) – act at the air–sea interface and may influence the background surface circulation state through pressure-gradient adjustment of the sea surface, upper-layer stratification and mixing, and associated potential ageostrophic flow components, particularly under conditions where coherent responses coincide with dominant atmospheric forcing fluctuations. Additional analyses are conducted to evaluate the model’s accuracy and enhance the understanding of sea surface current variability in the study area. The paper is organized as follows: Section 2 outlines the data and methodologies used to introduce the surrogate forecasting model; Section 3 presents the results and analyses; and Section 4 discusses the findings, the implications, and the opportunities for implementation.

2. Data and method

2.1. Sea surface current data

In this study, daily sea surface current maps have been extracted from the Baltic Sea reanalysis products, the Copernicus Marine Service (BalticSea Multiyear Phy 003 011, 2024). These maps are outputs from a hydrodynamic model based on the Nucleus for European Modelling of the Ocean (NEMO) 4.0 ocean modeling engine (Madec et al., 2017). Specifically, NEMO is configured for the North Sea and Baltic Sea as part of the Nemo-Nordic 2.0 system (Kärnä et al., 2021). The dataset spans from January 1993 to December 2023, with a spatial resolution of 1 nautical mile (≈ 1.852 km). Comprehensive validation details for this dataset are provided in Panteleit et al. (2023). Running hydrodynamic models such as NEMO is computationally intensive, and extending their simulations is equally expensive. This makes the dataset particularly valuable for studies in the Baltic region while simultaneously motivating the development of methods to update simulation results without incurring high computational costs. Therefore, this study treats the NEMO-produced CMEMS dataset as the original data for gridded sea surface current fields and explores its predictability. The zonal (u) and meridional (v) components of the original data were cropped to focus on the Gulf of Riga (longitude: 22°E to $\sim 24.5^\circ\text{E}$ and latitude: $\sim 57^\circ\text{N}$ to $\sim 58.5^\circ\text{N}$). The cropped area consists of 96 grid points along the longitude axis and 104 grid points along the latitude axis.

2.2. sciCUN model

2.2.1. sciCUN: Design rationale

In the rapidly evolving field of deep learning, convolutional neural networks (CNNs) and U-Net architectures have emerged as particularly effective tools for prediction, owing to their ability to capture and model intricate spatial patterns in multi-dimensional datasets (O’Shea and Nash, 2015; Ronneberger et al., 2015; Li et al., 2022). CNNs excel at extracting spatial features from structured inputs, potentially enabling the identification of complex relationships between target variables and their drivers. Furthermore, the U-Net architecture, with its encoder–decoder framework and integrated skip connections, facilitates hierarchical feature extraction while preserving fine-grained spatial details. This capability makes U-Net particularly well-suited for identifying and further simulating the complex spatial dynamics of ocean processes, ensuring reliable predictions for both scalar and vector fields, as demonstrated by recent studies such as Zhu and Zhang (2023), Xu et al. (2024b), Ren et al. (2024). Based on these potentials and capabilities, we propose a novel deep learning model for surface current inference using CNN-U-Net (sciCUN) to be able to forecast daily fields. In summary, the sciCUN architecture is designed to combine convolutional layers with U-Net’s encoder–decoder structure. To reduce computational complexity, the design intentionally avoids the inclusion of time-sequential prediction algorithms, such as long short-term memory (LSTM) networks. Instead, the model directly incorporates prior sea surface current fields into its input data; thus, the burden of prediction in time is also inherently placed on the shoulders of convolutional layers. This approach enables sciCUN to capture the spatial relationships between sea surface current fields from the previous day and their potential atmospheric drivers for the present day, facilitating the prediction of current fields for the present day. This design is inspired by the fundamental principles of hydrodynamic modeling, particularly the role of temporal derivatives in governing equations and their interactions with initial conditions. By embedding this physically meaningful concept into the preparation of input and output data, sciCUN seeks to emulate an essential aspect of ocean modeling for sea surface current inference, ensuring accurate and computationally efficient forecasts within a deep learning framework.

For the atmospheric drivers, five atmospheric variables with potential influence on sea surface current variability were selected: mean sea level pressure, zonal and meridional wind components (u-wind and v-wind), air temperature, and dew point temperature. These variables were chosen based on the hypothesis that mean sea level pressure and

wind fields can be related to the geostrophic components through their connection to sea level anomalies. Previous studies have also confirmed that sea level anomalies in the study area can be predicted using data-driven models based on atmospheric forcing, including variables such as wind and mean sea level pressure (Rajabi-Kiasari et al., 2023; Barzandeh et al., 2025). Additionally, their variability – along with air temperature and dew point temperature – reflects intricate dynamical and thermodynamical processes, including indirect associations with surface temperature and relative humidity, which can considerably influence the variability of the upper layer stratification and sea level fluctuation in the study area (Hordoir and Meier, 2012; Rajabi-Kiasari et al., 2025). These factors offer deeper insights into sea surface advective and diffusive processes, which are not solely governed by geostrophic stability in the short-term variability of the Baltic Sea and its subbasins' dynamical states (Liblik et al., 2022; Suursaar et al., 2022). Therefore, it is assumed that combining these atmospheric variables can effectively represent various aspects of total surface current variability within the data-driven emulation system, as they potentially exert direct and indirect influences on oceanic processes through air-sea interactions. However, all of these atmospheric variables have also been included in the input datasets of hydrodynamical modeling.

2.2.2. sciCUN: Data preparation

As mentioned in Section 2.2.1, sciCUN operates on the assumption that the sea surface current fields of the present day can be predicted using a combination of present-day atmospheric inputs, which drive current variability, and the previous day's sea surface current fields. The five selected atmospheric variables were extracted from the ERA5 global atmospheric reanalysis dataset (Hersbach et al., 2020), covering the period from 1993 to 2023. Daily means were calculated from the hourly data provided by the Copernicus Climate Change Service, Climate Data Store (Hersbach et al., 2023). These data were extracted for the study area and subsequently resampled using linear interpolation to match the spatial grid (1-nautical mile resolution) of the surface current data. To avoid the varying numerical ranges of the atmospheric variables, each variable was normalized as described in Eq. (1):

$$A_{\text{normalized}}(i, j, t) = 2 \cdot \frac{A(i, j, t) - \min_{i,j,t}(A)}{\max_{i,j,t}(A) - \min_{i,j,t}(A)} - 1, \quad (1)$$

where A represents each atmospheric variable, and $\min_{i,j,t}(A)$ and $\max_{i,j,t}(A)$ are the minimum and maximum values observed in the data record, respectively. Here, (i, j, t) denote the spatial and temporal indices of the variables across the study area and period. This normalization of atmospheric variable values ensures that inputs are well-scaled, allowing the model to learn efficiently without being influenced by variations in feature magnitudes. The sea surface current values were not normalized, as their numerical range was already within almost similar orders of magnitude. An initial analysis of the sea surface current revealed that the minimum and maximum observed values for the u -current (zonal component) were -0.78 m/s and $+0.61$ m/s, respectively. Similarly, the minimum and maximum observed values for the v -current (meridional component) were -0.65 m/s and $+0.89$ m/s. For the sea surface current data, the masked land areas were filled with zeros (representing no motion), whereas the atmospheric data retained values over land areas and therefore remained unchanged during masking.

To summarize, each input's time-instance to the model is a 3D tensor $\mathbf{X} \in \mathbb{R}^{96 \times 104 \times 7}$, where the spatial dimensions correspond to a gridded domain with height $H = 96$ and width $W = 104$. The seven input channels ($C_{\text{in}} = 7$) comprise the following variables: the zonal and meridional mean sea surface current components (u -current and v -current) from the previous day ($t-1$), defined as the vertically averaged currents over the 0–0.5 m surface layer available from the NEMO-based CMEMS reanalysis; the zonal and meridional wind components (u -wind and v -wind) at 10 m above sea level; mean sea level pressure; 2 m air temperature; and 2 m dew-point temperature for the present day (t), all obtained from the ERA5 atmospheric reanalysis.

2.2.3. sciCUN: Model architecture

The architecture of sciCUN, illustrated in Fig. 2, consists of four main components. The *Encoder* includes three encoder blocks with progressively increasing filters (32, 128, 256) to extract hierarchical features. The *Bottleneck* is a single convolutional block with 512 filters, serving as the bridge between the encoder and decoder. The *Decoder* comprises three decoder blocks with decreasing filters (256, 128, 32) to reconstruct spatial details. Finally, the *Output Layer* applies a convolutional operation followed by a regression layer to generate the final prediction. Each encoder block includes a two-dimensional convolutional layer (*Conv2D*) to apply filters for spatial feature extraction, a batch normalization layer (*BN*) to stabilize and accelerate training by normalizing the feature maps, a rectified linear unit (*ReLU*) activation function to introduce non-linearity, and a max-pooling layer (*MaxP2D*) that reduces spatial resolution by a factor of two, enabling the network to capture hierarchical features effectively (Lecun et al., 1998; Nair and Hinton, 2010; Ioffe and Szegedy, 2015). It should be noted that sciCUN has been fully designed, implemented and tested in MATLAB, utilizing its Deep Learning Toolbox (The MathWorks Inc., 2024).

For a sample block, the operations are described as follows:

Conv2D: The input feature map $\mathbf{X} \in \mathbb{R}^{H \times W \times C_{\text{in}}}$ is convolved with a set of filters $\mathbf{W} \in \mathbb{R}^{k \times k \times C_{\text{in}} \times C_{\text{out}}}$ of size $k \times k$ (in this study, $k = 3$), producing the intermediate output feature map:

$$\mathbf{Z}_{\text{Conv2D}} = \mathbf{W} * \mathbf{X} + \mathbf{b}, \quad (2)$$

where $*$ denotes the convolution operation, and $\mathbf{b} \in \mathbb{R}^{C_{\text{out}}}$ is the bias vector. The detailed mathematical expression for the convolution operation at each spatial position (i, j) and output channel c' is:

$$Z_{i,j,c'} = \sum_{m=1}^k \sum_{n=1}^k \sum_{c=1}^{C_{\text{in}}} W_{m,n,c,c'} \cdot X_{i+m-1,j+n-1,c} + b_{c'}, \quad (3)$$

where $Z_{i,j,c'}$ is the value of the intermediate output feature map at spatial position (i, j) and channel c' , $X_{i+m-1,j+n-1,c}$ is the value of the input feature map at spatial position $(i+m-1, j+n-1)$ and channel c , $W_{m,n,c,c'}$ is the filter weight connecting input channel c to output channel c' , and $b_{c'}$ is the bias term for output channel c' .

BN: The intermediate output $\mathbf{Z}_{\text{Conv2D}}$ is normalized to have zero mean and unit variance:

$$\mathbf{Z}_{\text{BN}} = \frac{\mathbf{Z}_{\text{Conv2D}} - \mu_{c'}}{\sigma_{c'}} \quad (4)$$

where μ is the mean of the feature map $\mathbf{Z}_{\text{Conv2D}}$, and σ is its standard deviation.

ReLU: A ReLU activation is applied element-wise to the normalized output:

$$\mathbf{Z}_{\text{ReLU}} = \max(0, \mathbf{Z}_{\text{BN}}), \quad (5)$$

MaxP2D: The spatial dimensions of the feature map are reduced by pooling the maximum value within non-overlapping windows of size $p \times p$ (in this study, $p = 2$) and stride s :

$$\mathbf{Z}_{\text{MaxP2D}}[i, j, c'] = \max_{(a,b) \in P} \mathbf{Z}_{\text{ReLU}}[i \cdot s + a, j \cdot s + b, c'], \quad (6)$$

where s is the stride of the pooling operation (default $s = p$), $(a, b) \in \{0, \dots, p-1\} \times \{0, \dots, p-1\}$, defining the pooling window relative to the top-left corner $(i \cdot s, j \cdot s)$ of the window. The processed output $\mathbf{Z}_{\text{MaxP2D}}$ is then passed to the next encoder block or bottleneck.

By focusing on the most prominent features within each pooling window, MaxP2D makes the network less sensitive to small translations or shifts in the input, enhancing its robustness to spatial variations. Simultaneously, it improves computational efficiency by reducing the spatial dimensions of the feature maps, which decreases the number of parameters and computations required in subsequent layers.

The decoder progressively reconstructs spatial information from the compressed feature representations generated by the encoder. To achieve this, each decoder block reverses the encoder's operations and

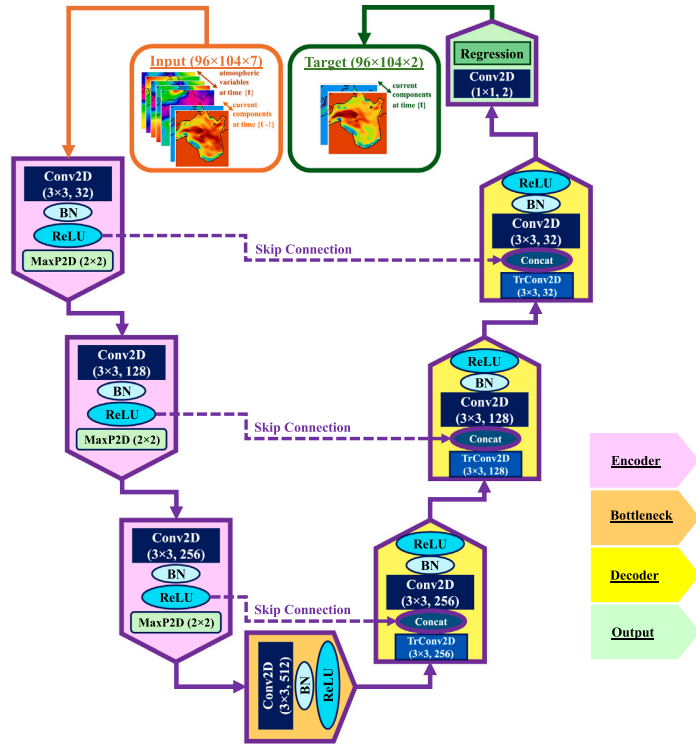


Fig. 2. sciCUN's architecture.

integrates additional spatial details through skip connections from the corresponding encoder blocks. During downsampling in the encoder (e.g., via MaxP2D), fine-grained spatial information is inevitably lost. Skip connections address this limitation by directly transferring high-resolution features from the encoder to the decoder. This preserves critical spatial details, such as edges and boundaries, enabling more accurate reconstruction. Each decoder block begins with a transposed convolutional layer (*TrConv2D*), which upsamples the feature maps, increasing their spatial resolution (Long et al., 2015):

$$\mathbf{Z}_{\text{TrConv2D}} = \mathbf{W}_{\text{TrConv2D}} * \mathbf{Z}_{\text{ReLU}_{\text{Decoder}}} + \mathbf{b}, \quad (7)$$

where $\mathbf{W}_{\text{TrConv2D}}$ represents the transposed convolutional filters.

This layer performs learnable upsampling while applying filters to refine the reconstructed features. Skip connections integrate features from the encoder by concatenating (*Concat*) the encoder features $\mathbf{Z}_{\text{ReLU}_{\text{Encoder}}}$ with the upsampled feature maps $\mathbf{Z}_{\text{TrConv2D}}$, reintroducing fine-grained spatial information lost during downsampling:

$$\mathbf{Z}_{\text{concat}} = \text{Concat}(\mathbf{Z}_{\text{ReLU}_{\text{Encoder}}}, \mathbf{Z}_{\text{TrConv2D}}). \quad (8)$$

In addition to preserving spatial resolution, skip connections enable effective multi-scale feature fusion by combining localized, high-frequency information from the encoder with the more global, contextual representations learned in deeper layers. This interaction allows the network to simultaneously capture large-scale circulation patterns and smaller-scale spatial variability, which is essential for accurately reconstructing sea surface current magnitude and direction. Furthermore, skip connections facilitate improved gradient propagation during backpropagation, enhancing training stability and reducing the risk of vanishing gradients in deeper architectures. A subsequent Conv2D layer refines the combined feature maps, followed by a BN layer to stabilize training and a ReLU activation to introduce non-linearity.

The final output layer applies a 1×1 convolution to map the reconstructed feature maps to the desired number of output channels (*u*-current and *v*-current), which represent the target variables. Following this, a regression layer predicts the sea surface current vector fields, including the *u*-current (zonal component) and *v*-current (meridional component), ensuring the outputs correspond to the physical quantities of interest:

$$\mathbf{Y} = \mathbf{W}_{\text{final}} * \mathbf{Z}_{\text{final}} + \mathbf{b}_{\text{final}}, \quad (9)$$

where $\mathbf{Y} \in \mathbb{R}^{96 \times 104 \times 2}$ represents the ultimate output (predicted *u*- and *v*-current fields), $\mathbf{Z}_{\text{final}}$ is the output of the last decoder block, $\mathbf{W}_{\text{final}}$ is the weight matrix of the regression layer, and $\mathbf{b}_{\text{final}}$ is the corresponding bias vector.

2.2.4. sciCUN: Training and testing

The training process for the model was designed to ensure optimal performance and computational efficiency. The training data spanned the period from January 2, 1993, to December 31, 2019, comprising 9860 instances. Model performance was validated by comparing the emulated sea surface currents to the original current data collected during the testing period. The model was trained using the Adam optimizer (Kingma and Ba, 2017). The initial learning rate was set to 5×10^{-4} , chosen to ensure gradual updates to model parameters, minimizing the risk of overshooting during optimization. The maximum number of epochs was set to 32 to balance computational cost and convergence. A mini-batch size of 16 was used to optimize GPU memory utilization while maintaining stable gradient updates. Data shuffling was performed at the beginning of each epoch to prevent temporal biases in the sequential data, ensuring the model learned representative patterns. Validation data was used during training to

monitor the model's generalization ability. Internal validation checks were performed every 16 iterations, allowing early detection of overfitting or performance degradation. For this internal validation, the data extracted from every 16th time instances of training data (in total 617 time instances). Real-time monitoring of the training progress was enabled through graphical plots of the loss and accuracy metrics. It is worth noting that the parameters in sciCUN were configured through several trial-and-error tests to achieve a level of manual optimization that makes it sufficient for its current performance needs.

2.3. sciCUN: Performance analysis

2.3.1. Quantitative validation metrics

Quantitative error metrics were employed to assess pointwise agreement between predicted and reference sea surface current fields. Differences between surface current vectors were quantified using the Euclidean distance, as shown in Eq. (10). This metric provides a single index for assessing the difference between two vectors and is expressed as:

$$\text{Euclidean distance}(i,j,t) = \sqrt{\left(u_{i,j,t}^o - u_{i,j,t}^m\right)^2 + \left(v_{i,j,t}^o - v_{i,j,t}^m\right)^2}, \quad (10)$$

Here, the superscripts o and m denote the original and modeled sea surface current vectors, respectively. This approach can be applied to a specific grid point across multiple timesteps to calculate the averaged distance for that point. Also, it can be spatially averaged across all available grid points in the original and modeled fields to produce a single index that quantifies the overall degree of deviation between two daily maps.

In addition, the separate validation metrics for the surface current components (u , v) in the present study include the Mean Absolute Error (MAE) and the Pearson correlation coefficient. MAE is given by Eq. (11):

$$\text{MAE}(i,j) = \frac{1}{n} \sum_{t=1}^n |c_{i,j,t,m} - c_{i,j,t,o}|, \quad (11)$$

where n represents the total number of time instances, and c refers to either u or v component. Correlation coefficient also is defined by Eq. (12):

$$\text{Correlation}(i,j) = \frac{\sum_{t=1}^n \left(c_{i,j,t,m} - \bar{c}_{i,j,m}\right) \left(c_{i,j,t,o} - \bar{c}_{i,j,o}\right)}{\sigma_{c_{i,j,m}} \sigma_{c_{i,j,o}}}. \quad (12)$$

where $\bar{}$ and σ are the mean and standard deviation (STD) operators, respectively.

2.3.2. Qualitative pattern-based evaluation using SOM

To complement the quantitative evaluation, a Self-Organizing Map (SOM) was employed as a qualitative, pattern-based diagnostic of daily sea surface current fields. SOM is an unsupervised machine learning algorithm that projects high-dimensional data onto a low-dimensional topological grid while preserving neighborhood relationships in the input space (Vesanto and Alhoniemi, 2000; Hewitson and Crane, 2002; Kohonen, 2013). The SOM analysis was conducted using MATLAB R2024a and the Deep Learning Toolbox™.

Previous studies such as Liu and Weisberg (2005), Liu et al. (2016), Dey et al. (2023) have demonstrated the effectiveness of SOM in identifying characteristic patterns in sea surface current vector fields. In shallow and semi-enclosed basins such as the Gulf of Riga, daily sea surface currents exhibit substantial variability due to the combined effects of atmospheric forcing, basin geometry, and mesoscale dynamics. In such contexts, pattern-oriented analyses provide insight into circulation regimes and spatial coherence that are not explicitly captured by pointwise error metrics.

In this study, SOM was applied as a post-processing diagnostic to evaluate whether sciCUN reproduces dominant circulation patterns observed in the reference dataset. The SOM analysis was performed

over the testing period, which consists of $n = 1461$ (2020–2023) daily sea surface current fields. The horizontal model grid (i,j) has dimensions 96×104 , of which only 5243 grid points correspond to sea surface locations after land masking. These sea surface points are indexed by

$$s = 1, \dots, 5243.$$

Let $u_{s,t}$ and $v_{s,t}$ denote the zonal and meridional sea surface current components at sea surface index s and time t . For SOM analysis, each daily sea surface current field was reshaped into a one-dimensional representation by concatenating the velocity components at all sea surface points, with the zonal component followed immediately by the meridional component. Each daily field therefore consists of $10486 = 2 \times 5243$ scalar values.

The SOM input data are collected in a single matrix \mathbf{D} , defined as

$$\mathbf{D} = \begin{bmatrix} u_{1,1} & v_{1,1} & u_{2,1} & v_{2,1} & \cdots & u_{5243,1} & v_{5243,1} \\ u_{1,2} & v_{1,2} & u_{2,2} & v_{2,2} & \cdots & u_{5243,2} & v_{5243,2} \\ \vdots & \vdots & \vdots & \vdots & \ddots & \vdots & \vdots \\ u_{1,1461} & v_{1,1461} & u_{2,1461} & v_{2,1461} & \cdots & u_{5243,1461} & v_{5243,1461} \end{bmatrix}, \quad (13)$$

where each of the 1461 rows corresponds to one daily sea surface current field and contains 10486 scalar values, representing the spatially sampled zonal and meridional currents at all sea surface grid points.

Given the input matrix \mathbf{D} , SOMs with one-dimensional topological grids of size $m \times 1$ ($m = 2, \dots, 12$) were trained to obtain a set of prototype (codebook) vectors, defined as

$$\{\mathbf{w}_k \in \mathbb{R}^{10486} \mid k = 1, \dots, m\}, \quad (14)$$

where each prototype \mathbf{w}_k represents a characteristic circulation regime. For each day t , the best-matching unit (BMU), denoted by $\epsilon(t)$, was defined as the index of the prototype that minimizes the Euclidean distance to the corresponding daily input field,

$$\epsilon(t) = \arg \min_{k \in \{1, \dots, m\}} \|\mathbf{D}_{t,:} - \mathbf{w}_k\|_2, \quad (15)$$

where $\mathbf{D}_{t,:}$ denotes the t th row of the input matrix \mathbf{D} .

The SOMs were trained using a batch learning scheme on one-dimensional hexagonal topologies, in which prototype vectors are updated once per training epoch based on the aggregated influence of all daily samples. This approach provides stable convergence and is well suited for high-dimensional circulation fields, where robust extraction of dominant spatial patterns is preferred over sensitivity to individual realizations.

After training, each prototype vector \mathbf{w}_k was reshaped back into sea surface fields $u_s^{(k)}$ and $v_s^{(k)}$, which were then mapped back onto the original 96×104 horizontal grid. These prototypes represent condensed circulation regimes and enable qualitative assessment of spatial coherence, regime similarity, and temporal variability. By comparing the SOM-based regime assignments of reference and sciCUN-predicted fields, this analysis evaluates whether sciCUN preserves physically meaningful circulation structures, even in the presence of localized magnitude or directional differences. To directly connect SOM diagnostics to sciCUN performance, the SOM is trained using the reference fields, and the resulting prototypes are then used to assign each reference and sciCUN-predicted daily map to a best-matching unit. Agreement is quantified by the fraction of days for which the sciCUN-predicted map is assigned to the same prototype as the corresponding reference map.

3. Results

3.1. Quantitative assessment of sciCUN performance

Fig. 3 illustrates the daily averaged performance of sciCUN over the 4-year testing period (2020–2023), evaluated using three primary metrics: correlation, MAE, and the difference in standard deviations (STDs)

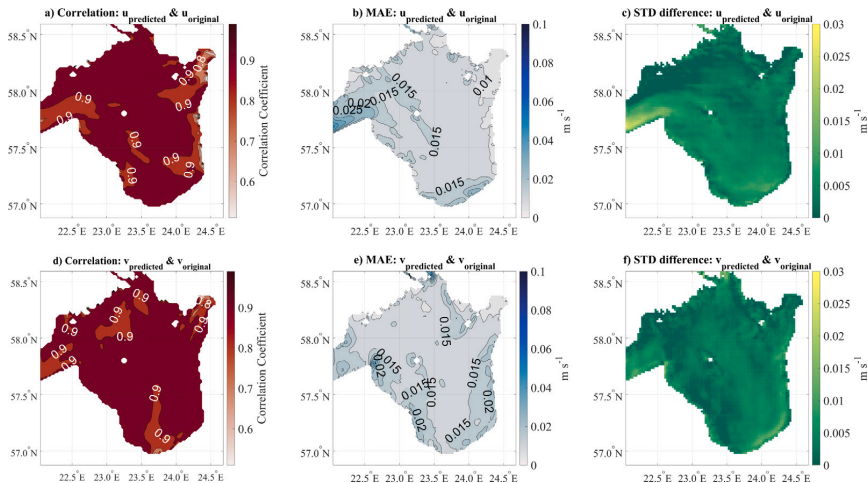


Fig. 3. Component-wise performances of sciCUN.

between the original surface current data and the sciCUN-predicted outputs. These metrics are analyzed separately for the u -current and v -current components. The correlation distribution maps (Fig. 3, panels a and d) highlight regions of strong alignment between the modeled and observed sea surface currents. High correlation values (> 0.9) indicate that sciCUN effectively captures daily fluctuations of surface currents across much of the domain. However, lower correlation values are noted in the coastal area near the river mouths and also near the western entrance to the Gulf of Riga – the Irbe Strait – reflecting reduced performance in these boundary areas. For the u -component, a more significant drop in correlation is observed along the eastern coastline, indicating reduced agreement in these localized regions. Despite these declines, correlation values generally remain above 0.8 and 0.7, indicating that sciCUN reproduces substantial day-to-day variability even where performance is lower.

Spatially averaged correlation values for the u - and v -components (panels a and d) are 0.916 and 0.923, respectively. The MAE distribution maps (Fig. 3, panels b and e) indicate that most of the domain exhibits an MAE below 0.020 m/s. However, slightly higher MAE values, reaching up to 0.030 m/s, are observed in coastal regions, around the inner islands, and near the Irbe Strait, indicating larger local deviations from the original data. The spatially averaged MAE values for the u - and v -components are 0.014 m/s and 0.015 m/s, respectively. The STD difference distribution maps (Fig. 3, panels c and f) reveal that most of the domain exhibits a standard deviation difference below 0.010 m/s. These findings indicate that sciCUN reproduces the spatial distribution of variability in sea surface currents, with only minor discrepancies in specific coastal and boundary regions. Spatially averaged STD differences are 0.004 m/s for the u -component and 0.003 m/s for the v -component.

Fig. 4 shows the spatial distribution of the daily averaged Euclidean distance between the original data and the sciCUN-predicted outputs. This metric quantifies the spatial discrepancy in both current magnitudes and directions, averaged over the entire testing period. Lower Euclidean distance values signify a closer alignment between the modeled outputs and the original data in terms of speed and direction. The results reveal strong sciCUN performance, with Euclidean distance ranging from 0.010 to 0.040 m/s. The spatially averaged value for Fig. 4 is 0.023 m/s. Regions with the lowest Euclidean distances are primarily located in the central and northern areas of the domain. In contrast, regions with higher Euclidean distances, particularly in the Irbe Strait, around nearby islands, and along coastal boundaries where

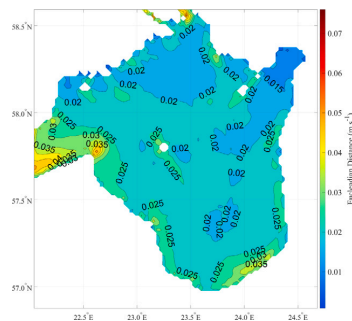


Fig. 4. Spatial distribution of Euclidean distances for the performance of sciCUN.

river mouths are located, indicate locations of larger magnitude and/or directional differences between sciCUN predictions and the original fields.

Fig. 5 illustrates the temporal distribution of the daily averaged Euclidean distance between the original data and the sciCUN outputs. The results indicate that the 91st percentile of the daily Euclidean distance series is 0.03 m/s, with rare instances reaching as high as 0.061 m/s. The minimum Euclidean distance can drop below 0.012 m/s. In addition, higher Euclidean distances are generally associated with summer dates.

To further evaluate sciCUN’s performance, Fig. 6 presents three cases of prediction results for distinct days. The left panels depict the original fields, while the right panels show the corresponding predictions. Fig. 6a illustrates the day with the highest spatially averaged Euclidean distance between sciCUN predictions and the original data, which occurred on June 30, 2020, as highlighted in Fig. 5. Fig. 6b corresponds to April 15, 2023, when the highest recorded current speeds in the original fields were observed. Finally, Fig. 6c depicts July 30, 2021, when the spatially averaged current speed fields reached their maximum.

As defined in Eq. (10), Euclidean distance serves as a metric for evaluating the differences between vectors, accounting for both magnitude and directional discrepancies. In Fig. 6a, the predicted current vector directions on June 30, 2020, closely resemble the original fields,

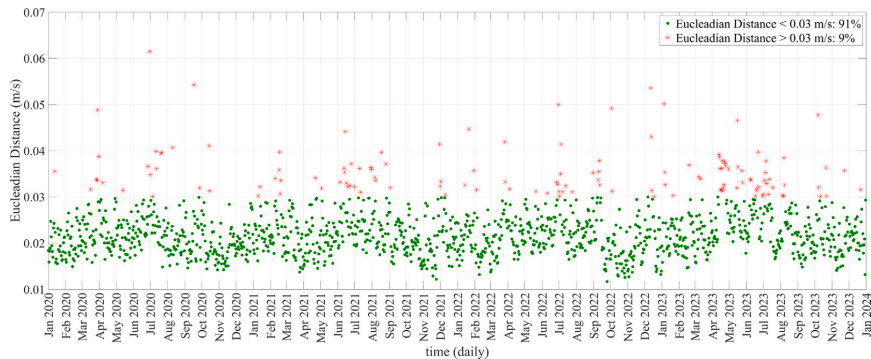


Fig. 5. sciCUN performances temporal distribution.

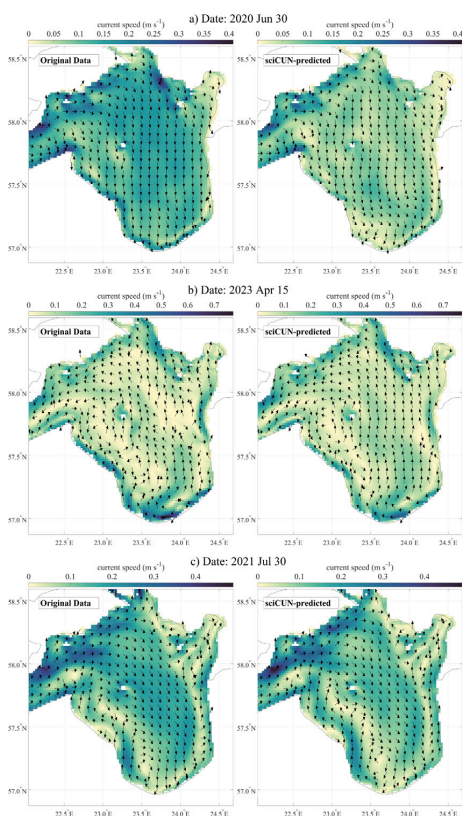


Fig. 6. Sample cases of sciCUN daily forecasts: the day with the highest averaged Euclidean distance between predictions and original data, the day with the highest recorded surface current speed in the original fields, and the day with the highest spatially averaged current speed in the original fields.

while current magnitudes are underestimated in parts of the domain. However, the current speeds were significantly underestimated in the sciCUN results. While this case represents a rare instance of exaggerated underestimation, as shown in Fig. 5, the overall circulation structure remains similar between the original and predicted fields. In contrast, Figs. 6b and 6c demonstrate highly accurate predictions of the maxima

of the current fields, capturing both speed and direction with precision with spatially averaged Euclidean distances of 0.036 m/s in both cases. These results confirm that the rare high Euclidean distance observed on June 30, 2020, was not indicative of a common issue with sciCUN but rather probably a specific anomaly in the input data for that particular day. These three examples span both typical and upper-tail error conditions within the testing period.

3.2. Pattern-based evaluation using SOM

To complement the quantitative validation metrics, this study employed SOM analysis to classify the original sea surface current fields during the testing period. Here, SOM is used as a regime-based verification of sciCUN by comparing prototype assignments of sciCUN-predicted and reference daily fields for the same dates. Subsequently, the trained SOM clustering networks were applied to the sciCUN-produced outputs to assess how well the sciCUN daily predictions fit into the correct clusters. To gain deeper insights into the variability of the original sea surface currents, the SOM was applied 11 times, starting with a 2×1 grid structure (2 clusters) and progressively increasing to a 12×1 grid structure (12 clusters). Fig. 7 presents the SOM clustering results and their averaged accordance with the original fields, represented as the radius of each prototype's fluctuation on the topological space of data variability. The average Euclidean distance between each SOM cluster prototype maps and their corresponding surface current maps within the cluster decreases as the number of assigned clusters increases, since a larger number of clusters results in more detailed prototypes. This distance reduces from 0.056 m/s for 2 clusters (2×1 SOM grid structure) to 0.044 m/s for 12 clusters (12×1 SOM grid structure). For each SOM configuration, the trained SOM network was applied to the sciCUN-produced daily fields to determine how often the outputs were assigned to the correct clusters. The percentage of correct assignments decreased slightly with an increasing number of clusters, from 97% for 2 clusters (2×1 SOM grid structure) to 87% for 12 clusters (12×1 SOM grid structure).

SOM prototypes for 2 clusters (Fig. 8a) and 12 clusters (Fig. 8b) provide additional detail on dominant circulation regimes represented in the original dataset. The prototypes are labeled according to the SOM configuration and the number of clusters; for instance, when SOM is applied with grid dimensions of (2×1), the prototypes are referred to as SOM 1 and SOM 2. The percentages shown in Fig. 8 are rounded and represent the frequency of occurrence for each prototype. In Fig. 8a, where 2 prototypes are used, the surface currents in the Gulf of Riga are broadly characterized by flow patterns entering/exiting and exiting/entering through the western/northern entrance, combined with internal circulation toward the eastern and western regions. There are also some mesoscale cyclonic and anticyclonic features inside each

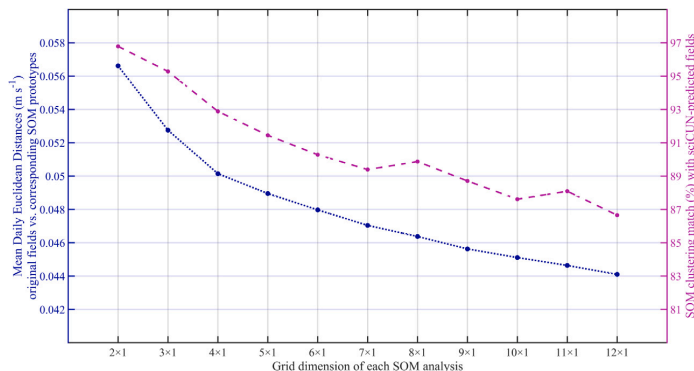


Fig. 7. SOM clustering performance compared with the original fields (left y-axis) and the performance of sciCUN outputs in being assigned to the correct clusters (right y-axis).

map. By increasing the number of clusters to 12 (Fig. 8b), the prototypes provide a more detailed representation of current dynamics, capturing finer variations in speed and direction. Distinct inlet and outlet patterns are captured in the Irbe Strait between its northern and southern sections. Within the Gulf, the curvature of currents varies significantly, accompanied by coastal currents with diverse directional tendencies. Additionally, the spatial variability of current intensity and the signatures of mesoscale cyclonic and anticyclonic features differ among the prototypes. These variations further underscore the complex nature of surface current vector variability in the Gulf of Riga, making them more challenging to predict.

Besides, Figs. 9a and 9b illustrate the daily variability in the occurrence of SOM application prototypes for the (2 × 1) and (12 × 1) cases. Notably, neither figure reveals distinct temporal patterns governing the occurrence of each current prototype. This absence of discernible temporal regularity further underscores the complexity of daily variability in the sea surface current fields of the Gulf of Riga.

Furthermore, we assessed the mismatch distribution in clustering for the SOM analysis with a 12 × 1 grid structure, where the highest mismatches were reported (Fig. 7). Considering the 1461 time instances in the testing period, 87% correctness indicates that approximately 160 time instances could have been better predicted to align with the correct cluster. Fig. 10 primarily reveals that the mismatch frequency was higher between clusters with similar prototypes. For instance, the highest mismatches occurred between the 9th and 10th prototypes (SOM 9 and SOM 10). Looking back to Fig. 8b shows that both SOM 9 and SOM 10 include general circulation patterns of discharge from the Irbe Strait and inlet from the northern entrance, with slight differences in coastal current patterns and southwestward current curvatures. These slight differences are also evident in other hotspots of mismatches, such as between SOM 9, SOM 10 and SOM 11 (where the current patterns predominantly indicate outlet flow through the Irbe Strait, with slight variations in internal basin direction, ranging from southward to eastward tendencies), or SOM 2, SOM 5 and SOM 6 (where the current patterns mainly represent inlet flow through the Irbe Strait, with minor directional deviations within the basin from northward to westward tendencies). By "slight differences", we mean that the variations of current vectors between these prototypes are significantly smaller than those in between other clusters. This suggests that even prediction with errors are still provide close representation to the actual surface circulation patterns. Overall, mismatches occur primarily between prototypes with more similar internal circulation structures. This behavior indicates that most SOM "errors" correspond to confusion among closely related regimes, rather than assignment to fundamentally different circulation patterns. In this way, SOM agreement complements the pointwise metrics by confirming that sciCUN preserves the dominant daily circulation structures even when localized vector differences exist.

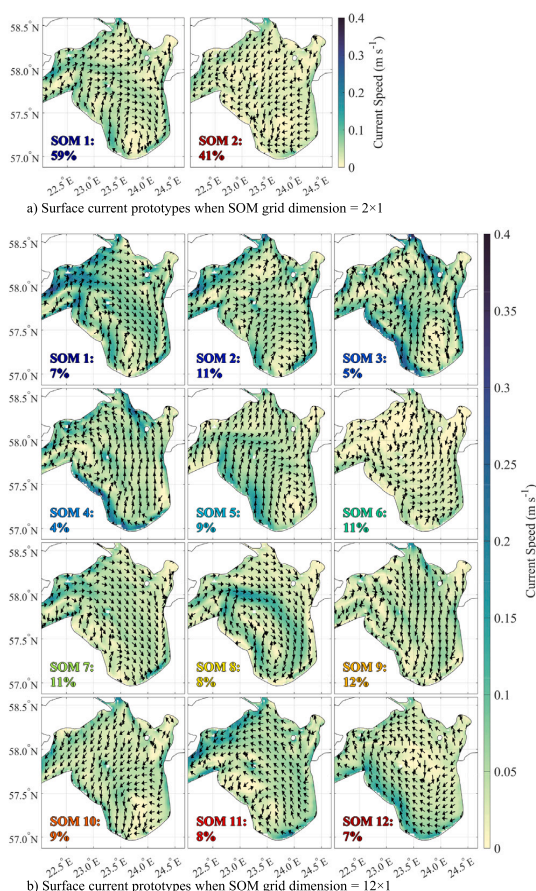


Fig. 8. Differences in SOM prototypes for a 2 × 1 grid structure and a 12 × 1 grid structure. Each prototype represents a distinct cluster of sea surface currents, demonstrating the unique and dominant circulation patterns within the original dataset. For better visibility of vector directions, they are illustrated at every fourth grid point with uniform size.

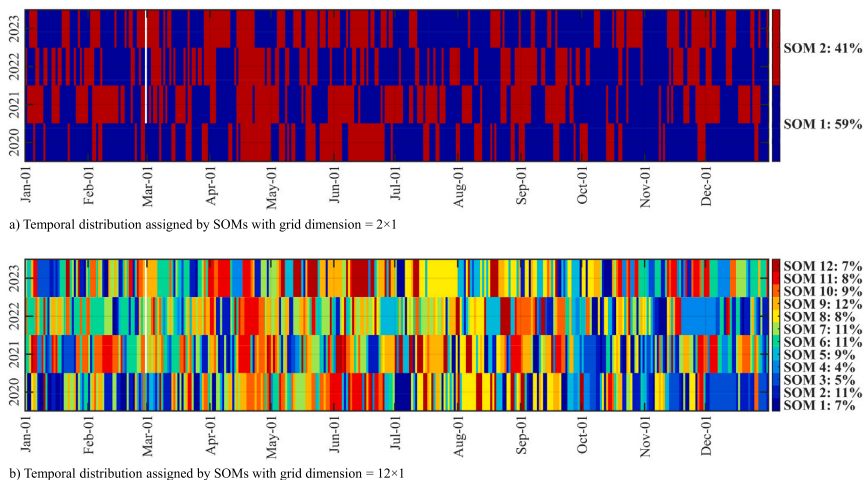


Fig. 9. Temporal distribution of clustering assignments from SOM prototypes with a 2 × 1 grid structure and a 12 × 1 grid structure.

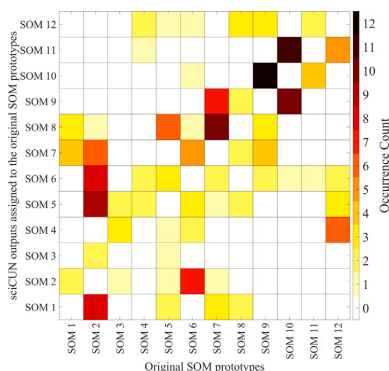


Fig. 10. Frequency of mismatches in SOM cluster assignments when applied to the sciCUN outputs, illustrating deviations from patterns inside the original Data.

3.3. Case study of consecutive-day surface current evolution

As a final case study for benchmarking sciCUN’s performance in predicting daily variability of sea surface current patterns, Fig. 11 presents predictions for four consecutive days in September 2023 (16–19 September). For each day, the left panels show the original sea surface current fields, while the right panels display the corresponding sciCUN predictions. The spatially averaged Euclidean distances for these four days are 0.022 m/s, 0.021 m/s, 0.021 m/s, and 0.028 m/s, respectively, indicating consistently low prediction errors.

On 16 September (Fig. 11a, left panel), eastward currents enter the Gulf of Riga from the northern part of the Irbe Strait. Part of this inflow turns northward, while the remaining currents merge with coastal flows, initiating the formation of a mesoscale anticyclonic eddy in the central gulf. The corresponding sciCUN prediction (right panel) successfully reproduces both the magnitude and direction of these currents.

A pronounced shift in circulation occurs on the following day (17 September; Fig. 11b, left panel), when currents in the northern region reverse direction and flow southward into the Gulf of Riga, accompanied by stronger discharges from the southern part of the Irbe Strait.

At the same time, the anticyclonic eddy formed on the previous day further intensifies in the central basin. The sciCUN prediction accurately captures these contrasting dynamics, demonstrating its ability to represent abrupt changes in current direction and intensity.

The current fields from 16 September served as part of the input for predicting the circulation on 17 September, illustrating that sciCUN effectively exploits the combination of atmospheric forcing and prior-day current information to reproduce the evolving circulation state. This behavior is consistent with the design of the model and its intended emulation of temporal dependencies.

Similar performance is observed for 18 and 19 September (Figs. 11c and 11d), during which the circulation patterns differ substantially from the preceding days due to variations in inlet–outlet dynamics and basin-scale mesoscale features. Despite these changes, sciCUN consistently reproduces the main spatial structures and variability of the sea surface currents, indicating stable performance under rapidly evolving circulation conditions.

4. Discussion

In general, the insights gained from the results of this study highlight the potential of sciCUN for operational applications (Röhrs et al., 2023). In operational settings, the model can serve as an efficient tool for predicting sea surface currents with high accuracy, enabling timely and informed decision-making in various marine activities. The results in Section 3 show that sciCUN achieves consistently low emulation errors relative to the magnitude and variability of sea surface currents in the Gulf of Riga. During the testing period, temporally averaged daily current speeds reached up to 0.180 m/s, while instantaneous currents at individual grid points occasionally exceeded 0.75 m/s. In this context, the spatially averaged Euclidean distance of 0.023 m/s – with 91% of daily values below 0.03 m/s – represents only a small fraction (approximately 10%) of both mean and upper-bound current magnitudes. Consistently, sciCUN attains high predictive skill, with component-wise average correlation coefficients of 0.92, MAE on the order of 10^{−2} m/s, and standard deviation differences below 0.005 m/s, indicating that both the amplitude and temporal variability of the surface current components are well captured.

Localized discrepancies in sciCUN predictions are most apparent near coastal boundaries and at the western entrance of the Gulf of Riga, particularly the Irbe Strait, indicating regions of reduced model accuracy. These errors are primarily associated with boundary-driven

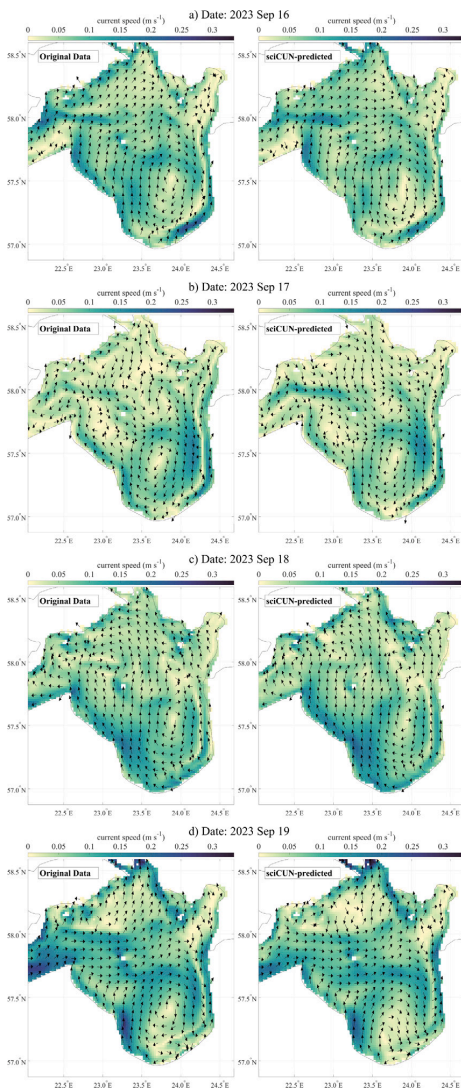


Fig. 11. sciCUN daily forecast cases from September 16 to September 19, 2023.

processes that are not explicitly represented in sciCUN, as the model relies on relationships between prior-day surface currents and contemporaneous atmospheric forcing while neglecting additional boundary-related drivers such as river discharge and advective exchanges with adjacent basins. In particular, substantial freshwater inflows from major rivers along the southern and eastern coasts of the Gulf of Riga, including the Daugava and Pärnu Rivers, can generate localized density gradients and stratification during high-discharge periods, thereby altering circulation patterns within the basin (Suursaar et al., 2002; Yurkovskis, 2004; Soosaar et al., 2016). As shown in Fig. 5, higher Euclidean distances – indicating reduced sciCUN prediction accuracy – are more pronounced during the warmer months, consistent with the seasonal cycle of freshwater content in the Gulf of Riga, which is lowest in winter and peaks in summer (Raudsepp et al., 2023). These freshwater impacts can propagate to adjacent areas, depending on the

magnitude and persistence of the outflows, and may interfere with predictions based solely on atmospheric drivers. Moreover, the primary exchange of water between the Gulf of Riga and the Baltic Proper occurs through the Irbé Strait (Lilover et al., 1998; Väli et al., 2024). This interaction introduces additional variability, particularly during events of anomalous inflows from the Baltic Proper, which are not explicitly accounted for in sciCUN’s input data. These boundary-driven processes, especially under irregular conditions, can further complicate predictions by altering the coastal and basin-wide current systems. Therefore, it can be stated that while sciCUN’s architecture is designed to emulate temporal derivatives and forcing interactions within the hydrodynamic model, it does not explicitly account for the effects of spatial derivatives at boundaries. Capturing these dynamics – particularly the interactions between boundary conditions and basin-wide processes – may require enhancements in future iterations of the model, such as incorporating additional drivers or refining the representation of boundary-related spatial derivatives. For the present study, this challenge was compounded by the inherently inconsistent data structure it creates. In hydrodynamic models, rivers are typically inserted into only a limited number of grid points, yet the complex mathematical processes in these models generalize such localized effects to neighboring grid points over time. Similarly, at basin boundaries, even small perturbations along hypothetical boundary lines can amplify and propagate into significant spatial variations in the basin’s flow dynamics. Consequently, the primary challenge lies in reconciling input and target data with mismatched dimensions. As a result, the model exclusively utilizes input data that can be dimensionally matched to the target data, ensuring that each prediction target point is paired with a consistent, fair, and unbiased dataset. While this approach does not address all limitations, the results still demonstrate that sciCUN produces meaningful and reliable predictions, offering significant insights within the study’s scope.

In addition, the use of SOM in this study highlights its value as a post-processing and benchmarking tool for gridded vector fields of sea surface currents. While conventional metrics such as correlation, MAE, and Euclidean distance quantify pointwise agreement, SOM analysis evaluates the similarity of entire circulation patterns and their variability across time. The regime-assignment agreement therefore provides a direct, map-level check that the quantitative skill reported in Section 3 corresponds to the correct reproduction of dominant circulation structures. As demonstrated in Figs. 7 & 10, SOM effectively organizes daily current maps into a hierarchy of dominant circulation regimes, enabling a pattern-based comparison between modeled and original fields. Importantly, the SOM-based error assessments indicate that the quantified deviations primarily reflect moderate variations within otherwise correctly reproduced circulation regimes, rather than fundamentally different flow structures. This provides a more advanced and physically interpretable assessment of model performance than pointwise statistics alone, particularly for applications where the preservation of circulation regimes and mesoscale structures is critical. In this sense, SOM results can confirm that sciCUN preserves the dominant sea surface current patterns, even in cases where localized amplitude or directional errors occur. Furthermore, SOM analysis using a larger number of nodes demonstrates that sea surface currents in the Gulf of Riga exhibit diverse daily patterns, which do not simply repeat (Figs. 8 and 9).

Nevertheless, in conjunction with evaluating the implications of the model’s capability in emulating temporal dynamics – achieved solely through the CNN-UNet architecture and structured during the data preparation phase by incorporating previous days’ current fields alongside the present day’s atmospheric forcing – the case studies presented in Fig. 11 provide further insight into sciCUN’s behavior under strong day-to-day variability. The model successfully reproduces abrupt directional changes, evolving inlet–outlet dynamics, and mesoscale features over consecutive days, while maintaining low spatially averaged errors. This behavior suggests that sciCUN has successfully learned how

to model the relationship between atmospheric forcing (the present-day driver) and previous days' current fields (the historical context) to produce accurate representations of the present-day current fields. Such capability aligns with the fundamental principles underlying hydrodynamic forecasting systems, where the dynamics of the ocean are modeled based on interactions between current states and external forcing.

Previous studies have used CNN-based methods to support surface-current estimation either through local diagnostic relationships (Sinha and Abernathy, 2021) or through super-resolution of scalar surface fields (Ciani et al., 2025), in which dynamically consistent scalar fields are reconstructed and currents are subsequently derived diagnostically. Building on the demonstrated applicability of CNNs to such dynamics, the present study addresses a complementary problem by directly emulating regional sea surface current fields using atmospheric forcing and prior-day states, without requiring concurrent sea surface data. More recent studies have explored physics-informed and operator-learning strategies for surface-current estimation and forecasting, primarily targeting energetic, large-scale ocean regimes. For example, Zhang et al. (2024) showed that incorporating dynamical constraints through weighted loss functions improves the prediction of high-magnitude surface currents in geostrophically dominated open-ocean settings. In addition, neural-operator-based systems such as those introduced by El Aouni et al. (2025) aim to approximate the prognostic behavior of global ocean models through learned state-to-state mappings. Although sciCUN yields comparatively low errors in sea surface current estimation, direct error-based comparisons with these studies are not meaningful and should be avoided, as the model domains, spatial scales, and numerical ranges of the target variables differ substantially. What is important to note is that those advanced approaches also introduce considerable model complexity, technical overhead, and computational demands. From a broader modeling perspective, the primary motivation for data-driven emulation is not to replicate numerical ocean simulations at comparable or greater cost, but to provide a computationally efficient alternative when only a limited subset of variables is required for specific applications. It should always be recognized that numerical ocean simulations remain essential for advancing physical understanding and for future projections, as they are grounded in well-established governing equations and physical principles. Data-driven emulation, in contrast, is based on the assumption that these physical processes are implicitly embedded within historical datasets, and that learning these embedded relationships can provide useful guidance for anticipating their recurrence under similar future conditions. So, if an emulation framework approaches the complexity and resource requirements of the underlying hydrodynamic model, its practical advantage over direct numerical simulation becomes questionable.

In the present study, the Gulf of Riga exemplifies a regime where partial emulation is both justified and effective. It is a small, shallow semi-enclosed basin with relatively weak mean currents compared to global scales, but pronounced day-to-day variability, in which reliable daily surface-current information is essential due to dense shipping traffic and intensive human activities. Within this context, the present results indicate that a purely data-driven CNN-U-Net, combined with a physically consistent data-preparation strategy that encodes temporal dependence through prior-day states, can effectively capture daily surface-current variability. While extension to larger or more energetic domains would likely necessitate more complex physics-informed or operator-learning architectures, sciCUN, in its current configuration, still provides a computationally efficient and sufficiently accurate partial-emulation solution tailored to the dynamics and operational needs of the Gulf of Riga.

In the case study of the Gulf of Riga presented here, sciCUN completes its training in about 30 min on a standard desktop workstation equipped with an NVIDIA GeForce RTX 3060 GPU, using a total dataset size of less than 5 GB. This represents a substantial reduction in

data and computational resource requirements compared to traditional hydrodynamic modeling approaches. Consequently, deep-learning surrogate models like sciCUN can be stabilized to play a key role in the development of Digital Twins and associated impact models (Li et al., 2023). As hydrodynamic simulations are continuously extended in time and updated through improved configurations, surrogate models can be periodically retrained to remain aligned with the evolving simulation archive. In this context, relatively short training times are advantageous, as they enable regular model updating and long-term applicability without incurring prohibitive computational costs. At the same time, sciCUN serves to showcase the capability of deep-learning partial emulation for producing a targeted surface-current product efficiently, as reflected by the skill quantified in Section 3, while relying on hydrodynamic simulations as the physically consistent basis for training and periodic updating, particularly when further improvements are required. Accordingly, continued advances in hydrodynamic model accuracy are expected to translate into more reliable surrogate learning and, in turn, improved partial-emulation performance, so that such surrogates act as complementary components, at least in the near term, within operational modeling chains rather than substitutes for comprehensive hydrodynamic simulations.

Beyond this, accurate sea surface current data are essential for numerous research applications. For instance, previous studies have demonstrated the critical role of current data in enhancing the performance of wave models (Kanarik et al., 2021; Christakos et al., 2021). sciCUN addresses this need by providing a resource-efficient approach for updating sea surface current data to align with the temporal requirements of such models, provided sufficient historical data are available for training. Beyond wave modeling, sciCUN can support a wide range of research disciplines, including climate studies, particle tracking, and ecological modeling (e.g., Mishra et al. 2022, Pärt et al. 2023, Hsu et al. 2024). By enabling cost-effective and accurate emulation of sea surface currents, sciCUN can contribute to advancing scientific research across these domains.

Future work could focus on enhancing sciCUN's ability to capture finer-scale variability and localized features, potentially through the integration of additional atmospheric and oceanographic variables or the adoption of hybrid deep-learning architectures. These improvements would enable the model to better represent complex dynamics and broaden its applicability to diverse oceanographic challenges.

CRediT authorship contribution statement

Amirhossein Barzandeh: Writing – review & editing, Writing – original draft, Visualization, Validation, Software, Methodology, Investigation, Formal analysis, Data curation, Conceptualization. **Ilya Maljutenko:** Writing – review & editing, Supervision. **Sander Rikka:** Writing – review & editing, Supervision. **Urmaz Raudsepp:** Writing – review & editing, Supervision, Conceptualization.

Declaration of competing interest

The authors declare that they have no known competing financial interests or personal relationships that could have appeared to influence the work reported in this paper.

Acknowledgment

This work was supported by the AIMES project (AI-based Emulator for Marine Environmental Simulations; project No. PSG1130), funded by the Estonian Research Council. The authors also acknowledge support from the European Union and the Estonian Research Council under the Digital Twin of Marine Renewable Energy project (project No. TEM-TA38).

Appendix A. sciCUN core codes

The sciCUN model is implemented in MATLAB R2024a using the Deep Learning Toolbox™ (Version 24.1, License 40687166). The practical application of sciCUN can be divided into two main phases: data preparation and the implementation of the training architecture, including layers and options. As detailed in Section 2.2.2, the input data must be prepared as a 4D matrix. The first two dimensions represent longitude and latitude, the third dimension represents the channels (either current components or atmospheric variables), and the fourth dimension corresponds to time. Similarly, the target data should also be organized as a 4D matrix. However, while the input data contains 7 channels (third dimension), the target data is limited to 2 channels. An important recommendation for applying sciCUN to a new study area is that the gridded maps of the study area (the first and second dimensions of the input and target data) must have lengths that are multiples of 8. This requirement stems from the encoding and decoding procedures within the sciCUN structure.

To maintain simplicity as a surrogate model, we have chosen not to upload the model to an external repository. We believe that sciCUN can be easily implemented for any new study area by following the instructions provided in this study. However, those interested in obtaining sample case study setup files are encouraged to contact the corresponding author. The core part of the code related to the architecture and training options is as follows:

```
% Load the input and target data
load(inputData_train.mat) % size(inputData_train) = [96, 104, 7, 9860]
load(targetData_train.mat) % size(targetData_train) = [96, 104, 2, 9860]

% Define Input Layer
InLay = size(inputData_train, 1:3); % size(inputData_train) = [96, 104, 7, 9860]

% Define sciCUN Layers
layers = [
    imageInputLayer(InLay, 'Name', 'input')

    % Encoder
    convolution2dLayer(3, 32, 'Padding', 'same', 'Name', 'conv1_1')
    batchNormalizationLayer('Name', 'batchnorm1')
    reluLayer('Name', 'relu1_1')
    maxPooling2dLayer(2, 'Stride', 2, 'Name', 'pool1')

    convolution2dLayer(3, 128, 'Padding', 'same', 'Name', 'conv2_1')
    batchNormalizationLayer('Name', 'batchnorm2')
    reluLayer('Name', 'relu2_1')
    maxPooling2dLayer(2, 'Stride', 2, 'Name', 'pool2')

    convolution2dLayer(3, 256, 'Padding', 'same', 'Name', 'conv3_1')
    batchNormalizationLayer('Name', 'batchnorm3')
    reluLayer('Name', 'relu3_1')
    maxPooling2dLayer(2, 'Stride', 2, 'Name', 'pool3')

    % Bottleneck
    convolution2dLayer(3, 512, 'Padding', 'same', 'Name', 'conv4_1')
    batchNormalizationLayer('Name', 'batchnorm4')
    reluLayer('Name', 'relu4_1')

    % Decoder
    transposedConv2dLayer(3, 256, 'Stride', 2, 'Cropping', 'same', 'Name', 'upconv3')
    concatenationLayer(3, 2, 'Name', 'concat3')
    convolution2dLayer(3, 256, 'Padding', 'same', 'Name', 'conv3_2')
    batchNormalizationLayer('Name', 'batchnorm5')
    reluLayer('Name', 'relu3_2')

    transposedConv2dLayer(3, 128, 'Stride', 2, 'Cropping', 'same', 'Name', 'upconv2')
    concatenationLayer(3, 2, 'Name', 'concat2')
    convolution2dLayer(3, 128, 'Padding', 'same', 'Name', 'conv2_2')
    batchNormalizationLayer('Name', 'batchnorm6')
    reluLayer('Name', 'relu2_2')

    transposedConv2dLayer(3, 32, 'Stride', 2, 'Cropping', 'same', 'Name', 'upconv1')
    concatenationLayer(3, 2, 'Name', 'concat1')
    convolution2dLayer(3, 32, 'Padding', 'same', 'Name', 'conv1_2')
    batchNormalizationLayer('Name', 'batchnorm7')
    reluLayer('Name', 'relu1_2')

    % Output
    convolution2dLayer(1, 2, 'Padding', 'same', 'Name', 'conv_final')
    regressionLayer('Name', 'output')
];
```

```
% Build Layer Graph and Add Skip Connections
lgraph = layerGraph(layers);
lgraph = connectLayers(lgraph, 'relu1_1', 'concat1/in2');
lgraph = connectLayers(lgraph, 'relu2_1', 'concat2/in2');
lgraph = connectLayers(lgraph, 'relu3_1', 'concat3/in2');

% Define Training Options
options = trainingOptions('adam', ...
    'InitialLearnRate', 5e-4, ...
    'MaxEpochs', 32, ...
    'MiniBatchSize', 16, ...
    'Shuffle', 'every-epoch', ...
    'Plots', 'training-progress', ...
    'ValidationData', {inputData_val, targetData_val}, ...
    'ValidationFrequency', 16, ...
    'Verbose', true, ...
    'ExecutionEnvironment', 'gpu');

% Training
sciCUN = trainNetwork(inputData_train, targetData_train, lgraph, options);
```

Appendix B. sciCUN all testing time instances

In addition to the results presented in the manuscript, the complete records of sciCUN's performance during its testing period, visually compared with the original data, are available in the attached video accessible through the link below:

[Download Video](#)

Data availability

Data will be made available on request.

References

- Astok, V., Otsmann, M., Suursaar, Ü., 1999. Water exchange as the main physical process in semi-enclosed marine systems: the Gulf of Riga case. *Hydrobiologia* 393, 11–18. <http://dx.doi.org/10.1023/A:1003517110726>.
- BalticSea Multiyear Phy 003 011, 2024. E.u. Copernicus marine service information (CMEMS). Marine data store (MDS). <http://dx.doi.org/10.48670/moi-00013>, URL <https://documentation.marine.copernicus.eu/PUM/CMEMS-BAL-PUM-003-011-012.pdf>. (Accessed on 01 December 2024).
- Barzandeh, A., Ličer, M., Rus, M., Kristan, M., Maljutenko, I., Elken, J., Lagema, P., Uiboupin, R., 2025. Application of the HIDRA2 deep-learning model for sea level forecasting along the estonian coast of the Baltic Sea. *Ocean. Sci.* 21 (4), 1315–1327. <http://dx.doi.org/10.5194/os-21-1315-2025>.
- Barzandeh, A., Maljutenko, I., Rikka, S., Lagema, P., Männik, A., Uiboupin, R., Raudsepp, U., 2024. Sea surface circulation in the Baltic Sea: decomposed components and pattern recognition. *Sci. Rep.* 14 (1), 18649. <http://dx.doi.org/10.1038/s41598-024-69463-8>.
- Christakos, K., Björkqvist, J.-V., Breivik, Ø., Tuomi, L., Furevik, B.R., Albreten, J., 2021. The impact of surface currents on the wave climate in narrow fjords. *Ocean. Model.* 168, 101894. <http://dx.doi.org/10.1016/j.ocemod.2021.101894>.
- Ciani, D., Fanelli, C., Buongiorno Nardelli, B., 2025. Estimating ocean currents from the joint reconstruction of absolute dynamic topography and sea surface temperature through deep learning algorithms. *Ocean. Sci.* 21 (1), 199–216. <http://dx.doi.org/10.5194/os-21-199-2025>.
- Dey, S., Sikkakolli, R., Dogra, D.P., Sil, S., 2023. On the variability of ocean surface current in the bay of bengal using self-organizing map (SOM). *Deep. Sea Res. Part I: Ocean. Res. Pap.* 199, 104103. <http://dx.doi.org/10.1016/j.dsr.2023.104103>.
- Dohan, K., Maximenko, N., 2010. Monitoring ocean currents with satellite sensors. *Oceanography* 23 (4), 94–103, URL <http://www.jstor.org/stable/24860865>.
- Dong, C., Xu, G., Han, G., Bethel, B.J., Xie, W., Zhou, S., 2022. Recent developments in artificial intelligence in oceanography. *Ocean-Land-Atmosphere Res.* 2022, 9870950. <http://dx.doi.org/10.34133/2022/9870950>.
- Durand, C., Finn, T.S., Farchi, A., Boquet, M., Boutin, G., Ólason, E., 2024. Data-driven surrogate modeling of high-resolution sea-ice thickness in the arctic. *Cryosphere* 18 (4), 1791–1815. <http://dx.doi.org/10.5194/tc-18-1791-2024>.
- Eelsalu, M., Pihlo, L., Aigars, J., Kelpšaitis-Rimkienė, L., Kondrat, V., Kruusmaa, M., Parnell, K.E., Ristolainen, A., Šakurova, I., Skudra, M., et al., 2025. Exponential distribution of wave-driven near-bed water speeds under short-crested waves: a case study in the eastern Gulf of Riga, the Baltic Sea. *Proc. Est. Acad. Sci.* 74 (1), 23–42. <http://dx.doi.org/10.3176/proc.2025.1.03>.
- El Aouni, A., Gaudel, Q., Regnier, C., Van Gennip, S., Le Galloudec, O., Devrillon, M., Drillet, Y., Lellouche, J.-M., 2025. GLONET: Mercator's end-to-end neural global ocean forecasting system. *J. Geophys. Res.: Mach. Learn. Comput.* 2 (3), <http://dx.doi.org/10.1029/2025JH000686>, e2025JH000686.

- Elken, J., Barzandeh, A., Maljutenko, I., Rikka, S., 2024. Reconstruction of baltic gridded sea levels from tide gauge and altimetry observations using spatiotemporal statistics from reanalysis. *Remote. Sens.* 16 (15), 2702. <http://dx.doi.org/10.3390/rs16152702>.
- Griffiths, R.W., Killworth, P.D., Stern, M.E., 1982. Ageostrophic instability of ocean currents. *J. Fluid Mech.* 117, 343–377. <http://dx.doi.org/10.1017/S0022112082001669>.
- Grossi, M.D., Kubat, M., Özgökmen, T.M., 2020. Predicting particle trajectories in oceanic flows using artificial neural networks. *Ocean. Model.* 156, 101707. <http://dx.doi.org/10.1016/j.ocemod.2020.101707>.
- Hersbach, H., Bell, B., Berrisford, P., Biavati, G., Horányi, A., Muñoz Sabater, J., Nicolas, J., Peubey, C., Radu, R., Schepers, D., Simmons, A., Soci, C., Dee, D., Thépaut, J.-N., 2023. ERA5 hourly data on single levels from 1940 to present. <http://dx.doi.org/10.24381/cds.adbb2d47>, (Accessed on 01 December 2024).
- Hersbach, H., Bell, B., Berrisford, P., Hirahara, S., Horányi, A., Muñoz-Sabater, J., Nicolas, J., Peubey, C., Radu, R., Schepers, D., Simmons, A., Soci, C., Abdalla, S., Abellan, X., Balsamo, G., Bechtold, P., Biavati, G., Bidlot, J., Bonavita, M., De Chiara, G., Dahlgren, P., Dee, D., Diamantakis, M., Dragani, R., Flemming, J., Forbes, R., Fuentes, M., Geer, A., Haimberger, L., Healy, S., Hogan, R.J., Hólm, E., Janisková, M., Keeley, S., Laloyaux, P., Lopez, P., Lupu, C., Radnoti, G., de Rosnay, P., Rozum, I., Vamborg, F., Villaume, S., Thépaut, J.-N., 2020. The ERA5 global reanalysis. *Q. J. R. Meteorol. Soc.* 146 (730), 1999–2049. <http://dx.doi.org/10.1002/qj.3803>.
- Hewitson, B.C., Crane, R.G., 2002. Self-organizing maps: applications to synoptic climatology. *Clim. Res.* 22 (1), 13–26. <http://dx.doi.org/10.3354/cr022013>.
- Hordoir, R., Meier, H., 2012. Effect of climate change on the thermal stratification of the baltic sea: a sensitivity experiment. *Clim. Dyn.* 38, 1703–1713. <http://dx.doi.org/10.1007/s00382-011-1036-y>.
- Hsu, P.-C., Macagga, R.A.T., Lu, C.-Y., Lo, D.-Y.-J., 2024. Investigation of the kuroshio-coastal current interaction and marine heatwave trends in the coral habitats of northeastern Taiwan. *Reg. Stud. Mar. Sci.* 71, 103431. <http://dx.doi.org/10.1016/j.rmsa.2024.103431>.
- Ioffe, S., Szegedy, C., 2015. Batch normalization: Accelerating deep network training by reducing internal covariate shift. [arXiv:1502.03167](https://arxiv.org/abs/1502.03167). URL <https://arxiv.org/abs/1502.03167>.
- J. M. Sánchez-Reales, S.J., Chao, B.F., 2012. Global surface geostrophic ocean currents derived from satellite altimetry and GOCE geoid. *Mar. Geod.* 35 (sup1), 175–189. <http://dx.doi.org/10.1080/01490419.2012.718696>.
- Jahnmard, V., Ellmann, A., Delpeche-Ellmann, N., 2025. Quantification of baltic sea water budget components using dynamic topography. *Ocean. Sci.* 21 (3), 913–930. <http://dx.doi.org/10.5194/os-21-913-2025>.
- Kanarik, H., Tuomi, L., Björkqvist, J.-V., Kärnä, T., 2021. Improving Baltic Sea wave forecasts using modelled surface currents. *Ocean. Dyn.* 71 (6), 635–653. <http://dx.doi.org/10.1007/s10236-021-01455-y>.
- Kärnä, T., Ljungemyr, P., Falahat, S., Ringgaard, I., Axell, L., Korabel, V., Murawski, J., Maljutenko, I., Lindenthal, A., Jandt-Scheelke, S., 2021. Nemo-nordic 2.0: Operational marine forecast model for the baltic sea. *Geosci. Model. Dev.* 14, 5731–5749. <http://dx.doi.org/10.5194/gmd-14-5731-2021>.
- Kingma, D.P., Ba, J., 2017. Adam: A method for stochastic optimization. [arXiv:1412.6980](https://arxiv.org/abs/1412.6980). URL <https://arxiv.org/abs/1412.6980>.
- Klemas, V., 2012. Remote sensing of coastal and ocean currents: An overview. *J. Coast. Res.* 28 (3), 576–586. <http://dx.doi.org/10.2112/JCOASTRES-D-11-00197.1>.
- Kohonen, T., 2013. Essentials of the self-organizing map. *Neural Netw.* 37, 52–65. <http://dx.doi.org/10.1016/j.neunet.2012.09.018>, Twenty-fifth Anniversay Commemorative Issue.
- Köuts, T., Håkansson, B., 1995. Observations of water exchange, currents, sea levels and nutrients in the Gulf of Riga. <https://smhi.se/publikationer-fran-smhi/sok-publikationer/1995-09-16-observations-of-water-exchange-currents-sea-levels-and-nutrients-in-the-gulf-of-riga>. SMHI Reports Oceanography (RO) No. 23 December 1995.
- Laignel, B., Vignudelli, S., Almar, R., Becker, M., Bentamy, A., Benveniste, J., Birol, F., Frappart, F., Idier, D., Salameh, E., Passaro, M., Menende, M., Simard, M., Turki, E.I., Verpoort, C., 2023. Observation of the Coastal Areas, Estuaries and Deltas from Space. *Surv. Geophys.* 44 (5), 1309–1356. <http://dx.doi.org/10.1007/s10712-022-09757-6>.
- Lecun, Y., Bottou, L., Bengio, Y., Haffner, P., 1998. Gradient-based learning applied to document recognition. *Proc. IEEE* 86 (11), 2278–2324. <http://dx.doi.org/10.1109/5.726791>.
- Lee, E.A., Kim, S.Y., 2021. A diagnosis of surface currents and sea surface heights in a coastal region. *Cont. Shelf Res.* 226, 104486. <http://dx.doi.org/10.1016/j.csr.2021.104486>.
- Lehmann, A., Myrberg, K., Post, P., Chubarenko, I., Daillidienė, I., Hinrichsen, H.-H., Hüsey, K., Liblik, T., Meier, H.E.M., Lips, U., Bukanova, T., 2022. Salinity dynamics of the baltic sea. *Earth Syst. Dyn.* 13 (1), 373–392. <http://dx.doi.org/10.5194/esd-13-373-2022>.
- Li, X., Feng, M., Ran, Y., Su, Y., Liu, F., Huang, C., Shen, H., Xiao, Q., Su, J., Yuan, S., et al., 2023. Big data in earth system science and progress towards a digital twin. *Nat. Rev. Earth Environ.* 4 (5), 319–332. <http://dx.doi.org/10.1038/s43017-023-00409-w>.
- Li, Z., Liu, F., Yang, W., Peng, S., Zhou, J., 2022. A survey of convolutional neural networks: Analysis, applications, and prospects. *IEEE Trans. Neural Netw. Learn. Syst.* 33 (12), 6999–7019. <http://dx.doi.org/10.1109/TNNLS.2021.3084827>.
- Liblik, T., Skudra, M., Lips, U., 2017. On the buoyant sub-surface salinity maxima in the Gulf of Riga. *Oceanologia* 59 (2), 113–128. <http://dx.doi.org/10.1016/j.oceano.2016.10.001>.
- Liblik, T., Väli, G., Salm, K., Laanemets, J., Lilover, M.-J., Lips, U., 2022. Quasi-steady circulation regimes in the Baltic Sea. *Ocean. Sci.* 18 (3), 857–879. <http://dx.doi.org/10.5194/os-18-857-2022>.
- Lilover, M.J., Lips, U., Laaneur, J., Liljebland, B., 1998. Flow regime in the Irbe Strait. *Aquat. Sci.* 60 (3), 253–265. <http://dx.doi.org/10.1007/s000270050040>.
- Lips, U., Zhurbas, V., Skudra, M., Väli, G., 2016a. A numerical study of circulation in the Gulf of Riga, Baltic Sea. Part I: Whole-basin gyres and mean currents. *Cont. Shelf Res.* 112, 1–13. <http://dx.doi.org/10.1016/j.csr.2015.11.008>.
- Lips, U., Zhurbas, V., Skudra, M., Väli, G., 2016b. A numerical study of circulation in the Gulf of Riga, Baltic Sea. Part II: Mesoscale features and freshwater transport pathways. *Cont. Shelf Res.* 115, 44–52. <http://dx.doi.org/10.1016/j.csr.2015.12.018>.
- Liu, Y., Weisberg, R.H., 2005. Patterns of ocean current variability on the West Florida shelf using the self-organizing map. *J. Geophys. Res.* Ocean. 110 (C6), <http://dx.doi.org/10.1029/2004JC002786>.
- Liu, Y., Weisberg, R.H., Vignudelli, S., Mitchum, G.T., 2016. Patterns of the loop current and regions of sea surface height variability in the eastern gulf of Mexico revealed by the self-organizing maps. *J. Geophys. Res.* Ocean. 121 (4), 2347–2366. <http://dx.doi.org/10.1002/2015JC011493>.
- Liu, Y., Zhang, L., Hao, W., Zhang, L., Huang, L., 2024. Predicting temporal and spatial 4-D ocean temperature using satellite data based on a novel deep learning model. *Ocean. Model.* 188, 102333. <http://dx.doi.org/10.1016/j.ocemod.2024.102333>.
- Long, J., Shelhamer, E., Darrell, T., 2015. Fully convolutional networks for semantic segmentation. In: 2015 IEEE Conference on Computer Vision and Pattern Recognition. CVPR, IEEE Computer Society, Los Alamitos, CA, USA, pp. 3431–3440. <http://dx.doi.org/10.1109/CVPR.2015.7298965>.
- Maded, G., Bourdallé-Badie, R., Bouttier, P.-A., Bricaud, C., Bruciaferri, D., Calvert, D., Chanut, J., Clementi, E., Coward, A., Delrosso, D., 2017. NEMO ocean engine. URL https://epic.awi.de/id/eprint/39698/1/NEMO_book_v6039.pdf.
- Maljutenko, I., 2019. Water Circulation in Gulf Type Regions of Freshwater Influence – the Gulf of Finland and Gulf of Riga (Ph.D. thesis). Tallinn University of Technology, Tallinn, Estonia. <http://dx.doi.org/10.23658/taitech.41/2019>.
- McWilliams, J.C., 2016. Submesoscale currents in the ocean. *Proc. R. Soc. A: Math. Phys. Eng. Sci.* 472 (2189), 20160117. <http://dx.doi.org/10.1098/rspa.2016.0117>.
- Minuzzi, F.C., Farina, L., 2023. A deep learning approach to predict significant wave height using long short-term memory. *Ocean. Model.* 181, 102151. <http://dx.doi.org/10.1016/j.ocemod.2022.102151>.
- Mishra, A., Buhalko, N., Lind, K., Lips, I., Liblik, T., Väli, G., Lips, U., 2022. Spatiotemporal variability of microplastics in the Eastern Baltic Sea. *Front. Mar. Sci.* 9, <http://dx.doi.org/10.3389/fmars.2022.875984>.
- Morales-Márquez, V., Hernández-Carrasco, I., Simarro, G., Rossi, V., Orfila, A., 2021. Regionalizing the impacts of wind- and wave-induced currents on surface ocean dynamics: A long-term variability analysis in the mediterranean sea. *J. Geophys. Res.* Ocean. 126 (9), e2020JC017104. <http://dx.doi.org/10.1029/2020JC017104>, e2020JC017104 2020JC017104.
- Myrberg, K., Lehmann, A., 2013. Topography, hydrography, circulation and modelling of the baltic sea. In: Somere, T., Quak, E. (Eds.), *Preventive Methods for Coastal Protection: Towards the Use of Ocean Dynamics for Pollution Control*. Springer International Publishing, Heidelberg, pp. 31–64. http://dx.doi.org/10.1007/978-3-319-00440-2_2.
- Nair, V., Hinton, G.E., 2010. Rectified linear units improve restricted boltzmann machines. In: *Proceedings of the 27th International Conference on Machine Learning (ICML-10)*, pp. 807–814.
- Najafzadeh, F., Jankowski, M.Z., Giudici, A., Männik, R., Suursaar, Ü., Viška, M., Somere, T., 2024. Spatiotemporal variability of wave climate in the Gulf of Riga. *Oceanologia* 66 (1), 56–77. <http://dx.doi.org/10.1016/j.oceano.2023.11.001>.
- Omstedt, A., Elken, J., Lehmann, A., Leppäranta, M., Meier, H., Myrberg, K., Rutgersson, A., 2014. Progress in physical oceanography of the Baltic Sea during the 2003–2014 period. *Prog. Oceanogr.* 128, 139–171. <http://dx.doi.org/10.1016/j.pcean.2014.08.010>.
- O’Shea, K., Nash, R., 2015. An introduction to convolutional neural networks. [arXiv:1511.08458](https://arxiv.org/abs/1511.08458).
- Ouala, S., Chapron, B., Collard, F., Gaultier, L., Fablet, R., 2023. Online calibration of deep learning sub-models for hybrid numerical modeling systems. [arXiv:2311.10665](https://arxiv.org/abs/2311.10665).
- Panteleiti, T., Verjovkina, S., Jandt-Scheelke, S., Spruch, L., Huess, V., 2023. Quality Information Document: Baltic Sea Physics Reanalysis Product (BALTICSEA_MULTI-YEAR_PHY_003_011). pp. 1–57, URL <https://documentation.marine.copernicus.eu/QUID/CMEMS-BAL-QUID-003-011.pdf>. Baltic Sea Production Centre.
- Pärt, S., Björkqvist, J.-V., Alari, V., Maljutenko, I., Uiboupin, R., 2023. An ocean-wave-trajectory forecasting system for the eastern Baltic Sea: Validation against drifting buoys and implementation for oil spill modeling. *Marine Poll. Bull.* 195, 115497. <http://dx.doi.org/10.1016/j.marpolbul.2023.115497>.

- Pindsoo, K., Soomere, T., 2020. Basin-wide variations in trends in water level maxima in the baltic sea. *Cont. Shelf Res.* 193, 104029. <http://dx.doi.org/10.1016/j.csr.2019.104029>.
- Rajabi-Kiasari, S., Delpeche-Ellmann, N., Ellmann, A., 2023. Forecasting of absolute dynamic topography using deep learning algorithm with application to the Baltic Sea. *Comput. Geosci.* 178, 105406. <http://dx.doi.org/10.1016/j.cageo.2023.105406>.
- Rajabi-Kiasari, S., Ellmann, A., Delpeche-Ellmann, N., 2025. Sea level forecasting using deep recurrent neural networks with high-resolution hydrodynamic model. *Appl. Ocean Res.* 157, 104496. <http://dx.doi.org/10.1016/j.apor.2025.104496>.
- Raudsepp, U., 2001. Interannual and seasonal temperature and salinity variations in the Gulf of Riga and corresponding saline water inflow from the baltic proper. *Hydrol. Res.* 32 (2), 135–160. <http://dx.doi.org/10.2166/nh.2001.0009>.
- Raudsepp, U., Beletsky, D., Schwab, D.J., 2003. Basin-scale topographic waves in the gulf of riga. *Journal Phys. Oceanography* 33 (5), 1129–1140. [http://dx.doi.org/10.1175/1520-0485\(2003\)033<1129:BTWITG>2.0.CO;2](http://dx.doi.org/10.1175/1520-0485(2003)033<1129:BTWITG>2.0.CO;2).
- Raudsepp, U., Maljutenko, I., Barzandeh, A., Uiboupin, R., Lagema, P., 2023. Baltic sea freshwater content. *State the Planet* 1-osr7, 7. <http://dx.doi.org/10.5194/sp-1-osr7-7-2023>.
- Ren, J., Wang, C., Sun, L., Huang, B., Zhang, D., Mu, J., Wu, J., 2024. Prediction of sea surface temperature using U-net based model. *Remote. Sens.* 16 (7), <http://dx.doi.org/10.3390/rs16071205>.
- Röhrs, J., Sutherland, G., Jeans, G., Bedington, M., Sperrevik, A.K., Dagestad, K.-F., Gusdal, Y., Mauritzen, C., Dale, A., LaCase, J.H., 2023. Surface currents in operational oceanography: Key applications, mechanisms, and methods. *J. Oper. Ocean.* 16 (1), 60–88. <http://dx.doi.org/10.1080/1755876X.2021.1903221>.
- Ronneberger, O., Fischer, P., Brox, T., 2015. U-Net: Convolutional networks for biomedical image segmentation. In: Navab, N., Hornegger, J., Wells, W.M., Frangi, A.F. (Eds.), *Medical Image Computing and Computer-Assisted Intervention. MICCAI 2015*, Springer International Publishing, Cham, pp. 234–241.
- Savchuk, O.P., 2002. Nutrient biogeochemical cycles in the Gulf of Riga: scaling up field studies with a mathematical model. *J. Mar. Syst.* 32 (4), 253–280. [http://dx.doi.org/10.1016/S0924-7963\(02\)00039-8](http://dx.doi.org/10.1016/S0924-7963(02)00039-8).
- Sinha, A., Abernathy, R., 2021. Estimating ocean surface currents with machine learning. *Front. Mar. Sci.* 8, 672477. <http://dx.doi.org/10.3389/fmars.2021.672477>.
- Skudra, M., Lips, U., 2017. Characteristics and inter-annual changes in temperature, salinity and density distribution in the Gulf of Riga. *Oceanologia* 59 (1), 37–48. <http://dx.doi.org/10.1016/j.oceano.2016.07.001>.
- Sonnenwald, M., Lguensat, R., Jones, D.C., Dueben, P.D., Brajard, J., Balaji, V., 2021. Bridging observations, theory and numerical simulation of the ocean using machine learning. *Environ. Res. Lett.* 16 (7), 073008. <http://dx.doi.org/10.1088/1748-9326/ac0eb0>.
- Soosaar, E., Maljutenko, I., Raudsepp, U., Elken, J., 2014. An investigation of anticyclonic circulation in the southern Gulf of Riga during the spring period. *Cont. Shelf Res.* 78, 75–84. <http://dx.doi.org/10.1016/j.csr.2014.02.009>.
- Soosaar, E., Maljutenko, I., Uiboupin, R., Skudra, M., Raudsepp, U., 2016. River bulge evolution and dynamics in a non-tidal sea — Daugava River plume in the Gulf of Riga. *Baltic Sea. Ocean. Sci.* 12 (2), 417–432. <http://dx.doi.org/10.5194/os-12-417-2016>.
- Stipa, T., Tamminen, T., Seppälä, J., 1999. On the creation and maintenance of stratification in the Gulf of Riga. *J. Mar. Syst.* 23 (1), 27–49. [http://dx.doi.org/10.1016/S0924-7963\(99\)00049-4](http://dx.doi.org/10.1016/S0924-7963(99)00049-4).
- Sudre, J., Maes, C., Garçon, V., 2013. On the global estimates of geostrophic and Ekman surface currents. *Limnol. Ocean.: Fluids Environ.* 3 (1), 1–20. <http://dx.doi.org/10.1215/21573689-2071927>.
- Suursaar, Ü., Elken, J., Belkin, I.M., 2022. Fronts in the baltic sea: A review with a focus on its north-eastern part. In: Belkin, I.M. (Ed.), *Chemical Oceanography of Frontal Zones*. Springer Berlin Heidelberg, Berlin, Heidelberg, pp. 143–181. <http://dx.doi.org/10.1007/978-2021-813>.
- Suursaar, Ü., Kullas, T., Aps, R., 2012. Currents and waves in the northern Gulf of Riga: measurement and long-term hindcast. *Oceanologia* 54 (3), 421–447. <http://dx.doi.org/10.5697/oc.54-3.421>.
- Suursaar, Ü., Kullas, T., Otsmann, M., 2002. Flow modelling in the pärnu bay and the kihnu strait. In: *Proceedings of the Estonian Academy of Sciences. Engineering*, vol. 8, pp. 189–203. <http://dx.doi.org/10.3176/eng.2002.3.04>.
- Szaniawska, A., 2018. *The Gulf of Riga*. In: *Baltic Crustaceans*. Springer, Cham, http://dx.doi.org/10.1007/978-3-319-56354-1_5.
- The MathWorks Inc., 2024. MATLAB version: 24.1.0.2689473 (r2024a) update 6. URL <https://www.mathworks.com>.
- Travkin, V.S., Tikhonova, N.A., Zakharchuk, E.A., 2024. Mesoscale eddies of the baltic sea according to the physical reanalysis. *Russ. Meteorol. Hydrol.* 49, 784–794. <http://dx.doi.org/10.3103/S1068373924090048>.
- Ubelmann, C., Dibarbouré, G., Gaultier, L., Ponte, A., Arduhuin, F., Ballarotta, M., Faugère, Y., 2021. Reconstructing ocean surface current combining altimetry and future spaceborne Doppler data. *J. Geophys. Res.: Ocean.* 126 (3), <http://dx.doi.org/10.1029/2020JC016560>, e2020JC016560.
- Väli, G., Meier, H.M., Liblik, T., Radtke, H., Klingbeil, K., Gräwe, U., Lips, U., 2024. Submesoscale processes in the surface layer of the central baltic sea: A high-resolution modelling study. *Oceanologia* 66 (1), 78–90. <http://dx.doi.org/10.1016/j.oceano.2023.11.002>.
- Vesanto, J., Alhoniemi, E., 2000. Clustering of the self-organizing map. *IEEE Trans. Neural Netw.* 11 (3), 586–600. <http://dx.doi.org/10.1109/72.846731>.
- Weisse, R., Dailidienė, I., Hünicke, B., Kahma, K., Madsen, K., Omstedt, A., Parnell, K., Schöne, T., Soomere, T., Zhang, W., Zorita, E., 2021. Sea level dynamics and coastal erosion in the Baltic Sea region. *Earth Syst. Dyn.* 12 (3), 871–898. <http://dx.doi.org/10.5194/esd-12-871-2021>.
- Xu, Z., Ren, J., Zhang, Y., Ondina, J.M.G., Olabarrieta, M., Xiao, T., He, W., Liu, Z., Chen, S., Smith, K., Jiang, Z., 2024a. A fast AI surrogate for coastal ocean circulation models. *arXiv:2410.14952*.
- Xu, G., Xie, W., Lin, X., Liu, Y., Hang, R., Sun, W., Liu, D., Dong, C., 2024b. Detection of three-dimensional structures of oceanic eddies using artificial intelligence. *Ocean. Model.* 190, 102385. <http://dx.doi.org/10.1016/j.oceomod.2024.102385>.
- Yurkovskis, A., 2004. Dynamics of particulate major and trace elements in the lower reaches of the Daugava River and adjacent area of the Gulf of Riga (Baltic Sea). *Marine Poll. Bull.* 49 (3), 249–263. <http://dx.doi.org/10.1016/j.marpolbul.2004.02.013>.
- Yurkovskis, A., Wulff, F., Rahm, L., Andrulaitis, A., Rodriguez-Medina, M., 1993. A nutrient budget of the Gulf of Riga; Baltic Sea. *Estuar. Coast. Shelf Sci.* 37 (2), 113–127. <http://dx.doi.org/10.1006/eess.1993.1046>.
- Zhang, L., Duan, W., Cui, X., Liu, Y., Huang, L., 2024. Surface current prediction based on a physics-informed deep learning model. *Appl. Ocean Res.* 148, 104005. <http://dx.doi.org/10.1016/j.apor.2024.104005>.
- Zhao, Q., Peng, S., Wang, J., Li, S., Hou, Z., Zhong, G., 2024. Applications of deep learning in physical oceanography: a comprehensive review. *Front. Mar. Sci.* 11, <http://dx.doi.org/10.3389/fmars.2024.1396322>.
- Zhu, Y., Zhang, R.-H., 2023. A deep learning-based U-net model for ENSO-related precipitation responses to sea surface temperature anomalies over the tropical Pacific. *Atmospheric Ocean. Sci. Lett.* 16 (4), 100351. <http://dx.doi.org/10.1016/j.aosl.2023.100351>, Special Issue: Machine Learning Applications for Atmospheric and Oceanic Sciences.

Appendix 4

IV

A. Barzandeh, C. Manss, F. Stahl, I. Maljutenko, S. Rikka, and U. Raudsepp, "Data-driven emulation of numerically simulated Baltic Sea surface currents with a deep convolutional U-Net: Explainability and potential forecast skill," *JGR: Machine Learning and Computation*, 2026. Accepted for publication / In press

1 **Data-Driven Emulation of Numerically Simulated Baltic**
2 **Sea Surface Currents with a Deep Convolutional U-Net:**
3 **Explainability and Potential Forecast Skill**

4 **Amirhossein Barzandeh¹, Christoph Manss², Frederic Stahl², Ilja Maljutenko¹,**
5 **Sander Rikka¹, and Urmas Raudsepp¹**

6 ¹Department of Marine Systems, Tallinn University of Technology (TalTech), Akadeemia tee 15a, Tallinn,
7 12618, Estonia

8 ²Marine Perception, German Research Center for Artificial Intelligence (DFKI), Marie-Curie-Straße 1,
9 Oldenburg, 26129, Germany

10 **Key Points:**

- 11 • A deep U Net emulates daily Baltic Sea surface currents from prior state and next-day
12 wind
13 • Explainable AI identifies spatial distributions of input contributions to surface current
14 emulation
15 • Autoregressive forecasts show gradual error growth and stable medium range behavior

Corresponding author: Amirhossein Barzandeh, amirhossein.barzandeh@taltech.ee

Abstract

Ocean models can represent surface circulation at kilometer scales, but their computational cost limits broad experimentation. We present DeepCUN, a deep convolutional encoder–decoder (U-Net) that emulates daily-mean Baltic Sea surface current components on a 1-nautical-mile grid. DeepCUN is trained on 2015–2023 reanalysis currents with atmospheric reanalysis forcing. An occlusion-sensitivity channel ablation indicates that wind provides the dominant predictive information when combined with the antecedent surface-current state, while additional atmospheric variables contribute negligibly. Accordingly, DeepCUN is configured to use only the prior surface-current state and the subsequent-day wind components to predict next-day surface current fields. On an independent 2024 test year, DeepCUN captures the dominant spatial patterns and temporal variability, with the highest errors concentrated in the southwestern boundary exchange corridor and narrow straits and lower errors across the basin interior, where correlations exceed 0.9 in most locations. For post hoc explainability of this data-driven mapping, we apply layer-wise relevance propagation to characterize attributed support and a diagonal Jacobian elasticity metric to quantify local responsiveness, revealing spatially varying reliance on state memory in the southwestern boundary-influenced region and wind-modulated adjustment across the basin interior. In addition, to assess the potential forecast skill of this approach, we perform recursive rollouts, which show domain-mean absolute error increasing smoothly from $\sim 2.5 \text{ cm s}^{-1}$ at 1 day to $\sim 6.0 \text{ cm s}^{-1}$ at 21 days while correlation decreases from > 0.9 to ~ 0.65 , indicating stable multi-week behavior under idealized forcing conditions. The framework provides an efficient and interpretable template for configuring, pruning, and stress-testing reduced-input emulators of regional surface circulation.

Plain Language Summary

High-resolution ocean models can simulate sea surface currents realistically, but they are expensive to run because they compute the full three-dimensional ocean state.

We developed an AI model called DeepCUN that predicts the next day’s surface currents for the Baltic Sea using only two inputs: the previous day’s surface currents and the wind for the day being predicted. DeepCUN learns this relationship from many years of reanalysis data and then produces current fields on the same high-resolution grid much faster than running a full ocean model.

We also used explainable AI methods to better understand how DeepCUN uses its inputs. These analyses show where the model relies more on the previous current state and where it responds more strongly to wind forcing, helping to interpret the behavior of an otherwise black-box model. Finally, we tested potential forecast stability by running DeepCUN repeatedly in a step-by-step mode to benchmark, under idealized forcing, how errors grow gradually over multiple weeks.

1 Introduction

Observations of the ocean surface are essential for understanding and predicting key physical processes, yet they remain sparse in both space and time. Satellite and in situ measurements provide invaluable information, but they do not continuously resolve surface dynamics at the spatiotemporal scales required for many scientific and operational applications (Gould et al., 2013; Legler et al., 2015; Traon et al., 2015). To bridge these gaps, numerical hydrodynamic models are routinely employed (Allen et al., 2013; Eschenbach, 2017). These models solve the primitive equations over discretized regional domains with prescribed initial and boundary conditions, thereby representing the coupled dynamical and thermodynamic evolution of the ocean (Kantha & Clayson, 2000; Grooms & Julien, 2018; Fox-Kemper et al., 2019; Chassignet & Xu, 2021). Because surface currents are dynamically coupled to subsurface momentum, stratification, and boundary exchanges (Bryan,

1969), even applications focused on near-surface fields typically require time-integrating the full three-dimensional system with short time steps, making regional simulations computationally demanding.

Recent studies emphasize complementary, lower-cost strategies—including equation-free surrogates, hybrid corrections within dynamical cores, and data-driven parameterizations—that aim to preserve physical fidelity while reducing computational burden (Pawar & San, 2022; Ross et al., 2023; Perezhogin et al., 2023; Liu et al., 2023). In this context, artificial intelligence (AI) provides an efficient route to partial emulation, in which models are trained to reproduce selected outputs of numerical ocean models from a reduced set of inputs, enabling rapid inference of target variables without rerunning computationally expensive regional simulations (Bolton & Zanna, 2019; Sonnewald et al., 2021; Song et al., 2023; Heimbach et al., 2025). Recent work demonstrates that such approaches can emulate and downscale regional ocean states, correct systematic model errors (offline or online), and support physically informed parameterizations in specific settings (Jiang et al., 2023; Liu et al., 2023; Ross et al., 2023; C. Zhang et al., 2023; Sane et al., 2023; Finn et al., 2024). Because partial emulators are designed around a limited set of outputs, they can often operate with an optimized subset of input variables compared with full primitive-equation configurations, reducing data requirements and computational cost while retaining useful skill for the target domain and metrics (Ryzhov et al., 2019; Agarwal et al., 2021). We use the term partial emulation to distinguish this setting from full emulation, in which an entire dynamical core would be replaced by a surrogate.

Although nominally different ocean models—such as MITgcm (Adcroft et al., 2004), ROMS (Haidvogel et al., 2008), NEMO (Madec et al., 2017), etc.—are all based on the same primitive equations, their numerical schemes and parameterizations differ, requiring careful configuration and optimization for each new region. In contrast, AI models for oceanographic applications can be adapted to new basins or target variables through relatively straightforward architectural modifications and retraining (Rus et al., 2023; Barzandeh et al., 2025). Compared with the substantial configuration and computational programming effort required to deploy numerical ocean models, adapting an AI model is typically more streamlined and faster, providing greater flexibility to design, test, and tailor models to specific basins and tasks (Dong et al., 2022; Q. Zhao et al., 2024). Additionally, their ability to bypass computationally expensive full-basin simulations further underscores the value of AI as a powerful and scalable tool for partial-emulation applications. Machine learning, a subset of AI, provides the foundational framework for computers to learn from data, while Deep Learning (DL) is a powerful subset of machine learning that utilizes multi-layered neural networks (NNs) to automatically extract high-level features from complex datasets, making it exceptionally relevant for emulating intricate systems like the ocean (Lou et al., 2023; Hao et al., 2025). Recently, DL-based emulators have been developed as components of digital twins for marine applications, achieving skill levels comparable to regional dynamical forecasts while operating at a fraction of the computational cost (Chattopadhyay et al., 2024; Xu et al., 2024; Miedtank et al., 2024; Dheeshjith et al., 2025). Among DL architectures, convolutional neural networks (CNNs) are particularly adept at processing spatial data (O’Shea & Nash, 2015; Manucharyan et al., 2021; C. Zhang et al., 2025). CNNs are particularly well suited for emulating oceanic multi-dimensional fields because their convolutional filters excel at recognizing and learning spatial patterns, hierarchies, and multi-scale structures—such as eddies, fronts, and large-scale currents—directly from gridded data. This capability enables highly efficient and accurate DL-based modelling, as demonstrated in several recent studies (Bai et al., 2022; Huang et al., 2022; Yuan et al., 2024; Fanelli et al., 2024; Ciani et al., 2025). Within this family, U-Net–style autoencoder CNNs are especially effective for gridded geophysical data (Ronneberger et al., 2015; van der Meer et al., 2023; Bône et al., 2024; Heuer et al., 2024), as the encoder aggregates basin-scale context while the decoder, aided by the skip connections, restores sharp coastal and frontal structures at full resolution. This makes U-Nets naturally suited to dense, pixelwise regression of ocean model outputs.

119 Considering the above, the present study focuses on the partial emulation of sea sur-
120 face currents (SSC), a target variable of paramount operational significance. SSCs are a
121 primary driver for numerous critical applications, including maritime navigation, search-
122 and-rescue operations, oil spill trajectory forecasting, and the transport of marine debris
123 and plankton (Breivik et al., 2013; Röhrs et al., 2023). The study area is the Baltic Sea,
124 a semi-enclosed marginal sea located between approximately 54°N–66°N and 9°E–31°E. It
125 is characterized by a complex bathymetry, multiple sub-basins, and narrow connections to
126 the North Sea through the Danish Straits, which regulate saline inflows and exert a first-
127 order control on basin-wide transports and ventilation (Mohrholz, 2018; Lehmann et al.,
128 2022; Elken & Omstedt, 2025). Surface circulation in the Baltic Sea is strongly driven by
129 local wind forcing, sea-level variations, river discharge, and inflow events from the North
130 Sea, resulting in a highly dynamic and spatially heterogeneous flow field shaped by both
131 geostrophic and ageostrophic components (Leppäranta & Myrberg, 2009; Omstedt et al.,
132 2014; Barzandeh et al., 2024). Its high-latitude location leads to pronounced and sometimes
133 unique responses to climate change, including severe storms and marine heatwaves (Meier
134 et al., 2022; Rutgersson et al., 2022; Bashiri et al., 2025). The circulation exhibits multi-
135 scale dynamics, from basin-wide gyres and estuarine exchange flows (Soosaar et al., 2014;
136 Elken et al., 2015; Lips et al., 2016b; Maljutenko & Raudsepp, 2019) to mesoscale and
137 submesoscale processes that influence mixing, upwelling events, and nutrient transport in
138 the surface layer (Väli et al., 2017, 2024; Salm et al., 2025). Water exchange through
139 narrow straits can significantly impact salinity and ecosystem conditions when blocked or
140 reduced (Liblik et al., 2024). SSCs are thus a key regulators of basin-scale variability of the
141 physical properties (Lips et al., 2016a; Elken & Omstedt, 2025), sea-level variability, and
142 the regional water budgets (Raudsepp et al., 2023; Elken et al., 2024; Jahanmard, Ellmann,
143 & Delpêche-Ellmann, 2025). Beyond emphasizing the role of coastal currents and eddies in
144 particle dispersion and ecosystem connectivity in the Baltic Sea (Hariri et al., 2025), sev-
145 eral studies have highlighted that reliable gridded SSC data are critical for improving wave
146 forecasts, Lagrangian particle tracking, and pollutant dispersion modeling (Kanarik et al.,
147 2021; Christakos et al., 2021; Pärt et al., 2023). Therefore, efficient partial emulation of SSC
148 offers a transformative pathway to support operational services, such as search-and-rescue
149 and pollution response, while advancing scientific understanding of the Baltic Sea’s complex
150 circulation without incurring the high computational cost of full 3D numerical simulations.
151 In this regard, a previous work introduced the SSC emulator sciCUN, a CNN–U–Net–based
152 framework that infers next-day SSC fields in the Gulf of Riga from contemporaneous SSC
153 conditions and five atmospheric drivers on the target day (Barzandeh et al., 2026). Although
154 strong predictive skill was achieved in this relatively homogeneous subregion, performance
155 degraded when the same approach was extended to the full Baltic Sea, where the Gulf of
156 Riga represents only about 4% of the total area (Fig. 1). Such degradation is expected when
157 a model trained or tuned for a compact and comparatively uniform domain is applied to a
158 larger, more heterogeneous basin unless model capacity and representational flexibility are
159 increased. Deeper neural networks are often better able to capture multi-scale and spatially
160 varying features and can generalize more effectively across complex domains (Mhaskar et al.,
161 2017; Eslami & Yun, 2023; X. Zhao et al., 2024; Zavala-Romero et al., 2025). Motivated by
162 these considerations, we introduce **DeepCUN**, a **deeper** and more expressive Convolutional
163 **U–Net** variant designed for SSC emulation over the full Baltic Sea at 1-nautical-mile res-
164 olution. In addition, we aim to examine the explainability of this data-driven “black-box”
165 mapping by assessing how the emulator allocates reliance across the available input informa-
166 tion when generating SSC fields throughout the basin. Explainable AI (XAI) is increasingly
167 emphasized in aquatic applications to support user trust and to diagnose model behavior
168 in safety- and mission-critical settings (Elsayed et al., 2025). Recent work also highlights
169 the value of quantitatively evaluating post hoc explanations (e.g., localization and faithful-
170 ness) for marine data-driven models (Manss & El-Mihoub, 2026). Furthermore, we aim to
171 evaluate the potential multi-day predictability of the learned mapping, by characterizing
172 how forecast errors may grow and skill may change with lead time under idealized forcing
173 conditions.

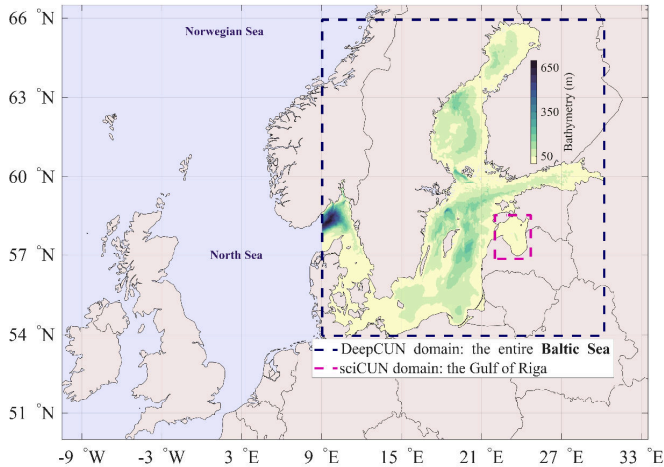


Figure 1. Baltic Sea geography and bathymetry

2 Data and Methods

We begin by designing a framework to train a one-step emulator for daily-mean Baltic SSC. The emulator learns a conditional daily update that maps the SSC state on day t together with daily-mean atmospheric forcing aligned to day $t+1$ to the SSC field on day $t+1$.

2.1 Data for the study domain

2.1.1 SSC.

Daily gridded zonal (u_{SSC}) and meridional (v_{SSC}) SSC components are taken from the Copernicus Marine Environment Monitoring Service (CMEMS) Baltic Sea reanalysis (E.U. Copernicus Marine Service Information (CMEMS), 2025), produced with the Nemo-Nordic 2.0 configuration of NEMO 4.0 (Madec et al., 2017; Kärnä et al., 2021). The native horizontal grid is 1 nautical mile, spanning approximately $\sim 9.0^\circ\text{E} \sim 30.2^\circ\text{E}$ and $\sim 53.0^\circ\text{N} \sim 65.9^\circ\text{N}$ (spatial size: 763 longitudinal grid points \times 774 latitudinal grid points). After applying the land mask, each daily field contains $\mathcal{O}(1.5 \times 10^5)$ wet grid points. We treat these reanalysis SSC fields as reference targets for training and evaluation; validation of the product is documented in (Panteleit et al., 2025).

2.1.2 Atmospheric forcing

Atmospheric variables are obtained from ERA5 (Hersbach et al., 2020, 2023). Following prior Baltic Sea studies of air–sea forcing pathways (Myrberg & Lehmann, 2013; Omstedt et al., 2014; Lehmann et al., 2022), we initially consider mean sea level pressure (msl), 2 m air temperature (t2m), 2 m dew point temperature (d2m), and 10 m wind components (u_{WIND} , v_{WIND}).

2.1.3 Preprocessing and data partitioning

All variables are placed on a common analysis grid obtained by slight cropping of the native products and are indexed by $(i, j) \in \{1, \dots, S_1\} \times \{1, \dots, S_2\}$ with $S_1 = 736$ and

199 $S_2 = 768$ (spanning approximately $\sim 9.8^\circ\text{E} - \sim 30.2^\circ\text{E}$ and $\sim 53.1^\circ\text{N} - \sim 65.9^\circ\text{N}$). The
 200 crop primarily removes land along the western and southern margins, which removes rows
 201 and columns that contain mainly land points and yields spatial dimensions divisible by
 202 $2^5 = 32$, consistent with five successive factor-two downsampling operations in DeepCUN
 203 architecture (Table 1). The SSC land mask on this grid defines the ocean domain $\Omega \subset$
 204 $\{1, \dots, S_1\} \times \{1, \dots, S_2\}$, and all channels are set to zero at land points $(i, j) \notin \Omega$.

205 The dataset is partitioned into a 2015–2023 training period and an independent 2024
 206 test period. Each year provides 364 samples, or 365 in leap years such as 2016 and 2020,
 207 formed from consecutive day pairs $(t, t+1)$. To preserve physical units and interpretability,
 208 SSC channels are left unnormalized. Atmospheric channels are first masked using Ω , and
 209 per-variable extrema are then computed over $(i, j) \in \Omega$ and all times in 2015–2023. Each at-
 210 mospheric channel is normalized using these ocean-only extrema and then linearly (affinely)
 211 rescaled to the pooled SSC range over the same ocean-only training set. For an atmospheric
 212 channel ATM_c this gives

$$\text{ATM}_c^{\text{norm}}(i, j, t) = \left(\frac{\text{ATM}_c(i, j, t) - \min_{\Omega}(\text{ATM}_c)}{\max_{\Omega}(\text{ATM}_c) - \min_{\Omega}(\text{ATM}_c)} \right) (\max_{\Omega}(\text{SSC}) - \min_{\Omega}(\text{SSC})) + \min_{\Omega}(\text{SSC}), \quad (1)$$

213 where $\min_{\Omega}(\cdot)$ and $\max_{\Omega}(\cdot)$ denote extrema taken over $(i, j) \in \Omega$ and all training times, and
 214 $\min_{\Omega}(\text{SSC})$ and $\max_{\Omega}(\text{SSC})$ are computed over $(i, j) \in \Omega$ and all training times by pooling
 215 both SSC components.

2.2 One-step emulation problem

216 For each day t , define an input tensor $\mathbf{X}(\cdot, \cdot, \cdot, t) \in \mathbb{R}^{S_1 \times S_2 \times C_{\text{in}}}$ and output tensor
 217 $\mathbf{Y}(\cdot, \cdot, \cdot, t+1) \in \mathbb{R}^{S_1 \times S_2 \times C_{\text{out}}}$ with $C_{\text{out}} = 2$ corresponding to $(\hat{u}_{\text{SSC}}, \hat{v}_{\text{SSC}})$. In this sense,
 218 DeepCUN is formulated here as a forced one-step partial emulator rather than as an au-
 219 tonomous causal forecast model. The objective is to emulate the daily SSC response of the
 220 NEMO-based reanalysis under a prescribed atmospheric forcing over the target-day interval.
 221 In this formulation, wind at day $t+1$ is treated as external forcing for the update from day
 222 t to day $t+1$, analogous to the atmospheric forcing supplied to a numerical ocean model
 223 during an integration step. In the present study this forcing is taken from ERA5 reanalysis,
 224 so the one-step results quantify emulation skill under realized atmospheric forcing. Opera-
 225 tional use would require replacing ERA5 winds with forecast wind products and explicitly
 226 accounting for forcing uncertainty.
 227

228 To determine which atmospheric channels provide independent predictive information
 229 beyond SSC persistence, we perform an occlusion-sensitivity ablation on the DeepCUN test
 230 set. The analysis indicates negligible incremental contribution from msl, t2m, and d2m once
 231 SSC at day t and wind on day $t+1$ are included. Accordingly, the finalized DeepCUN input
 232 retains only u_{WIND} and v_{WIND} (Appendix Appendix B; Fig. B1) to emulate the next-day
 233 SSC response under prescribed target-day wind forcing:

$$\mathbf{Y}(\cdot, \cdot, \cdot, t+1) = \text{DeepCUN}(\mathbf{X}(\cdot, \cdot, \cdot, t)), \quad (2)$$

234 with channel definitions

$$\begin{aligned} Y(i, j, 1, t+1) &= \hat{u}_{\text{SSC}}(i, j, t+1), \\ Y(i, j, 2, t+1) &= \hat{v}_{\text{SSC}}(i, j, t+1), \\ X(i, j, 1, t) &= u_{\text{SSC}}(i, j, t), \\ X(i, j, 2, t) &= v_{\text{SSC}}(i, j, t), \\ X(i, j, 3, t) &= u_{\text{WIND}}^{\text{norm}}(i, j, t+1), \\ X(i, j, 4, t) &= v_{\text{WIND}}^{\text{norm}}(i, j, t+1). \end{aligned} \quad (3)$$

235 so that the wind channels are aligned with the predicted day ($t+1$), while SSC at day t
 236 provides the antecedent state for the one-step update ($C_{\text{in}} = 4$). Thus, the model learns a

forced state update conditioned on antecedent SSC and prescribed target-day wind, rather than an autonomous forecast model that also predicts future atmospheric forcing.

2.3 DeepCUN architecture

The network follows a five-level encoder–decoder architecture with skip connections, making it deeper than sciCUN, which uses three downsampling levels (Barzandeh et al., 2026), and increasing its multi-scale representational capacity for Baltic-wide heterogeneity. The five-level depth was chosen because the full Baltic Sea domain contains both basin-scale circulation patterns and localized structures associated with coastlines, narrow straits, gulfs, and the western boundary exchange corridor. Repeated downsampling increases the effective receptive field and allows the encoder to aggregate broader spatial context, while skip connections preserve high-resolution information needed to reconstruct coastal and frontal details. This design choice is supported by the architecture ablation in Appendix B2, where the finalized five-level DeepCUN configuration outperforms the shallower sciCUN-style three-level architecture on the independent 2024 test period. Each encoder block applies a 3×3 convolution, group normalization (GN), and ReLU (Wu & He, 2020; Nair & Hinton, 2010), followed by 2×2 max pooling with stride 2 (Nagi et al., 2011). GN is used instead of batch normalization (BN) because the full-domain training setup uses a mini-batch size of 1, for which BN statistics are poorly estimated and can become unstable. In contrast, GN normalizes feature groups within each sample and is therefore better suited to the memory-limited streaming training strategy used here. The BN comparison in Appendix B2 further supports this choice, showing that replacing GN with BN in DeepCUN increases the emulation error. Channel widths increase with depth as (32, 64, 128, 256, 512), followed by a bottleneck convolution with 1024 channels. The decoder mirrors the encoder using transposed convolutions for learnable upsampling (Glorot & Bengio, 2010; He et al., 2015), followed at each level by concatenation with the corresponding encoder activations and a 3×3 Conv–GN–ReLU refinement block. This U-Net-style design combines the coarse contextual information recovered by the decoder with high-resolution encoder features (Ronneberger et al., 2015). Because transposed convolutions can introduce checkerboard-like artifacts in some image-generation settings (Odena et al., 2016), each DeepCUN upsampling step is followed by skip-feature concatenation and convolutional refinement. A final 1×1 convolution maps the decoder features to $C_{\text{out}} = 2$ output channels. The full layer-by-layer configuration is reported in Table 1.

2.4 Training strategy and evaluation

Training minimizes the half mean squared error between predicted and reference SSC components, augmented by an L_2 regularization term on the learnable weights:

$$\mathcal{L}_{\text{tot}} = \mathcal{L}_{\text{data}} + \lambda \|\mathbf{W}\|_2^2, \quad \mathcal{L}_{\text{data}} = \frac{1}{2} \left[(\hat{u}_{\text{SSC}} - u_{\text{SSC}})^2 + (\hat{v}_{\text{SSC}} - v_{\text{SSC}})^2 \right], \quad (4)$$

where \hat{u}_{SSC} and \hat{v}_{SSC} are the predicted SSC components and u_{SSC} and v_{SSC} are the corresponding reference components, \mathbf{W} denotes the collection of learnable weights, and $\lambda = 10^{-4}$.

A practical objective of SSC emulation is computational cost reduction relative to running full ocean circulation models; consequently, a training workflow that depends on repeated access to supercomputing resources would weaken this premise. We therefore adopt a training strategy that is feasible on a single workstation/desktop computer equipped with one commodity GPU while still exposing the network to multi-year variability. Because the full multi-year dataset at 1 nautical-mile resolution does not fit in typical GPU memory, training is conducted in a memory-efficient streaming scheme that processes one calendar year at a time. The network is initialized on the first annual chunk, and subsequent years are warm-started from the previously learned weights while keeping the architecture fixed. To improve temporal mixing, the 9 training years (2015–2023) are cycled through for 8 passes;

Table 1. DeepCUN architecture summary. Tensor dimensions are reported consistently as (longitude) \times (latitude) \times (channels). The input tensor has dimensions $S_1 \times S_2 \times C_{\text{in}}$. $\text{Conv}(k, k, n)$ denotes a 2-D convolution with a $k \times k$ kernel and n output feature channels (spatial dimensions preserved within the block by padding), followed by GN and ReLU as indicated. GN_g partitions the feature channels into g groups prior to normalization. $\text{MaxPool}_{[p,p] \rightarrow st} \downarrow$ denotes $p \times p$ max pooling with stride st , and the symbol \downarrow indicates downsampling by a factor of 2 in each horizontal dimension. In the decoder, $\text{TConv}(k, k, n) \uparrow$ denotes a transposed convolution used for upsampling; the symbol \uparrow indicates upsampling by a factor of 2 in each horizontal dimension. $\text{Concat}(E\ell)$ concatenates (along the channel dimension) the decoder feature maps with the corresponding encoder activations from level $E\ell$ (skip connection). The arrow \rightarrow denotes sequential composition of operations within a stage. The finalized configuration values for the Baltic Sea scenario considered in this study are $k = 3$, $p = 2$, $st = 2$, $n_F = 2^5$, and $n_G = 2^2$, selected empirically through systematic trial-and-error experiments.

Stage	Operation(s)	Output
Input	Preprocessed input tensor \mathbf{X}	$S_1 \times S_2 \times C_{\text{in}}$
E1	$\text{Conv}(k, k, n_F 2^0) \text{GN}_{n_G 2^0} \rightarrow \text{ReLU} \rightarrow \text{MaxPool}_{[p,p] \rightarrow st} \downarrow$	$\frac{S_1}{2^1} \times \frac{S_2}{2^1} \times n_F 2^0$
E2	$\text{Conv}(k, k, n_F 2^1) \text{GN}_{n_G 2^1} \rightarrow \text{ReLU} \rightarrow \text{MaxPool}_{[p,p] \rightarrow st} \downarrow$	$\frac{S_1}{2^2} \times \frac{S_2}{2^2} \times n_F 2^1$
E3	$\text{Conv}(k, k, n_F 2^2) \text{GN}_{n_G 2^2} \rightarrow \text{ReLU} \rightarrow \text{MaxPool}_{[p,p] \rightarrow st} \downarrow$	$\frac{S_1}{2^3} \times \frac{S_2}{2^3} \times n_F 2^2$
E4	$\text{Conv}(k, k, n_F 2^3) \text{GN}_{n_G 2^3} \rightarrow \text{ReLU} \rightarrow \text{MaxPool}_{[p,p] \rightarrow st} \downarrow$	$\frac{S_1}{2^4} \times \frac{S_2}{2^4} \times n_F 2^3$
E5	$\text{Conv}(k, k, n_F 2^4) \text{GN}_{n_G 2^4} \rightarrow \text{ReLU} \rightarrow \text{MaxPool}_{[p,p] \rightarrow st} \downarrow$	$\frac{S_1}{2^5} \times \frac{S_2}{2^5} \times n_F 2^4$
B	$\text{Conv}(k, k, n_F 2^5) \text{GN}_{n_G 2^5} \rightarrow \text{ReLU}$	$\frac{S_1}{2^5} \times \frac{S_2}{2^5} \times n_F 2^5$
D5	$\text{TConv}(k, k, n_F 2^4) \uparrow \rightarrow \text{Concat}(E5) \rightarrow \text{Conv}(k, k, n_F 2^4) \text{GN}_{n_G 2^4} \rightarrow \text{ReLU}$	$\frac{S_1}{2^4} \times \frac{S_2}{2^4} \times n_F 2^4$
D4	$\text{TConv}(k, k, n_F 2^3) \uparrow \rightarrow \text{Concat}(E4) \rightarrow \text{Conv}(k, k, n_F 2^3) \text{GN}_{n_G 2^3} \rightarrow \text{ReLU}$	$\frac{S_1}{2^3} \times \frac{S_2}{2^3} \times n_F 2^3$
D3	$\text{TConv}(k, k, n_F 2^2) \uparrow \rightarrow \text{Concat}(E3) \rightarrow \text{Conv}(k, k, n_F 2^2) \text{GN}_{n_G 2^2} \rightarrow \text{ReLU}$	$\frac{S_1}{2^2} \times \frac{S_2}{2^2} \times n_F 2^2$
D2	$\text{TConv}(k, k, n_F 2^1) \uparrow \rightarrow \text{Concat}(E2) \rightarrow \text{Conv}(k, k, n_F 2^1) \text{GN}_{n_G 2^1} \rightarrow \text{ReLU}$	$\frac{S_1}{2^1} \times \frac{S_2}{2^1} \times n_F 2^1$
D1	$\text{TConv}(k, k, n_F 2^0) \uparrow \rightarrow \text{Concat}(E1) \rightarrow \text{Conv}(k, k, n_F 2^0) \text{GN}_{n_G 2^0} \rightarrow \text{ReLU}$	$S_1 \times S_2 \times n_F 2^0$
O	$\text{Conv}(1, 1, C_{\text{out}})$	$S_1 \times S_2 \times C_{\text{out}}$

285 within each pass, each annual chunk is trained for 6 epochs using Adam with mini-batch size
 286 1 (enabled by GN), shuffled samples, and an initial learning rate of 8×10^{-4} (Marquardt,
 287 1963; Bishop, 2006; Kingma & Ba, 2017). On a single NVIDIA GeForce RTX 3060 GPU
 288 (12 GB), training requires about one minute per annual chunk per epoch per pass, corre-
 289 sponding to a total of approximately 9 (years) \times 8 (passes) \times 6 (epochs) \approx 432 minutes (\sim 7
 290 hours), which is sufficient for convergence in this configuration. For inference, the finalized
 291 DeepCUN model contains approximately 18.9 million trainable parameters, corresponding
 292 to about 75.5 MB of FP32 weights. On the same NVIDIA GeForce RTX 3060 GPU used
 293 for training, the forward pass for one full-domain 736×768 daily SSC field with batch size
 294 1 requires approximately 0.043 s and uses about 0.13 GB of GPU memory. These estimates
 295 exclude data loading, preprocessing, and post-processing. Therefore, the reported values
 296 characterize the inference cost of the trained neural emulator itself.

297 Model performance is evaluated on the held-out 2024 test period using vector-error
 298 and component-wise measures, and we additionally assess rotational structure using relative
 299 vorticity diagnostics. Because interpretation of surface circulation depends on both
 300 current magnitude and current direction, we use complementary metrics rather than a single
 301 scalar error. The primary metrics are Euclidean distance (ED), mean absolute error
 302 (MAE), and the Pearson correlation coefficient (CC), computed gridwise and summarized
 303 spatially where needed. In addition to velocity-component and vector-error statistics, the
 304 vorticity-based diagnostics are included because circulation assessment depends on both
 305 current magnitude and flow orientation. The vorticity sign agreement used in the case stud-
 306 ies evaluates whether predicted and reference fields have the same cyclonic or anticyclonic
 307 orientation. However, sign agreement alone does not quantify whether the spatial organiza-
 308 tion or relative strength of rotational structures is reproduced. We therefore also compute
 309 a normalized vorticity pattern skill (VPS) over the full 2024 test period. VPS combines
 310 the spatial correlation between predicted and reference relative-vorticity fields with a nor-
 311 malized vorticity-amplitude similarity term, providing a scale-normalized dynamical metric
 312 that complements the sign-agreement diagnostic. Full definitions of the skill metrics are
 313 provided in Appendix Appendix A.

314 2.5 XAI assessment

315 In this study, we implemented a two-stage XAI workflow that separates input configura-
 316 tion from post hoc interpretation. First, during model-configuration finalization, we per-
 317 formed an occlusion-sensitivity analysis to refine the candidate input set, in which individual
 318 channels were systematically masked and the resulting change in out-of-sample forecast skill
 319 was evaluated relative to the unmasked baseline (Appendix Appendix B). This masking-
 320 based ablation served as a channel-selection step by quantifying each input’s net contribution
 321 to predictive skill under a prescribed intervention. By construction, however, it provides
 322 only a domain-aggregated measure of channel influence and does not yield spatially resolved
 323 attribution patterns or pointwise measures of local input–output dependence. Second, after
 324 training the final network using the occlusion-selected inputs, we carried out a post hoc
 325 interpretability assessment that conditions on the learned parameters and thus character-
 326 izes how the trained model exploits the retained information; this stage was organized into
 327 two phases, described below. In summary, occlusion is an intervention-based, skill-level test
 328 that does not require access to internal gradients or relevance propagation rules, whereas
 329 the post hoc methods are explicitly weight-conditioned analyses of the trained DeepCUN
 330 mapping that use the learned parameters to attribute and differentiate input influence.

331 To structure the post hoc interpretation, we use two complementary notions of input
 332 importance. The first is attributed support, which describes where and through which input
 333 channels the trained model recruits information to construct the predicted SSC field. This
 334 quantity is evaluated with Layer-wise Relevance Propagation (LRP), which redistributes the
 335 model output backward through the network and yields spatial relevance maps (Montavon
 336 et al., 2019). The second is local responsiveness, or elasticity, which describes how strongly

337 the predicted SSC component magnitude at a grid point responds to a small co-located
 338 perturbation of an input variable. This quantity is evaluated with the Diagonal Jacobian
 339 Elasticity (DJE) metric, a gradient-based diagnostic inspired by attribution and saliency
 340 analyses (LeCun et al., 2012; Simonyan et al., 2014). The two diagnostics are intention-
 341 ally non-redundant because LRP characterizes attributed support pathways, whereas DJE
 342 quantifies local co-located magnitude responsiveness.

343 **2.5.1 post-hoc XAI—Phase 1: LRP for attributed support**

344 Considering Eq. (3), we design and apply an architecture-aware version of LRP to our
 345 SSC emulator to quantify attributed support, or the importance of the presence of infor-
 346 mative input-channel evidence, defined here as the spatial distribution of input evidence
 347 supporting each predicted SSC component. DeepCUN maps the input tensor $X(i, j, c, t)$ to
 348 the output field $Y(i, j, k, t+1)$ through the encoder–decoder operators in Table 1. LRP mir-
 349 rors this computation in reverse and assigns to each input element a relevance score, yielding
 350 an input relevance tensor $R_{c,k}(i, j, t)$ consistent with the indexing of Eq. (3). Specifically,
 351 relevance is propagated through the full DeepCUN computation graph, applying redistribu-
 352 tion rules at each operator in Table 1 (Conv/TCConv, GN, ReLU, pooling/unpooling, and
 353 skip concatenations), yielding an operator-wise backward pass that is conditioned on the
 354 forward activations.

355 LRP is applied independently for each output component $k \in \{1, \dots, C_{\text{out}}\}$. Because
 356 SSC predictions are signed, we implement a two-sided initialization in which positive and
 357 negative predicted values are treated as separate nonnegative targets. For each sample t
 358 and output component k , relevance is initialized at the network output as

$$R_k^{(0)+}(i, j, t) = \max(Y(i, j, k, t+1), 0), \quad R_k^{(0)-}(i, j, t) = \max(-Y(i, j, k, t+1), 0). \quad (5)$$

359 Each branch is propagated back to the inputs using the same redistribution rules, yielding
 360 input-side relevance tensors $\tilde{R}_{c,k}^+(i, j, t)$ and $\tilde{R}_{c,k}^-(i, j, t)$. We report a direction-independent
 361 attributed-support map by combining the two branches as

$$R_{c,k}(i, j, t) = \tilde{R}_{c,k}^+(i, j, t) + \tilde{R}_{c,k}^-(i, j, t), \quad (6)$$

362 which is nonnegative in typical cases under the z^+ redistribution used below; any residual
 363 negative values (arising, e.g., from negative forward activations multiplying positive back-
 364 ward messages) are set to zero for scoring and visualization, and do not affect the relevance
 365 propagation rules.

366 For each linear operator Op (e.g. Conv or TCConv), relevance is redistributed using an ε -
 367 stabilized z^+ rule retaining only positive contributions. Here and below, $R(i, j, \cdot, k, t)$ denotes
 368 the relevance tensor at an intermediate layer (the output of the current operator), whereas
 369 $R_{c,k}(i, j, t)$ denotes relevance evaluated at the input layer in channel c . Let $A(i, j, \cdot, t)$ denote
 370 the forward activation entering Op, let $R(i, j, \cdot, k, t)$ denote the relevance at its output for
 371 component k , and let $W^+ = \max(W, 0)$. Here W denotes the weight tensor of the current
 372 linear operator Op (not the full parameter set \mathbf{W} in Eq. (4)). With stabilization constant
 373 ε_{LRP} , we compute

$$Z^+(i, j, \cdot, t) = \text{Op}(A, W^+) + \varepsilon_{\text{LRP}},$$

$$R_{\text{in}}(i, j, \cdot, k, t) = A(i, j, \cdot, t) \odot \text{Op}^\top \left(\frac{R(i, j, \cdot, k, t)}{Z^+(i, j, \cdot, t)}, W^+ \right), \quad (7)$$

374 where Op^\top is the exact transpose of the forward operator implemented with the same
 375 padding, stride, and cropping conventions as in Table 1, and \odot denotes elementwise multi-
 376 plication. In all experiments, $\varepsilon_{\text{LRP}} = 10^{-6}$.

377 Nonlinear and routing layers follow the forward topology, with relevance gated by ReLU
 378 support, max-pooling relevance returned to recorded argmax locations via max-unpooling,

379 and concatenation relevance split into upsample and skip branches according to the forward
 380 channel partition, with skip relevance accumulated at the matched encoder resolution. GN
 381 is handled in a GN-aware manner by caching the per-sample forward group statistics (mean
 382 and inverse standard deviation) and propagating relevance through the corresponding fixed
 383 normalization transform via an ε -stabilized z^+ rule acting on the effective per-channel gain
 384 and centered activations (Wu & He, 2020). Interpretability is restricted to the ocean do-
 385 main Ω defined by the land-sea mask; relevance is set to zero over land. LRP is computed
 386 on all daily samples from 2023 (in-distribution inputs, $N_{\text{samp}:2023} = 364$) by applying the
 387 trained DeepCUN and propagating relevance backward through the fixed network, yielding
 388 maps $R_{c,k}(i, j, t)$ for $(i, j) \in \Omega$, $c \in \{1, \dots, C_{\text{in}}\}$, and $k \in \{1, \dots, C_{\text{out}}\}$. Using in-distribution
 389 2023 samples (for which benchmarking indicates near-saturated skill and minimal systematic
 390 residual structure on inputs drawn from the training distribution) emphasizes attribution
 391 patterns tied to learned features of the mapping, enabling the relevance maps to be inter-
 392 preted as the model’s intrinsic evidence pathways rather than responses to distribution shift
 393 or extrapolative error compensation under unseen test conditions.

394 To reduce sensitivity to rare extreme values and to place all channels and both velocity
 395 components on a common within-sample scale, each sample is rescaled by a robust ocean-
 396 only factor $\mathcal{S}_{LRP}(t)$ computed from the pooled distribution of strictly positive relevance
 397 values across all (c, k) over Ω :

$$\mathcal{S}_{LRP}(t) = P_{99} \left(\left\{ R_{c,k}(i, j, t) : (i, j) \in \Omega, c, k, R_{c,k}(i, j, t) > 0 \right\} \right), \quad (8)$$

398 where P_{99} denotes the 99th percentile. The normalized per-sample score is

$$\text{Score}_{LRP}(i, j, c, k, t) = \min \left\{ 100, \max \left\{ 0, 100 \frac{R_{c,k}(i, j, t)}{\mathcal{S}_{LRP}(t)} \right\} \right\}, \quad (9)$$

399 and the reported LRP support score is the sample mean,

$$\overline{\text{Score}}_{LRP}(i, j, c, k) = \frac{1}{N_{\text{samp}:2023}} \sum_{t=1}^{N_{\text{samp}:2023}} \text{Score}_{LRP}(i, j, c, k, t), \quad (10)$$

400 with $\overline{\text{Score}}_{LRP}(i, j, c, k) = 0$ for $(i, j) \notin \Omega$. The tensor $\overline{\text{Score}}_{LRP}(i, j, c, k)$ (percent) summa-
 401 rizes persistent attributed-support patterns across 2023 under the finalized inputs in Eq. (3)
 402 and the operators in Table 1.

403 **2.5.2 post-hoc XAI – Phase 2: DJE for quantifying local responsiveness** 404 **(elasticity)**

405 For each output component $k \in \{1, \dots, C_{\text{out}}\}$ and input channel $c \in \{1, \dots, C_{\text{in}}\}$, DJE
 406 targets the spatial-diagonal input–output derivative

$$D_{c,k}(i, j, t) := \frac{\partial \tilde{Y}_k(i, j, t+1)}{\partial X(i, j, c, t)}, \quad (11)$$

407 i.e., the derivative of the prediction at grid point (i, j) with respect to the input at the same
 408 grid point (i, j) . It is important to emphasize that DJE is a spatial-diagonal diagnostic. It
 409 measures the same-grid sensitivity of the predicted SSC component magnitude at (i, j) to
 410 an input perturbation applied at the same grid point (i, j) . Therefore, DJE should not be
 411 interpreted as a full spatial influence map. Nonlocal dependencies between distant input
 412 and output locations may exist through the convolutional receptive field, pooling operations,
 413 skip connections, and decoder structure of DeepCUN, but these off-diagonal Jacobian terms
 414 are excluded by construction in Eq. (11). DJE is therefore used here as a diagnostic of local
 415 co-located responsiveness, complementary to LRP, which is used to characterize broader
 416 attributed support pathways.

417 Although Eq. (11) is written as an input–output derivative, it is evaluated for the
 418 trained DeepCUN mapping. Let F_{θ} denote the trained network with parameters θ , so that

$$\mathbf{Y}(\cdot, \cdot, \cdot, t+1) = F_{\theta}(\mathbf{X}(\cdot, \cdot, \cdot, t)) \quad (\text{equivalently, Eq. (2)}). \quad (12)$$

419 Then $D_{c,k}(i, j, t)$ is the (i, j) -diagonal element of the Jacobian of the composite map $\mathbf{X} \mapsto$
 420 $\phi \circ F_{\theta}(\mathbf{X})$. It is computed by automatic differentiation through the complete DeepCUN
 421 computation graph (all operators in Table 1) via the chain rule. Therefore, every intermedi-
 422 ate operator (Conv/TConv, GN, ReLU, max pooling, and skip concatenations) affects $D_{c,k}$
 423 through its Jacobian evaluated at the realized forward-pass state for that sample and, where
 424 applicable, through learned weights. DJE reports only this end-to-end local derivative and
 425 does not decompose $D_{c,k}$ into per-layer contributions.

426 Because the predicted SSC components are signed, we apply a smooth pointwise mag-
 427 nitude transform to each scalar component prediction:

$$\phi : \mathbb{R} \rightarrow \mathbb{R}_+, \quad \phi(y) = \sqrt{y^2 + \varepsilon_{\phi}^2}, \quad \varepsilon_{\phi} = 10^{-6}, \quad (13)$$

428 which is a differentiable approximation of $|y|$. We then define

$$\tilde{Y}_k(i, j, t+1) := \phi(Y(i, j, k, t+1)) = \sqrt{Y(i, j, k, t+1)^2 + \varepsilon_{\phi}^2}. \quad (14)$$

429 The use of ϕ has an important interpretive consequence. Because ϕ maps signed SSC-
 430 component predictions to a smooth magnitude-like quantity, DJE quantifies sensitivity of
 431 the predicted component magnitude rather than sensitivity of the signed component itself.
 432 Directional information associated with the sign of $Y(i, j, k, t+1)$ is therefore not retained
 433 in the reported DJE score. In addition, the derivative of the transform is

$$\phi'(y) = \frac{y}{\sqrt{y^2 + \varepsilon_{\phi}^2}}, \quad (15)$$

434 which approaches zero as y approaches zero. Consequently, DJE is less sensitive in regions
 435 or times where the predicted SSC component is close to zero. We therefore interpret DJE as
 436 a magnitude-responsiveness diagnostic rather than as a diagnostic of signed flow-direction
 437 sensitivity.

438 Computing Eq. (11) at all (i, j) by forming the full spatial Jacobian is prohibitively
 439 expensive. We therefore estimate the spatial-diagonal field using a randomized Rademacher-
 440 probe diagonal estimator (Hutchinson/Bekas-style probing) with $n_{\text{probe}} = 8$ probes (Hutchinson,
 441 1990; Bekas et al., 2007; Avron & Toledo, 2011). This value was selected from a probe-count
 442 ablation that balanced stability of the DJE visualization against the approximately linear
 443 increase in computational cost with the number of probes (Appendix B3).

444 Fix a day t and output component k . Perform one forward pass of the trained network to
 445 obtain $Y(i, j, k, t+1)$ and $\tilde{Y}_k(i, j, t+1)$ (Eq. (14)). The same forward-pass state (activations,
 446 ReLU gating, and max-pooling argmax routing) is used for all probes $r = 1, \dots, n_{\text{probe}}$.

447 For each probe r , draw a probe field $V_r(i, j)$ such that $V_r(i, j) \in \{-1, +1\}$ on ocean
 448 points $(i, j) \in \Omega$ with equal probability, and $V_r(i, j) = 0$ on land points $(i, j) \notin \Omega$. The draws
 449 are independent across probes r and across ocean grid points within each probe. Define the
 450 scalar objective

$$J_{k,r}(t) := \sum_{i=1}^{S_1} \sum_{j=1}^{S_2} V_r(i, j) \tilde{Y}_k(i, j, t+1), \quad (16)$$

451 and compute its gradient with respect to the full input tensor,

$$G_{c,k,r}(i, j, t) := \frac{\partial J_{k,r}(t)}{\partial X(i, j, c, t)}. \quad (17)$$

452 The stochastic diagonal estimator is then

$$\widehat{D}_{c,k}(i, j, t) := \frac{1}{n_{\text{probe}}} \sum_{r=1}^{n_{\text{probe}}} V_r(i, j) G_{c,k,r}(i, j, t). \quad (18)$$

453 To see why this targets the spatial diagonal, write $J_{k,r}(t) = \sum_{p,q} V_r(p, q) \widetilde{Y}_k(p, q, t+1)$
 454 and apply the chain rule:

$$G_{c,k,r}(i, j, t) = \sum_{p,q} V_r(p, q) \frac{\partial \widetilde{Y}_k(p, q, t+1)}{\partial X(i, j, c, t)}. \quad (19)$$

455 Multiplying by $V_r(i, j)$ and taking expectation over probe randomness uses

$$\mathbb{E}[V_r(i, j)V_r(p, q)] = \delta_{(i,j),(p,q)} \quad \text{for } (i, j), (p, q) \in \Omega, \quad (20)$$

456 and the expectation is zero if either index lies on land because $V_r = 0$ there. Hence off-
 457 diagonal terms $(p, q) \neq (i, j)$ cancel in expectation, giving

$$\mathbb{E}[\widehat{D}_{c,k}(i, j, t)] = \frac{\partial \widetilde{Y}_k(i, j, t+1)}{\partial X(i, j, c, t)}. \quad (21)$$

458 Therefore, $\widehat{D}_{c,k}(i, j, t)$ is an unbiased (in expectation over probes) Monte Carlo estimator
 459 of the spatial-diagonal derivative in Eq. (11), with sampling noise decreasing as n_{probe}
 460 increases.

461 To compare responsiveness across input channels with different units and variance,
 462 define an ocean-only scale σ_c as the standard deviation of input channel c over $(i, j) \in \Omega$
 463 and all samples in the analysis year. Define the standardized elasticity

$$\widehat{E}_{c,k}(i, j, t) := \left| \widehat{D}_{c,k}(i, j, t) \right| \sigma_c, \quad (22)$$

464 and set $\widehat{E}_{c,k}(i, j, t) = 0$ for $(i, j) \notin \Omega$.

465 As in the LRP analysis, DJE is computed for all daily samples in 2023. For each day t ,
 466 we compute $\widehat{E}_{c,k}(\cdot, \cdot, t)$ for all (c, k) and define a single robust normalizer shared across all
 467 $C_{\text{in}}C_{\text{out}}$ maps:

$$\mathcal{S}_{\text{DJE}}(t) = \text{P}_{99} \left(\left\{ \widehat{E}_{c,k}(i, j, t) : (i, j) \in \Omega, c = 1, \dots, C_{\text{in}}, k = 1, \dots, C_{\text{out}}, \widehat{E}_{c,k}(i, j, t) > 0 \right\} \right). \quad (23)$$

468 The per-sample normalized elasticity score is

$$\text{Score}_{\text{DJE}}(i, j, c, k, t) = \min \left\{ 100, \max \left\{ 0, 100 \frac{\widehat{E}_{c,k}(i, j, t)}{\mathcal{S}_{\text{DJE}}(t)} \right\} \right\}, \quad (24)$$

469 and the reported elasticity score is the sample mean

$$\overline{\text{Score}}_{\text{DJE}}(i, j, c, k) = \frac{1}{N_{\text{samp}:2023}} \sum_{t=1}^{N_{\text{samp}:2023}} \text{Score}_{\text{DJE}}(i, j, c, k, t). \quad (25)$$

470 The tensor $\overline{\text{Score}}_{\text{DJE}}(i, j, c, k)$ (percent) summarizes persistent local responsiveness (elasticity)
 471 patterns across 2023 under the finalized inputs in Eq. (3) and the forward operators in
 472 Table 1.

473 2.6 Autoregressive multi-day rollout under prescribed forcing

474 DeepCUN is trained for one-step forced emulation (Eq. (3)). To evaluate stability under
 475 recursive deployment and to quantify potential medium-range behavior under prescribed

476 forcing, we run DeepCUN in an autoregressive loop in which predicted SSCs are recycled
 477 as SSC inputs for subsequent steps, while wind forcing is prescribed at the corresponding
 478 lead time.

479 For a forecast initialized at day t , set

$$\widehat{Y}(i, j, 1, t) = u_{\text{SSC}}(i, j, t), \quad \widehat{Y}(i, j, 2, t) = v_{\text{SSC}}(i, j, t), \quad (26)$$

480 and for lead $n \geq 0$ form the next-step input tensor (with $C_{\text{in}} = 4$)

$$\begin{aligned} \widehat{X}(i, j, 1, t+n) &= \widehat{Y}(i, j, 1, t+n), \\ \widehat{X}(i, j, 2, t+n) &= \widehat{Y}(i, j, 2, t+n), \\ \widehat{X}(i, j, 3, t+n) &= u_{\text{WIND}}^{\text{norm}}(i, j, t+n+1), \\ \widehat{X}(i, j, 4, t+n) &= v_{\text{WIND}}^{\text{norm}}(i, j, t+n+1), \end{aligned} \quad (27)$$

481 so that wind remains aligned with the predicted day, as in Eq. (3). The recursion is

$$\widehat{Y}(i, j, :, t+n+1) = \text{DeepCUN}\left(\widehat{X}(i, j, :, t+n)\right), \quad n = 0, 1, \dots, N-1, \quad (28)$$

482 yielding the N -day sequence

$$\left\{ \widehat{Y}(i, j, :, t+1), \widehat{Y}(i, j, :, t+2), \dots, \widehat{Y}(i, j, :, t+N) \right\}. \quad (29)$$

483 This experiment is designed as a controlled potential and stability assessment, not as
 484 an operationally deployable forecast system. In the present setup, (i) the wind forcing is
 485 taken from ERA5 reanalysis (not from real-time numerical weather prediction forecasts),
 486 and (ii) the initial SSC state is taken from reanalysis. Therefore, the experiment quantifies
 487 how forecast errors accumulate under recursion when the forcing is effectively ‘perfect’ and
 488 when only the SSC state is being propagated by the network. Operational deployment
 489 would require near-real-time SSC initialization, forecast wind products, and an explicit
 490 treatment of forcing uncertainty and data latency; these considerations are outside the scope
 491 of the current study, which focuses on partial emulation and interpretability using reanalysis-
 492 consistent inputs. Figure 2 schematizes the network and the autoregressive deployment.

493 3 Results

494 3.1 DeepCUN Performance in SSC Emulation

495 Figure 3 summarizes DeepCUN performance for the zonal and meridional SSC compo-
 496 nents during the 2024 test period. The annual-mean MAE fields (Fig. 3b,d, right panels)
 497 show that prediction errors are largest along the western boundary, the principal exchange
 498 corridor between the Baltic Sea and the North Sea, where MAE reaches about 10 cm s^{-1} .
 499 In contrast, errors remain below 5 cm s^{-1} across most of the basin interior, indicating sub-
 500 stantially improved predictive accuracy. Additional basin-wide statistics were computed to
 501 summarize the annual performance quantitatively. The domain-mean MAE is 2.2 cm s^{-1} for
 502 u_{SSC} and 2.3 cm s^{-1} for v_{SSC} , while the annual mean spatially averaged ED is 3.6 cm s^{-1} .

503 The ground-truth fields (hereafter denoted by the NEMO suffix), derived from the
 504 CMEMS Baltic Sea reanalysis (Section 2.1.1), exhibit an annual velocity range of approxi-
 505 mately $\pm 270 \text{ cm s}^{-1}$, with extremes concentrated near the western boundary due to ener-
 506 getic exchange flows. Despite this strong variability, DeepCUN maintains robust skill over
 507 both the coastal zones and the interior basin east of the Danish Straits (roughly east of
 508 12°E), capturing the dominant circulation patterns with consistently low errors. The left-
 509 side panels of Figure 3 (a,c) display the spatial distribution of CC computed grid point
 510 by grid point over the entire year. The CC remains consistently high, generally exceeding
 511 0.9, which indicates that DeepCUN captures the temporal variability and direction of the

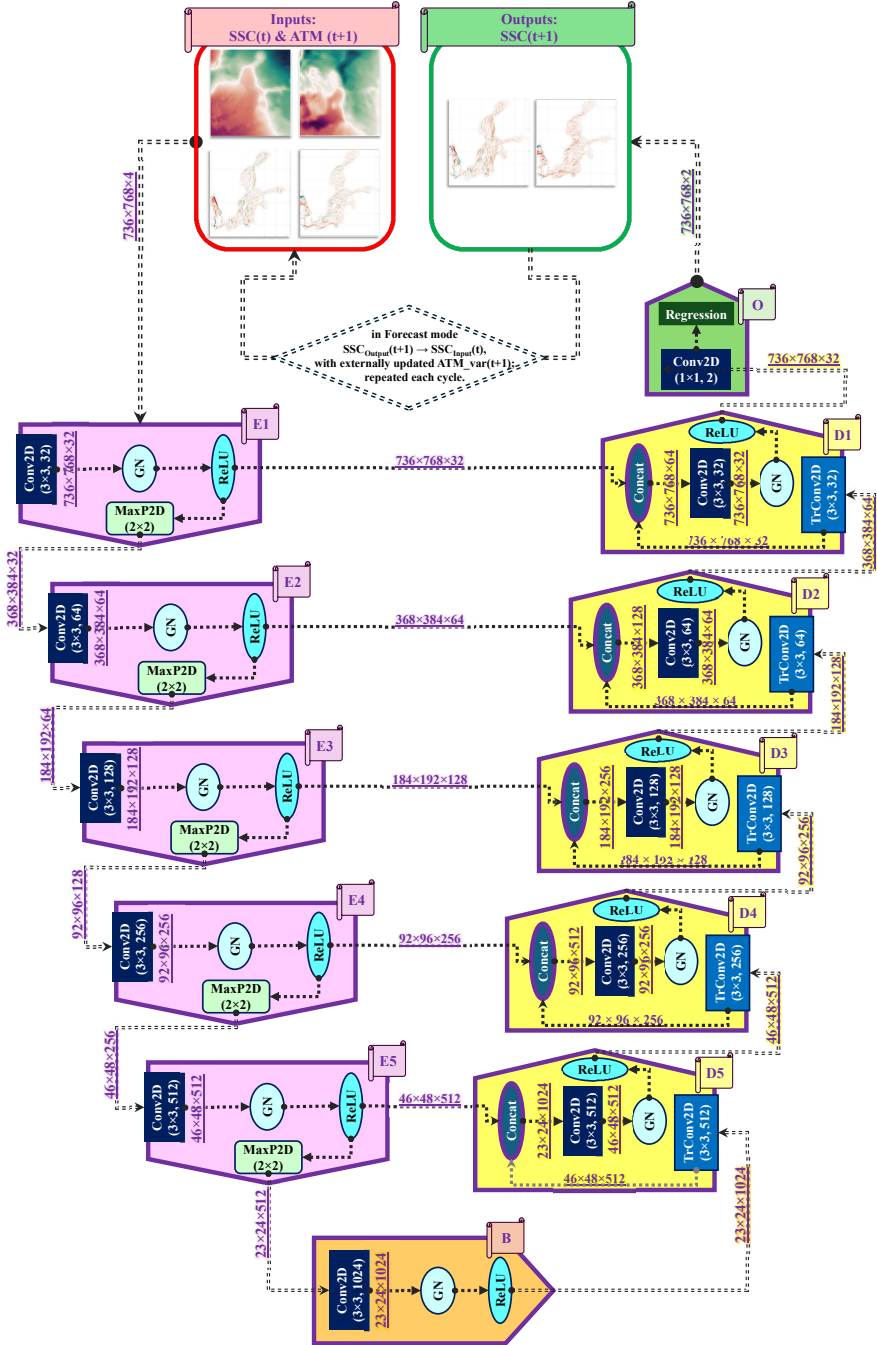


Figure 2. DeepCUN architecture and multi-day forecasting framework. Encoder (E1–E5, pink), bottleneck (B, orange), decoder (D5–D1, yellow), and output head (O, green; 1x1 Conv → regression loss).

512 flow reliably, even where MAE is elevated. Additional basin-wide correlation statistics were
 513 computed to complement the spatial CC maps. The domain-mean CC is 0.9 for both u_{SSC}
 514 and v_{SSC} , with corresponding domain-median values of 0.93 and 0.92, respectively. The
 515 western-boundary error maximum is physically consistent with the regional dynamics of the
 516 southwestern Baltic exchange corridor. This area includes the Danish Straits and the ad-
 517 jacent transition region toward the North Sea, where surface currents are strongly affected
 518 by narrow straits, complex bathymetry, coastal steering, and rapidly varying inflow–outflow
 519 conditions. Previous Baltic Sea studies have shown that exchange through this region is
 520 controlled by sea-level gradients, large-scale atmospheric circulation patterns, wind forcing,
 521 barotropic adjustment, and episodic inflow events, producing sharp velocity gradients and
 522 energetic, spatially confined current structures (Gustafsson, 1997; Elken et al., 2008; Bendt-
 523 sen et al., 2009; Karabil et al., 2018; Börgel et al., 2026). In such regions, even small errors
 524 in the timing, width, or lateral position of an exchange jet can produce comparatively large
 525 component-wise MAE and ED, although the broader circulation pattern may remain well
 526 correlated. This explains why the western boundary exhibits the largest absolute errors
 527 while retaining high temporal correlation.

528 The elevated errors also reflect a limitation of the reduced-input DeepCUN formulation.
 529 The model receives antecedent SSC and target-day wind forcing, but it does not receive ex-
 530 plicit open-boundary information such as boundary sea level, boundary transports, salinity-
 531 driven exchange structure, or externally imposed barotropic pressure gradients. Therefore,
 532 variability associated with the North Sea–Baltic exchange must be inferred indirectly from
 533 the previous SSC state and the wind field. This makes the exchange corridor more chal-
 534 lenging than the basin interior, where the daily surface-current evolution is more directly
 535 constrained by spatially coherent wind forcing and local persistence. Nonetheless, the com-
 536 bination of high CC and elevated MAE suggests that the dominant errors are primarily due
 537 to under- or overestimation of the zonal and meridional SSC component magnitudes rather
 538 than misrepresentation of their role in circulation patterns. Figure 3e shows the time series
 539 of spatially averaged ED throughout the testing period, which varies on a day-to-day basis
 540 between approximately $3\text{--}7\text{ cm s}^{-1}$.

541 To further assess DeepCUN’s predictive skill under contrasting conditions, Figure 4
 542 presents two benchmark case studies corresponding to the minimum and maximum spa-
 543 tially averaged ED during the 2024 testing period (Figure 3e). Panel (a) shows a best-case
 544 scenario on 7 August 2024, for which ED values between the NEMO reference and Deep-
 545 CUN prediction remain low over nearly the entire basin. The spatially averaged ED is below
 546 3 cm s^{-1} , with local values rarely exceeding 10 cm s^{-1} , and both zonal and meridional SSC
 547 structures are closely reproduced, particularly in the interior Baltic Sea. The corresponding
 548 vorticity fields exhibit strong dynamical consistency, with approximately 88% agreement in
 549 vorticity sign, indicating accurate representation of the dominant rotational structures. This
 550 sign-based comparison also provides a simple visual aid for recognizing whether the main
 551 positive and negative vorticity regions in the two maps are arranged consistently. Panel (b)
 552 illustrates the most challenging case on 17 March 2024. Here, ED locally exceeds 20--
 553 30 cm s^{-1} along the western boundary, where strong exchange currents and sharp velocity
 554 gradients dominate. Despite these elevated errors, both NEMO and DeepCUN reproduce
 555 the same large-scale jet structures between approximately 54°N and 60°N west of 12°E .
 556 The increased ED primarily reflects differences in jet width and marginal positioning, with
 557 localized overestimation of current magnitude in the DeepCUN prediction rather than a
 558 breakdown of the circulation pattern. Away from this energetically active boundary region,
 559 ED decreases rapidly and remains below 10 cm s^{-1} across most of the interior basin. The
 560 corresponding vorticity fields retain sign agreement exceeding 80%, with localized disagree-
 561 ments mainly confined to offshore regions of weak SSC magnitude where vorticity values
 562 are near zero. Taken together, these contrasting cases demonstrate that DeepCUN’s largest
 563 errors are concentrated in high-energy boundary regions, while the interior Baltic Sea con-
 564 sistent exhibits low ED and strong dynamical consistency. The preservation of vorticity
 565 sign and coherent circulation patterns in both cases indicates that DeepCUN captures the

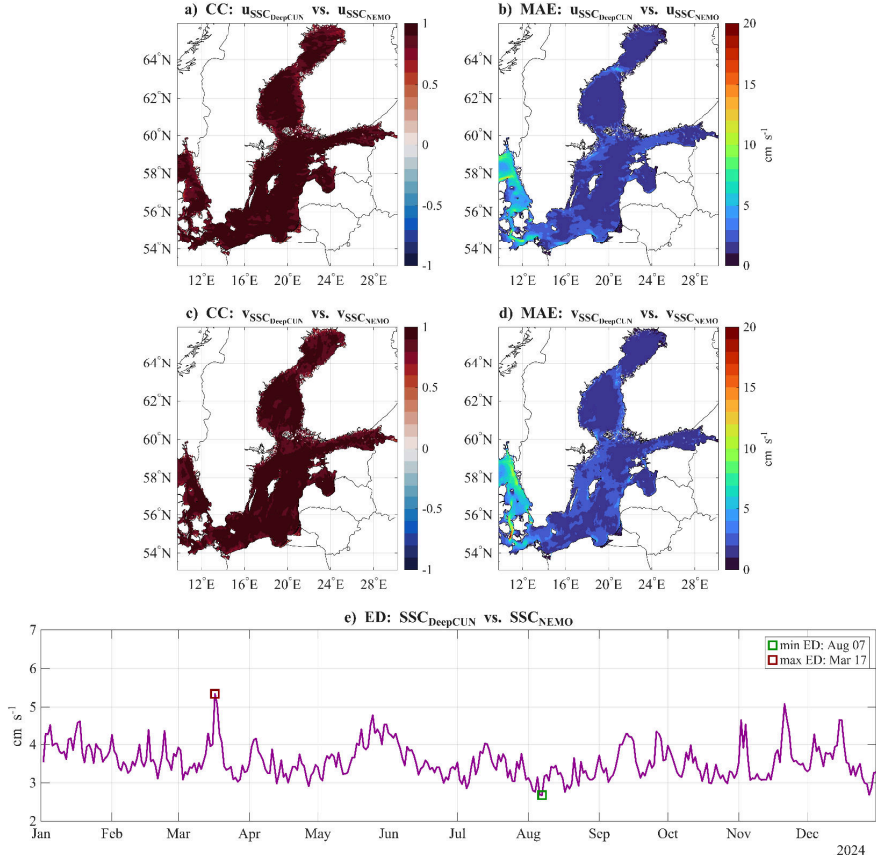


Figure 3. Annual evaluation of DeepCUN performance during 2024. Panels (a,c): spatial distribution of CC for u - and v -components, respectively. Panels (b,d): MAE maps for u - and v -components. Panel (e): daily time series of spatially averaged ED.

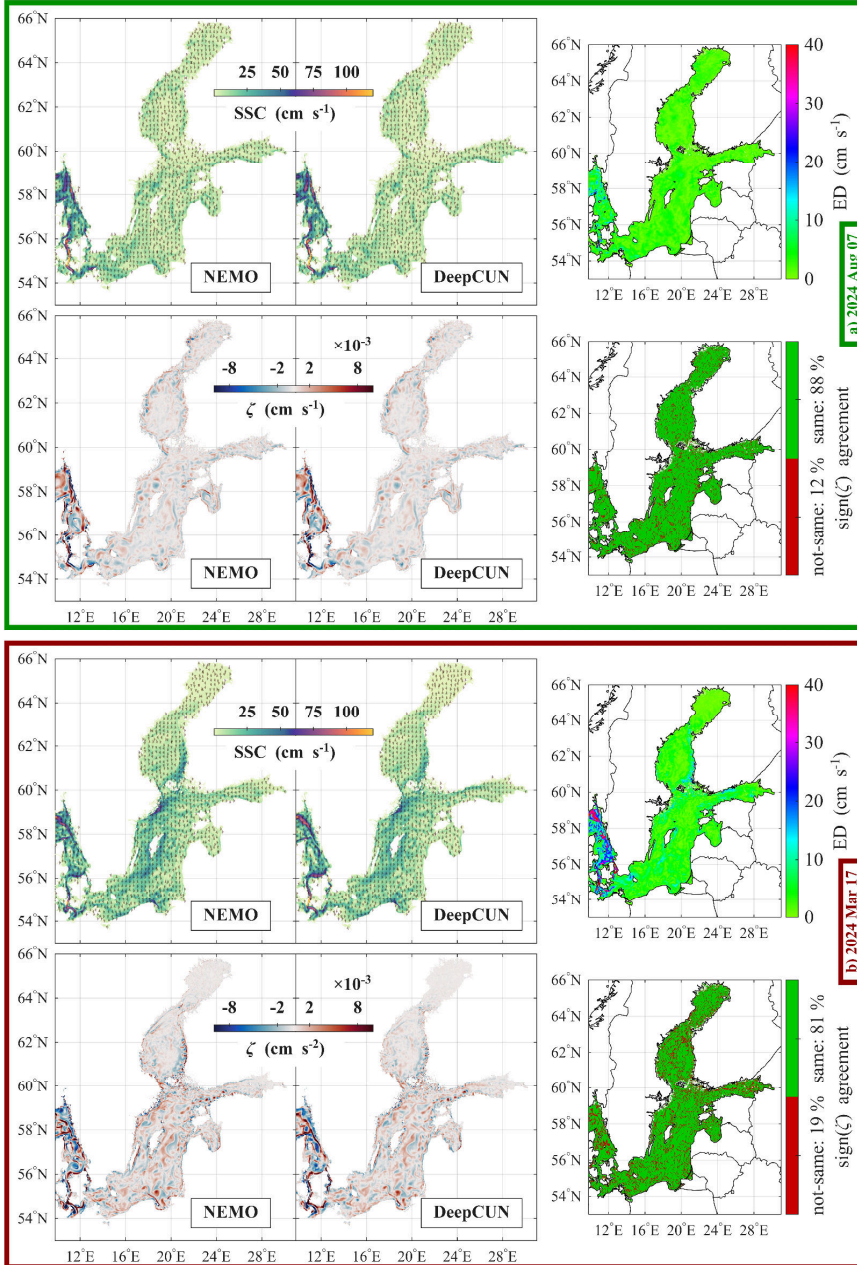


Figure 4. DeepCUN prediction examples for days corresponding to a) minimum and b) maximum spatially averaged ED during the 2024 testing period. Top panels: SSC fields from NEMO (reference) and DeepCUN (prediction). For clarity, SSC vectors are plotted at every 12th grid point. Bottom panels: corresponding vorticity fields ζ . The comparison highlights that DeepCUN reproduces both SSC vector structure and rotational organization based on the ζ sign agreement.

566 essential rotational structure of the surface flow even when local current magnitudes are
 567 imperfectly estimated. Additional vorticity-based statistics were computed to complement
 568 the case-study sign-agreement diagnostic with a basin-wide annual dynamical assessment
 569 (Appendix A4). Over the full 2024 test period, the annual vorticity-pattern correlation is
 570 $R_\zeta = 0.85$, showing that DeepCUN reproduces the basin-wide spatial organization of the
 571 relative-vorticity field. The normalized vorticity-amplitude similarity is $A_\zeta = 0.99$, showing
 572 that the relative strength of the vorticity field is also preserved. The annual mean vorticity
 573 sign agreement is 84.7%. These results indicate that DeepCUN reproduces not only the
 574 rotational orientation of the flow, but also the basin-wide pattern and relative strength of
 575 rotational structures.

576 3.2 XAI for DeepCUN

577 The XAI results are computed from 2023 samples to characterize the learned behavior
 578 of the trained DeepCUN mapping under in-distribution conditions. They are therefore in-
 579 terpreted as diagnostics of model reliance and local responsiveness, whereas the independent
 580 2024 period is used for predictive-skill evaluation.

581 3.2.1 Insights from LRP

582 Figure 5 summarizes LRP score maps averaged over all $N_{\text{samp}} = 364$ daily samples in
 583 2023. To place all input–output pairs on a common robust scale, the daily relevance fields
 584 are normalized by a single ocean-only P_{99} factor pooled across all 4×2 input–output maps,
 585 then clipped to $[0, 100]$ and averaged over time. Consequently, locations with higher values
 586 indicate where the trained network finds stronger input support for forming the next-day
 587 SSC prediction.

588 Across panels, relevance is consistently highest in the southwestern straits, the main
 589 exchange corridor between the Baltic Sea and the adjacent North Sea basin, indicating that
 590 dynamically constrained boundary regions carry strong model support. A clear scale separa-
 591 tion is evident between forcing and state: wind inputs at $t+1$ ($u_{\text{WIND}}, v_{\text{WIND}}$) show broadly
 592 elevated relevance across the Baltic interior (longitudes $> 12^\circ\text{E}$) and often along coherent
 593 coastal bands, whereas SSC-state inputs at time t are more localized and spatially hetero-
 594 geneous, with hotspots concentrated near coasts and straits. For $u_{\text{SSC}}(t+1)$ (top row), the
 595 wind fields dominate the basin-wide attribution, while SSC-state support is patchier and
 596 boundary-focused. For $v_{\text{SSC}}(t+1)$ (bottom row), $v_{\text{SSC}}(t)$ provides the strongest state con-
 597 tribution; $u_{\text{SSC}}(t)$ is weaker overall except near the southwestern boundary. Non-negligible
 598 relevance in the cross-component panels further shows that the network exploits coupled hor-
 599 izontal structure rather than treating u and v independently. Collectively, the maps indicate
 600 a spatially varying balance in which winds provide basin-scale support for next-day SSC,
 601 while state persistence (i.e. SSC memory) and cross-component terms are most influential
 602 in coastal and strait regions where the circulation is strongly constrained. The enhanced
 603 LRP support from the antecedent SSC channels in the southwestern exchange corridor also
 604 helps explain the spatial pattern of prediction error in Figure 3. In this boundary-influenced
 605 region, the next-day SSC prediction depends strongly on the previous SSC state, indicat-
 606 ing that DeepCUN uses state memory to represent exchange-related variability that is not
 607 supplied through explicit open-boundary forcing. Consequently, errors are expected to be
 608 larger there when the antecedent state does not fully encode the timing, strength, or spatial
 609 position of rapidly changing inflow–outflow structures.

610 3.2.2 Insights from DJE

611 Figure 6 summarizes DJE as a spatially resolved measure of local responsiveness in the
 612 trained DeepCUN one-day update. High DJE values occur where infinitesimal perturbations
 613 to an input channel at a grid point produce large, co-located changes in the predicted
 614 next-day SSC component magnitude. The resulting patterns are distinctly coastal. Respon-

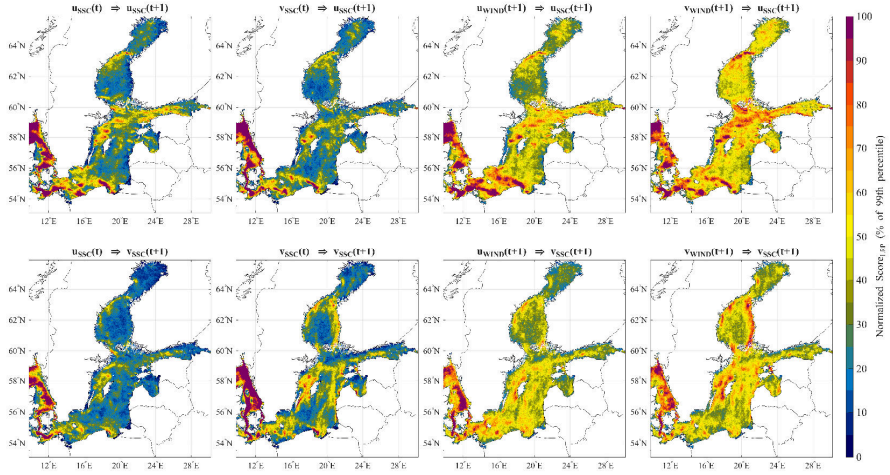


Figure 5. LRP results for DeepCUN averaged over all 2023 samples. Panels show spatial relevance maps for each input channel contributing to the prediction of $u_{SSC}(t+1)$ and $v_{SSC}(t+1)$. Relevance is normalized per sample by an ocean-only P_{99} factor pooled across all 4×2 input-output maps and clipped to $[0, 100]$ before averaging.

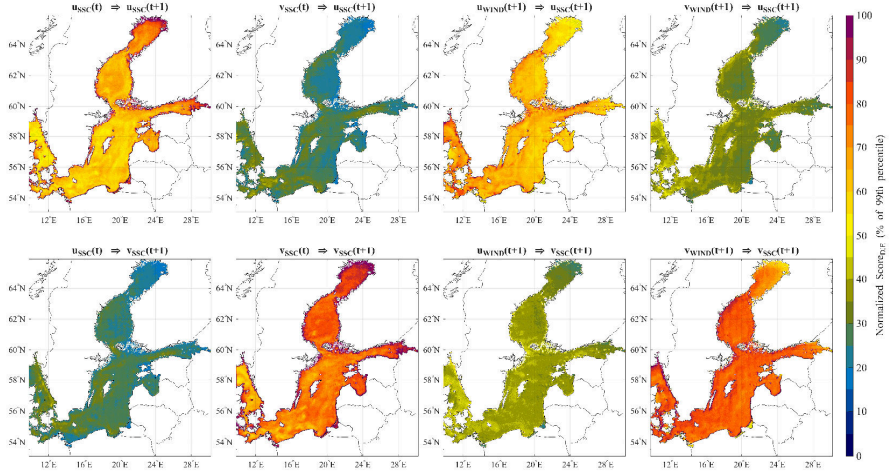


Figure 6. DJE results for DeepCUN averaged over all 2023 samples. Panels show spatial-diagonal elasticity maps (0–100%) quantifying the local sensitivity of the predicted SSC component magnitude to infinitesimal perturbations in each input channel at the same grid point. Elasticity is standardized by the ocean-domain variability of each input channel and normalized per sample by an ocean-only P_{99} factor pooled across all 4×2 input-output maps before averaging.

siveness is enhanced along shorelines and in narrow sub-basins and gulfs, while it is lower and more uniform over much of the open interior. This implies that local perturbations to the retained inputs have the strongest potential to affect predicted SSC magnitude in coastal and geometrically constrained regions, where flows are tightly steered and gradients are sharper.

Channel-wise, DJE is dominated by same-component pathways and shows a consistent row-wise structure. For the $u_{\text{SSC}}(t+1)$ target, the strongest maps are $u_{\text{SSC}}(t) \Rightarrow u_{\text{SSC}}(t+1)$ and $u_{\text{WIND}}(t+1) \Rightarrow u_{\text{SSC}}(t+1)$, whereas the corresponding cross-component and cross-wind panels are substantially weaker. For the $v_{\text{SSC}}(t+1)$ target, the strongest maps switch accordingly to $v_{\text{SSC}}(t) \Rightarrow v_{\text{SSC}}(t+1)$ and $v_{\text{WIND}}(t+1) \Rightarrow v_{\text{SSC}}(t+1)$, with the remaining cross panels again low. This indicates that, at the spatial-diagonal level, local responsiveness is governed primarily by persistence of the matching SSC component and by locally aligned wind forcing, while pointwise cross-component effects are minor. Any additional inter-component coupling is therefore more likely to act through spatially distributed pathways that are excluded by DJE by construction, consistent with the complementary role of LRP in revealing nonlocal information use. Taken together with Figure 5, LRP and DJE separate two aspects of input importance. LRP indicates where information is recruited to construct the prediction, whereas DJE indicates where co-located input perturbations most strongly modulate the predicted SSC magnitude.

3.3 Potential Forecast Behavior Under Prescribed Forcing

Figure 7 summarizes the performance of the multi-day autoregressive rollout under prescribed forcing, following the framework described in Section 2.6. The blue curves show the spatially averaged MAE of the DeepCUN predictions relative to the NEMO reference as a function of forecast lead time from $n = 1$ to $n = 21$ days. As expected for an autoregressive setup, forecast errors increase monotonically with lead time due to cumulative error propagation. MAE grows from approximately $2.4\text{--}2.6 \text{ cm s}^{-1}$ at day 1 to about $5.6\text{--}5.8 \text{ cm s}^{-1}$ by day 21 for both velocity components. Error growth is most rapid during the first 5–7 forecast days and then progressively flattens, indicating a gradual loss of predictability rather than an abrupt breakdown of forecast stability. The maroon curves show the corresponding spatially averaged CC for each SSC component. Correlation decreases smoothly from values above 0.9 at day 1 to approximately 0.65 by day 21, with the strongest decay occurring within the first 7–10 days. Despite this reduction, correlations remain moderate at extended lead times, indicating that the large-scale directional structure of the surface currents degrades progressively with the forecast horizon. The near-identical evolution of MAE and CC for u_{SSC} and v_{SSC} indicates balanced, component-consistent forecast behavior and provides no evidence of a lead-time-dependent, component-specific bias associated with the unified normalization based on global SSC extrema (Eq. 1).

Figure 8 provides a spatial perspective on forecast degradation by showing mean ED (top row) and mean CC (bottom row) for lead times of 1, 7, 14, and 21 days, averaged over the 2024 testing period. At a 1-day lead time, ED values are low across most of the domain, with slightly elevated values confined to the western boundary and narrow inflow–outflow regions, consistent with the single-day performance shown in Figure 3. By day 7, ED increases but remains spatially localized, with highest values along the western boundary and southern coastal regions, while offshore areas in the central and northern basin retain comparatively lower ED. At lead times of 14 and 21 days, regions of elevated ED expand, particularly along the western boundary and into offshore parts of the southern and eastern Baltic, with a localized maximum west of Gotland near 18°E and 58°N . In contrast, large portions of the northern basin consistently exhibit lower ED. The corresponding CC fields provide complementary insight into pattern agreement. While correlations decrease with lead time, high CC values persist over much of the basin, especially in coastal and northern regions, even at 14- and 21-day lead times. Overall, the ED and CC maps indicate that forecast degradation is spatially structured, with increasing magnitude errors and reduced

667 pattern agreement concentrated in specific western, southern, and offshore regions, whereas
 668 large areas of the interior basin retain ED values below 10 cm s^{-1} together with relatively
 669 high correlation even at a three-week forecast horizon.

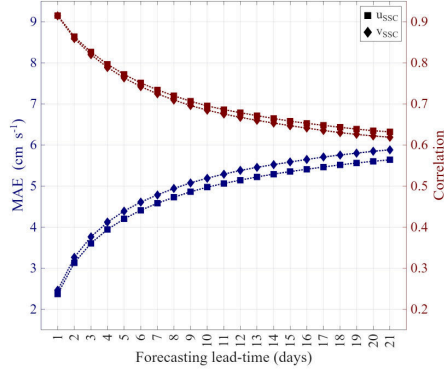


Figure 7. Performance of DeepCUN under autoregressive multi-day forecasting. The blue curve (left axis) shows the spatially averaged MAE between predictions and reference SSC components as a function of forecast lead time (1–21 days). The maroon curve (right axis) shows the spatially averaged CC (mean of u_{SSC} and v_{SSC}).

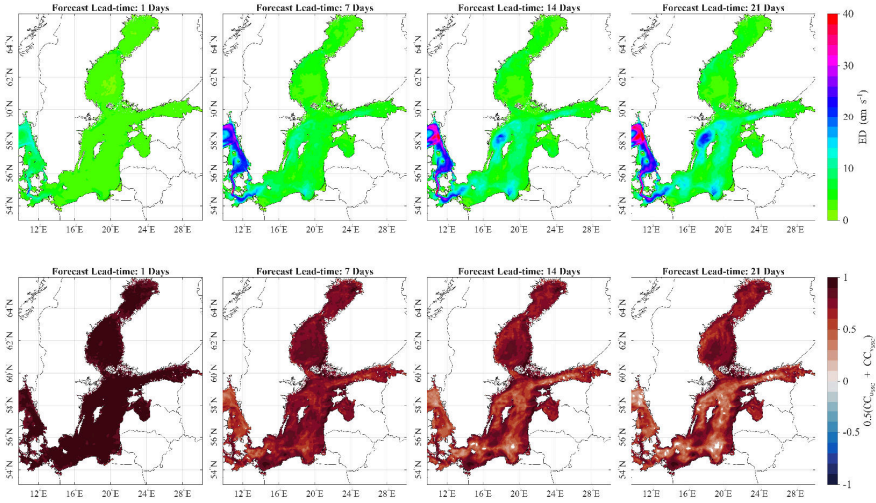


Figure 8. Spatial distribution of DeepCUN forecasting skill at selected lead times. Top row: ED between predicted and reference SSC. Bottom row: spatially averaged CC for the u and v components of SSC $\overline{CC} = \frac{1}{2}(CC_{u_{SSC}} + CC_{v_{SSC}})$. Shown are averages for lead times of 1, 7, 14, and 21 days over the 2024 testing period.

4 Discussion

The present study develops and evaluates DeepCUN for emulating daily Baltic Sea SSC fields on a structured grid at approximately 1 nautical-mile resolution. The network learns a one-day SSC state update from the previous-day SSC state and next-day wind forcing, and performance is evaluated against NEMO-based reanalysis to quantify predictive skill and support explainability analyses. This formulation targets partial emulation of simulated surface circulation without integrating a three-dimensional ocean model. A methodological contribution is the use of occlusion sensitivity to guide input-channel pruning during model configuration rather than solely as a post hoc interpretability tool (Bolmer et al., 2022; Wang et al., 2025). To benchmark channel reliance under generalization (and avoid in-sample underestimation due to learned inter-channel correlations), we apply occlusion to a trained 7-channel baseline on the independent 2024 year; the resulting reduced input set is then retrained with the retained channels. The occlusion results indicate negligible incremental predictive value from mean sea level pressure and near-surface thermodynamic variables once SSC persistence and wind forcing are included (Figure B1), allowing the input set to be reduced to four channels without measurable loss of skill. This illustrates the practical value of targeted input pruning for partial emulation, where efficiency within a defined scope is prioritized over including a broad set of potentially relevant drivers. The reduced 4-channel configuration should therefore be interpreted as a task-specific input design choice. The removed variables (msl, t2m, and d2m) may remain physically relevant for Baltic Sea air-sea interaction, but they do not provide appreciable additional predictive skill beyond antecedent SSC and next-day wind forcing in the tested DeepCUN configuration.

One-day-ahead results (Figures 3 and 4) show that DeepCUN reproduces the dominant basin-scale structure and temporal variability of both SSC components. Errors are spatially structured, with higher discrepancies concentrated in the dynamically active southwestern exchange corridor and lower errors together with stronger correlations over much of the basin interior. This pattern is consistent with enhanced dynamical complexity and stronger gradients in boundary-influenced regions (Gustafsson, 1997; Nielsen, 2005; Gröger et al., 2019). The southwestern Baltic is not simply a lateral edge of the model domain; it is the main exchange pathway between the Baltic Sea and the North Sea. Currents there are shaped by narrow straits, abrupt bathymetric and coastline changes, sea-level-driven exchange, episodic inflows and outflows, and strong wind-modulated pressure-gradient variability. These processes can generate narrow jets and sharp velocity gradients, so small phase or displacement errors in the predicted exchange flow can produce large local MAE and ED even when the large-scale current pattern remains realistic.

Because the mapping in Eq. (3) does not include explicit boundary forcing, DeepCUN represents boundary influence indirectly through spatial dependencies learned from the simulation data. This interpretation is supported by the LRP results in Figure 5, which show enhanced attributed support from the antecedent SSC channels in the southwestern exchange corridor. The model therefore appears to rely strongly on the previous SSC state to infer boundary-controlled variability that is not explicitly prescribed through open-boundary sea level, transport, or hydrographic information. This also helps interpret the autoregressive results in Figure 8: the same boundary-influenced region where antecedent SSC support is strong exhibits persistent ED growth with lead time. Because predicted SSC fields are recursively reused as inputs during autoregressive deployment, errors in this state-dependent exchange corridor can propagate into subsequent steps more strongly than in regions where the update is more directly constrained by wind forcing. Incorporating external boundary information could reduce errors in the exchange corridor, but boundary data are often defined on spatial supports that differ from the interior grid and may require additional transformations (Bhardwaj et al., 2025) or specialized architectures such as graph neural networks (Holmberg et al., 2025). If such information is only available from running the same numerical model at inference time, the emulation objective is weakened because the network remains dependent on the simulation it seeks to approximate.

723 Under recursive deployment, domain-mean errors increase smoothly with lead time
 724 (Figure 7) and the highest-error regions remain largely confined to the southwestern ex-
 725 change corridor and other dynamically active areas (Figure 8), while substantial parts of
 726 the interior retain comparatively lower degradation. The recursive experiment uses ERA5 re-
 727 analysis winds rather than forecast winds and therefore represents a potential, upper-bound
 728 estimate of recursive skill under realized atmospheric forcing, highlighting that practical de-
 729 ployment will depend on the accuracy of available wind forecasts over the Baltic Sea. The
 730 spatially structured degradation nevertheless suggests stable autoregressive behavior of the
 731 learned one-step operator and is noteworthy given the highly variable SSC regime of the
 732 Baltic Sea, where strong atmospheric forcing and shallow bathymetry amplify temporal and
 733 spatial variability (Jeřdrasik & Kowalewski, 2019; Bednorz et al., 2021). Recent work has also
 734 explored physics-informed learning and neural-operator formulations that embed dynamical
 735 constraints or global state-to-state mappings (L. Zhang et al., 2024; El Aouni et al., 2025;
 736 Jahanmard, Hordoir, et al., 2025). While these approaches pursue different objectives, the
 737 present results indicate that a purely data-driven CNN-U-Net architecture can be effective
 738 for regional SSC emulation on structured grids when the goal is short-horizon prediction
 739 based on limited inputs, consistent with earlier CNN-based studies of surface-current esti-
 740 mation and enhancement (Sinha & Abernathey, 2021; Ciani et al., 2025). This also aligns
 741 with recent Baltic Sea applications in which convolutional latent-space representations were
 742 used to reduce high-dimensional ocean fields while preserving physically meaningful spatial
 743 structure (Hayatijozani et al., 2026).

744 From an XAI perspective, a central outcome of this work is the explicit separation of
 745 attributed support and elasticity as complementary notions of interpretability for the pre-
 746 dicted SSC field with respect to the input channels, quantified here with LRP and DJE,
 747 respectively (Sections 2.5.1–2.5.2). LRP is well matched to DeepCUN because the network
 748 represents a deterministic, feed-forward surrogate of a one-day update operator, so relevance
 749 maps provide a direct view of which input features are repeatedly recruited to construct the
 750 next-day SSC field. DJE adds information that relevance alone cannot provide by quanti-
 751 fying how strongly the predicted SSC magnitude at a grid point responds to infinitesimal,
 752 co-located perturbations in each input channel. Computing both diagnostics on an entire
 753 in-distribution year and reporting annual means reduces event-specific noise and yields at-
 754 tribution patterns that characterize the typical behavior of the trained operator rather than
 755 a single case study.

756 Interpreted jointly, the two diagnostics yield a physically consistent and non-redundant
 757 picture of how DeepCUN combines prior state and forcing. The LRP results (Figure 5) indi-
 758 cate that wind inputs at $t+1$ provide broad basin-scale support for next-day SSC prediction,
 759 especially across the Baltic interior, while SSC persistence, $u_{\text{SSC}}(t)$ and $v_{\text{SSC}}(t)$, provides
 760 more localized structural support in the western exchange corridor, coastal passages, and
 761 straits where currents are energetic and gradients are sharp. This distinction is consistent
 762 with the role of wind as a basin-scale external forcing and the role of antecedent SSC as
 763 a state-memory term that is particularly informative in dynamically constrained bound-
 764 ary and coastal regions. DJE complements this interpretation by showing that coastal
 765 and constricted regions exhibit the highest local responsiveness, implying that local input
 766 perturbations in these regions have the strongest potential to affect the predicted current
 767 magnitude (Figure 6). Over offshore and interior areas, wind-related DJE remains strong
 768 and can exceed the SSC-state contribution, indicating that once wind forcing is provided to
 769 the network it becomes a primary local modulator of the predicted SSC magnitude.

770 A robust feature of Figure 6 is that wind responsiveness is largely component-aligned,
 771 with $u_{\text{wind}}(t+1) \Rightarrow u_{\text{SSC}}(t+1)$ and $v_{\text{wind}}(t+1) \Rightarrow v_{\text{SSC}}(t+1)$ exceeding the corresponding
 772 cross-wind panels. This is expected for daily-mean near-surface currents in a semi-enclosed
 773 basin where the response to synoptic forcing is shaped by coastal steering, wind-driven
 774 setup and associated pressure gradients, inertial variability, and mixing-mediated coupling
 775 to deeper layers (Lehmann & Hinrichsen, 2000; Placke et al., 2018; Vortmeyer-Kley et

776 al., 2019; Onken et al., 2020; Liblik et al., 2022). The component-aligned DJE response
 777 should therefore be interpreted as a local sensitivity pattern of the retained wind channels,
 778 rather than as a complete description of the full air–sea momentum pathway, which can also
 779 involve wave-modified stress and roughness-dependent mixing (Haapaniemi et al., 2026).
 780 Consistent with Baltic Sea analyses that separate geostrophic and ageostrophic components,
 781 wind influence becomes relatively more prominent as the averaging window shortens toward
 782 daily means, both directly through surface stress and indirectly through wind-set sea-level
 783 gradients and mixing adjustments (Barzandeh et al., 2024; Lehmann & Myrberg, 2008;
 784 Dietze & Löptien, 2016; Delpeche-Ellmann et al., 2021; Bulczak et al., 2024; Elken et al.,
 785 2024). At the same time, exchanges through the western boundary and episodic inflow events
 786 shape the evolving background state and constrain variability in boundary corridors (Meier,
 787 2007; Neumann et al., 2017; Mohrholz, 2018), which aligns with the stronger persistence-
 788 related relevance in Figure 5.

789 These attribution patterns are consistent with the model formulation adopted here, in
 790 which SSC at time t provides the initial state and wind at time $t + 1$ provides external
 791 forcing (Eq. (3)). Although DeepCUN does not explicitly enforce governing equations, the
 792 combined LRP–DJE results indicate a clear separation between state-supported structure in
 793 boundary-influenced regions and wind-modulated adjustment over the basin interior. The
 794 maps should be interpreted as data-consistent diagnostics of how DeepCUN represents the
 795 dynamics embedded in the CMEMS–NEMO reanalysis and ERA5 forcing, and they provide
 796 actionable guidance on where improvements are most likely to matter, particularly in coastal
 797 and constricted regions where responsiveness is highest.

798 Beyond the climatological averages reported here, the same LRP–DJE workflow can be
 799 applied to individual forecast instances. This enables case-based analysis of specific events,
 800 including days with unusually strong winds, extreme SSC magnitudes, rapid reversals, or
 801 large prediction errors, by comparing event-wise attributions against the annual-mean base-
 802 line. Such analysis can indicate whether an extreme prediction is supported by physically
 803 consistent input pathways, whether the network relies disproportionately on localized coastal
 804 information, and which input channels and locations contribute most to forecast degradation
 805 in high-impact conditions.

806 Nevertheless, a limitation of DJE is that it reports only the spatial-diagonal part of
 807 the input–output Jacobian after applying a magnitude transform to the predicted SSC
 808 component. It therefore identifies where local perturbations most strongly modulate the
 809 predicted component magnitude, but it does not describe the full nonlocal influence of an
 810 input field, nor does it retain the sign of the response. Accordingly, DJE is interpreted
 811 here together with LRP. LRP provides broader attributed-support patterns, whereas DJE
 812 isolates local co-located magnitude responsiveness.

813 Overall, this study demonstrates that DeepCUN achieves a balance between accuracy,
 814 efficiency, and interpretability that is well suited to partial emulation of SSC in a complex
 815 marginal sea. While the approach does not replace full dynamical models, it provides a
 816 fast and physically plausible surrogate that can support ensemble forecasting, sensitivity
 817 studies, and operational applications where rapid surface-current estimates are required.
 818 The combination of optimized data design, interpretable deep learning, and rigorous spatial
 819 evaluation establishes a framework that can be extended to other regions and variables,
 820 while also highlighting key challenges—such as boundary representation—that merit further
 821 investigation.

822 Appendix A Validation metrics

823 This appendix collects the full metric definitions used for one-step emulation and for
 824 the autoregressive multi-day experiment. All metrics are computed over the ocean domain

825 Ω defined by the land–sea mask; land grid points are excluded (or equivalently set to zero
826 by masking) in the reported fields.

827 **A1 Euclidean distance (vector error)**

828 The gridwise Euclidean distance (ED) between predicted and reference SSC vectors is

$$\text{ED}(i, j, t) = \sqrt{\left(\hat{u}_{\text{SSC}}(i, j, t) - u_{\text{SSC}}(i, j, t)\right)^2 + \left(\hat{v}_{\text{SSC}}(i, j, t) - v_{\text{SSC}}(i, j, t)\right)^2}. \quad (\text{A1})$$

829 **A2 Mean absolute error (component-wise)**

830 For a given evaluation period of length T (e.g., $T = 365$ for year 2024), for the zonal
831 component,

$$\text{MAE}_u(i, j) = \frac{1}{T} \sum_{t=1}^T \left| \hat{u}_{\text{SSC}}(i, j, t) - u_{\text{SSC}}(i, j, t) \right|, \quad (\text{A2})$$

832 and analogously for the meridional component $\text{MAE}_v(i, j)$.

833 **A3 Pearson correlation coefficient (component-wise)**

834 For the zonal component,

$$\text{CC}_u(i, j) = \frac{\sum_{t=1}^T (\hat{u}_{\text{SSC}}(i, j, t) - \overline{\hat{u}_{\text{SSC}}(i, j)}) (u_{\text{SSC}}(i, j, t) - \overline{u_{\text{SSC}}(i, j)})}{\sqrt{\sum_{t=1}^T (\hat{u}_{\text{SSC}}(i, j, t) - \overline{\hat{u}_{\text{SSC}}(i, j)})^2} \sqrt{\sum_{t=1}^T (u_{\text{SSC}}(i, j, t) - \overline{u_{\text{SSC}}(i, j)})^2}}, \quad (\text{A3})$$

835 where the overbar denotes the temporal mean at (i, j) computed over the evaluation period.
836 The same formulation defines $\text{CC}_v(i, j)$ for the meridional component.

837 **A4 Relative vorticity diagnostic**

838 We validate rotational structure using the vertical component of relative vorticity de-
839 rived from SSC:

$$\zeta(i, j, t) = \frac{\partial v_{\text{SSC}}}{\partial x}(i, j, t) - \frac{\partial u_{\text{SSC}}}{\partial y}(i, j, t), \quad (\text{A4})$$

840 with predicted vorticity $\hat{\zeta}(i, j, t)$ computed by applying the same discrete derivative operators
841 to $(\hat{u}_{\text{SSC}}, \hat{v}_{\text{SSC}})$. We interpret the fraction of ocean grid points with $\text{sign}(\zeta) = \text{sign}(\hat{\zeta})$ as
842 a measure of consistency in identifying cyclonic versus anticyclonic structures, while $|\zeta|$
843 characterizes the strength of rotational features.

844 To complement this binary sign-based diagnostic, we compute VPS as follows: For each
845 day t , the spatial vorticity-pattern correlation is defined as

$$R_\zeta(t) = \text{corr} \left(\hat{\zeta}(i, j, t), \zeta(i, j, t) \right), \quad (\text{A5})$$

846 The corresponding normalized vorticity-amplitude similarity is

$$A_\zeta(t) = \frac{2\sigma_{\hat{\zeta}}(t)\sigma_\zeta(t)}{\sigma_{\hat{\zeta}}^2(t) + \sigma_\zeta^2(t)}, \quad (\text{A6})$$

847 where $\sigma_{\hat{\zeta}}(t)$ and $\sigma_\zeta(t)$ are the spatial standard deviations of predicted and reference vorticity
848 over finite ocean values. The daily VPS is then

$$\text{VPS}(t) = A_\zeta(t) \max(0, R_\zeta(t)). \quad (\text{A7})$$

849 The annual VPS reported for the 2024 test period is

$$\overline{\text{VPS}}_{2024} = \frac{1}{T} \sum_{t=1}^T \text{VPS}(t). \quad (\text{A8})$$

850 VPS approaches one when the predicted and reference vorticity fields agree in both spa-
 851 tial pattern and relative amplitude. It decreases when rotational structures are misplaced,
 852 over-smoothed, over-amplified, or oppositely oriented. Because VPS combines vorticity-
 853 pattern correlation with normalized amplitude similarity, it provides a scale-normalized
 854 dynamical complement to vorticity sign agreement without using a raw vorticity MAE.

855 Appendix B Model-Design Ablation Analyses

856 B1 Input-channel ablation and reduced-input comparison

857 This appendix provides the complete occlusion sensitivity methodology used to opti-
 858 mize the DeepCUN input set. The procedure follows the same seven-channel formulation
 859 previously used in sciCUN (Barzandeh et al., 2026), initially extended here from the Gulf
 860 of Riga to the full Baltic Sea. Let \hat{u}_{SSC} and \hat{v}_{SSC} denote model predictions and $u_{\text{SSC}}, v_{\text{SSC}}$
 861 the reference values. The baseline (pre-pruning) input tensor uses $C_{\text{in}} = 7$ channels:

$$\begin{aligned} (\hat{u}_{\text{SSC}}(i, j, t+1), \hat{v}_{\text{SSC}}(i, j, t+1)) &= \text{DeepCUN}(\mathbf{X}(i, j, :, t)), \\ X(i, j, 1, t) &= u_{\text{SSC}}(i, j, t), \\ X(i, j, 2, t) &= v_{\text{SSC}}(i, j, t), \\ X(i, j, 3, t) &= u_{\text{WIND}}^{\text{norm}}(i, j, t+1), \\ X(i, j, 4, t) &= v_{\text{WIND}}^{\text{norm}}(i, j, t+1), \\ X(i, j, 5, t) &= \text{msl}^{\text{norm}}(i, j, t+1), \\ X(i, j, 6, t) &= \text{t2m}^{\text{norm}}(i, j, t+1), \\ X(i, j, 7, t) &= \text{d2m}^{\text{norm}}(i, j, t+1). \end{aligned} \quad (\text{B1})$$

862 Input importance is assessed on the held-out 2024 test year ($T = 365$ daily instances
 863 from 2 January to 31 December). For each channel $c \in \{1, \dots, C_{\text{in}}\}$, we replace that channel
 864 by its temporally averaged (daily-mean) gridded field computed over the test year, while
 865 leaving all other channels unchanged:

$$\bar{X}_c(i, j) = \frac{1}{T} \sum_{\tau=1}^T X(i, j, c, \tau), \quad (\text{B2})$$

$$\mathbf{X}^{\text{occ} \rightarrow c}(i, j, :, t) = \left(X(i, j, 1, t), \dots, \bar{X}_c(i, j), \dots, X(i, j, C_{\text{in}}, t) \right). \quad (\text{B3})$$

867 We then compute reference predictions (no occlusion) and occluded predictions:

$$\begin{aligned} (\hat{u}_{\text{SSC}}^{\text{ref}}(i, j, t+1), \hat{v}_{\text{SSC}}^{\text{ref}}(i, j, t+1)) &= \text{DeepCUN}(\mathbf{X}(i, j, :, t)), \\ (\hat{u}_{\text{SSC}}^{\text{occ} \rightarrow c}(i, j, t+1), \hat{v}_{\text{SSC}}^{\text{occ} \rightarrow c}(i, j, t+1)) &= \text{DeepCUN}(\mathbf{X}^{\text{occ} \rightarrow c}(i, j, :, t)). \end{aligned} \quad (\text{B4})$$

868 Occlusion is intended here as an out-of-sample intervention test of channel reliance.
 869 When performed on data used for optimization (training years), masking a channel can
 870 yield overly optimistic conclusions because the network may have learned to impute the
 871 missing information from other covarying channels in-sample, reducing the apparent skill
 872 drop. Evaluating occlusion on the independent 2024 year mitigates this effect and better
 873 reflects sensitivity under generalization. The occlusion experiment itself does not alter model
 874 parameters; however, once negligible channels are identified, the network is retrained with

875 the reduced channel set because the input dimensionality (and thus the first-layer weights)
 876 changes. Performance is quantified using the gridwise ED between predicted and reference
 877 SSC vectors, averaged over the evaluation period (Eq. (A1)). Let ED_{ref} be the ED field
 878 for the unoccluded (reference) prediction and $ED_{\text{occ} \rightarrow c}$ the ED field for channel- c occlusion.
 879 Channel influence is summarized by the occlusion ratio

$$OR_c = 1 - \frac{ED_{\text{ref}}}{ED_{\text{occ} \rightarrow c}}. \quad (\text{B5})$$

880 Here $OR_c \approx 0$ indicates negligible influence, while $OR_c \approx 1$ indicates strong dependence.
 881 (Negative values would indicate slight improvement after occlusion; none were observed.)

882 Applied to 2024, the occlusion analysis indicates negligible contribution from msl, t2m,
 883 and d2m once SSC persistence and wind forcing are included (Fig. B1). These channels are
 884 therefore removed, yielding the finalized $C_{\text{in}} = 4$ input set used throughout the main text
 (Eq. (3)).

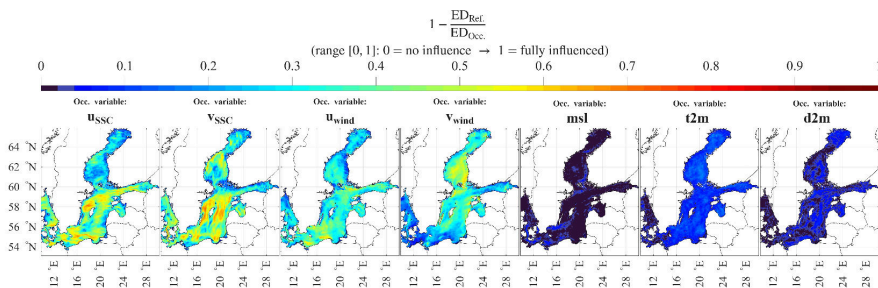


Figure B1. Occlusion sensitivity analysis.

885

886 To further consolidate the reduced-input design, we also performed a direct test-period
 887 comparison between the trained seven-channel baseline and the finalized four-channel Deep-
 888 CUN model on the same independent 2024 evaluation set. Both models were evaluated
 889 using the same reference fields and the same annual metrics. The seven-channel model pro-
 890 duced only marginal differences relative to the four-channel model, with domain-mean MAE
 891 changing from 2.22 to 2.21 cm s^{-1} for u_{SSC} and from 2.32 to 2.29 cm s^{-1} for v_{SSC} . The
 892 annual mean spatially averaged ED changed from 3.57 to 3.54 cm s^{-1} . The corresponding
 893 domain-mean CC values remained essentially unchanged, with u_{SSC} staying at 0.901 and
 894 v_{SSC} changing only slightly from 0.902 to 0.901. These differences are small relative to the
 895 overall error levels and do not indicate an appreciable annual skill gain from retaining msl,
 896 t2m, and d2m in this one-day SSC emulation setting.

897 Because the independent evaluation is based on a single test year, we additionally
 898 assessed whether the 2024 forcing conditions were anomalous relative to the 2015–2023
 899 training period. This check focused on ERA5 10 m wind because the finalized DeepCUN
 900 configuration retains u_{WIND} and v_{WIND} as the only atmospheric forcing channels after input-
 901 channel ablation. We evaluated both basin-scale and spatially resolved wind-speed statistics,
 902 using $U_{\text{WIND}} = \sqrt{u_{\text{WIND}}^2 + v_{\text{WIND}}^2}$. For the area-weighted daily domain-mean wind speed,
 903 the 2024 annual mean was 3.87 m s^{-1} , close to the 2015–2023 mean of $3.94 \pm 0.14 \text{ m s}^{-1}$.
 904 The corresponding upper-tail statistics were also within the training-period interannual
 905 range, with 2024 P_{95} and P_{99} values of 6.03 and 7.24 m s^{-1} , compared with 6.04 ± 0.29
 906 and $7.15 \pm 0.46 \text{ m s}^{-1}$ for 2015–2023. The fraction of days exceeding the 2015–2023
 907 domain-mean P_{95} threshold was 4.64% in 2024, compared with $4.99 \pm 2.39\%$ during 2015–
 908 2023. When all grid points and days were considered, the 2024 wind-speed range also

909 remained within the 2015–2023 range, with a maximum of 19.91 m s^{-1} compared with
 910 20.05 m s^{-1} during training. However, 2024 was not simply a repeated realization of the
 911 training years: the spatial P_{99} and annual-maximum wind-speed maps exceeded the 2015–
 912 2023 interannual envelope over 9.14% and 7.42% of grid cells, respectively. These diagnostics
 913 indicate that 2024 is not an outlier as an independent test year, but it contains new localized
 914 wind patterns while remaining largely within the wind-speed range sampled during training.

915 B2 Architecture Ablation and Baseline Comparison

916 DeepCUN uses a five-level encoder–decoder structure with skip connections and GN
 917 (Table 1). This design was selected to increase the representational capacity of the network
 918 for the larger and more heterogeneous full Baltic Sea domain. To support this finalized
 919 design choice, we performed an architecture ablation and baseline comparison using the
 independent 2024 test period.

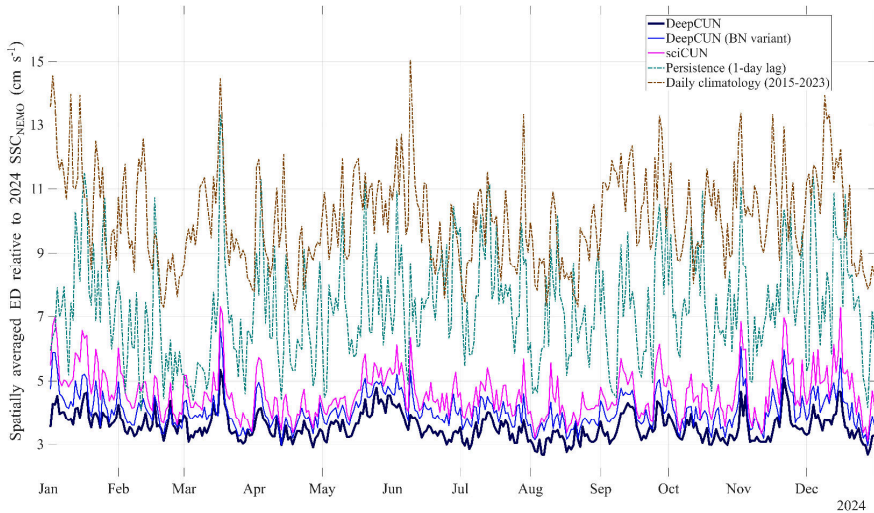


Figure B2. Architecture ablation and baseline comparison during the independent 2024 test period. Curves show the daily spatially averaged ED relative to SSC_{NEMO} for three trainable neural-network configurations and two naive reference baselines. The trainable configurations are the finalized DeepCUN model, the DeepCUN variant with batch normalization (BN), and the previous sciCUN-style three-level architecture trained for the whole Baltic Sea. The naive baselines are one-day persistence and daily climatology computed from 2015–2023. Lower ED indicates better agreement with SSC_{NEMO} .

920

921 Figure B2 compares the finalized DeepCUN model with two trainable variants, a Deep-
 922 CUN variant in which GN is replaced by BN and a sciCUN-style three-level architecture,
 923 as well as two naive baselines, one-day persistence and daily climatology from 2015–2023.
 924 The finalized DeepCUN configuration generally maintains the lowest ED throughout the
 925 independent 2024 test period. Using BN instead of GN slightly but consistently increases
 926 the error, supporting the use of GN under the adopted training setup. The larger errors
 927 of the sciCUN-style model indicate that the additional depth in DeepCUN improves representation
 928 of the full Baltic Sea’s spatial heterogeneity. The persistence and daily climatology
 929 baselines produce substantially larger errors than the trainable neural-network configura-

930 tions, showing that the trained models learn a nontrivial one-day mapping beyond simple
 931 persistence and stable climatological assumptions.

932 B3 DJE Probe-Count Ablation

933 The DJE estimator uses randomized Rademacher probes to approximate the spatial-
 934 diagonal derivative in Eq. (18). Increasing the number of probes reduces stochastic sampling
 935 noise, but it also increases the computational cost approximately linearly because each
 936 additional probe requires an additional gradient evaluation. We therefore performed a probe-
 937 count ablation to evaluate whether the selected value, $n_{\text{probe}} = 8$, is sufficient for the DJE
 938 visualization shown in Figure 6.

939 The ablation was carried out using $n_{\text{probe}} \in \{2, 4, 8, 16, 32\}$. For each probe count, the
 940 same complete DJE analysis was recomputed. The resulting DJE maps were rescaled to the
 941 plotted normalized score range and summarized over ocean grid points for each of the eight
 942 input–output panels using the mean and standard deviation of the normalized DJE score.

943 Table B1 shows that the domain-mean and standard-deviation values vary only moder-
 944 ately with probe count, especially for the dominant same-component and component-aligned
 945 pathways. We also visually inspected the resulting DJE maps for different probe counts (not
 946 shown). Increasing the number of probes mainly reduced stochastic roughness and produced
 947 slight additional smoothing or shading changes, but did not provide additional interpretive
 948 information after $n_{\text{probe}} = 8$. The dominant local-responsiveness pathways remained the
 949 same from $n_{\text{probe}} = 8$ onward: $u_{\text{SSC}}(t) \rightarrow u_{\text{SSC}}(t+1)$ and $u_{\text{WIND}}(t+1) \rightarrow u_{\text{SSC}}(t+1)$ for
 950 the zonal target, and $v_{\text{SSC}}(t) \rightarrow v_{\text{SSC}}(t+1)$ and $v_{\text{WIND}}(t+1) \rightarrow v_{\text{SSC}}(t+1)$ for the merid-
 951 ional target. Weaker cross-component terms showed greater sensitivity to probe count, but
 952 this did not alter the main interpretation of Figure 6. Because larger probe counts subst-
 953 antially increase computation time while producing only incremental visual changes, we
 954 selected $n_{\text{probe}} = 8$ as a computationally efficient value for the DJE analysis.

Table B1. Probe-count ablation for the final DJE visualization. Values are ocean-domain mean \pm standard deviation of the normalized plotted DJE score for each plotted input–output map.

Input–output DJE map	$n_{\text{probe}} = 2$	$n_{\text{probe}} = 4$	$n_{\text{probe}} = 8$	$n_{\text{probe}} = 16$	$n_{\text{probe}} = 32$
$u_{\text{SSC}}(t) \rightarrow u_{\text{SSC}}(t+1)$	75.23 \pm 10.89	71.56 \pm 12.73	69.25 \pm 14.07	68.19 \pm 14.75	67.83 \pm 15.02
$v_{\text{SSC}}(t) \rightarrow u_{\text{SSC}}(t+1)$	45.97 \pm 8.33	35.57 \pm 6.40	26.90 \pm 4.85	20.52 \pm 3.80	16.21 \pm 3.26
$u_{\text{WIND}}(t+1) \rightarrow u_{\text{SSC}}(t+1)$	69.54 \pm 10.18	67.21 \pm 9.95	65.95 \pm 9.89	65.44 \pm 9.90	65.28 \pm 9.94
$v_{\text{WIND}}(t+1) \rightarrow u_{\text{SSC}}(t+1)$	49.21 \pm 9.26	41.31 \pm 8.09	35.32 \pm 7.27	31.58 \pm 6.79	29.61 \pm 6.55
$u_{\text{SSC}}(t) \rightarrow v_{\text{SSC}}(t+1)$	45.82 \pm 7.85	35.57 \pm 6.07	26.98 \pm 4.68	20.69 \pm 3.78	16.47 \pm 3.38
$v_{\text{SSC}}(t) \rightarrow v_{\text{SSC}}(t+1)$	84.27 \pm 8.22	81.79 \pm 9.74	80.31 \pm 10.95	79.65 \pm 11.59	79.44 \pm 11.83
$u_{\text{WIND}}(t+1) \rightarrow v_{\text{SSC}}(t+1)$	53.07 \pm 9.38	45.02 \pm 7.88	38.92 \pm 6.67	35.13 \pm 5.97	33.10 \pm 5.67
$v_{\text{WIND}}(t+1) \rightarrow v_{\text{SSC}}(t+1)$	80.20 \pm 8.84	79.61 \pm 8.74	79.47 \pm 8.83	79.45 \pm 8.98	79.45 \pm 9.07

The statistics are computed over ocean grid points only after applying the same normalization and plotted score range used for Figure 6. Increasing n_{probe} mainly reduces stochastic roughness in the DJE estimator. The dominant input–output responsiveness pathways remain unchanged from $n_{\text{probe}} = 8$ onward.

955 Open Research Section

956 This study was conducted using E.U. Copernicus Marine Service Information. The refer-
 957 ence sea-surface current fields used for training and evaluation are from the Copernicus Ma-
 958 rine Service product *Baltic Sea Physics Reanalysis* (Product ID: BALTICSEA_MULTITYEAR_PHY_003_011)
 959 (E.U. Copernicus Marine Service Information (CMEMS), 2025). Atmospheric forcing fields
 960 are from the Climate Data Store dataset *ERA5 hourly data on single levels from 1940 to*
 961 *present* (Hersbach et al., 2023). In this work, ERA5 hourly fields were aggregated to daily
 962 means and interpolated to the SSC grid as described in Section 2.1. The analyses in this
 963 manuscript use the 2015–2024 subsets of the above products.

964 The complete DeepCUN workflow, including source code for data preparation, training,
 965 ing, testing, explainability analyses (LRP and DJE), forecasting experiments, and figure-
 966 generation scripts, has been archived on Zenodo (Barzandeh, 2026). The Zenodo archive
 967 also includes the final trained DeepCUN model and the processed evaluation outputs re-
 968 quired to reproduce the results reported in this manuscript. The archive is distributed under
 969 the Creative Commons Attribution 4.0 International license (CC BY 4.0).

970 Conflict of Interest declaration

971 The authors declare there are no conflicts of interest for this manuscript.

972 Acknowledgments

973 This publication was supported by the Estonian Research Council through the AIMES
 974 project (AI-based Emulator for Marine Environmental Simulations; project No. PSG1130).
 975 In addition, Urmas Raudsepp and Ilja Maljutenko acknowledge support from the European
 976 Union and the Estonian Research Council (project No. RITA-MER1). Ilja Maljutenko
 977 also acknowledges support from the European Union and the Estonian Research Council
 978 through the Digital Twin of Marine Renewable Energy project (project No. TEM-TA38).

979 References

- 980 Adcroft, A., Hill, C., Campin, J.-M., Marshall, J., & Heimbach, P. (2004). Overview of the
 981 formulation and numerics of the mit gcm. In *Proceedings of the ecmwf seminar series*
 982 *on numerical methods, recent developments in numerical methods for atmosphere and*
 983 *ocean modelling* (pp. 139–149).
- 984 Agarwal, N., Kondrashov, D., Dueben, P., Ryzhov, E., & Berloff, P. (2021). A comparison of
 985 data-driven approaches to build low-dimensional ocean models. *Journal of Advances*
 986 *in Modeling Earth Systems*, *13*(9), e2021MS002537. doi: 10.1029/2021MS002537
- 987 Allen, E., Kruger, C., Leung, F.-Y., & Stephens, J. C. (2013). Diverse perceptions of
 988 stakeholder engagement within an environmental modeling research team. *Journal of*
 989 *Environmental Studies and Sciences*, *3*, 343–356. doi: 10.1007/s13412-013-0136-x
- 990 Avron, H., & Toledo, S. (2011). Randomized algorithms for estimating the trace of an
 991 implicit symmetric positive semi-definite matrix. *Journal of the ACM*, *58*(2). doi:
 992 10.1145/1944345.1944349
- 993 Bai, G., Wang, Z., Zhu, X., & Feng, Y. (2022). Development of a 2-d deep learning
 994 regional wave field forecast model based on convolutional neural network and the
 995 application in south china sea. *Applied Ocean Research*, *118*, 103012. doi: 10.1016/
 996 j.apor.2021.103012
- 997 Barzandeh, A. (2026, February). *DeepCUN [Software]*. Zenodo. Retrieved from [https://](https://doi.org/10.5281/zenodo.18669808)
 998 doi.org/10.5281/zenodo.18669808 (CC BY 4.0) doi: 10.5281/zenodo.18669808
- 999 Barzandeh, A., Ličer, M., Rus, M., Kristan, M., Maljutenko, I., Elken, J., ... Uiboupin,
 1000 R. (2025). Application of the hidra2 deep-learning model for sea level forecasting
 1001 along the estonian coast of the baltic sea. *Ocean Science*, *21*(4), 1315–1327. doi:
 1002 10.5194/os-21-1315-2025
- 1003 Barzandeh, A., Maljutenko, I., Rikka, S., Lagemaa, P., Männik, A., Uiboupin, R., & Raud-
 1004 sepp, U. (2024). Sea surface circulation in the baltic sea: decomposed components and
 1005 pattern recognition. *Scientific Reports*, *14*, 18649. doi: 10.1038/s41598-024-69463-8
- 1006 Barzandeh, A., Maljutenko, I., Rikka, S., & Raudsepp, U. (2026). sciCUN: A deep learning
 1007 model for daily sea surface current fields inference—a case study of the gulf of riga.
 1008 *Ocean Modelling*, *201*, 102693. doi: 10.1016/j.ocemod.2026.102693
- 1009 Bashiri, B., Barzandeh, A., Männik, A., Uiboupin, R., & Raudsepp, U. (2025). Marine
 1010 heatwave event maps in the baltic sea (1982–2023): A gridded dataset from satellite-
 1011 derived l4 sst. *Scientific Data*. doi: 10.1038/s41597-025-06251-7
- 1012 Bednorz, E., Półośniczak, M., & Tomczyk, A. M. (2021). Regional circulation patterns

- 1013 inducing coastal upwelling in the Baltic Sea. *Theoretical and Applied Climatology*,
 1014 *144*, 905–916. doi: 10.1007/s00704-021-03539-7
- 1015 Bekas, C., Kokiopoulou, E., & Saad, Y. (2007). An estimator for the diagonal of a matrix.
 1016 *Applied Numerical Mathematics*, *57*(11), 1214–1229. doi: 10.1016/j.apnum.2007.01
 1017 .003
- 1018 Bendtsen, J., Gustafsson, K. E., Söderkvist, J., & Hansen, J. L. (2009). Ventilation of
 1019 bottom water in the north sea–baltic sea transition zone. *Journal of Marine Systems*,
 1020 *75*(1), 138–149. doi: 10.1016/j.jmarsys.2008.08.006
- 1021 Bhardwaj, A., Balashankar, A., & Subramanian, L. (2025). *Fieldformer: Physics-informed*
 1022 *transformers for spatio-temporal field reconstruction from sparse sensors*. Retrieved
 1023 from <https://arxiv.org/abs/2510.03589>
- 1024 Bishop, C. M. (2006). *Pattern recognition and machine learning* (1st ed.). New York, NY:
 1025 Springer. Retrieved from <https://link.springer.com/book/9780387310732>
- 1026 Bolmer, E., Abulaitjiang, A., Kusche, J., & Roscher, R. (2022). Occlusion sensitivity
 1027 analysis of neural network architectures for eddy detection. In *Igarss 2022 - 2022 ieee*
 1028 *international geoscience and remote sensing symposium* (p. 623–626). doi: 10.1109/
 1029 IGARSS46834.2022.9884373
- 1030 Bolton, T., & Zanna, L. (2019). Applications of deep learning to ocean data inference and
 1031 subgrid parameterization. *Journal of Advances in Modeling Earth Systems*, *11*(1),
 1032 376–399. doi: 10.1029/2018MS001472
- 1033 Börgel, F., Ruvalcaba Baroni, I., Barghorn, L., Borchert, L., Cahill, B., Dutheil, C., ...
 1034 Voelker, G. S. (2026). Large-scale atmospheric circulation and its impact on the
 1035 baltic sea region: controls, predictability and consequences. *Earth System Dynamics*,
 1036 *17*(3), 415–450. doi: 10.5194/esd-17-415-2026
- 1037 Breivik, Ø., Allen, A. A., Maisondieu, C., & Olagnon, M. (2013). Advances in search and
 1038 rescue at sea. *Ocean Dynamics*, *63*(1), 83–88. doi: 10.1007/s10236-012-0581-1
- 1039 Bryan, K. (1969). Climate and the ocean circulation: III. the ocean model. *Monthly Weather*
 1040 *Review*, *97*(11), 806 - 827. doi: 10.1175/1520-0493(1969)097<0806:CATOC>2.3.CO;
 1041 2
- 1042 Bulczak, A. I., Nowak, K., Jakacki, J., Muzyka, M., Rak, D., & Walczowski, W. (2024).
 1043 Seasonal variability and long-term winter shoaling of the upper mixed layer in the
 1044 southern baltic sea. *Continental Shelf Research*, *276*, 105232. doi: 10.1016/j.csr.2024
 1045 .105232
- 1046 Bône, C., Gastineau, G., Thiria, S., Gallinari, P., & Mejia, C. (2024). Separation of internal
 1047 and forced variability of climate using a u-net. *Journal of Advances in Modeling Earth*
 1048 *Systems*, *16*(6), e2023MS003964. doi: 10.1029/2023MS003964
- 1049 Chassignet, E. P., & Xu, X. (2021). On the importance of high-resolution in large-scale
 1050 ocean models. *Advances in Atmospheric Sciences*, *38*, 1621–1634. doi: 10.1007/
 1051 s00376-021-0385-7
- 1052 Chattopadhyay, A., Gray, M., Wu, T., Lowe, A. B., & He, R. (2024). Oceannet: a principled
 1053 neural operator-based digital twin for regional oceans. *Scientific Reports*, *14*, 21181.
 1054 doi: 10.1038/s41598-024-72145-0
- 1055 Christakos, K., Björkvist, J.-V., Øyvind Breivik, Tuomi, L., Furevik, B. R., & Albretsen,
 1056 J. (2021). The impact of surface currents on the wave climate in narrow fjords.
 1057 *Ocean Modelling*, *168*, 101894. Retrieved from [https://www.sciencedirect.com/
 1058 science/article/pii/S1463500321001475](https://www.sciencedirect.com/science/article/pii/S1463500321001475) doi: <https://doi.org/10.1016/j.ocemod>
 1059 .2021.101894
- 1060 Ciani, D., Fanelli, C., & Buongiorno Nardelli, B. (2025). Estimating ocean currents from
 1061 the joint reconstruction of absolute dynamic topography and sea surface temperature
 1062 through deep learning algorithms. *Ocean Science*, *21*(1), 199–216. doi: 10.5194/
 1063 os-21-199-2025
- 1064 Delpeche-Ellmann, N., Giudici, A., Rätsep, M., & Soomere, T. (2021). Observations of
 1065 surface drift and effects induced by wind and surface waves in the baltic sea for the
 1066 period 2011–2018. *Estuarine, Coastal and Shelf Science*, *249*, 107071. doi: 10.1016/
 1067 j.ecss.2020.107071

- 1068 Dheeshjith, S., Subel, A., Adcroft, A., Busecke, J., Fernandez-Granda, C., Gupta, S., &
1069 Zanna, L. (2025). Samudra: An ai global ocean emulator for climate. *Geophysical*
1070 *Research Letters*, *52*(10), e2024GL114318. doi: 10.1029/2024GL114318
- 1071 Dietze, H., & Löptien, U. (2016). Effects of surface current–wind interaction in an eddy-rich
1072 general ocean circulation simulation of the baltic sea. *Ocean Science*, *12*(4), 977–986.
1073 doi: 10.5194/os-12-977-2016
- 1074 Dong, C., Xu, G., Han, G., Bethel, B. J., Xie, W., & Zhou, S. (2022). Recent developments
1075 in artificial intelligence in oceanography. *Ocean-Land-Atmosphere Research*, *2022*,
1076 9870950. doi: 10.34133/2022/9870950
- 1077 El Aoumi, A., Gaudel, Q., Regnier, C., Van Gennip, S., Le Galloudec, O., Drevillon, M., ...
1078 Lellouche, J.-M. (2025). Glonet: Mercator’s end-to-end neural global ocean forecasting
1079 system. *Journal of Geophysical Research: Machine Learning and Computation*, *2*(3),
1080 e2025JH000686. doi: 10.1029/2025JH000686
- 1081 Elken, J., Barzandeh, A., Maljutenko, I., & Rikka, S. (2024). Reconstruction of baltic
1082 gridded sea levels from tide gauge and altimetry observations using spatiotemporal
1083 statistics from reanalysis. *Remote Sensing*, *16*(15). doi: 10.3390/rs16152702
- 1084 Elken, J., Lehmann, A., & Myrberg, K. (2015). Second assessment of climate change
1085 for the baltic sea basin. In (pp. 131–144). Springer International Publishing. doi:
1086 10.1007/978-3-319-16006-1_7
- 1087 Elken, J., Matthäus, W., et al. (2008). Physical system description. *Assmesment of Climate*
1088 *Change for the Baltic Sea Basin, edited by: BACC Author Team, chap. Annex A, 1,*
1089 *379–386.*
- 1090 Elken, J., & Omstedt, A. (2025). Water exchange in the baltic sea: a historical view of
1091 research approaches from basin scales to submesoscale. *Frontiers in Earth Science*,
1092 *13*, 1598983. doi: 10.3389/feart.2025.1598983
- 1093 Elsayed, A. H., El-Mihoub, T. A., Manss, C., Miedtank, A., Nolle, L., & Stahl, F. (2025).
1094 Interactive simulator framework for xai applications in aquatic environments. In
1095 M. Brammer & F. Stahl (Eds.), *Artificial intelligence xli* (pp. 144–157). Springer Nature
1096 Switzerland.
- 1097 Eschenbach, C. A. (2017). Bridging the gap between observational oceanography and users.
1098 *Ocean Science*, *13*(1), 161–173. doi: 10.5194/os-13-161-2017
- 1099 Eslami, E., & Yun, H.-B. (2023). Comparison of deep convolutional neural network classifiers
1100 and the effect of scale encoding for automated pavement assessment. *Journal of Traffic*
1101 *and Transportation Engineering (English Edition)*, *10*(2), 258-275. doi: 10.1016/
1102 j.jtte.2022.08.002
- 1103 E.U. Copernicus Marine Service Information (CMEMS). (2025). *Baltic Sea Physics Reanal-*
1104 *ysis (BALTCSEA_MULTIYEAR_PHY_003_011) [Dataset]*. Copernicus Marine
1105 Service, Marine Data Store (MDS). Retrieved from [https://doi.org/10.48670/](https://doi.org/10.48670/moi-00013)
1106 [moi-00013](https://doi.org/10.48670/moi-00013) (Accessed 24 December 2025) doi: 10.48670/moi-00013
- 1107 Fanelli, C., Ciani, D., Pisano, A., & Buongiorno Nardelli, B. (2024). Deep learning for
1108 the super resolution of mediterranean sea surface temperature fields. *Ocean Science*,
1109 *20*(4), 1035–1050. doi: 10.5194/os-20-1035-2024
- 1110 Finn, T. S., Durand, M., Semenova, E., Sheinkman, A., James, T., et al. (2024). Generative
1111 diffusion for regional surrogate models from sea-ice simulations. *Journal of Advances*
1112 *in Modeling Earth Systems*, *16*, e2024MS004395. doi: 10.1029/2024MS004395
- 1113 Fox-Kemper, B., Adcroft, A., Böning, C. W., Chassignet, E. P., Curchitser, E., Danabasoglu,
1114 G., ... Yeager, S. G. (2019). Challenges and prospects in ocean circulation models.
1115 *Frontiers in Marine Science*, *6*, 65. doi: 10.3389/fmars.2019.00065
- 1116 Glorot, X., & Bengio, Y. (2010). Understanding the difficulty of training deep feedforward
1117 neural networks. In *Proceedings of the thirteenth international conference on artificial*
1118 *intelligence and statistics* (Vol. 9, pp. 249–256). Retrieved from [https://proceedings](https://proceedings.mlr.press/v9/glorot10a.html)
1119 [.mlr.press/v9/glorot10a.html](https://proceedings.mlr.press/v9/glorot10a.html)
- 1120 Gould, J., Sloyan, B., & Visbeck, M. (2013). Chapter 3 - in situ ocean observations: A
1121 brief history, present status, and future directions. In *Ocean circulation and climate*
1122 (Vol. 103, p. 59-81). Academic Press. doi: 10.1016/B978-0-12-391851-2.00003-9

- 1123 Gröger, M., Arneborg, L., Dieterich, C., Höglund, A., & Meier, H. (2019). Summer hy-
 1124 drographic changes in the baltic sea, kattegat and skagerrak projected in an ensemble
 1125 of climate scenarios downscaled with a coupled regional ocean–sea ice–atmosphere
 1126 model. *Climate Dynamics*, 53(9), 5945–5966. doi: 10.1007/s00382-019-04908-9
- 1127 Grooms, I., & Julien, K. (2018). Multiscale models in geophysical fluid dynamics. *Earth*
 1128 *and Space Science*, 5(11), 668–675. doi: 10.1029/2018EA000439
- 1129 Gustafsson, B. (1997). Interaction between baltic sea and north sea. *Deutsche Hydrografische*
 1130 *Zeitschrift*, 49(2), 165–183. doi: 10.1007/BF02764031
- 1131 Haapaniemi, V., Tuomi, L., Björkqvist, J.-V., Twelves, A., Murawski, J., Kanarik, H., ...
 1132 Nummelin, A. (2026). Surface wave impacts on turbulent roughness length parame-
 1133 terization. *Ocean Modelling*, 202, 102742. doi: 10.1016/j.ocemod.2026.102742
- 1134 Haidvogel, D., Arango, H., Budgell, W., Cornuelle, B., Curchitser, E., Di Lorenzo, E., ...
 1135 Wilkin, J. (2008). Ocean forecasting in terrain-following coordinates: Formulation
 1136 and skill assessment of the regional ocean modeling system. *Journal of Computational*
 1137 *Physics*, 227(7), 3595–3624. doi: 10.1016/j.jcp.2007.06.016
- 1138 Hao, R., Zhao, Y., Zhang, S., & Deng, X. (2025). Deep learning for ocean forecasting: A
 1139 comprehensive review of methods, applications, and datasets. *IEEE Transactions on*
 1140 *Cybernetics*, 55(6), 2879–2898. doi: 10.1109/TCYB.2025.3539990
- 1141 Hariri, S., Väli, G., & Meier, H. E. M. (2025). Impact of coastal currents and eddies on
 1142 particle dispersion in the baltic sea: a lagrangian approach to marine ecosystems.
 1143 *Frontiers in Marine Science*, 12, 1545035. doi: 10.3389/fmars.2025.1545035
- 1144 Hayatihozani, A., Barzandeh, A., Maljutenko, I., & Raudsepp, U. (2026). Convolutional
 1145 autoencoder latent-space modeling with climate-index-conditioned recurrent
 1146 networks for assessing subseasonal potential forecast skill of the baltic sea heat content. *Engineering Applications of Artificial Intelligence*, 176, 114807. doi: 10.1016/j.engappai.2026.114807
- 1149 He, K., Zhang, X., Ren, S., & Sun, J. (2015). Delving deep into rectifiers: Surpassing human-
 1150 level performance on imagenet classification. In *2015 IEEE international conference on*
 1151 *computer vision (iccv)* (p. 1026–1034). doi: 10.1109/ICCV.2015.123
- 1152 Heimbach, P., O’Donncha, F., Smith, T. A., Garcia-Valdecasas, J. M., Arnaud, A., & Wan,
 1153 L. (2025). Crafting the future: Machine learning for ocean forecasting. *State of the*
 1154 *Planet*, 5-opsr, 22. doi: 10.5194/sp-5-opsr-22-2025
- 1155 Hersbach, H., Bell, B., Berrisford, P., Biavati, G., Horányi, A., Muñoz Sabater, J., ...
 1156 Thépaut, J.-N. (2023). *ERA5 hourly data on single levels from 1940 to present*
 1157 *[Dataset]*. Copernicus Climate Change Service (C3S) Climate Data Store (CDS).
 1158 Retrieved from <https://doi.org/10.24381/cds.adbb2d47> (Accessed 31 July 2025)
 1159 doi: 10.24381/cds.adbb2d47
- 1160 Hersbach, H., Bell, B., Berrisford, P., Hirahara, S., Horányi, A., Muñoz-Sabater, J., ...
 1161 Thépaut, J.-N. (2020). The era5 global reanalysis. *Quarterly Journal of the Royal*
 1162 *Meteorological Society*, 146(730), 1999–2049. doi: 10.1002/qj.3803
- 1163 Heuer, H., Schwabe, M., Gentine, P., Giorgetta, M. A., & Eyering, V. (2024). Inter-
 1164 pretable multiscale machine learning-based parameterizations of convection for
 1165 icon. *Journal of Advances in Modeling Earth Systems*, 16(8), e2024MS004398. doi:
 1166 10.1029/2024MS004398
- 1167 Holmberg, D., Clementi, E., Epicoco, I., & Roos, T. (2025). Accurate mediterranean
 1168 sea forecasting via graph-based deep learning. *Scientific Reports*, 15, 45051. doi:
 1169 10.1038/s41598-025-31177-w
- 1170 Huang, L., Jing, Y., Chen, H., Zhang, L., & Liu, Y. (2022). A regional wind wave prediction
 1171 surrogate model based on cnn deep learning network. *Applied Ocean Research*, 126,
 1172 103287. doi: 10.1016/j.apor.2022.103287
- 1173 Hutchinson, M. (1990). A stochastic estimator of the trace of the influence matrix for lapla-
 1174 cian smoothing splines. *Communications in Statistics - Simulation and Computation*,
 1175 19(2), 433–450. doi: 10.1080/03610919008812866
- 1176 Jahanmard, V., Ellmann, A., & Delpeche-Ellmann, N. (2025). Quantification of baltic sea
 1177 water budget components using dynamic topography. *Ocean Science*, 21(3), 913–930.

- doi: 10.5194/os-21-913-2025
- Jahanmard, V., Hordoir, R., Ramezani-Kebrya, A., Ellmann, A., Delpeche-Ellmann, N., et al. (2025). Principled fourier neural operators for high-resolution regional ocean modeling. *Authorea Preprints*. doi: 10.22541/essoar.176279300.07801097/v1
- Jiang, P., Yang, Z., Wang, J., Huang, C., Xue, P., Chakraborty, T., ... Qian, Y. (2023). Efficient super-resolution of near-surface climate modeling using the fourier neural operator. *Journal of Advances in Modeling Earth Systems*, 15(7), e2023MS003800. doi: 10.1029/2023MS003800
- Jędrasik, J., & Kowalewski, M. (2019). Mean annual and seasonal circulation patterns and long-term variability of currents in the baltic sea. *Journal of Marine Systems*, 193, 1-26. doi: 10.1016/j.jmarsys.2018.12.011
- Kanarik, H., Tuomi, L., Björkqvist, J.-V., & Kärnä, T. (2021). Improving Baltic Sea wave forecasts using modelled surface currents. *Ocean Dynamics*, 71(6), 635–653. Retrieved from 10.1007/s10236-021-01455-y doi: 10.1007/s10236-021-01455-y
- Kantha, L. H., & Clayson, C. A. (2000). Chapter 2 - introduction to numerical solutions. In *Numerical models of oceans and oceanic processes* (Vol. 66, p. 127-245). Academic Press. doi: 10.1016/S0074-6142(00)80007-8
- Karabil, S., Zorita, E., & Hünicke, B. (2018). Contribution of atmospheric circulation to recent off-shore sea-level variations in the baltic sea and the north sea. *Earth System Dynamics*, 9(1), 69–90. doi: 10.5194/esd-9-69-2018
- Kingma, D. P., & Ba, J. (2017). *Adam: A method for stochastic optimization*. Retrieved from <https://arxiv.org/abs/1412.6980>
- Kärnä, T., Ljungemyr, P., Falahat, S., Ringgaard, I., Axell, L., Korabel, V., ... Jandt-Scheelke, S. (2021). Nemo-nordic 2.0: Operational marine forecast model for the baltic sea. *Geosci. Model Dev.*, 14, 5731–5749. doi: 10.5194/gmd-14-5731-2021
- LeCun, Y. A., Bottou, L., Orr, G. B., & Müller, K.-R. (2012). Efficient backprop. In G. Montavon, G. B. Orr, & K.-R. Müller (Eds.), *Neural networks: Tricks of the trade: Second edition* (pp. 9–48). Berlin, Heidelberg: Springer Berlin Heidelberg. doi: 10.1007/978-3-642-35289-8_3
- Legler, D., Freeland, H., Lumpkin, R., Ball, G., McPhaden, M., North, S., ... Merrifield, M. (2015). The current status of the real-time in situ global ocean observing system for operational oceanography. *Journal of Operational Oceanography*, 8(sup2), s189–s200. doi: 10.1080/1755876X.2015.1049883
- Lehmann, A., & Hinrichsen, H.-H. (2000). On the wind driven and thermohaline circulation of the baltic sea. *Physics and Chemistry of the Earth, Part B: Hydrology, Oceans and Atmosphere*, 25(2), 183–189.
- Lehmann, A., & Myrberg, K. (2008). Upwelling in the baltic sea — a review. *Journal of Marine Systems*, 74, S3-S12. (Baltic Sea Science Congress 2007) doi: 10.1016/j.jmarsys.2008.02.010
- Lehmann, A., Myrberg, K., Post, P., Chubarenko, I., Dailidienė, I., Hinrichsen, H.-H., ... Bukanova, T. (2022). Salinity dynamics of the baltic sea. *Earth System Dynamics*, 13(1), 373–392. doi: 10.5194/esd-13-373-2022
- Leppäranta, M., & Myrberg, K. (2009). *Physical oceanography of the baltic sea*. Springer Science & Business Media. doi: 10.1007/978-3-540-79703-6
- Liblik, T., Buschmann, F., Siht, E., Kuprijanov, I., Väli, G., Lipp, M., ... Zekker, I. (2024). Environmental impact of water exchange blocking in a strait – a multidisciplinary study in the baltic sea. *Oceanologia*, 66(1), 9-25. doi: 10.1016/j.oceano.2023.06.002
- Liblik, T., Väli, G., Salm, K., Laanemets, J., Lilover, M.-J., & Lips, U. (2022). Quasi-steady circulation regimes in the baltic sea. *Ocean Science*, 18(3), 857–879. doi: 10.5194/os-18-857-2022
- Lips, U., Zhurbas, V., Skudra, M., & Väli, G. (2016a). A numerical study of circulation in the gulf of riga, baltic sea. part ii: Mesoscale features and freshwater transport pathways. *Continental Shelf Research*, 115, 44-52. doi: 10.1016/j.csr.2015.12.018
- Lips, U., Zhurbas, V., Skudra, M., & Väli, G. (2016b). A numerical study of circulation in the gulf of riga, baltic sea. part i: Whole-basin gyres and mean currents. *Continental*

- 1233 *Shelf Research*, 112, 1-13. doi: 10.1016/j.csr.2015.11.008
- 1234 Liu, G., Bracco, A., & Brajard, J. (2023). Systematic bias correction in ocean mesoscale
1235 forecasting using machine learning. *Journal of Advances in Modeling Earth Systems*,
1236 15, e2022MS003426. doi: 10.1029/2022MS003426
- 1237 Lou, R., Lv, Z., Dang, S., Su, T., & Li, X. (2023). Application of machine learning in ocean
1238 data. *Multimedia systems*, 29(3), 1815–1824. doi: 10.1007/s00530-020-00733-x
- 1239 Madec, G., Bourdallé-Badie, R., Bouttier, P.-A., Bricaud, C., Bruciaferri, D., Calvert, D.,
1240 ... Delrosso, D. (2017). *Nemo ocean engine*. Retrieved from [https://epic.awi.de/
1241 id/eprint/39698/1/NEMO_book_v6039.pdf](https://epic.awi.de/id/eprint/39698/1/NEMO_book_v6039.pdf)
- 1242 Maljutenko, I., & Raudsepp, U. (2019). Long-term mean, interannual and seasonal circula-
1243 tion in the gulf of finland — the wide salt wedge estuary or gulf type rofi. *Journal of
1244 Marine Systems*, 195, 1-19. doi: 10.1016/j.jmarsys.2019.03.004
- 1245 Manss, C., & El-Mihoub, T. A. (2026). Evaluation of explanations for object detection using
1246 transformers with sonar data. In M. Bramer & F. Stahl (Eds.), *Artificial intelligence
1247 xlii* (pp. 165–178). Springer Nature Switzerland.
- 1248 Manucharyan, G. E., Siegelman, L., & Klein, P. (2021). A deep learning approach to
1249 spatiotemporal sea surface height interpolation and estimation of deep currents in
1250 geostrophic ocean turbulence. *Journal of Advances in Modeling Earth Systems*, 13(1),
1251 e2019MS001965. doi: 10.1029/2019MS001965
- 1252 Marquardt, D. W. (1963). An algorithm for least-squares estimation of nonlinear paramete-
1253 rs. *Journal of the Society for Industrial and Applied Mathematics*, 11(2), 431-441.
1254 doi: 10.1137/0111030
- 1255 Meier, H. E. M. (2007). Modeling the pathways and ages of inflowing salt- and freshwater
1256 in the baltic sea. *Estuarine, Coastal and Shelf Science*, 74(4), 717–734. doi: 10.1016/
1257 j.ecss.2007.05.019
- 1258 Meier, H. E. M., Kniebusch, M., Dieterich, C., Gröger, M., Zorita, E., Elmgren, R., ...
1259 Zhang, W. (2022). Climate change in the baltic sea region: a summary. *Earth System
1260 Dynamics*, 13(1), 457–593. doi: 10.5194/esd-13-457-2022
- 1261 Mhaskar, H., Liao, Q., & Poggio, T. (2017). When and why are deep networks better than
1262 shallow ones? In *Proceedings of the aaai conference on artificial intelligence* (Vol. 31).
1263 Retrieved from [https://doi.org/10.1609/aaai.
1264 v31i1.10913](https://doi.org/10.1609/aaai.v31i1.10913) doi: 10.1609/aaai.v31i1.10913
- 1265 Miedtank, A., Schneider, J., Manss, C., & Zielinski, O. (2024). Marine digital twins for en-
1266 hanced ocean understanding. *Remote Sensing Applications: Society and Environment*,
1267 36, 101268. doi: 10.1016/j.rsase.2024.101268
- 1268 Mohrholz, V. (2018). Major baltic inflow statistics – revised. *Frontiers in Marine Science*,
1269 5, 384. doi: 10.3389/fmars.2018.00384
- 1270 Montavon, G., Binder, A., Lapuschkin, S., Samek, W., & Müller, K.-R. (2019). Layer-
1271 wise relevance propagation: An overview. In W. Samek, G. Montavon, A. Vedaldi,
1272 L. K. Hansen, & K.-R. Müller (Eds.), *Explainable ai: Interpreting, explaining and
1273 visualizing deep learning* (pp. 193–209). Cham: Springer International Publishing.
1274 doi: 10.1007/978-3-030-28954-6_10
- 1275 Myrberg, K., & Lehmann, A. (2013). Topography, hydrography, circulation and modelling
1276 of the baltic sea. In T. Soomere & E. Quak (Eds.), *Preventive methods for coastal
1277 protection: Towards the use of ocean dynamics for pollution control* (pp. 31–64). Hei-
1278 delberg: Springer International Publishing. doi: 10.1007/978-3-319-00440-2_2
- 1279 Nagi, J., Ducatelle, F., Di Caro, G. A., Cireşan, D., Meier, U., Giusti, A., ... Gambardella,
1280 L. M. (2011). Max-pooling convolutional neural networks for vision-based hand gesture
1281 recognition. In *2011 ieee international conference on signal and image processing
1282 applications (icsipa)* (p. 342-347). doi: 10.1109/ICSIPA.2011.6144164
- 1283 Nair, V., & Hinton, G. E. (2010). Rectified linear units improve restricted boltzmann
1284 machines. In *Proceedings of the 27th international conference on international confer-
1285 ence on machine learning* (p. 807–814). Retrieved from [https://dl.acm.org/doi/
1286 10.5555/3104322.3104425](https://dl.acm.org/doi/10.5555/3104322.3104425)
- 1287 Neumann, T., Radtke, H., & Seifert, T. (2017). On the importance of major baltic inflows

- 1288 for oxygenation of the central baltic sea. *Journal of Geophysical Research: Oceans*,
1289 *122*(2), 1090-1101. doi: 10.1002/2016JC012525
- 1290 Nielsen, M. H. (2005). The baroclinic surface currents in the kattegat. *Journal of Marine*
1291 *Systems*, *55*(3), 97-121. doi: 10.1016/j.jmarsys.2004.08.004
- 1292 Odena, A., Dumoulin, V., & Olah, C. (2016). Deconvolution and checkerboard artifacts.
1293 *Distill*. Retrieved from <http://distill.pub/2016/deconv-checkerboard> doi: 10
1294 .23915/distill.00003
- 1295 Omstedt, A., Elken, J., Lehmann, A., Leppäranta, M., Meier, H., Myrberg, K., & Rut-
1296 gersson, A. (2014). Progress in physical oceanography of the baltic sea during
1297 the 2003–2014 period. *Progress in Oceanography*, *128*, 139-171. doi: 10.1016/
1298 j.pocean.2014.08.010
- 1299 Onken, R., Baschek, B., & Angel-Benavides, I. M. (2020). Very high-resolution modelling
1300 of submesoscale turbulent patterns and processes in the baltic sea. *Ocean Science*,
1301 *16*(3), 657–684. doi: 10.5194/os-16-657-2020
- 1302 O’Shea, K., & Nash, R. (2015). An introduction to convolutional neural networks. *CoRR*,
1303 *abs/1511.08458*. Retrieved from <http://arxiv.org/abs/1511.08458>
- 1304 Panteleit, T., Verjovkina, S., Jandt-Scheelke, S., Spruch, L., & Huess, V. (2025).
1305 *Quality information document: Baltic sea physics reanalysis product (baltic-*
1306 *sea-multiyear_phy_003_011)*. Retrieved from [https://documentation.marine](https://documentation.marine.copernicus.eu/QUID/CEMS-BAL-QUID-003-011.pdf)
1307 [.copernicus.eu/QUID/CEMS-BAL-QUID-003-011.pdf](https://documentation.marine.copernicus.eu/QUID/CEMS-BAL-QUID-003-011.pdf) (Baltic Sea Production Centre)
1308
- 1309 Pawar, S., & San, O. (2022). Equation-free surrogate modeling of geophysical flows at
1310 the intersection of machine learning and data assimilation. *Journal of Advances in*
1311 *Modeling Earth Systems*, *14*, e2022MS003170. doi: 10.1029/2022MS003170
- 1312 Perezhogin, P., Fernandez-Granda, C., & Zanna, L. (2023). Generative data-driven ap-
1313 proaches for stochastic subgrid parameterizations in an idealized ocean model. *Jour-*
1314 *nal of Advances in Modeling Earth Systems*, *15*, e2023MS003681. doi: 10.1029/
1315 2023MS003681
- 1316 Placke, M., Meier, H. E. M., Gräwe, U., Neumann, T., Frauen, C., & Liu, Y. (2018). Long-
1317 term mean circulation of the baltic sea as represented by various ocean circulation
1318 models. *Frontiers in Marine Science*, *5*, 287. doi: 10.3389/fmars.2018.00287
- 1319 Pärt, S., Björkqvist, J.-V., Alari, V., Maljutenko, I., & Uiboupin, R. (2023). An
1320 ocean–wave–trajectory forecasting system for the eastern baltic sea: Validation against
1321 drifting buoys and implementation for oil spill modeling. *Marine Pollution Bulletin*,
1322 *195*, 115497. doi: 10.1016/j.marpolbul.2023.115497
- 1323 Raudsepp, U., Maljutenko, I., Barzandeh, A., Uiboupin, R., & Lagemaa, P. (2023). Baltic
1324 sea freshwater content. *State of the Planet, 1-osr7*, 7. doi: 10.5194/sp-1-osr7-7-2023
- 1325 Ronneberger, O., Fischer, P., & Brox, T. (2015). U-net: Convolutional networks for biomed-
1326 ical image segmentation. In N. Navab, J. Hornegger, W. M. Wells, & A. F. Frangi
1327 (Eds.), *Medical image computing and computer-assisted intervention – miccai 2015*
1328 (pp. 234–241). Cham: Springer International Publishing.
- 1329 Ross, A. S., Li, Z., Perezhogin, P., & Zanna, L. (2023). Benchmarking of machine learn-
1330 ing ocean subgrid parameterizations in an idealized model. *Journal of Advances in*
1331 *Modeling Earth Systems*, *15*(1), e2022MS003258. doi: 10.1029/2022MS003258
- 1332 Rus, M., Fettich, A., Kristan, M., & Ličer, M. (2023). Hidra2: deep-learning ensemble sea
1333 level and storm tide forecasting in the presence of seiches – the case of the northern
1334 adriatic. *Geoscientific Model Development*, *16*(1), 271–288. doi: 10.5194/gmd-16-271
1335 -2023
- 1336 Rutgersson, A., Kjellström, E., Haapala, J., Stendel, M., Danilovich, I., Drews, M., ...
1337 Wasmund, N. (2022). Natural hazards and extreme events in the baltic sea region.
1338 *Earth System Dynamics*, *13*(1), 251–301. doi: 10.5194/esd-13-251-2022
- 1339 Ryzhov, E., Kondrashov, D., Agarwal, N., & Berloff, P. (2019). On data-driven augmen-
1340 tation of low-resolution ocean model dynamics. *Ocean Modelling*, *142*, 101464. doi:
1341 10.1016/j.ocemod.2019.101464
- 1342 Röhrs, J., Sutherland, G., Jeans, G., Bedington, M., Sperrevik, A. K., Dagstad, K.-F., ...

- 1343 LaCasce, J. H. (2023). Surface currents in operational oceanography: Key applica-
 1344 tions, mechanisms, and methods. *Journal of Operational Oceanography*, *16*(1), 60–88.
 1345 doi: 10.1080/1755876X.2021.1903221
- 1346 Salm, K., Väli, G., Liblik, T., & Lips, U. (2025). Forcing-dependent submesoscale variability
 1347 and subduction in a coastal sea area (gulf of finland, baltic sea). *Ocean Science*, *21*(5),
 1348 2555–2577. doi: 10.5194/os-21-2555-2025
- 1349 Sane, A., Reichl, B. G., Adcroft, A., & Zanna, L. (2023). Parameterizing vertical mix-
 1350 ing coefficients in the ocean surface boundary layer using neural networks. *Jour-
 1351 nal of Advances in Modeling Earth Systems*, *15*(10), e2023MS003890. doi: 10.1029/
 1352 2023MS003890
- 1353 Simonyan, K., Vedaldi, A., & Zisserman, A. (2014). *Deep inside convolutional networks:
 1354 Visualising image classification models and saliency maps*. Retrieved from [https://
 1355 arxiv.org/abs/1312.6034](https://arxiv.org/abs/1312.6034)
- 1356 Sinha, A., & Abernathey, R. (2021). Estimating ocean surface currents with machine
 1357 learning. *Frontiers in Marine Science*, *8*, 672477. doi: 10.3389/fmars.2021.672477
- 1358 Song, T., Pang, C., Hou, B., Xu, G., Xue, J., Sun, H., & Meng, F. (2023). A review of
 1359 artificial intelligence in marine science. *Frontiers in Earth Science*, *11*, 1090185. doi:
 1360 10.3389/feart.2023.1090185
- 1361 Sonnewald, M., Lguensat, R., Jones, D. C., Dueben, P. D., Brajard, J., & Balaji, V. (2021).
 1362 Bridging observations, theory and numerical simulation of the ocean using machine
 1363 learning. *Environmental Research Letters*, *16*(7), 073008. doi: 10.1088/1748-9326/
 1364 ac0eb0
- 1365 Soosaar, E., Maljutenko, I., Raudsepp, U., & Elken, J. (2014). An investigation of anticy-
 1366 clonic circulation in the southern gulf of riga during the spring period. *Continental
 1367 Shelf Research*, *78*, 75–84. doi: 10.1016/j.csr.2014.02.009
- 1368 Traon, P.-Y. L., Antoine, D., Bentamy, A., Bonekamp, H., Breivik, L., Chapron, B., ...
 1369 Wilkin, J. (2015). Use of satellite observations for operational oceanography: recent
 1370 achievements and future prospects. *Journal of Operational Oceanography*, *8*(sup1),
 1371 s12–s27. doi: 10.1080/1755876X.2015.1022050
- 1372 van der Meer, M., Selten, F., Haarsma, R., & Hazeleger, W. (2023). Deep learning re-
 1373 gional climate model emulators: A comparison of two downscaling training frame-
 1374 works. *Journal of Advances in Modeling Earth Systems*, *15*(3), e2022MS003593. doi:
 1375 10.1029/2022MS003593
- 1376 Vortmeyer-Kley, R., Holtermann, P., Feudel, U., & Gräwe, U. (2019). Comparing eulerian
 1377 and lagrangian eddy census for a tide-less, semi-enclosed basin, the baltic sea. *Ocean
 1378 Dynamics*, *69*(6), 701–717. doi: 10.1007/s10236-019-01269-z
- 1379 Väli, G., Meier, H. M., Liblik, T., Radtke, H., Klingbeil, K., Gräwe, U., & Lips, U. (2024).
 1380 Submesoscale processes in the surface layer of the central baltic sea: A high-resolution
 1381 modelling study. *Oceanologia*, *66*(1), 78–90. doi: 10.1016/j.oceano.2023.11.002
- 1382 Väli, G., Zhurbas, V., Lips, U., & Laanemets, J. (2017). Submesoscale structures related
 1383 to upwelling events in the gulf of finland, baltic sea (numerical experiments). *Journal
 1384 of Marine Systems*, *171*, 31–42. doi: 10.1016/j.jmarsys.2016.06.010
- 1385 Wang, Q., Qian, J., Mu, M., Liang, P., & Qin, B. (2025). The predictability study of oceanic
 1386 deep learning models: Taking kuroshio intrusion into south china sea as an example.
 1387 *Ocean Modelling*, *198*, 102622. doi: 10.1016/j.ocemod.2025.102622
- 1388 Wu, Y., & He, K. (2020). Group normalization. *International Journal of Computer Vision*,
 1389 *128*, 742–755. doi: 10.1007/s11263-019-01198-w
- 1390 Xu, Z., Ren, J., Zhang, Y., Gonzalez Ondina, J. M., Olabarrieta, M., et al. (2024). *A fast
 1391 ai surrogate for coastal ocean circulation models*. arXiv:2410.14952. Retrieved from
 1392 <https://arxiv.org/abs/2410.14952>
- 1393 Yuan, B., Jacob, B., Chen, W., & Staneva, J. (2024). Downscaling sea surface height
 1394 and currents in coastal regions using convolutional neural network. *Applied Ocean
 1395 Research*, *151*, 104153. doi: 10.1016/j.apor.2024.104153
- 1396 Zavala-Romero, O., Bozec, A., Chassignet, E. P., & Miranda, J. R. (2025). Convolutional
 1397 neural networks for sea surface data assimilation in operational ocean models: test case

- 1398 in the gulf of mexico. *Ocean Science*, 21(1), 113–132. doi: 10.5194/os-21-113-2025
- 1399 Zhang, C., Perezhogin, P., Adcroft, A., & Zanna, L. (2025). Addressing out-of-sample
1400 issues in multi-layer convolutional neural-network parameterization of mesoscale ed-
1401 dies applied near coastlines. *Journal of Advances in Modeling Earth Systems*, 17(5),
1402 e2024MS004819. doi: 10.1029/2024MS004819
- 1403 Zhang, C., Perezhogin, P., Gultekin, C., Adcroft, A., Fernandez-Granda, C., & Zanna, L.
1404 (2023). Implementation and evaluation of a machine learned mesoscale eddy parame-
1405 terization into a numerical ocean circulation model. *Journal of Advances in Modeling*
1406 *Earth Systems*, 15(12), e2023MS003697. doi: 10.1029/2023MS003697
- 1407 Zhang, L., Duan, W., Cui, X., Liu, Y., & Huang, L. (2024). Surface current prediction based
1408 on a physics-informed deep learning model. *Applied Ocean Research*, 148, 104005. doi:
1409 <https://doi.org/10.1016/j.apor.2024.104005>
- 1410 Zhao, Q., Peng, S., Wang, J., Li, S., Hou, Z., & Zhong, G. (2024). Applications of deep learn-
1411 ing in physical oceanography: a comprehensive review. *Frontiers in Marine Science*,
1412 11, 1396322. doi: 10.3389/fmars.2024.1396322
- 1413 Zhao, X., Wang, L., Zhang, Y., et al. (2024). A review of convolutional neural networks
1414 in computer vision. *Artificial Intelligence Review*, 57(99). doi: 10.1007/s10462-024-
1415 -10721-6

Curriculum Vitae

1. Personal data

Name Amirhossein Barzandeh
Date and place of birth 21 March 1991 Amol, Iran
Nationality Iranian

2. Contact information

Address Tallinn University of Technology, School of Science,
Department of Marine Systems,
Akadeemia tee 15a (2nd stairway, 3rd floor), 12618 Tallinn, Estonia
Phone +372 58437115
E-mail amirhossein.barzandeh@taltech.ee

3. Education

2021–2026 Tallinn University of Technology, School of Sciences,
Earth Science, PhD
2014–2017 University of Isfahan, Faculty of Physics,
Physical Oceanography, MSc
2010–2014 Petroleum University of Technology, Faculty of Marine Engineering,
Marine Engineering, BSc

4. Language competence

Persian native
English fluent
Estonian beginner

5. Defended theses

- 2017, Sensible Kinetic Heat Flux of Ocean-Atmosphere: Calculation and Effect of the Physical Parameters, MSc, supervisor Prof. Smaeyl Hassanzadeh, University of Isfahan, Faculty of Physics
- 2014, Multidisciplinary Design Optimization for Fuel Performance of a Tanker by the Genetic Algorithm, BSc, supervisor Dr. Pedram Edalat, Petroleum University of Technology, Faculty of Marine Engineering

6. Field of research

- Physical Oceanography
- Numerical Simulation
- Data-driven Emulation

Papers

1. A. Hayatijozani, **A. Barzandeh**, I. Maljutenko, and U. Raudsepp. *Convolutional auto-encoder latent-space modeling with climate-index-conditioned recurrent networks for assessing subseasonal potential forecast skill of the Baltic Sea heat content*. Engineering Applications of Artificial Intelligence, 176, 114807, 2026.

2. **A. Barzandeh**, C. Manss, F. Stahl, I. Maljutenko, S. Rikka, and U. Raudsepp. Data-Driven Emulation of Numerically Simulated Baltic Sea Surface Currents with a Deep Convolutional U-Net: Explainability and Potential Forecast Skill. *JGR: Machine Learning and Computation* (Accepted), 2026.
3. **A. Barzandeh**, I. Maljutenko, S. Rikka, and U. Raudsepp. *sciCUN: A deep learning model for daily sea surface current fields inference—A case study of the Gulf of Riga*. *Ocean modeling*, 201, 102693, 2026.
4. B. Bashiri, **A. Barzandeh**, A. Männik, R. Uiboupin, and U. Raudsepp. *Marine Heat-wave Event Maps in the Baltic Sea (1982–2023): A Gridded Dataset from Satellite-Derived L4 SST*. *Scientific Data*, 2025.
5. V. V. Gudimetla, A. Hayatijozani, **A. Barzandeh**, I. Maljutenko, R. Uiboupin, A. Männik, and U. Raudsepp. *Self-Organizing Map–Derived Regimes as a Basis for Basin-Integrated Diagnostics of Baltic Sea Hydrographic Change (1993–2023)*. *Research Square*, preprint, Version 1, 2025.
6. U. Raudsepp, I. Maljutenko, J.-V. Björkqvist, **A. Barzandeh**, S. Rikka, A. Männik, S. Pärt, P. Lagemaa, V. Alari, K. Vahter, and R. Uiboupin. *Metocean study for the planning of the FSRU terminal: a case study at the Estonian coast of the Gulf of Finland*. *State of the Planet Discussions*, 2025, 1–25, 2025.
7. U. Raudsepp, U. Ahmadov, I. Maljutenko, **A. Barzandeh**, M. Kõuts, and P. Lagemaa. *Long term trends and variability of the mixed layer depth in the Baltic Sea*. *State of the Planet Discussions*, 2025, 1–17, 2025.
8. **A. Barzandeh**, M. Ličer, M. Rus, M. Kristan, I. Maljutenko, J. Elken, P. Lagemaa, and R. Uiboupin. *Application of the HIDRA2 deep-learning model for sea level forecasting along the Estonian coast of the Baltic Sea*. *Ocean Science*, 21(4), 1315–1327, 2025.
9. F. Salimi, **A. Barzandeh**, and N. Eshghi. *Wave energy extracting near Siri Island by using new energy converter type selection coefficient*. *International Journal of Energy and Water Resources*, 9(3), 1221–1236, 2025.
10. N. Eshghi, **A. Barzandeh**, and F. Salimi. *Interannual and interseasonal variability of the Persian Gulf surface wave energy in the recent decade*. *Marine Systems & Ocean Technology*, 19(1), 155–164, 2024.
11. B. Bashiri, **A. Barzandeh**, A. Männik, and U. Raudsepp. *Variability of marine heat-waves' characteristics and assessment of their potential drivers in the Baltic Sea over the last 42 years*. *Scientific Reports*, 14(1), 22419, 2024.
12. **A. Barzandeh**, I. Maljutenko, S. Rikka, P. Lagemaa, A. Männik, R. Uiboupin, and U. Raudsepp. *Sea surface circulation in the Baltic Sea: decomposed components and pattern recognition*. *Scientific Reports*, 14(1), 18649, 2024.
13. J. Elken, **A. Barzandeh**, I. Maljutenko, and S. Rikka. *Reconstruction of Baltic Gridded Sea Levels from Tide Gauge and Altimetry Observations Using Spatiotemporal Statistics from Reanalysis*. *Remote Sensing*, 16(15), 2702, 2024.
14. M. Z. Zarandi, **A. Barzandeh**, S. Hassanzadeh, and R. Z. Zarandi. *Investigating an upwelling system along the eastern Makran coast*. *Bulletin of Geophysics & Oceanography*, 65(1), 2024.

15. U. Raudsepp, I. Maljutenko, **A. Barzandeh**, R. Uiboupin, and P. Lagemaa. *Baltic Sea freshwater content*. State of the Planet, 1-osr7, 7, 2023.
16. N. Eshghi, **A. Barzandeh**, F. Hosseinibalam, and S. Hassanzadeh. *Investigating dynamic and static aspects of regional sea level changes in the north-western Indian Ocean*. Bollettino di Geofisica Teorica ed Applicata, 61(2), 2020.
17. **A. Barzandeh**, N. Eshghi, F. Hosseinibalam, and S. Hassanzadeh. *Wind-driven coastal upwelling along the northern shoreline of the Persian Gulf*. Bollettino di Geofisica Teorica ed Applicata, 59(3), 2018.
18. P. Edalat and **A. Barzandeh**. *Fuel efficiency optimization of tanker with focus on hull parameters*. Journal of Ocean Engineering and Science, 2(2), 76–82, 2017.

Conference presentations

1. **A. Barzandeh**, C. Manß, F. Stahl, I. Maljutenko, S. Rikka, and U. Raudsepp. *Partial Emulation of Simulated Sea-Surface Currents in the Baltic Sea: An Assessment of Explainability and Potential Forecast Skill*. EGU General Assembly 2026, 3–8 May 2026, Vienna, Austria.
2. **A. Barzandeh**, I. Maljutenko, S. Rikka, and U. Raudsepp. *Data-Driven Retrieval of Ageostrophic Surface Currents from Satellite Geostrophy and Reanalysis Winds in a Marginal Sea*. 5th ECMWF–ESA Machine Learning Workshop, 13–17 April 2026, Bologna, Italy.
3. **A. Barzandeh**, I. Maljutenko, S. Rikka, and U. Raudsepp. *Sea Surface Current Fields Prediction with a Surrogate Deep Learning Model Using CNN-UNET: A Case Study of the Gulf of Riga*. Baltic Sea Science Congress 2025, 26–30 May 2025, Sopot, Poland.
4. A. Hayatijozani, **A. Barzandeh**, I. Maljutenko and U. Raudsepp. *Spatiotemporal variation of ocean heat content: insight from 31 years of Baltic Sea Reanalysis Data (1993-2023)*. Baltic Sea Science Congress 2025, 26–30 May 2025, Sopot, Poland.
5. B. Bashiri, **A. Barzandeh**, A. Männik and U. Raudsepp. *Marine Heatwave Event Maps in the Baltic Sea (1982–2023): A High-Resolution Dataset from Satellite-Derived L4 SST Observations*. Baltic Sea Science Congress 2025, 26–30 May 2025, Sopot, Poland.
6. V. V. Gudimetla, **A. Barzandeh** and U. Raudsepp. *Long term monthly evolution of a coupled temperature and salinity stratification of the Baltic Sea*. Baltic Sea Science Congress 2025, 26–30 May 2025, Sopot, Poland.
7. U. Ahmadov, U. Raudsepp, **A. Barzandeh**, I. Maljutenko, and P. Lagemaa. *Long term trends and variability of the mixed layer depth in the Baltic Sea*. Baltic Sea Science Congress 2025, 26–30 May 2025, Sopot, Poland.
8. **A. Barzandeh**, I. Maljutenko, S. Rikka, and U. Raudsepp. *A Surrogate Model for Daily Sea Surface Current Fields Prediction Using CNN-UNET*. EGU General Assembly 2025, 27 April–2 May 2025, Vienna, Austria.
9. **A. Barzandeh**, M. Rus, M. Ličer, I. Maljutenko, J. Elken, P. Lagemaa, R. Uiboupin. *Evaluating the application of deep-learning ensemble sea-level and storm surge forecasting in the Baltic Sea*. EGU General Assembly 2024, 14 April–19 April 2024, Vienna, Austria.

10. **A. Barzandeh.** *Sea surface current components in the Baltic Sea.* The School of Science XV Conference 2023, 29 November 2023, Tallinn, Estonia.
11. **A. Barzandeh,** I. Maljutenko, S. Rikka, and U. Raudsepp. *Geostrophic and Ageostrophic Components of Sea Surface Currents in the Baltic Sea.* Baltic Sea Science Congress 2023, 21–25 May 2023, Helsinki, Finland.
12. **A. Barzandeh,** I. Maljutenko, S. Rikka, and U. Raudsepp. *Geostrophic component of sea surface current in the Baltic Sea.* International Baltic Earth Winter School for Young Scientists on "Earth System Science for the Baltic Sea Region" 2023, 17–21 March 2023, Warnemünde, Germany.

Elulookirjeldus

1. Isikuandmed

Nimi	Amirhossein Barzandeh
Sünniaeg ja -koht	21. märts 1991, Amol, Iraan
Kodakondsus	Iraan

2. Kontaktandmed

Adress	Tallinna Tehnikaülikool, loodusteaduskond, Meresüsteemide osakond, Akadeemia tee 15a (2. trepikoda, 3. korrus), 12618 Tallinn, Eesti
Telefon	+372 58437115
E-post	amirhossein.barzandeh@taltech.ee

3. Haridus

2021–2026	Tallinna Tehnikaülikool, loodusteaduskond, maateadus, doktoriõpe
2014–2017	Isfahani Ülikool, füüsikateaduskond, füüsikaline okeanograafia, magistriõpe
2010–2014	Naftatehnoloogia Ülikool, meretehnika teaduskond, meretehnika, bakalaureuseõpe

4. Keelteoskus

pärsia keel	emakeel
inglise keel	sorav
eesti keel	algaja

5. Kaitstud lõputööd

- 2017, *Sensible Kinetic Heat Flux of Ocean-Atmosphere: Calculation and Effect of the Physical Parameters*, magistritöö, juhendaja Prof. Smaeyl Hassanzadeh, Isfahani Ülikool, füüsikateaduskond
- 2014, *Multidisciplinary Design Optimization for Fuel Performance of a Tanker by the Genetic Algorithm*, bakalaureusetöö, juhendaja Dr. Pedram Edalat, Naftatehnoloogia Ülikool, meretehnika teaduskond

6. Teadustöö põhisuunad

- Füüsikaline okeanograafia
- Numbriline modelleerimine
- Andmepõhine emulatsioon

ISSN 2585-6901 (PDF)
ISBN 978-9916-80-522-0 (PDF)